Molecular Iridium Oxidation Catalysts

Sackville, Emma

Award date:
2018

Awarding institution:
University of Bath

Molecular Iridium Oxidation Catalysts

E. V. Sackville

A thesis submitted for the Degree of Doctor of Philosophy

Department of Chemistry

University of Bath

June 2018

'I'm-a keep running 'cause a winner don't quit on themselves'

FREEDOM

Beyoncé ft. Kendrick Lamar

Acknowledgements

In all honesty, this has been one of the hardest things I've ever put myself through, and with that in mind the list of people who need thanking is a fairly extensive one.

Firstly, I'd like to thank my supervisor, Uli Hintermair, partly for taking me on as his first PhD student, but mainly for all his help and support during the PhD, and his insights and ideas for the project. Also for constantly reminding me that 'it's not complicated it's interesting'!

I'd also like to thank Frank Marken for his help with the electrochemistry. He was always available for advice and suggestions at a moment's notice and his expertise was invaluable. Thanks also to John Lowe for his help with setting up NMR experiments and to Antoine Buchard and Janet Scott who have also been constantly supportive throughout my PhD.

A big thanks to the Hinterbaes (Matt, StuB, Andy, Kasia, Rachael, Dan, Stef, Izzy) and members of the extended 5W SusChem lab and offices, past and present, for all the fun lab times and socials. Also thanks for listening to endless rants about electrochemistry and for sitting through my eclectic mix of musical tastes – I know you'll miss Disney at some point!

A few random thank yous: to my netball team for getting me out of the Bath PhD student bubble (and especially to Wheeler and Tami and those rooftop cocktails); to Ange and Alan for letting me stay with them at various point and doing all my ironing and not letting me leave the house without loads of food; to Maria, Amelia and Lois for all the prosecco and girls nights.

Another big thank you to my ever-diminishing Cohort 13 and in particular Jon, Oli, Coombs, Leighton, Helena and Jemma, for games nights, pub nights, chair breaking, tree singing and general sustainable fun! And especially to Helena and Jemma for their support and Harry Potter/northern based jokes.

To my Bristol girlies - thank you for our great reunion weekends, for helping me through the particularly rough middle part and putting up with me, and especially to Laura for all the random jokes and calls, which always cheered me up and to Cat and Ruth for mid-week dinners.

My parents also deserve a massive thank you for their constant love and encouragement throughout the PhD, with random trips to Bath for dinners, letting me move back home at various points, looking after me and for being there with a big bottle of prosecco at the end!

To my top baes Cait and Maya (aka The Feminist Agenda League) what can I say? Thanks for all the memes, the WhatsApp rants about sexism, the Tiki/toilet crying/Parade breaks, putting up with the thesis/viva stress, and all the sushi. But mainly thanks because you have been so supportive through the whole lot and generally just complete baes; you've been my Bath rocks.

And lastly an enormous thank you to Paul. For your help and insight with parts of my thesis and PhD, for dealing with all the rubbish that I've put you through over the last few years, for your constant and unwavering love and support despite everything, and for sticking by me through it all – thank you. You have been my anchor and I couldn't have done it without you.

Abstract

Oxidation reactions of both inorganic and organic substrates are among the most important chemical transformations, with application in sustainable chemistry and chemical synthesis. A library of half sandwich Ir^{III} oxidation complexes with varying ligands were synthesised (54-78% yield) and fully characterised (NMR, UV-vis, crystal data), in order to investigate the effect on catalyst activity for water and C-H oxidation reactions.

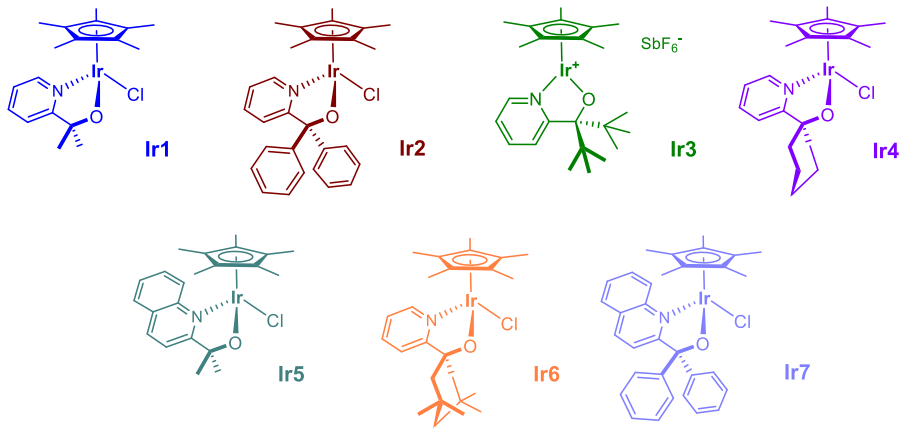

The electrochemical transition of Ir^{III} to Ir^{IV} was investigated (cyclic voltammetry (CV)) and found to vary between ligand sets, such that alkyl substituted compounds had a lower mid-point potential than aryl substituted. Solution speciation under aqueous conditions was also investigated for all complexes (UV-vis spectroscopy), as well as investigation into catalyst activation by oxidative loss of the pentamethylcyclopentadienyl ligand (^{1}H NMR, UV-vis spectroscopy).

The catalytic activity for complexes **Ir1**-**Ir7** was investigated for water oxidation with chemical oxidants, by oxygen evolution assays with a Clark electrode. All complexes evolved oxygen to some extent, with ligand effects causing significant variation in the rate of water oxidation (4.60 mM min^{-1} to 0.02 mM min^{-1} with sodium periodate in pure H_2O). Mechanistic studies including H/D kinetic isotope effects and reaction progress kinetic analysis showed primary KIEs of 1.3-2.5, indicating O-H cleavage to be in the rate determining step. Determination of the catalyst order revealed an order in iridium of 0.5-0.6 for **Ir1**-**Ir6** and 0.9 for **Ir7**, which was proposed to be due differences in the active catalyst species for **Ir7**.

The complexes were also tested for C-H oxidation performance and followed by ^{1}H NMR. The reaction profiles for precatalysts **Ir1**-**Ir7** all showed a plateau conversion with C-H oxidation, varying between 52% - 88%, which was attributed to a competition reaction with water oxidation. The varying ligands impart C-H/water oxidation selectivity onto the catalysts. The C-H oxidation scope was extended by investigations into the oxidation of several terpene-based compounds were also conducted (gas chromatography mass spectrometry, ^{1}H NMR).

Comparison of the water oxidation activity of the catalysts as driven by electrochemical potential (as followed by Clark electrode and chronoamperometry) exposed surprising trends that did not correlate with the chemical oxidant data and highlights the importance of reaction conditions when comparing water oxidation activity. Catalyst immobilisation was also attempted with a range of metal oxide supports (indium tin oxide on fluorine dope tin oxide glass, $BiVO_4$, Fe_2O_3) and analysis of the resulting electrode assessed by CV. Fourier transform alternating current voltammetry (FTACV) was employed in order to investigate the oxidation state of the iridium during electrochemical water oxidation, revealing a clear [Ir] redox transition at the foot of the catalytic wave, proposed to be a key transition to the active catalytic species.

Output

Publications

*Ligand Tuning in Pyridine-Alkoxide Ligated Cp*Ir^{III} Oxidation Catalysts*, E. Sackville, G. Kociok-Köhn, U. Hintermair, *Organometallics*, 2017, **36**, 3578-3588

*Evidence for Dimeric Active Sites in Molecular Water Oxidation Catalysts Derived from Cp*Ir(pyridine-alkoxide) Complexes*, E. Sackville, F. Marken, U. Hintermair, *ChemCatChem*, accepted, cover paper

Kinetics versus Charge Separation: Improving the Activity of Stoichiometric and Non-Stoichiometric Hematite Photoanodes Using a Molecular Iridium Water Oxidation Catalyst, J. Moir, E. Sackville, U. Hintermair, G. Ozin, J Phys Chem C, 2016, **24**, 12999-13012

Prizes

Jul 2017	CSCT Summer Showcase, best poster
Jun 2017	The Bolland Symposium, Bath, best oral presentation
May 2017	Finalist Vice Chancellor's Award for Public Engagement with Research
May 2017	Faculty of Science Winner/University Runner up 3 Minute Thesis
Jan 2016	11th AIESS, Melbourne, Australia, best poster
Apr 2016	Runner up Chemistry World Science Communication competition
Dec 2015	3rd Winter Processing Conference, Bath, best poster
May 2015	University of Bath Faculty of Science Research Symposium, best poster
May 2015	University of Bath Department of Chemistry Symposium, best poster
Apr 2015	South West regional winner/UK National Finalist FameLab
Jan 2015	3rd Solar Fuels Network Symposium, Edinburgh UK, poster commendation
Jul 2014	CSCT Summer Showcase, Bath UK, best poster

Conferences

Jul 2018	Great Western Electrochemistry Conference, Bath UK, oral presentation
Jan 2018	UK Catalysis Conference, Loughborough UK, oral presentation
Sep 2017	Dalton Younger Members Event, Bath UK, Conference Organiser
Apr 2017	RSC Dalton Division Sir Geoffry Wilkinson Poster Competition, London UK
Jun 2017	The Bolland Symposium, Bath UK, Conference Organiser
Sep 2016	MICRA, Bath UK, Conference Organiser
Apr 2015	Homogeneous Catalysis and Energy Conversion Symposium, Bath UK, oral communication and poster
May 2015	11th ECHEMS Meeting, Bad Zwischenahn Germany, poster presentation, RSC Electrochemistry travel bursary

Assorted

Mar 2017	Science Show Off Presenter
Sep 2016 – 2017	Co-chair of Bath Postgraduate Chemistry Committee
Aug 2016	Soap Box Science Presenter
Apr 2016	Internship with the Naked Scientists
Jan 2016	Internship at Monash University
Sep 2015 – 2017	PhD representative for RSC Dalton Division
Sep 2015 – 2016	Chair of CSCT Public Engagement Committee
Aug 2015	Einstein's Garden at Green Man, RSC outreach funding

Abbreviations

BDD – boron doped diamond

CAN – ceric ammonium nitrate

CE – counter electrode

Cp* – pentamethylcyclopentadienyl

CV – cyclic voltammetry

DCM – dichloromethane

dCV – direct current cyclic voltammetry

DLS – dynamic light scattering

DMA – dimethylacetamide

dTBP – distorted trigonal bipyrimidal

EBS – ethyl benzene sulphonate

EC' – electrochemical chemical reaction

EPR – electron paramagnetic resonance

EQCN – electrochemical quartz crystal nanobalance

FE – faradaic efficiencies

FOWA – foot of the wave analysis

FTAC – fourier transform alternating current

FTO – fluorine doped tin oxide

HMPA – hexamethylphosphoramide

Ir1* – activated iridium catalyst

IrOx – iridium oxides

ITO – indium tin oxide

KIE – kinetic isotope effect

MCPBA – meta-chloroperoxybenzoic acid

nanoITO|FTO – nanoITO on FTO glass

NMR – nuclear magnetic resonance

NPs – nanoparticles

OEC – oxygen evolving complex

ox – oxidant

PCET – proton coupled electron transfer

PSII – photosystem II

Pyalk – pyridine alkoxide

RDS – rate determining step

RE – reference electrode

RHE – reversible hydrogen electrode

RPKA – reaction progress kinetic analysis

ROC – radical oxyl coupling

tmbim – trimethyl-benzimidazolium

TOF – turnover frequency

TON – turnover number

UV-vis – ultraviolet-visible spectroscopy

VTNA – variable time normalised analysis

WE – working electrode

WNA – water nucleophilic attack

WOC – water oxidation catalyst

XPS – X-ray photoelectron spectroscopy

Contents

CHAPTER 1

INTRODUCTION

1. Introduction

First coined by Anastas in the early 1990s, the term Green Chemistry has become ever more ubiquitous as the scientific world focuses on the issues surrounding sustainability.[1,2] Arguably, one of the key driving forces towards Green Chemistry lies in the application of catalysis, both homogeneous and heterogeneous, as it can help reduce the need for auxiliaries, improve atom efficiency and therefore reduce waste, in addition to lowering the amount of reagent required and decreasing energy demands.[2,3]

The work reported herein addresses the application of catalysis to two key reactions: water and C-H oxidations. Iridium catalysts have previously shown great activity for both of these challenging oxidations and the development of such catalysts is crucial to expanding their application.

1.1 Water Oxidation

The current dependence on fossil fuels as a source of energy has led to myriad environmental issues, including global warming.[4] Notwithstanding the environmental concerns, increasing global energy demands and the finite nature of these resources has necessitated a focussed drive towards alternative, renewable energy sources such as solar, wind and tidal. [5–7]

However, one of the key drawbacks for renewable energy sources is that they tend to be diffuse and intermittent, and therefore require concentration and storage.[8] One way to circumvent this issue is to use the renewable energy generated to power electrolysis to produce hydrogen and oxygen.

Whilst hydrogen is well acknowledged as an energy carrier, in reality any reduced fuel can be produced. However, production of a reduced fuel requires reducing equivalents (i.e. electrons), which can only be achieved by a concurrent oxidation. The only viable and sufficiently plentiful source of reducing equivalents is from oxidation of water (Scheme 1.1).[8,9]

Scheme 1.1. *Water-oxidation (top) and proton reduction (bottom) half reactions of water splitting*

$$2H_2O \rightarrow O_2 + 4H^+ + 4e^- \qquad 1.23 \text{ V vs. RHE}$$

$$2H^+ + 2e^- \rightarrow H_2 \qquad 0.00 \text{ V vs. RHE}$$

It is the water oxidation half reaction which is often considered the energetic bottle neck of this technology because it is both thermodynamically uphill and has a high kinetic barrier, or over potential (1.23 V vs RHE (Reversible Hydrogen Electrode).[8,10] This is attributed to the multiple electron transfer steps required for production of four electrons and four protons.

In nature, water oxidation is driven by light energy in photosynthesis (Scheme 1.2), which is carried out in all green plants and algae by an enzyme, Photosystem II (PSII), where the reducing equivalents are used to synthesise sugars or carbohydrates.[10]

Scheme 1.2. *Photosynthesis reaction which occurs in green plants and algae*

$$H_2O + CO_2 \rightarrow [CH_2O] + O_2$$

The kinetic activation barrier to water oxidation requires a highly active metal centre which can support the multiple electron transfer steps. investigation into the active site in PSII by high resolution crystallographic data, revealed the active water oxidation centre, or the oxygen evolution complex (OEC), to be a tetra-manganese, Mn_4CaO_5 (Figure 1.1).[11]

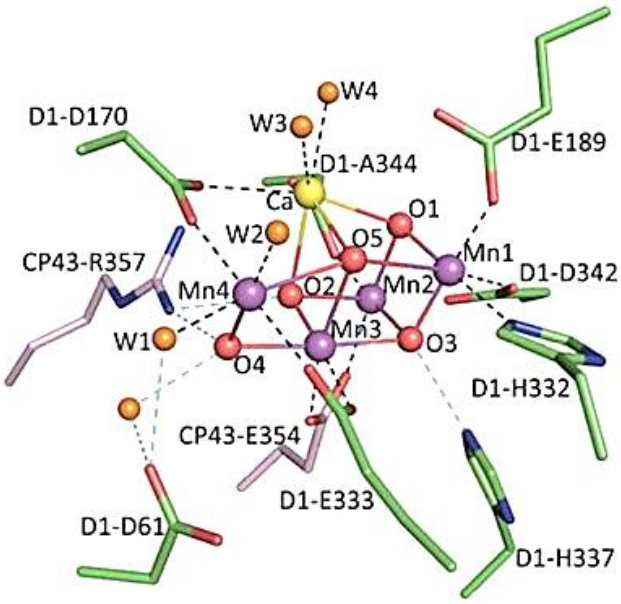

Figure 1.1. *The crystal structure of the oxygen evolving centre of PSII. Reproduced from Umena et al 2011*[11]

1.2 Synthetic water oxidation catalysts

Given the importance of the water oxidation reaction, the development of suitable water oxidation catalysts (WOCs) has been an active area of research, and a wide range of WOCs have been synthesised and characterised.[10] Both heterogeneous and homogeneous catalysts have been investigated, including metal oxides and poly-oxo-metallates[12–14] as well as molecular WOCs[15] and complexes based on the oxygen evolution complex found in photosystem II.[16,17] Many WOCs are multinuclear systems, due to belief that more than one metal centre was needed to perform the multiple electron transfer steps required in water oxidation.[5]

The first molecular homogeneous WOC was a dinuclear ruthenium complex (Figure 1.2) reported by Meyer in 1982,[18] and since then ruthenium has become a widely used as a water oxidation catalyst, with activity rivalling that of the OEC.[19] Despite the prevalent belief that WOCs needed several metal sites in order to accommodate multiple electron transfer, the first mononuclear WOC was reported in 2005 by Thummel.[20] Since this breakthrough, much work has been conducted into other suitable mononuclear catalysts.

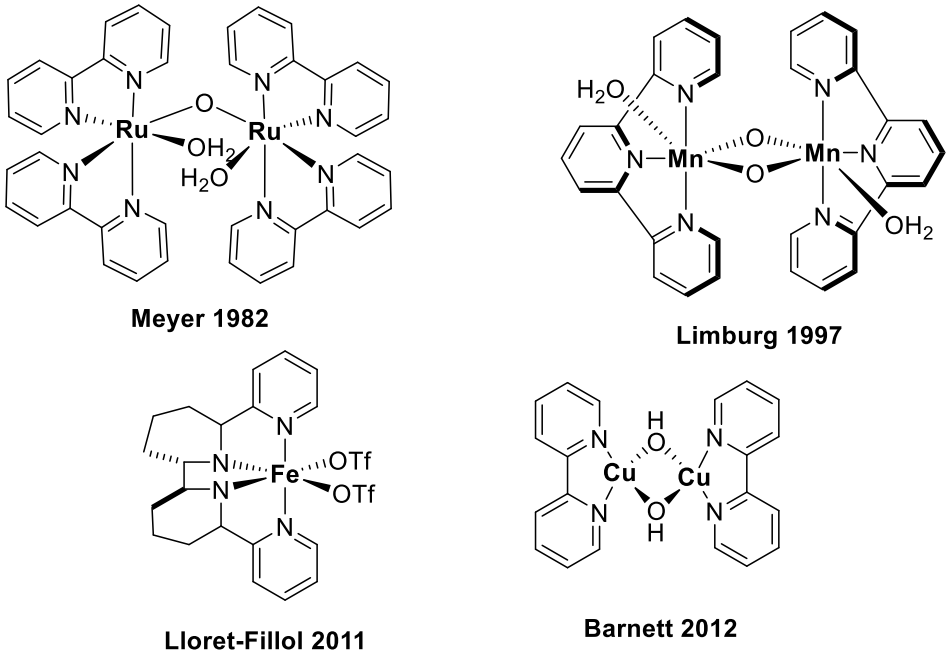

Figure 1.2. *Selection of molecular WOCs*[18,21–23]

Currently, a wide range of molecular WOCs can be found in the literature.[8,10,24] Examples can be found of manganese[12,17,25], ruthenium[20,26,27] and iridium[28–30] catalysts, and more recently there has been a surge of interest in base metal catalysts[9] for this reaction such as cobalt[31], iron[21,32] and copper[23,33] (Figure 1.2).

1.2.1 Mechanism of water oxidation

With regards to the mechanism of water oxidation, two prominent mechanisms have been suggested (Scheme 1.3): water nucleophilic attack (WNA) and radical oxyl coupling (ROC).

Scheme 1.3. *The key O-O bond forming step in the two suggested metal catalysed water oxidation mechanisms*[9]

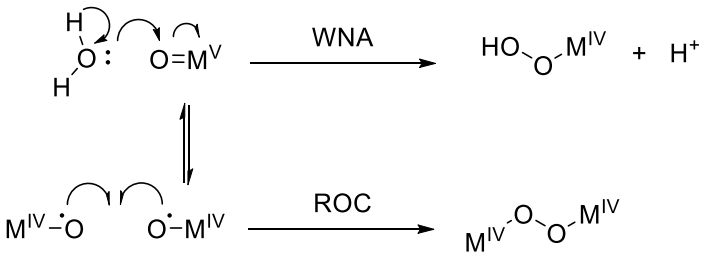

In WNA, the solvent water attacks a high valent, electrophilic, metal oxo or oxyl species. The resulting product is a hydroperoxo intermediate, which can undergo facile further oxidation to yield dioxygen.

For radical oxyl coupling, two open-shell oxyl- species combine to produce an O-O bond. This can either be a two or a four-electron process and can be symmetric (between two identical oxyl species) or asymmetric (between two distinct oxyl species). Again, further oxidation of the intermediate evolves oxygen.[9] Some catalysts can operate through either mechanism depending on the reaction conditions and ligand effects.

1.3 Iridium based water oxidation catalysts

Heterogeneous iridium oxides have been known to be highly active water oxidation catalysts since the early 1970s, but it was not until recently that molecular iridium complexes were reported. Bernhard and co-workers reported the first molecular iridium WOC in 2008 (Figure 1.3), bearing a similar set of supporting ligands as Meyer's blue ruthenium dimer, but with enhanced stability and activity.[29]

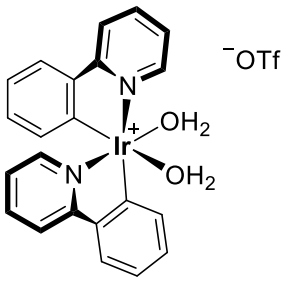

Bernhard 2008

Figure 1.3. *The first molecular iridium complex reported by Bernhard and co-workers in 2008*[29]

Based on the assumption that a high valent Ir-oxo species was responsible for the high activity, Crabtree and co-workers synthesised iridium complexes bearing a pentamethylcyclopentadienyl (Cp*) ligand (Figure 1.4)[30], with the logic that the strongly donating Cp* ligand would stabilise the high valent iridium species.

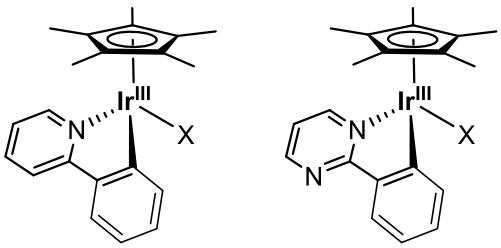

X = Cl^-, OTf^- X = Cl^-

Crabtree 2009

Figure 1.4. *The initial Cp* Ir^{III} complexes reported by Hull et al in 2009*[30]

The Cp* complexes showed faster rates for water oxidation than the original [Ir] complex, and since a wide range of Cp*Ir complexes were easily accessible from the $[Cp^*IrCl_2]_2$ precursor, a glut of half sandwich iridium catalysts were synthesised and investigated for their water oxidation activity (Figure 1.5).[28]

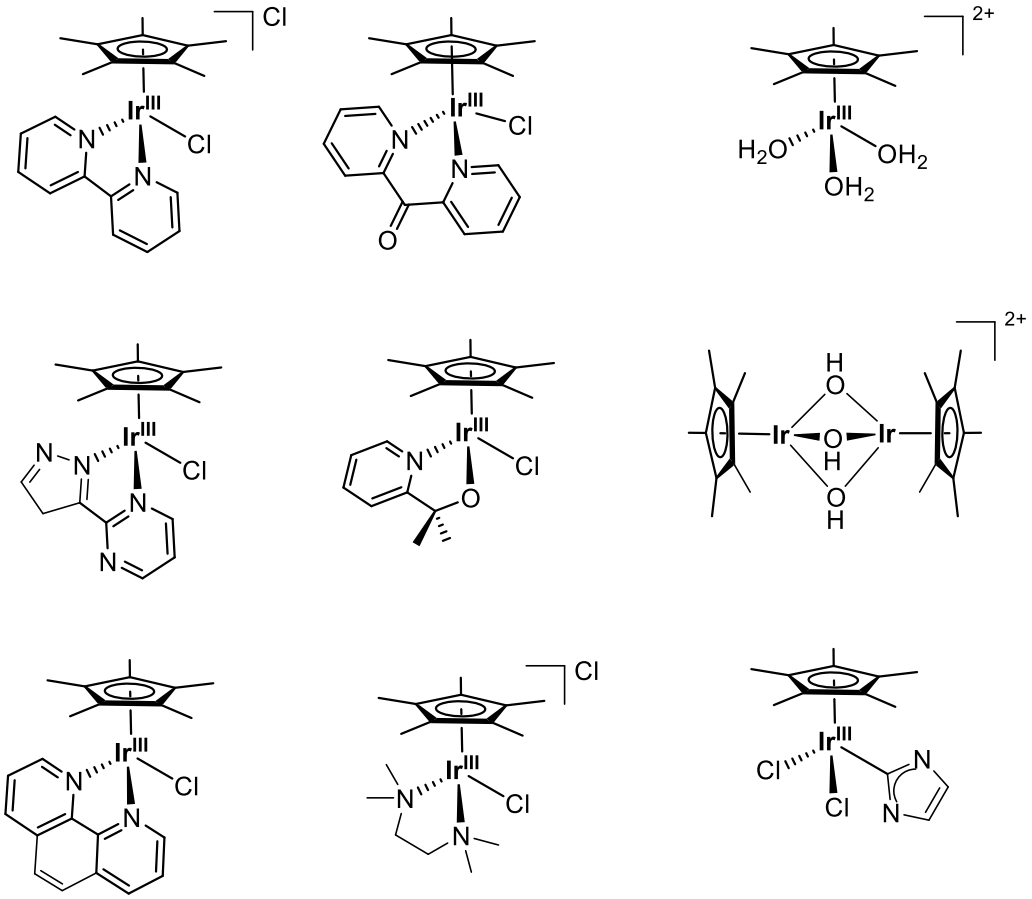

Figure 1.5. *Selection of Cp* Iridium WOCs*[28]

1.3.1 Degradation pathways of half sandwich iridium complexes

One of the motivations for investigating molecular WOCs rather than heterogeneous systems is that it allows for a better mechanistic understanding of the active catalyst thus allowing for improved catalyst design. Ironically, the improved rates of the Cp* iridium complexes and the presence of the Cp* ligand actually added complexity with regards to mechanistic investigation and determination of the active species.

Work by Macchioni and co-workers with extensive NMR experiments, showed that the Cp* ring was degraded in the presence of oxidant; by ^{1}H NMR, the Cp* peaks disappeared, and instead formation of organic acids was observed.[34,35] The group calculated that around four of the methyl units on the Cp* ring were converted to acetic acid. Characterisation of some of the degradation intermediates led to the hypothesis that the labile X ligand could exchange to form a superoxide iridium species, which could auto-degrade, or undergo a bimolecular attack (Figure 1.6).

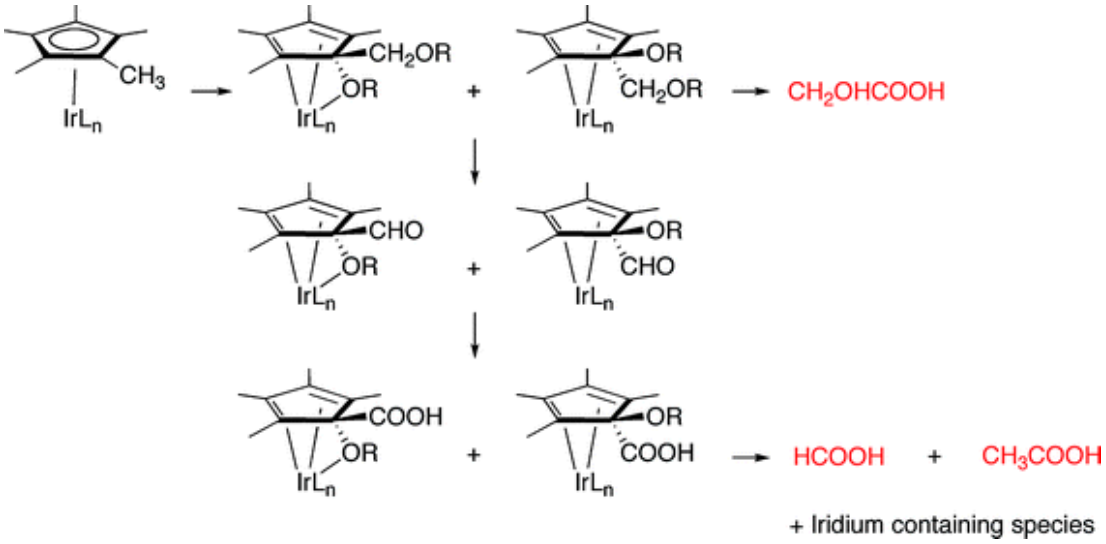

Figure 1.6. *Proposed degradation pathway for Cp*Ir complexes. Reproduced from Savini et al 2011*[35]

1.3.2 Investigations into the active species

With the clear demonstration of the oxidative degradation of the Cp* ligand during turnover, there were obvious questions about whether the active species of these iridium complexes were truly homogeneous. An observation that a blue colour was produced during water oxidation[36,37] led to speculation that the Cp* complexes decompose fully to heterogeneous iridium oxides (IrOx), which are known water oxidation catalysts.

Analysis by the Crabtree group with an electrochemical quartz crystal nanobalance (EQCN) showed that no heterogeneous material deposits on the anode during water oxidation[38]. Dynamic light scattering (DLS)[37] and a chemical oxidant showed that although the tris-aqua Cp* Ir complex formed nanoparticles under certain conditions, complexes bearing chelating ligands did not. Concurrent UV-vis data performed during the DLS experiments, showed evolution of a blue band at ~600 nm, which crucially occurred without any particle formation.[36,37] After establishing that nanoparticulate IrOx were not observed with chelate bearing ligands, the true active catalyst, and the exact nature of the species responsible for the blue colour was yet to be determined.

Further work by the Crabtree group into the nature of the active blue species was undertaken in 2013 using a Cp*Ir complex with a pyridine alkoxide (pyalk) ligand.[39] Detailed spectroscopic analysis (^{1}H and ^{17}O NMR, UV-vis, Raman, MALDI-time of flight (TOF) mass spectrometry, transmission electron microscopy energy-dispersive X-ray spectroscopy (TEM-EDX) and X-ray photoelectron spectroscopy (XPS)) as well as computational modelling using density functional theory (DFT), led to the conclusion that the Cp*Ir complex was a precursor for a dimeric bis-μ-oxo Ir^{IV} species.

Scheme 1.4. *Activation of Cp*Ir complex to dimeric species presumed to be the active water oxidation catalyst*

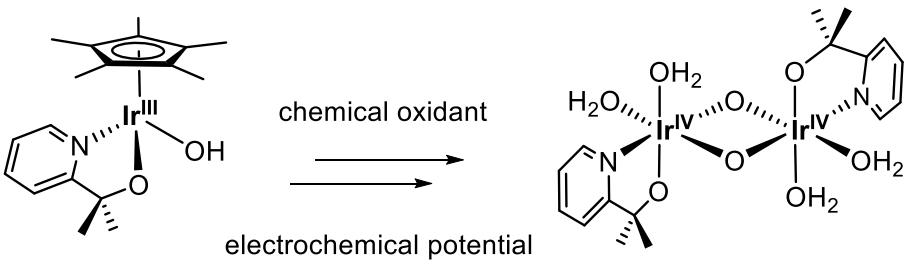

MALDI-TOF data was consistent with a Cp* free Ir dimer, and no large masses were detected, confirming that multinuclear Ir clusters were not formed. TEM-EDX and XPS data showed an N:Ir ratio of 1:1, again consistent with one pyalk ligand bound to one Ir metal in a dimer. ^{1}H NMR of the proposed dimer did not show ligand peaks, suggesting a paramagnetic Ir^{IV} species, but no EPR signal was observed.

Using DFT, five stable geometries were calculated for the dimeric Ir^{IV}-O-Ir^{IV} species (Figure 1.7), with relatively small energy barriers to interconversion. Modelling of the UV-vis spectra for Ir^{IV}-O-Ir^{IV} species showed a strong excitation at 663 nm, corresponding to the blue colour observed during turnover conditions.

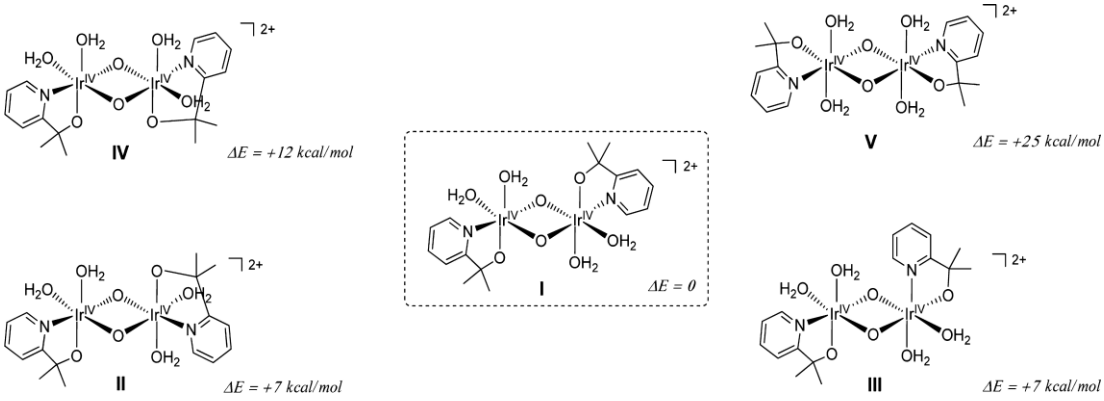

Figure 1.7. *Possible geometries and isomers for the proposed active Ir^{IV}-O-Ir^{IV} species. Reproduced from Hintermair et al 2013.*[39]

Despite the extensive evidence for a dimeric IrIV species as the active catalyst for water oxidation, analysis by solid state X-ray diffraction could not be achieved due to lack of a suitable crystal. One possible explanation for this is the range of geometries modelled by DFT, resulting in an active catalyst solution with multiple isomers and thus preventing crystallisation.

As the Cp* ligand is not retained during activation, other placeholder ligands such as COD and more recently, biscarbonyl, were tested and shown to be active water oxidation catalysts.[39,40]

In addition to chemical activation with $NaIO_4$, subsequent reports showed that the dimeric species could be accessed by electrochemical oxidation of the Cp* ligand, precluding the need for a chemical oxidant.[41] Electrochemistry of the pyalk precursor as investigated by cyclic voltammetry (CV) showed a trace with an apparent catalytic wave after 1.2 V (Figure

1.8). However, a lack of pH dependence for this feature suggested that it was not due to water oxidation, but rather incipient loss of the Cp* ligand under the oxidising potentials.

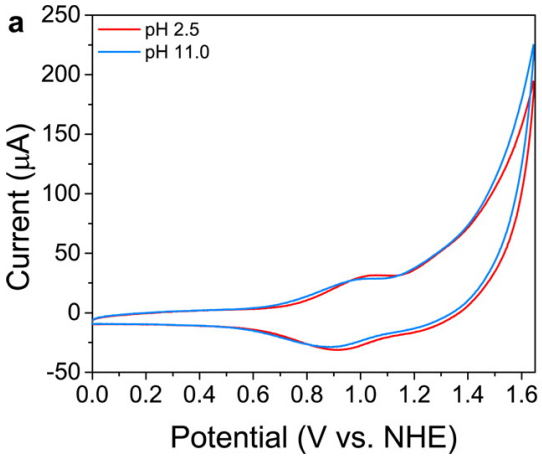

Figure 1.8. *Cyclic voltammogram of pyalk Cp* Ir precursor at varying pHs showing no variation in onset of catalytic wave. Reproduced from Thomsen et al 2014.*[41]

Sustained electrolysis of the Cp* pyalk complex (36 hours at 1.4 V) resulted in a blue solution which was still active for O_2 evolution at Faradaic efficiencies of 100% when driven electrochemically, and contained no nanoparticles by DLS.[41]

1.3.3 Heterogenisation of molecular oxidation catalysts

Despite the high activities and tunability of molecular WOCs, limited long term stability is a major drawback for application. Immobilisation of highly active molecular WOCs onto electrode surfaces is therefore often attempted to overcome this, often via a linking ligand. For example, phosphonate linkers have been used to modify Fe[42] and Ru[43,44] WOCs onto metal oxide surfaces. However, for electrode driven water oxidation, the anchoring ligand much be able to withstand the high oxidising potentials required, which is not always the case.[45] If the surface is also photoactive, there is also the potential to mimic nature and drive the water oxidation by sunlight.

Lin and co-workers circumvented the need for an anchoring ligand by incorporating a Cp* Ir complex in to a metal organic framework (Figure 1.9).[46]

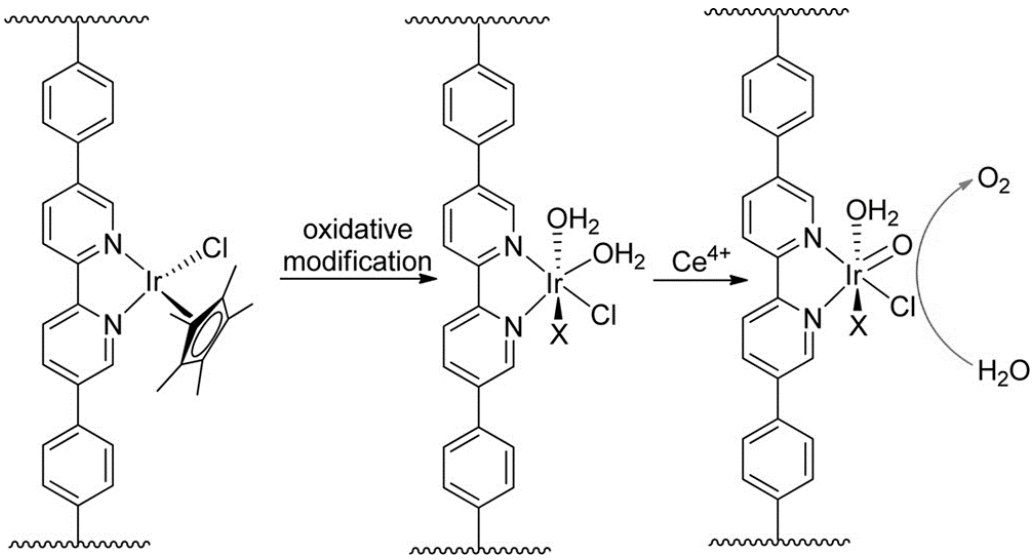

Figure 1.9. *Incorporation of a Cp* Ir complex into a MOF framework and subsequent activation by CAN yielding a 'mononuclear' iridium WOC. Reproduced from Wang et al 2012*[46]

Interestingly, the catalyst activation was still observed with application of CAN, and loss of the Cp*ligand resulted in an active monomeric species which could perform water oxidation.[46]

In 2015, the activated [Ir] dimer proposed in Scheme 1.4 was successfully deposited onto an electrode surface, by a simple self-absorbance.[47]

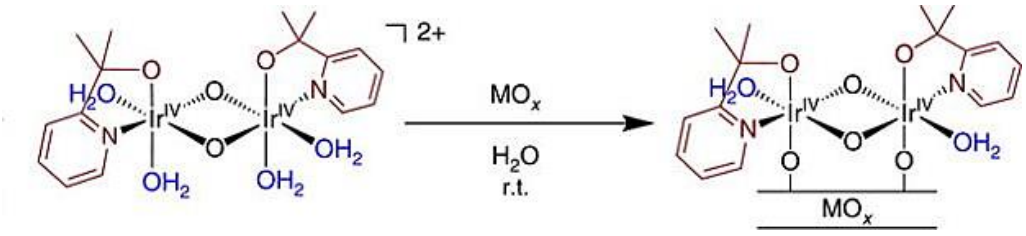

Figure 1.10. *Surface binding of proposed active dimeric complex for water oxidation. Reproduced from Sheehan et al 2015*[47]

With high efficiency, facile deposition and a self-limiting monolayer of [Ir], the electro-deposited WOC has one of the highest TONs and lowest overpotentials currently recoded.[47]

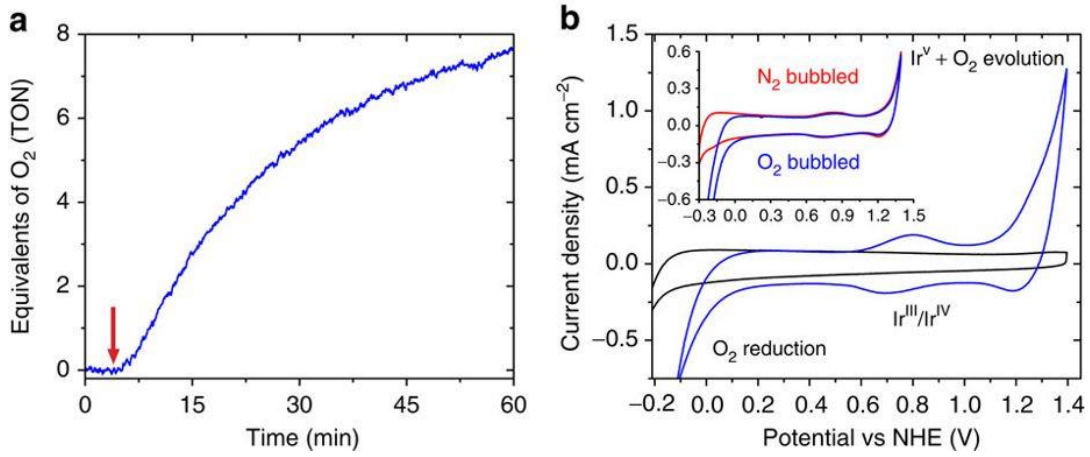

Figure 1.11. *Catalytic water oxidation with functionalised nanoITO|FTO electrodes. Reproduced from Sheehan et al 2015*[47]

As the pyalk ligand was shown to be retained during catalyst immobilisation, there is clearly scope for the production of molecularly tuneable anode materials by variation of the ligand structure.

1.4 C-H Oxidation

Despite their ubiquity, oxidation of C-H bonds remains one of the key challenges in synthetic chemistry a due to issues of kinetics and selectivity, and thus the need for a mild, general and selective route for these challenging reactions.[48,49]

The strength of the C-H bond (bond dissociation energy is typically 85-105 kcal mol^{-1}) and the kinetic inertness make manipulation of C-H bonds challenging.[48,49] As regards selectivity, reactivity of C-H bonds increases from methyl << methylene << methine, but most organic compounds contain more than one type. Even if the desired site selectivity can be achieved and the initial kinetic barrier overcome, the increased reactivity of the partially oxidised product towards further oxidation means that over oxidation is often a further issue.[48,49] Lastly, controlling the stereoselectvity of the oxidation becomes particularly significant in the synthesis of pharmacologically active compounds where stereocentres are often directly related to function. Amongst other methods, all of these issues can be moderated by use of a well-designed catalyst and ligand system. Thus the development of highly active, selective and robust catalysts is of paramount importance when attempting selective, partial C-H oxidation for chemical synthesis.[48,49]

As discussed previously, the move from fossil to renewable fuel sources is one of the major challenges of the 21st century. However, whilst renewables continue to develop and with the current surplus of natural gas now being extracted it seems likely that we will continue to use them at least in the interim. Therefore, development of more efficient technologies for utilising the natural gas arguably has a place. Whilst mild, selective partial oxidation catalysts are required for synthesis, efficient total electro-oxidation catalysts also have application in methane driven fuel cells. Although this does still produce carbon dioxide, a move to more efficient and less polluting (in terms of nitrous oxides and carbonaceous particulates) use of fossil fuels could prove useful in the short term.[50]

Returning to selective C-H oxidation, there are two general approaches to the transformation, which are summarised in Scheme 1.5. The first of these routes is by insertion of an electrophilic metal centre directly into a C-H bond (Scheme 1.5A) followed by functionalisation of the resulting metal alkyl species. The second strategy involves oxidation of the metal catalyst to a metal oxo species, which can then directly attack a C-H bond (Scheme 1.5B).[51]

Scheme 1.5. *Strategies for metal-catalysed C-H oxidation: metallic C-H activation followed by oxidative functionalization (A), and metal-oxo mediated functionalization (B)*[52]

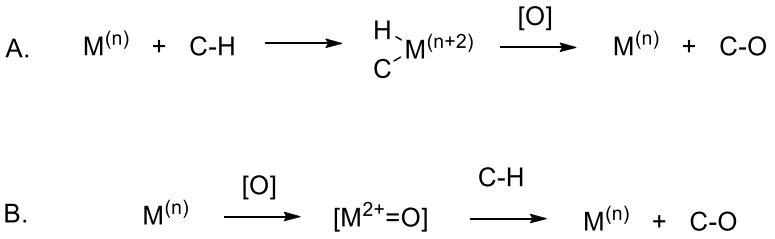

C-H activation (Scheme 1.5A) is an extensive topic,[48] but the relatively less explored method of direct oxyfunctionalisation presents an exciting new area for exploration.

As with water oxidation, biological enzymes have been investigated as they are capable of selectively oxidising C-H bonds, using aerobic oxygen. Two key classes of oxidation enzymes are cytochrome P450 and methane monooxygenases, and whilst their direct use is problematic,[53] investigation into their activity has led to the development of similar synthetic metal oxo complexes. Many of these catalysts are based on ruthenium oxo complexes[54], presumably due to the close relationship between ruthenium and iron, which features in the active centre of the monooxygenases.[55] However a wide range of metal oxo complexes have been reported for C-H bond oxidations[56], both inorganic metal oxides and organometallic compounds based on Ir[57], Mn[58] and Fe[53].

1.4.1 Half sandwich iridium complexes for C-H oxidation

Shortly after the Cp* Ir complexes were reported for water oxidation, they were also shown to be active for the selective C-H oxidation of cis-decalin, which proceeded with retention of the stereochemistry.[59]

Scheme 1.6. *Hydroxylation of cis-decalin by [Ir] water oxidation catalysts*[59]

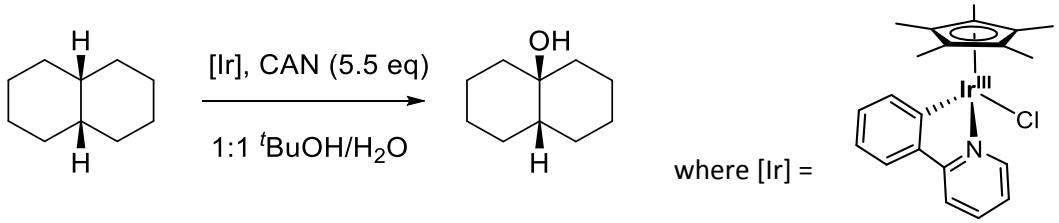

The observed stereoretentivity is interesting, because the mechanism for C-H oxidation is usually described as a radical rebound mechanism via a high valent metal oxo species. The radical mechanism would proceed via a tertiary carboradical, at which epimerisation is shown to happen at very high rates ($>10^8$ s^{-1}). Therefore, the observed retention of stereochemistry suggests this mechanism to be unlikely, as epimerisation of the intermediate would result in a racemic mix of isomers.[60]

It was therefore proposed that the Cp^*Ir^{III} catalysts performed C-H oxidation via direct insertion of oxygen from the high valent metal oxo species into the C-H bond; a hypothesis that was later supported by computational data, a first order dependence on [Ir], and a high H/D kinetic isotope effect (KIE) indicating that C-H bond cleavage was the rate determining step (RDS).[60]

The oxidation of cis-decalin and the subsequent stereoretention was initially shown with a phenylpyridine ligand bearing Cp*Ir complex and using cerium ammonium nitrate (CAN) as the oxidant. The same stereoretention was observed with varying iridium catalysts and when sodium periodate ($NaIO_4$) was used as the oxidant.[52]

These reports also highlighted the downsides of using CAN as the terminal oxidant, mainly due to its high reduction potential resulting in overoxidation of the products and thus complicating kinetic analysis. Whilst a range of oxidants were investigated (e.g. Oxone, meta-chloroperoxybenzoic acid (MCPBA), $NaIO_3$, H_2O_2), $NaIO_4$ gave the highest yields.[59]

It is worth noting that some degree of competition between the water and C-H oxidation reactions was observed when periodate was used as a terminal oxidant for C-H oxidation of ethyl benzene sulphonate (EBS). This was due to the fact that the Cp*Ir complexes are active for both water and C-H oxidations, and the oxidation reaction was conducted in water.[52]

High loadings of oxidant were used in this reaction (substrate:oxidant of 1:100), but oxygen was detected during the C-H oxidation (0.83 μmol C-H product detected via ^{1}H NMR compared to 0.20 μmol O_2 detected via Clark electrode). However, given the relative ratios of the concentrations for both water and C-H substrate, it was shown that the C-H substrate was favoured by a factor of 1 x10^4.[52] Further tunability of the pyalk ligand framework could allow for varying the catalyst selectivity.

More recently, Huang et al showed that instead of using half sandwich iridium complexes, the Cp* ligand could be replaced by carbonyl ligands (Figure 1.12). This complex still performs the oxidation of cis-decalin with stereoretention, but requires less oxidative activation resulting in a cleaner solution. Interestingly, acetic acid was required as a stabilising agent to prevent decomposition to IrOx nanoparticles, but the bis-carbonyl compound was shown to oxidise a wide range of C-H substrates.[61]

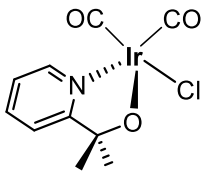

Figure 1.12. *Bis-carbonyl iridium complex reported by Huang et al*[61]

1.5 Proposed cycle for iridium oxidation catalysts

As evident from Schemes 1.3 and 1.5, both water oxidation and direct oxyfunctionalisation of C-H bonds require a high valent metal oxo species. In the initial reports for Cp*Ir catalysed C-H oxidations, it assumed that the same active high valent metal oxo species was responsible for both the water and the C-H oxidation activity; namely a dimeric species resulting from oxidative activation and loss of the Cp* ligand previously described.

It was therefore proposed that the C-H and water oxidation reactions were closely related with interlinked catalytic cycles and common intermediates in these systems (Figure 1.13), as evidenced by water being the source of oxygen for the C-H oxygenation.[60]

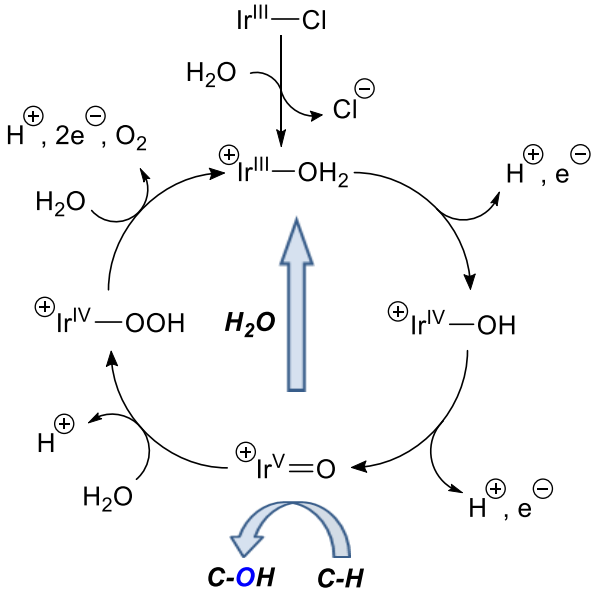

Figure 1.13. *Suggested catalytic cycles for water and C-H oxidations for half sandwich Cp* Ir complexes*[62]

The formulation of the active species as a closed shell oxene (most likely d^4 Ir^V)[63] was supported by first order kinetics in [Ir] for both water[62] and C-H oxidation[52] and retention of configuration in tertiary C-H hydroxylation,[59] observations that argue against the involvement of open shell oxyl species that would operate via radical rebound[51] and oxo coupling pathways[64,65].

Since the initial catalytic cycle was proposed in 2010 as seen above, little work has been conducted into the links between the water and C-H oxidation cycles.

1.6 The privileged pyridine alkoxide ligand

For catalysts to be active for oxidation reactions the metal centre must typically be able to access high oxidation states, but a highly active catalyst is likely to also oxidise the ligand set that surrounds the metal centre, as seen with the Cp* ligand.[34,39]

However, the pyalk ligand reported by Crabtree and co-workers holds a privileged position in these iridium oxidation complexes as it is oxidatively robust enough to persist under the harsh conditions.[66] It has been shown to be retained during catalyst activation, and persists throughout both water and C-H oxidation reactions, even such that it is still detected with catalyst immobilisation.[47]

It has recently been used to synthesise monomeric $[IrCl_2(pyalk)_2]$ complexes[67], supporting a range of geometric isomers. These monomers have also been successfully dimerised to form a mono-μ-oxo complex which has served as a model for the 'blue solution' previously described after activation of the half sandwich iridium complexes.[68]

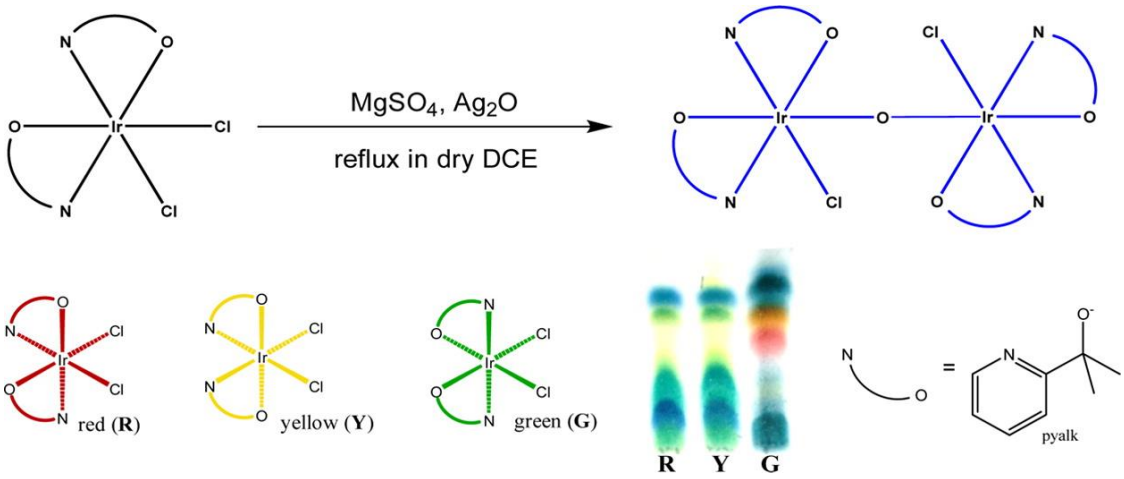

Figure 1.14. *The synthesis of a model mono-μ-oxo dimer bearing pyalk ligands. Reproduced from Sharninghausen et al 2016*[68]

Although the synthesised dimers are not active for oxidation catalysis, the remarkable stability of the pyalk ligand has allowed for the synthesis and isolation of Ir^{V} monomer, the first of its kind in an N^O organic ligand environment[69] (Figure 1.15), and investigation by CV into the $Ir^{IV/V}$ redox transition, reported to take place at around 1.0 – 1.1 V vs NHE.[69,70]

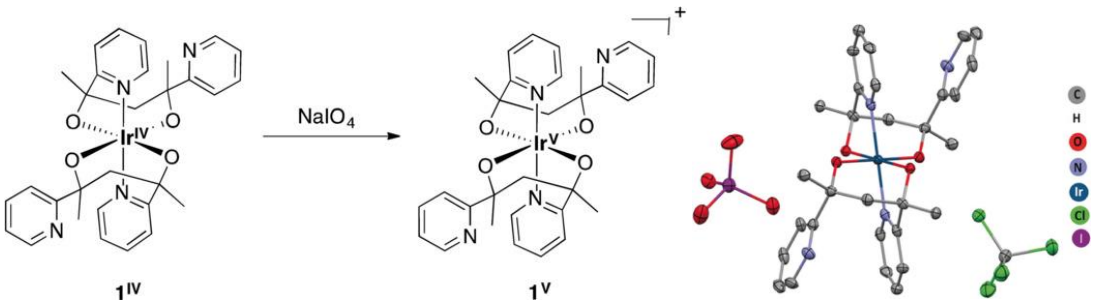

Figure 1.15 *Reproduced from Sharninghausen et al 2017.* [69]

Given that oxidation reactions require a high valent metal centre, it is likely that an Ir^{V} species is the active state in the iridium oxidation catalysts. However, it is worth noting that despite the similarities, the model dimeric species is not catalytically active, such that in situ investigation to observe an Ir^{V} species during catalysis has not yet been achieved for these complexes.

The fact that an Ir^{V} complex can be isolated and that the $Ir^{IV/V}$ transition occurs at such a low potential, highlights the importance and stability of the pyalk ligand. It is resistant to highly oxidising condition, strongly donating, compatible with both aqueous and non-aqueous solvents and has already resulted in highly novel research. Further investigation and manipulation of this privileged ligand is therefore clearly of interest.

1.7 References

1. Arends I., R. Sheldon, and U. Hanefeld, *Introduction: Green Chemistry and Catalysis*, Wiley, 2007.

2. P. Anastas and N. Eghbali, *Chem. Soc. Rev.*, 2010, **39**, 301–312.

3. R. H. Crabtree, *Organometallics*, 2011, **30**, 17–19.

4. IPCC, *Ipcc Wgiii Ar5*, 2014, 1–33.

5. D. G. H. Hetterscheid and J. N. H. Reek, *Angew. Chemie Int. Ed.*, 2012, **51**, 9740–9747.

6. D. Gust, T. A. Moore, and A. L. Moore, *Acc. Chem. Res.*, 2009, **42**, 1890–1898.

7. G. Centi and S. Perathoner, *Top. Catal.*, 2009, **52**, 948–961.

8. J. D. Blakemore, R. H. Crabtree, and G. W. Brudvig, *Chem. Rev.*, 2015, **115**, 12974–13005.

9. A. R. en. Parent and K. Sakai, *ChemSusChem*, 2014, **7**, 2070–2080.

10. M. D. Kärkäs, O. Verho, E. V Johnston, and B. Åkermark, *Chem. Rev.*, 2014, **114**, 11863–12001.

11. Y. Umena, K. Kawakami, J. R. Shen, and N. Kamiya, *Nature*, 2011, **473**, 55–60.

12. M. M. Najafpour, F. Rahimi, E. M. Aro, C. H. Lee, and S. I. Allakhverdiev, *J. R. Soc. Interface*, 2012, **9**, 2383–2395.

13. J. Kiwi and M. Gratzel, *Nature*, 1979, **281**, 657–658.

14. R. Nakamura and H. Frei, *J. Am. Chem. Soc. Commun.*, 2006, **94720**, 10668–10669.

15. R. J. Burford, W. E. Piers, D. H. Ess, and M. Parvez, *J. Am. Chem. Soc.*, 2014, **136**, 3256–3263.

16. C. W. Cady, R. H. Crabtree, and G. W. Brudvig, *Coord. Chem. Rev.*, 2008, **252**, 444–455.

17. R. Al-Oweini, A. Sartorel, B. S. Bassil, M. Natali, S. Berardi, F. Scandola, U. Kortz, and M. Bonchio, *Angew. Chemie - Int. Ed.*, 2014, **53**, 11182–11185.

18. S. W. Gersten, G. J. Samuels, and T. J. Meyer, *J. Am. Chem. Soc.*, 1982, **104**, 4029–4030.

19. L. Duan, F. Bozoglian, S. Mandal, B. Stewart, T. Privalov, A. Llobet, and L. Sun, *Nat. Chem.*, 2012, **4**, 418–423.

20. R. Zong and R. P. Thummel, *J. Am. Chem. Soc.*, 2005, **127**, 12802–12803.

21. J. L. Fillol, Z. Codolà, I. Garcia-Bosch, L. Gàmez, J. J. Pla, and M. Costas, *Nat. Chem.*, 2011, **3**, 807–813.

22. J. Limburg, J. S. Vrettos, H. Chen, J. C. De Paula, R. H. Crabtree, and G. W. Brudvig, *J. Am. Chem. Soc.*, 2001, **123**, 423–430.

23. S. M. Barnett, K. I. Goldberg, and J. M. Mayer, *Nat. Chem.*, 2012, **4**, 498–502.

24. A. Llobet, *Molecular Water Oxidation Catalysis*, Wiley, 2014.

25. R. Tagore, R. H. Crabtree, and G. W. Brudvig, *Inorg. Chem.*, 2008, **47**, 1815–1823.

26. J. J. Concepcion, J. W. Jurss, J. L. Templeton, and T. J. Meyer, *J. Am. Chem. Soc.*, 2008, **130**, 16462–16463.

27. J. J. Concepcion, J. W. Jurss, M. K. Brennaman, P. G. Hoertz, A. O. T. Patrocinio, N. Y. Murakami Iha, J. L. Templeton, and T. J. Meyer, *Acc. Chem. Res.*, 2009, **42**, 1954–1965.

28. J. M. Thomsen, D. L. Huang, R. H. Crabtree, and G. W. Brudvig, *Dalt. Trans.*, 2015, **44**, 12452–12472.

29. N. D. McDaniel, F. J. Coughlin, L. L. Tinker, and S. Bernhard, *J. Am. Chem. Soc.*, 2008, **130**, 23107–23114.

30. J. F. Hull, D. Balcells, J. D. Blakemore, C. D. Incarvito, O. Eisenstein, G. W. Brudvig, and R. H. Crabtree, *J. Am. Chem. Soc.*, 2009, **131**, 8730–8731.

31. Y. Surendranath, M. Dincă, and D. G. Nocera, *J. Am. Chem. Soc.*, 2009, **131**, 2615–2620.

32. A. R. Parent, T. Nakazono, S. Lin, S. Utsunomiya, and K. Sakai, *Dalt. Trans.*, 2014, **43**, 12501–12513.

33. F. Yu, F. Li, J. Hu, L. Bai, Y. Zhu, and L. Sun, *Chem. Commun.*, 2016, **52**, 10377–10380.

34. C. Zuccaccia, G. Bellachioma, S. Bolaño, L. Rocchigiani, A. Savini, and A. MacChioni, *Eur. J. Inorg. Chem.*, 2012, **9**, 1462–1468.

35. A. Savini, P. Belanzoni, G. Bellachioma, C. Zuccaccia, D. Zuccaccia, and A. MacChioni, *Green Chem.*, 2011, **13**, 3360–3374.

36. D. B. Grotjahn, D. B. Brown, J. K. Martin, D. C. Marelius, M. Abadjian, H. N. Tran, G. Kalyuzhny, K. S. Vecchio, Z. G. Specht, S. A. Cortes-llamas, V. Miranda-soto, V. Niekerk, C. E. Moore, and A. L. Rheingold, *J. Am. Chem. Soc.*, 2011, **133**, 19024–19027.

37. U. Hintermair, S. M. Hashmi, M. Elimelech, and R. H. Crabtree, *J. Am. Chem. Soc.*, 2012, **134**,

9785–9795.

38. N. D. Schley, J. D. Blakemore, N. K. Subbaiyan, C. D. Incarvito, F. Dsouza, R. H. Crabtree, and G. W. Brudvig, *J. Am. Chem. Soc.*, 2011, **133**, 10473–10481.

39. U. Hintermair, S. W. Sheehan, A. R. Parent, D. H. Ess, D. T. Richens, P. H. Vaccaro, G. W. Brudvig, and R. H. Crabtree, *J. Am. Chem. Soc.*, 2013, **135**, 10837–10851.

40. D. L. Huang, R. Beltrán-Suito, J. M. Thomsen, S. M. Hashmi, K. L. Materna, S. W. Sheehan, B. Q. Mercado, G. W. Brudvig, and R. H. Crabtree, *Inorg. Chem.*, 2016, **55**, 2427–2435.

41. J. M. Thomsen, L. Que Jr., S. M. Hashmi, J. Campos, U. Hintermair, R. H. Crabtree, and G. W. Brudvig, *J. Am. Chem. Soc.*, 2014, **136**, 13826–13834.

42. B. M. Klepser and B. M. Bartlett, *J. Am. Chem. Soc.*, 2014, **136**, 1694–1697.

43. D. K. Zhong, S. Zhao, D. E. Polyansky, and E. Fujita, *J. Catal.*, 2013, **307**, 140–147.

44. J. J. Concepcion, R. A. Binstead, L. Alibabaei, and T. J. Meyer, *Inorg. Chem.*, 2013, **52**, 10744–10746.

45. R. H. Crabtree, *J. Organomet. Chem.*, 2014, **751**, 174–180.

46. C. Wang, J. Wang, and W. Lin, *J. Am. Chem. Soc.*, 2012, **134**, 19895–19908.

47. S. W. Sheehan, J. M. Thomsen, U. Hintermair, R. H. Crabtree, G. W. Brudvig, and C. A. Schmuttenmaer, *Nat. Commun.*, 2015, **6**, 6469–6478.

48. A. R. Dick and M. S. Sanford, *Tetrahedron*, 2006, **62**, 2439–2463.

49. M. C. White, *Science (80-.).*, 2012, **335**, 807–809.

50. S. Park, J. M. Vohs, and R. J. Gorte, *Lett. to Nat.*, 2000, **404**, 265–267.

51. R. H. Crabtree, *J. Chem. Soc. Dalt. Trans.*, 2001, **17**, 2437–2450.

52. M. Zhou, U. Hintermair, B. G. Hashiguchi, A. R. Parent, S. M. Hashmi, M. Elimelech, R. A. Periana, G. W. Brudvig, and R. H. Crabtree, *Organometallics*, 2013, **32**, 957–965.

53. M. Bordeaux, A. Galarneau, and J. Drone, *Angew. Chemie - Int. Ed.*, 2012, **51**, 10712–10723.

54. S. I. Murahashi and D. Zhang, *Chem. Soc. Rev.*, 2008, **37**, 1490–1501.

55. M. Zhou and R. H. Crabtree, *Chem. Soc. Rev.*, 2011, **40**, 1875–1884.

56. A. Gunay and K. H. Theopold, *Chem. Rev.*, 2010, **110**, 1060–1081.

57. T. Suzuki, *Chem. Rev.*, 2011, **111**, 1825–1845.

58. A. S. Borovik, *Chem. Soc. Rev.*, 2011, **40**, 1870–1874.

59. M. Zhou, N. D. Schley, and R. H. Crabtree, *J. Am. Chem. Soc.*, 2010, **132**, 12550–12551.

60. M. Zhou, D. Balcells, A. R. Parent, R. H. Crabtree, and O. Eisenstein, *ACS Catal.*, 2012, **2**, 208–218.

61. D. L. Huang, D. J. Vinyard, J. D. Blakemore, S. M. Hashmi, and R. H. Crabtree, *Organometallics*, 2017, **36**, 199–206.

62. J. D. Blakemore, N. D. Schley, D. Balcells, J. F. Hull, G. W. Olack, C. D. Incarvito, O. Eisenstein, G. W. Brudvig, and R. H. Crabtree, *J. Am. Chem. Soc.*, 2010, **132**, 16017–16029.

63. T. Van Voorhis, T. A. Betley, Q. Wu, and D. G. Nocera, *Inorg. Chem.*, 2008, **47**, 1849–1861.

64. H. Dau, C. Limberg, T. Reier, M. Risch, S. Roggan, and P. Strasser, *ChemCatChem*, 2010, **2**, 724–761.

65. J. Graeupner, U. Hintermair, D. L. Huang, J. M. Thomsen, M. Takase, J. Campos, S. M. Hashmi, M. Elimelech, G. W. Brudvig, and R. H. Crabtree, *Organometallics*, 2013, **32**, 5384–5390.

66. T. K. Michaelos, D. Y. Shopov, S. B. Sinha, L. S. Sharninghausen, K. J. Fisher, H. M. C. Lant, R. H. Crabtree, and G. W. Brudvig, *Acc. Chem. Res.*, 2017, **50**, 952–959.

67. D. Y. Shopov, B. Rudshteyn, J. Campos, D. J. Vinyard, V. S. Batista, G. W. Brudvig, and R. H. Crabtree, *Chem. Sci.*, 2017, **8**, 1642–1652.

68. L. S. Sharninghausen, S. B. Sinha, D. Y. Shopov, B. Choi, B. Q. Mercado, X. Roy, D. Balcells, G. W. Brudvig, and R. H. Crabtree, *J. Am. Chem. Soc.*, 2016, **138**, 15917–15926.

69. L. S. Sharninghausen, S. B. Sinha, D. Y. Shopov, B. Q. Mercado, D. Balcells, G. W. Brudvig, and R. H. Crabtree, *Angew. Chemie - Int. Ed.*, 2017, **56**, 13047–13051.

70. S. B. Sinha, D. Y. Shopov, L. S. Sharninghausen, C. J. Stein, B. Q. Mercado, D. Balcells, T. B. Pedersen, M. Reiher, G. W. Brudvig, and R. H. Crabtree, *J. Am. Chem. Soc.*, 2017, **139**, 9672–9683.

CHAPTER 2

SYNTHESIS, CHARACTERISATION AND ACTIVATION OF IR COMPLEXES

This chapter is based on the following publications:

*Ligand Tuning in Pyridine-Alkoxide Ligated Cp*Ir^{III} Oxidation Catalysts*, E. Sackville, G. Kociok-Köhn, U. Hintermair, *Organometallics*, 2017, **36**, 3578-3588

*Electrochemical and Kinetic Insights into Molecular Water Oxidation Catalysts Derived from Cp*Ir(pyridine-alkoxide) Complexes*, E. Sackville, F. Marken, U. Hintermair, *ChemCatChem*, accepted

2. Synthesis, Characterisation and Activation of Ir complexes

2.1 Introduction

When designing molecular oxidation catalysts, it is crucial to use ligand scaffolds that are oxidatively robust enough to stabilise the high oxidation states required by the metal, without themselves being oxidised. The design of stable ligands that are able to withstand the harsh conditions usually employed during oxidation reactions, is therefore paramount in the development of effective molecular oxidation catalysts.[1]

For example, although many of the traditional "soft" organic ligands like carbonyls, olefins and phosphines have been shown to be effective in reductive catalysis, they are often oxidised during oxidative chemistry and are therefore unsuitable.[2] However, pyridines, pyrroles, amides and carboxylates show high oxidative stability when suitably substituted. Tertiary alcohols are also highly stable, despite primary and secondary alcohols being readily oxidised. A further benefit of alkoxides is that their π basicity can stabilize high-valent intermediates that are common in oxidation catalysis, and allow them to engage in proton management via lone pairs on the oxygen. N^O type ligands, in particular the pyridine alkoxide ligand seen in Figure 2.1, have been shown to have excellent stability and high activity for iridium catalysed oxidations, retaining their molecularity even under harsh oxidising conditions, and promoting high Ir oxidation states.[3]

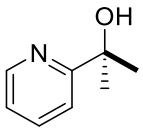

Figure 2.1. *Structure of the oxidatively robust pyridine alkoxide (pyalk) ligand*

This chapter will focus on the synthesis of the six novel pyalk bearing iridium complexes. Characterisation in the solid-state will be presented, as well as exploration of the electrochemical behaviour of the precatalysts by cyclic voltammetry. Finally, investigation into how the ligand variation affects the precatalyst activation step will be explored as recorded via NMR and UV-vis.

2.2 Synthesis

2.2.1 Ligand synthesis

A range of symmetrically substituted pyalk-type ligands (Figure 2.2) have been synthesized. The alkoxy substituents were varied in terms of steric bulk (dimethyl, cyclohexyl, di-^{t}butyl) and electronics (aliphatic vs. aromatic) and the pyridine was extended into a quinoline system.

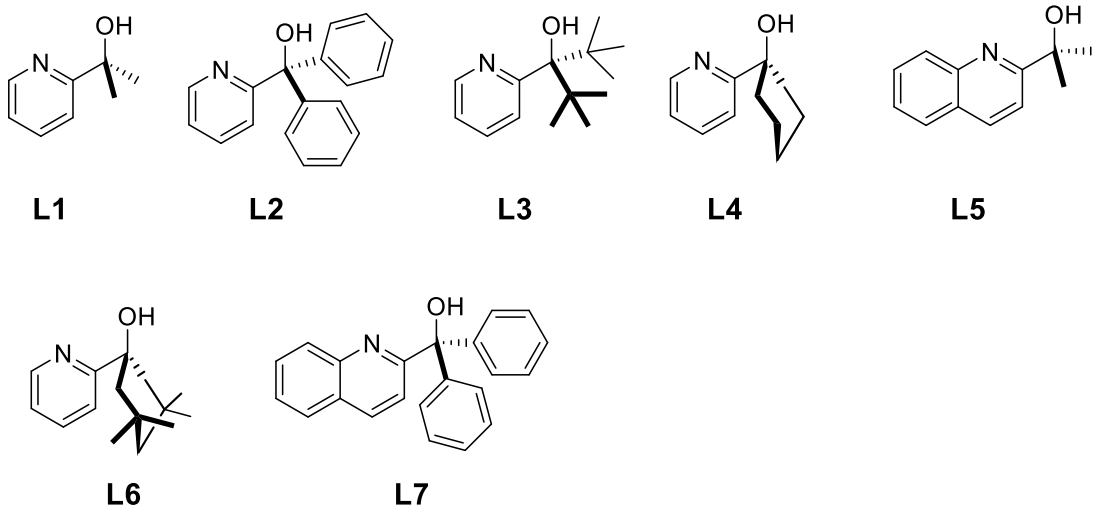

Figure 2.2. *Tertiary 2-pyridine/quinoline-alcohols synthesised as ligand precursors to support Ir-based oxidation catalysts (**L1** representing the reference compound from the literature).*[a]

The ligands described above are accessible via two synthetic routes: a) Grignard addition to 2-pyridyl(quinolyl) ketones[4] or b) lithiation of 2-bromo pyridines/quinolones followed by electrophilic addition of the relevant ketone[5] (Scheme 2.1). The parent dimethyl-pyalk ligand was synthesised using the commercially available Grignard ($MeMgBr/Et_2O$) and 2-acetylpyridine via route a). All other ligands were obtained *via* in-situ lithium-halide exchange of 2-bromopyridine/quinoline with *n*BuLi followed by addition of the appropriate symmetrical ketones.

[a] L2, L3,L 4 and L5 initially synthesised during MRes; included for later data and comparison. Optimised synthesis and yields reported from improvements during PhD.

Scheme 2.1. *Synthetic routes to ligands via a) Grignard addition or b) lithiation and electrophilic ketone addition*

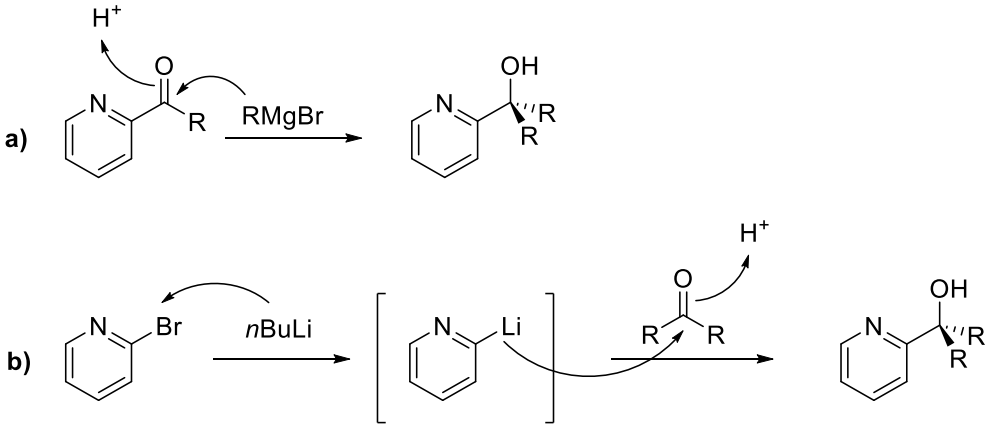

This strategy allows straightforward access to a range of N^O ligand precursors. Isolated yields of 15 – 72 % were obtained after purification by recrystallization, sublimation, or column chromatography (see experimental section for details). Variation in yield was attributed to the differences in purification method, as some of the bulkier R groups presented challenges for recrystallisation.

2.2.2 Complex synthesis

Synthesis of the complexes by κ^2 coordination of the pro-ligands onto the Cp^*Ir^{III} fragment was achieved by gentle heating with $[Cp^*IrCl_2]_2$ in the presence of a mild inorganic base (Scheme 2.2).

Scheme 2.2 *Synthesis of Cp^*Ir^{III} complexes using ligands* ***L1-7***

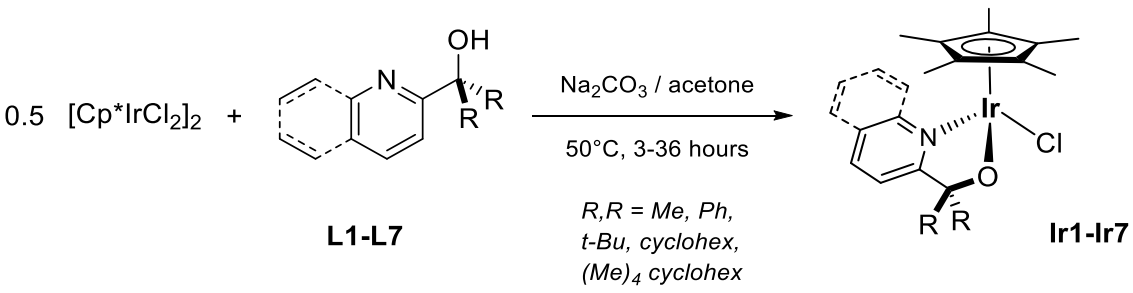

As acetic acid (HOAc) has been observed to H-bond to the alkoxide moiety of the coordinated ligand, Na_2CO_3 was used in all cases, yielding the neutral, monomeric chloro- complexes **Ir1**, **Ir2**, **Ir4-Ir7** in isolated yields of 54 – 81 % after recrystallization (Figure 2.3).

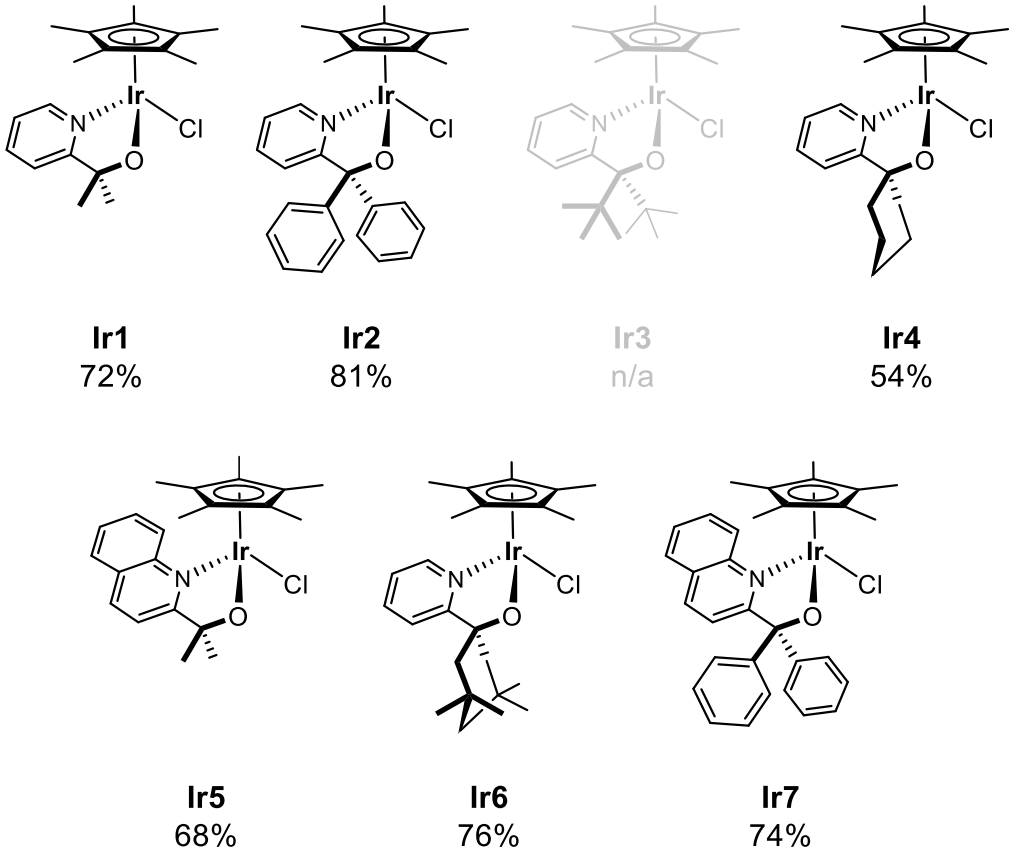

Figure 2.3. *Cp*Ir^{III} complexes **Ir1**-7 supported by pyalk-type ligands L1-7 synthesised according to Scheme 2.2 (**Ir1** representing the reference compound from the literature).*[b]

Only the bulky bis-^{t}butyl substituted 2-pyridine alcohol L3 did not bind to the Cp*Ir^{III} fragment under these conditions, plausibly due to steric clashes between the ^{t}butyl substituents and the Cp* methyl groups in an octahedral complex. Similar steric strain has been observed in related $[Cp^*Ir^{III}(NHC)_2Cl]^+$ complexes with ^{n}butyl substituents on the N-heterocyclic carbenes.[6,7] Addition of MeCN and $AgSbF_6$ to $[Cp^*IrCl_2]_2$ generated $[Cp^*Ir(MeCN)_3][SbF_6]_2$ *in situ* (Scheme 2.3),[8] which is more reactive towards the deprotonated pyalk ligand and permitted isolation of the cationic 16-electron five-coordinate $[Cp^*Ir(L3)]SbF_6$ complex **Ir3**.

[b] Ir2, Ir3, Ir4 and Ir5 initially synthesised during MRes; included for later data and comparison. Optimised synthesis and yields reported from improvements during PhD.

Scheme 2.3. *Method for the synthesis of cationic [Cp*Ir(LX)]⁺ species*

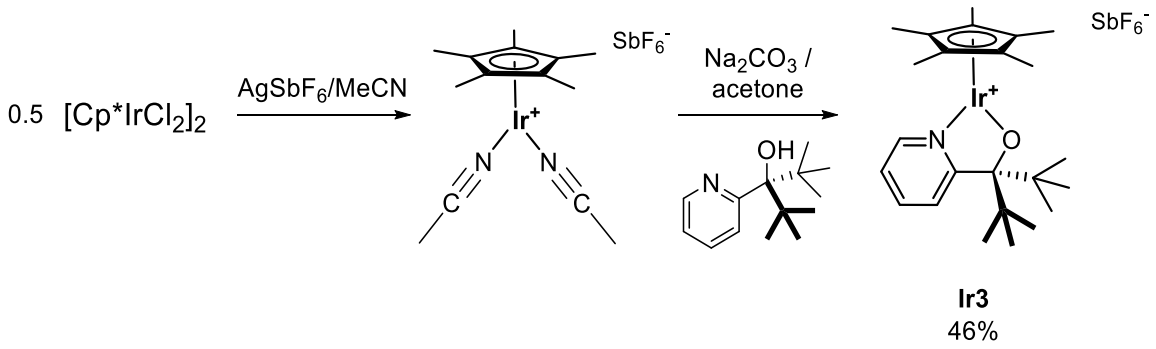

In this distorted trigonal bipyramidal (dTBP) structure, the pyalk ligand is orthogonal to the plane of the Cp* ligand, thus avoiding steric clash between the alkoxy substituents and the Cp* methyl groups. This coordination mode, involving π donation from the oxygen lone pairs into vacant metal d-orbitals is well known for various chelating alkoxides[9] and imides[10], and represents a key feature in ligand-assisted bifunctional hydrogenation catalysis.[11]

Cationic versions of complexes **Ir1** and **Ir7** were also synthesised for comparison purposes (Figure 2.4). Whilst **Ir7⁺** was accessed via the same method as **Ir3**, the cationic version of **Ir1⁺** was achieved according to previously published procedures.[9] Reaction of **L1** with $[Cp^*IrCl_2]_2$ and potassium hexafluorophosphate under biphasic basic conditions yielded **Ir1⁺** with a PF_6^- outer-sphere counter ion.

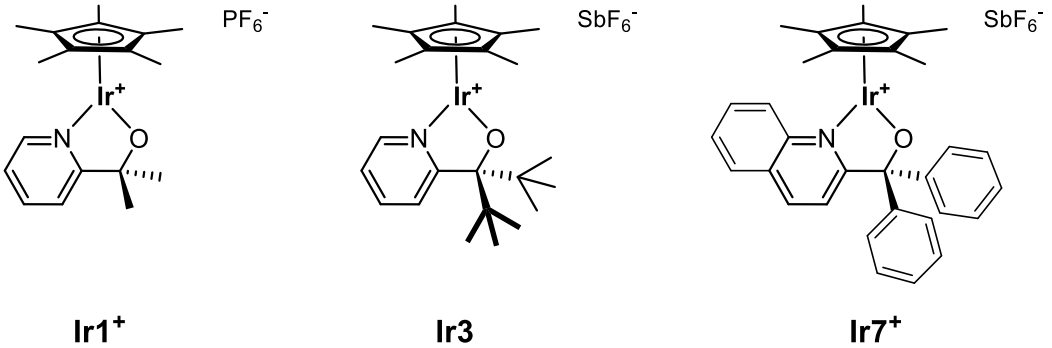

Figure 2.4. *Cationic Cp*Ir^{III} **Ir1⁺**, **Ir3** and **Ir7⁺** synthesised according to Scheme 2.3 (**Ir3** and **Ir7⁺**) or previously reported procedures*[9]

2.2.3 Crystal structures

All new Ir complexes were fully characterized including single crystal X-ray diffraction (Figure 2.5). The solid-state structures confirm the expected geometries with no noticeable deviations. Compounds **Ir1**, **Ir2**, **Ir4-Ir7** exhibit Ir-O distances of 2.05 ± 0.01 Å while in **Ir3** the Ir-O distance is 1.94 Å, consistent with some double bond character.[12]

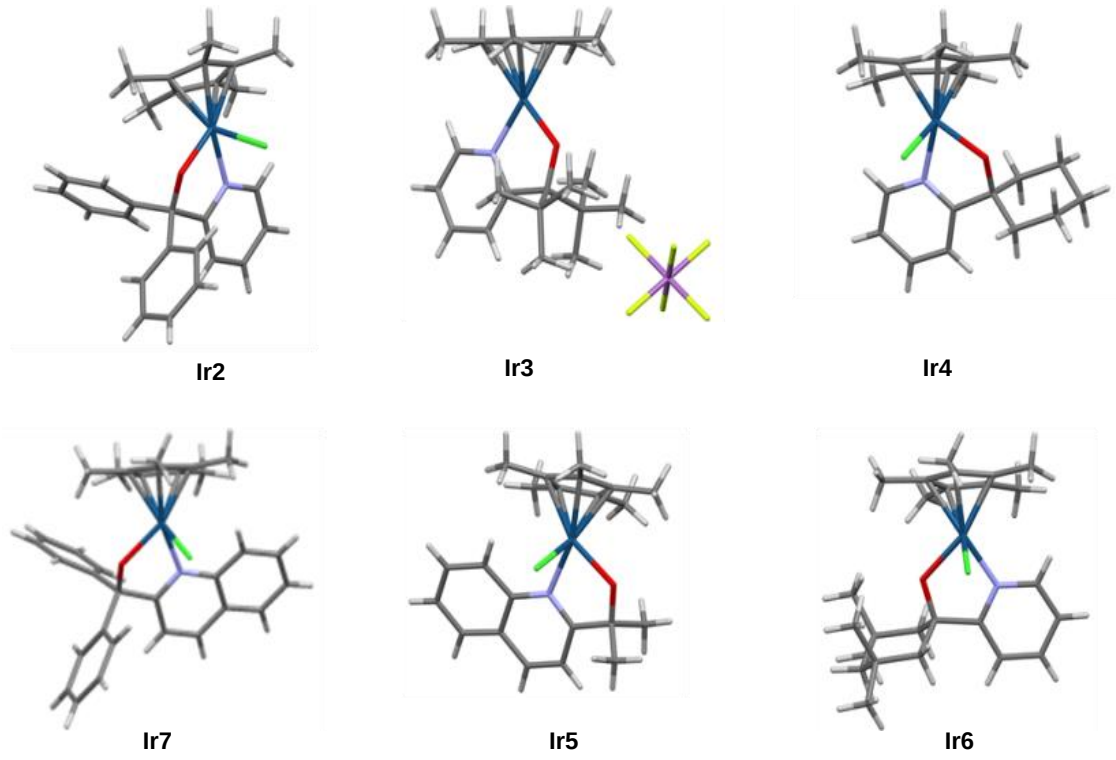

Figure 2.5. *X-ray crystal structures models of complexes* ***Ir2-Ir7*** *(solvent molecules omitted for clarity; for details see the experimental section)*[c]

In all complexes, the geometries observed in the crystal structures are in agreement with the complimentary solution phase data. Whilst it has been reported that bulky ligand groups can distort Cp* ligands, this is not observed for any of these complexes, and the Cp* ligand is bound as η^5. All complexes display similar N-Ir bond lengths (2.050 – 2.118 Å), but the O-Ir distance in complex **Ir3** is more than 0.1 Å shorter than the average length observed for the neutral species. Additionally, the dihedral angle between the N-C-C-O-Ir plane and the Cp*is at 90˚ for **Ir3**. The combination of these two data suggests significant π donation from oxygen lone pairs to stabilise the electron-deficient Ir centre.[9]

[c] Ir2, Ir3, Ir4 and Ir5 crystal structures obtained during MRes and included here for comparison.

When considering the effects of the steric bulk of the varied pyalk and quinalk ligands, the ^{t}butyl groups in **Ir3** are qualitatively seen to induce the largest degree of steric congestion; further evidenced by the synthetically inaccessible chloro- complex for **Ir3**. Conversely, the diphenyl substituents have flexibility of ring rotation around the C-C axis which helps to minimise steric clash with the Cp* ring. Cyclohexyl complexes **Ir4** and **Ir6** show similar bulk at the metal centre as the parent dimethyl compound **Ir1**. However, the additional flexibility of the cyclohexyl substituents results in two possible conformations: 'ring back' and 'ring front' (Scheme 2.4). The broad signals in the ^{1}H NMR data (Appendix, Figure 2.1) for the cyclohexyl protons suggest that this equilibrium is rapid in solution at ambient temperatures. The quinoline backbone of complexes **Ir5** and **Ir7** extends the steric bulk on the alternate side of the ligand. However, from the crystallographic data this does not appear to clash with the Cp* ligand.

Scheme 2.4 *The two possible chair conformations adopted by the cyclohexyl substituent in complexes* ***Ir4*** *and* ***Ir6***

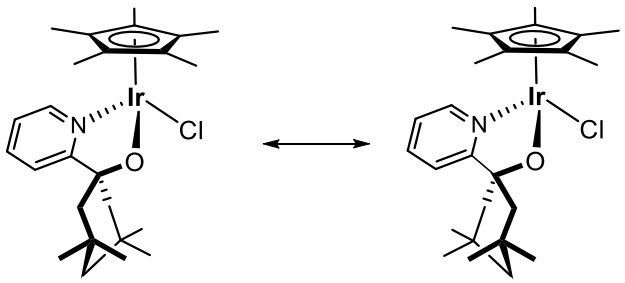

2.3 Solution Speciation

2.3.1 Solution equilibria

As previously discussed, stabilisation by π donation to the metal can facilitate ligand exchange, with the result that in solution several [Ir] species are expected to be present in equilibrium. The position of this equilibrium will vary between precatalysts due to the alkoxide ligand bulk but will also vary depending on the conditions in the solution. Expected species and conditions can be seen below, where ^{6}Ir-X denotes a 6-coordinate octahedral species (where X = Cl, OH or OH_2) and $^{5}Ir^{+}$ denotes a 5-coordinate cationic complex.

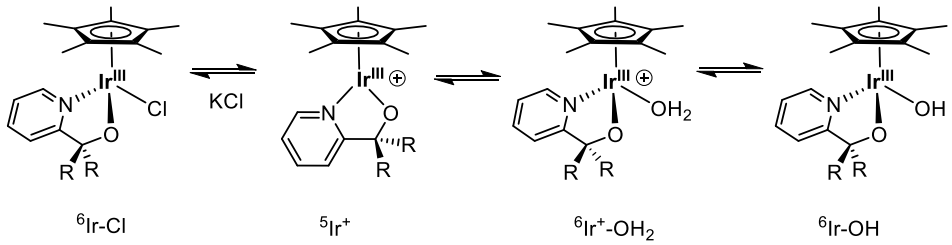

Figure 2.6. *Solution equilibria of Cp*Ir^{III} complexes with pyalk-type complexes in aqueous solution*

2.3.2 UV-vis titrations with additional chloride

In order to investigate the potential solution species suggested above, UV-vis spectroscopy was used to assess the effect of increasing chloride concentration (Figure 2.7). Particular attention was given to significant spectral changes and isosbestic points, which denote a complete change in species.

Upon KCl addition, all precatalysts showed different behaviour by UV-vis. **Ir3** showed very little change in absorbance and no isosbestic points; an expected result given that the chloro-complex of **Ir3** was synthetically unavailable. **Ir2** and **Ir7** showed a change upon addition of chloride, but the subsequent additions resulted in very minor changes (none for **Ir7**).

Both quinoline complexes (**Ir5** and **Ir7**) had variation between around 500-350 nm but both showed overlapping spectra outside of this range. The titration data for **Ir1** has clear isosbestic points at 447 and 378 nm although the absorbance changes were small.

The cyclohexyl compounds **Ir4** and **Ir6** showed the greatest changes upon chloride addition. There were three isosbectic points for each complex at ~300, 380 and 450 nm and a clear increase in absorbance at 350 nm and decrease in absorbance at 400 nm.

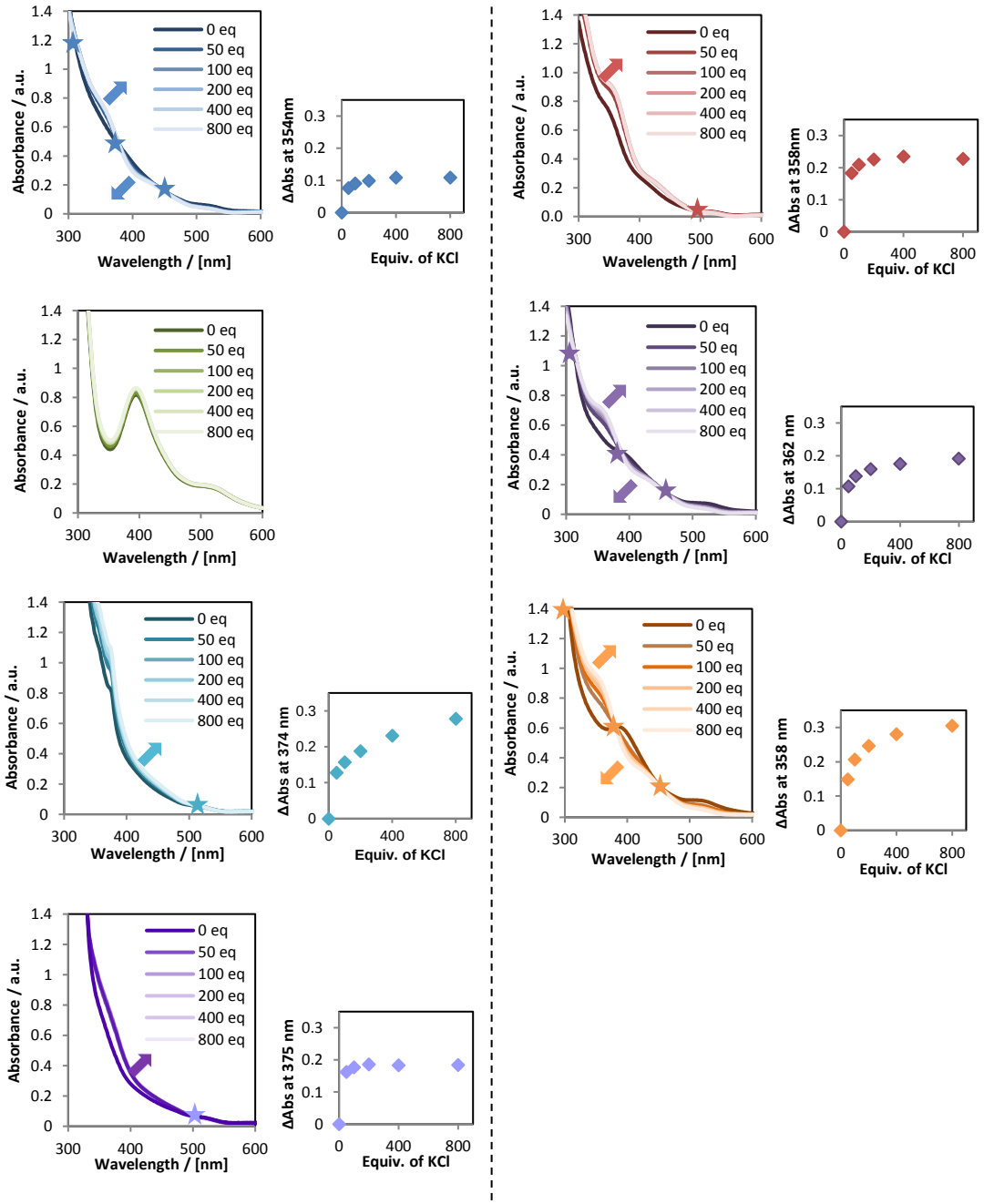

Figure 2.7. *UV-vis titration of increasing equivalents of KCl with 0.5 mM [Ir] in H_2O/ ^tBuOH. Isosbestic points are denoted with a star and the arrows indicate increasing [KCl]. Insets show the change in absorbance calculated for each dataset at ~370 nm*

The absorbance at 400 nm can be assigned to a cationic species whilst the band at 350 nm can be attributed to the chloro- complex. Thus, in aqueous solution, complexes **Ir2**, **Ir5** and **Ir7** appear to lie mainly towards the chloro- complex, whilst complexes **Ir1**, **Ir4** and **Ir6** must be at least partially in the cationic state. This is possibly due to the π systems of **Ir2**, **Ir5** and **Ir7**, which could remove some of the e^- density away from the metal centre, resulting in a less stabilised $16e^-$ cationic species.

2.4 Electrochemical characterisation

2.4.1 Electrochemical methods

Electrochemistry is a powerful tool that can be used to probe reactions in which there are electron transfers by measuring the potential, reversibility and kinetics of these redox events. For organometallic chemistry in particular, where the electron transfer is often the oxidation or reduction of a metal centre, electrochemistry is becoming more commonly used to investigate the effect of ligands.[13,14]

Cyclic voltammetry (CV) is usually the initial study undertaken when investigating the redox chemistry of a new system, due to the relative ease of set up and the large amount of information that can be obtained from a single scan. In a CV experiment, the potential is scanned from a starting potential E_1 to a fixed switching potential, E_2, (forward scan) and then swept back the other way on the reverse scan, usually to the initial potential E_1. The rate at which the potential is varied is the scan rate (v /V s^{-1}); a parameter which can be easily varied to provide kinetic information about the electron transfer. The relationship between scan rate (v /V s^{-1}), time (t /s) and potential (E /V) can be seen in the potential time step in Figure 2.8a.

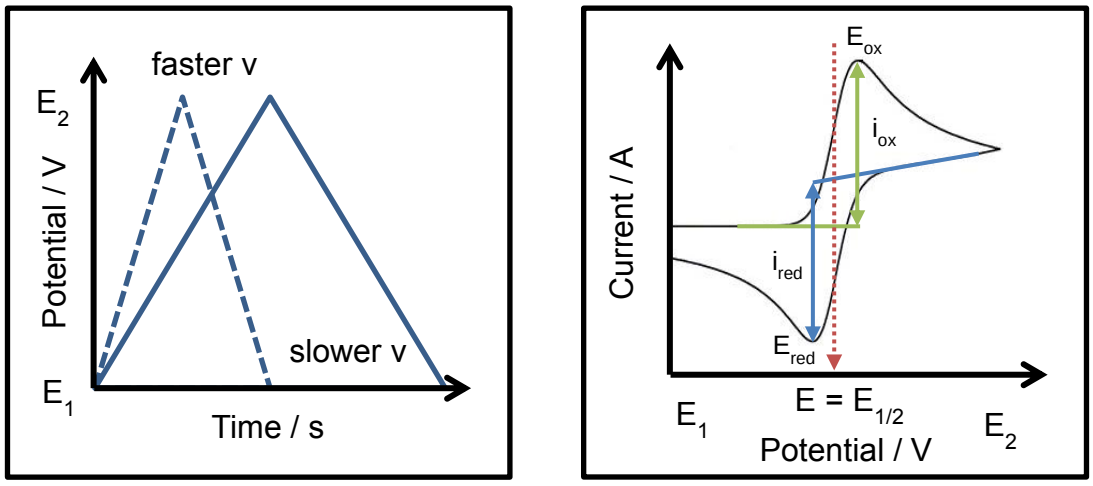

Figure 2.8 a) *The potential / time step input during a CV* ***b)*** *The potential / current data obtained during a typical scan, with mid-point potential $E_{1/2}$, peak oxidation and reduction potentials E_{ox} and E_{red}, and peak currents for the oxidation i_{ox} and reduction i_{red} events*

From setting the potential parameters E_1 and E_2 and the scan rate, the current can be recorded as the potential is varied; a typical CV response can be seen in Figure 2.8b showing the quantitative information that can be gathered.

The average of the anodic and cathodic peak potentials E_{ox} and E_{red} yields the mid-point potential $E_{1/2}$, and the difference between them gives the peak to peak separation (ΔE_p). By using the Nernst equation (E2.1), $E_{1/2}$ can be used to give an estimate of the formal potential of the species under consideration ($E^{0\prime}$) and ΔE_p can be used to give a measure of the reversibility of system.

$$E = E^{0\prime} + \frac{RT}{F} \ln \frac{[ox]}{[red]} \qquad \text{E2.1}$$

The Nernst equation predicts how the system responds to the changing potential experienced by the system during a CV scan. At the mid-point potential $E_{1/2}$, the concentrations of the reduced and oxidised species are equal, such that [red] = [ox] and $E_{1/2} \approx E^{0\prime}$.

For a perfectly reversible one electron redox process, the Nernst equation also determines that the ΔE_p will be 59 mV at 25 °C.[15] For a redox process to exhibit a perfectly reversible CV scan, the process must be both chemically reversible (the analyte can be oxidised, reduced and then fully re-oxidised again without any loss of current signal) and electrochemically reversible (the electron transfer kinetics must be fast). Of course, under real experimental conditions, even ideal Nernstian redox processes rarely show a ΔE_p of 59 mV, often due to uncompensated resistance in the system. The peak currents i_{ox} and i_{red} can also give an indication of the chemical reversibility of a system, because for a full reversible system, $i_{ox}/i_{red} \approx 1$.

Varying the scan rate between CV scans will change the size of the diffusion layer around the electrode surface, such that faster scan rates give higher currents. For an electrochemically reversible electron transfer and a freely diffusing analyte, the Randles-Sevcik equation (E2.2) can be applied.

$$i_p = 0.446nFAC^0 \sqrt{\frac{nF\nu D_0}{RT}} \qquad \text{E2.2}$$

The Randles-Sevcik equation relies on the analyte freely diffusing in solution such that a plot of the square root of the scan rate ($\sqrt{\nu}$) against peak current (i_p) would give a linear relationship. Deviation from linearity suggests that the analyte is absorbed on to the electrode surface. It also relies on electrochemical reversibility such that E_{ox} and E_{red}, and therefore ΔE_p, should remain independent of scan rate.

2.4.2 Aqueous cyclic voltammograms

To compare the electronic influences of ligands **L1-L7** on the Ir^{III} centre in the Cp* precursors, CVs were collected. Scanning to positive potentials should show the oxidation of the iridium centre to Ir^{IV} and the reduction back to Ir^{III}. The position of the $E_{1/2}$ would thus give an indication of the relative ease of oxidative activation of the individual precatalysts. Full activation of the precatalysts (as seen in Scheme 1.3) has been shown not to occur on the timescale of a typical CV experiment[16].

Initially the precursors were examined electrochemically in H_2O with 20% ^tBuOH to aid dissolution of the complexes. Using a three-electrode set up with a fluorine-doped tin oxide (FTO) working electrode (WE) and a Pt wire counter electrode (CE), CVs for **Ir1**-**Ir7** were collected from -0.5 to +1.5 V (vs. Ag/AgCl reference electrode (RE)) (Figure 2.9).

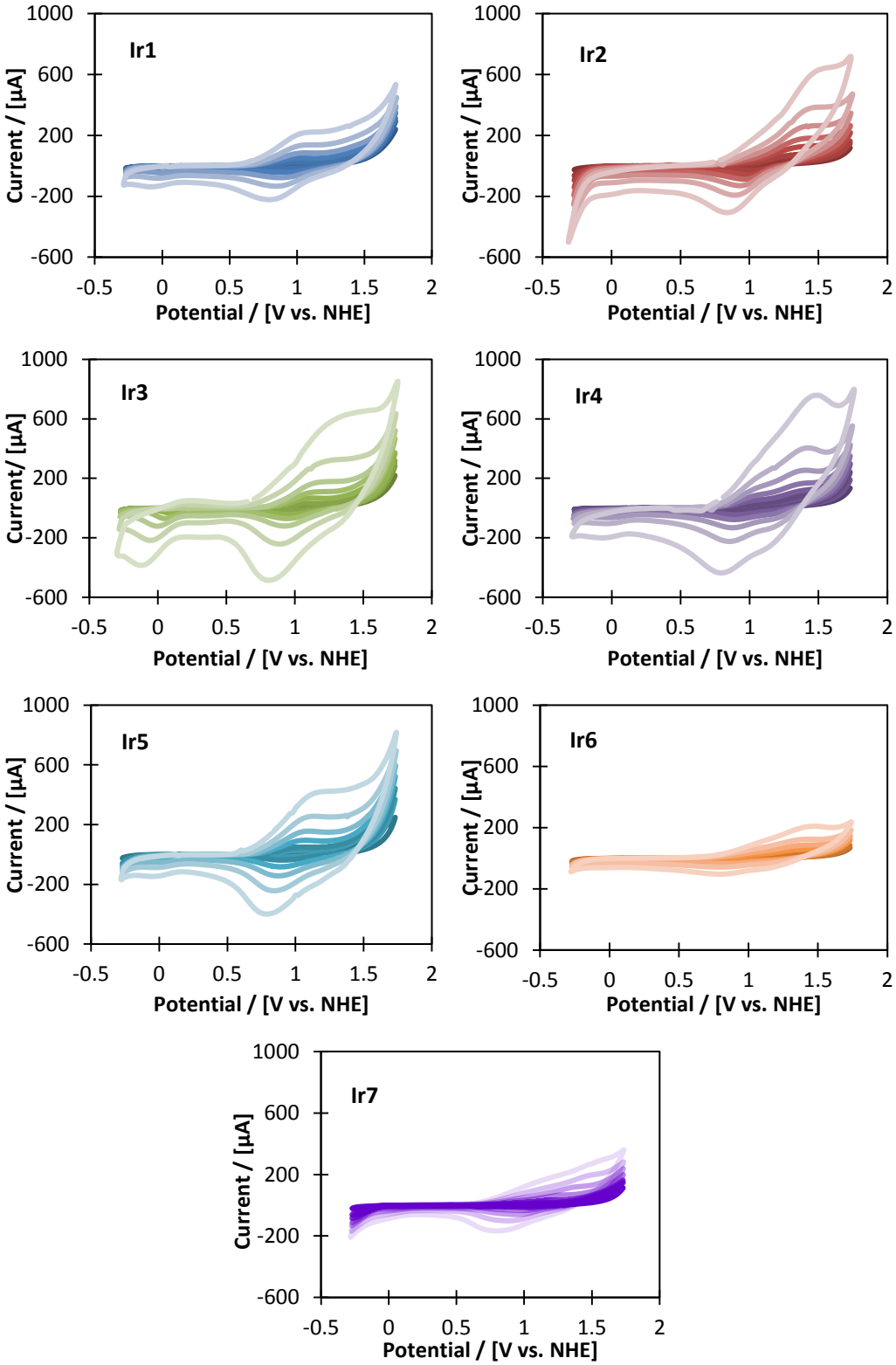

Figure 2.9. *Cyclic voltammograms of compounds* ***Ir1****-7 at 0.45 mM in 0.1 M* KNO_3 *in 4:1* $H_2O/^tBuOH$ *at native pH and room temperature. WE: 1* cm^2 *FTO glass, CE: Pt wire, RE: Ag/AgCl. Scan rate increases from dark to pale shades for 100, 250, 500, 1000, 2000, 5000* mVs^{-1}.

Generally, on scanning to oxidising potentials, no major features were observed until ~0.9 V. Quasi-reversible redox features were found at around 1 V for all complexes **Ir1**-**Ir7**, in the region of $Ir^{III} \rightarrow Ir^{IV}$ couples. At potentials above 1.5 V an irreversible oxidation wave occurs. This has often been assigned to catalytic water oxidation but as described in Chapter 1.3, was shown to represent incipient Cp* oxidation.[16]

Despite observable (although often poorly defined) redox couples for all complexes; the most noticeable feature is that **Ir4** and **Ir6** appear to show two overlapping redox events. In the UV-vis titration data, cyclohexyl complexes **Ir4** and **Ir6** also showed the greatest change upon KCl addition. Using the previously hypothesised solution speciation (Figure 2.6), the double redox features in the CVs suggests that in aqueous solution, **Ir4** and **Ir6** exist as more than one single species; thus, when scanning to oxidising potentials, a redox event is seen for both Ir species in solution. The double redox features, although interesting, complicate the traditional CV analysis. Approximate values for $E_{1/2}$ and Δ Ep can be seen in Table 2.1.

Table 2.1. *Peak potentials, mid-point potential and peak to peak separation data for precatalysts **Ir1**-**Ir7** from the 100 mVs^{-1} CV shown in Figure 2.9, reported vs. the normal hydrogen electrode (NHE). See experimental for details.*

	E_{ox} vs NHE / V	E_{red} vs NHE / V	ΔE / mV	E_{mid} vs NHE / V
Ir1	0.94	0.95	-13	0.95
Ir2	1.27	0.84	430	1.05
Ir3	1.05	1.00	45	1.02
Ir4	1.32/0.99	1.21/0.93	102/65	1.27/0.96
Ir5	1.01	0.91	94	0.96
Ir6	1.30/0.98	1.23/0.93	74/50	1.26/0.96
Ir7	1.16	1.06	100	1.11

Taking the first value for the peaks for **Ir4** and **Ir6**, the E_{mid} values roughly increase such that dimethyl ≈ cyclohexyl < di-^{t}butyl < aryls, but a lack of Nernstian reversibility and without clear redox peaks for **Ir4** and **Ir6**, a comparative discussion of the ligand effects on the $Ir^{III/IV}$ couple is not possible. Additionally, the peak to peak separation observed for 100 mVs^{-1} varies dramatically between precatalysts, with the value for the E_{red} for **Ir1** actually being slightly higher than that for the E_{ox}. Further complications were uncovered when re-checking the FTO working electrodes in a fresh electrolyte solution after the catalyst scan (Figure 2.10).

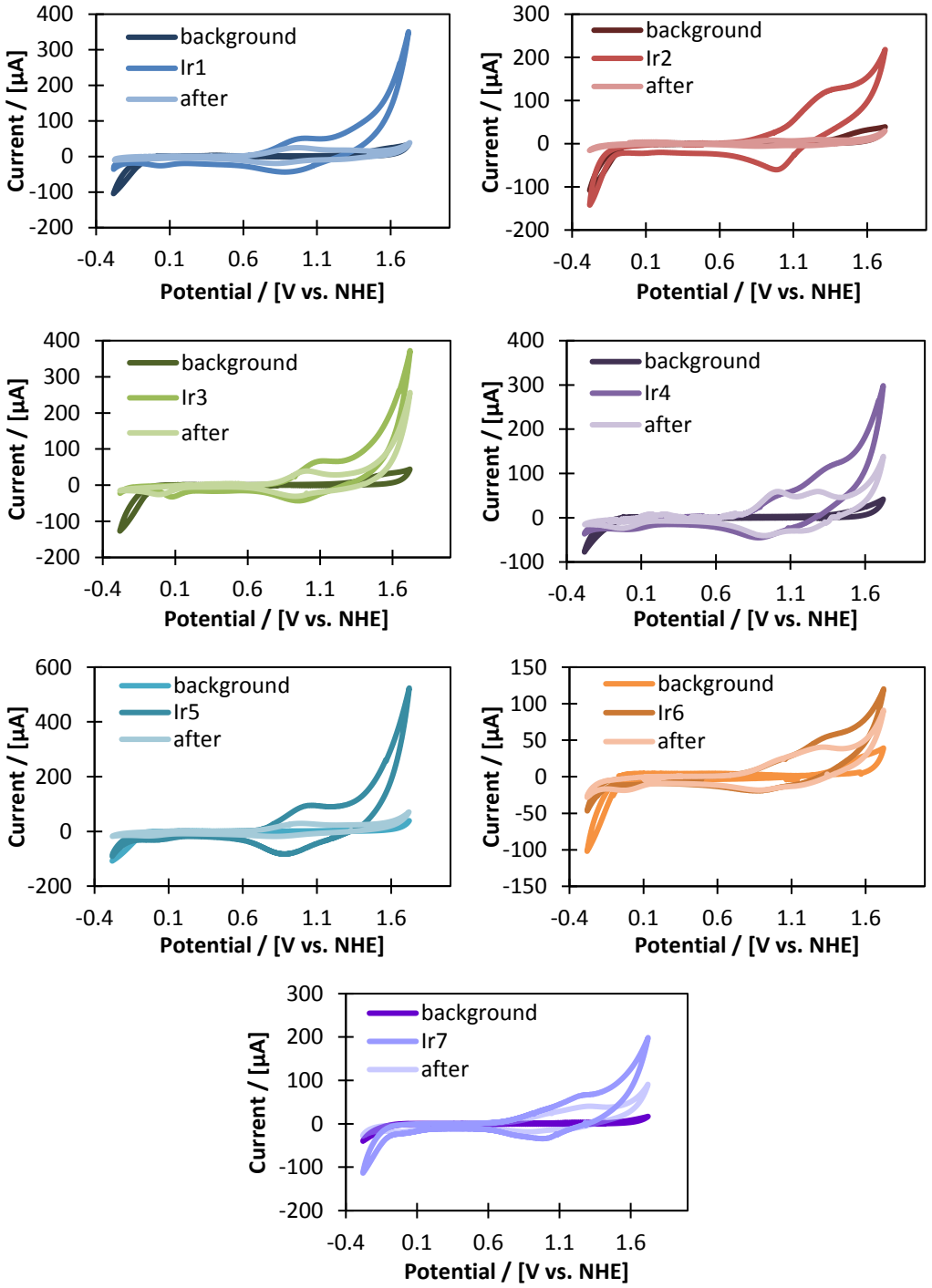

Figure 2.10. *CV data of an FTO working electrode before, during and after cycling with* ***Ir1****-****Ir7*** *at 0.45 mM in 0.1 M* KNO_3 *electrolyte at 250* mVs^{-1} *scan rate. RE: Ag/AgCl, CE: Pt wire*

Particularly noticeable for **Ir3**, **Ir4**, **Ir6** and **Ir7**, the CV scans after the catalyst CVs appear to show deposition of an Ir species on to the FTO working electrode. Binding of the fully activated catalyst has been demonstrated on to indium tin oxide (ITO)[17], but again complicates analysis of the mid-point potential.

Aqueous CVs were repeated for **Ir1**-**Ir7** with 800 equivalents of KCl (Figure 2.11), in order to attempt to vary the solution speciation as per the UV-vis experiments described in Figure 2.7.

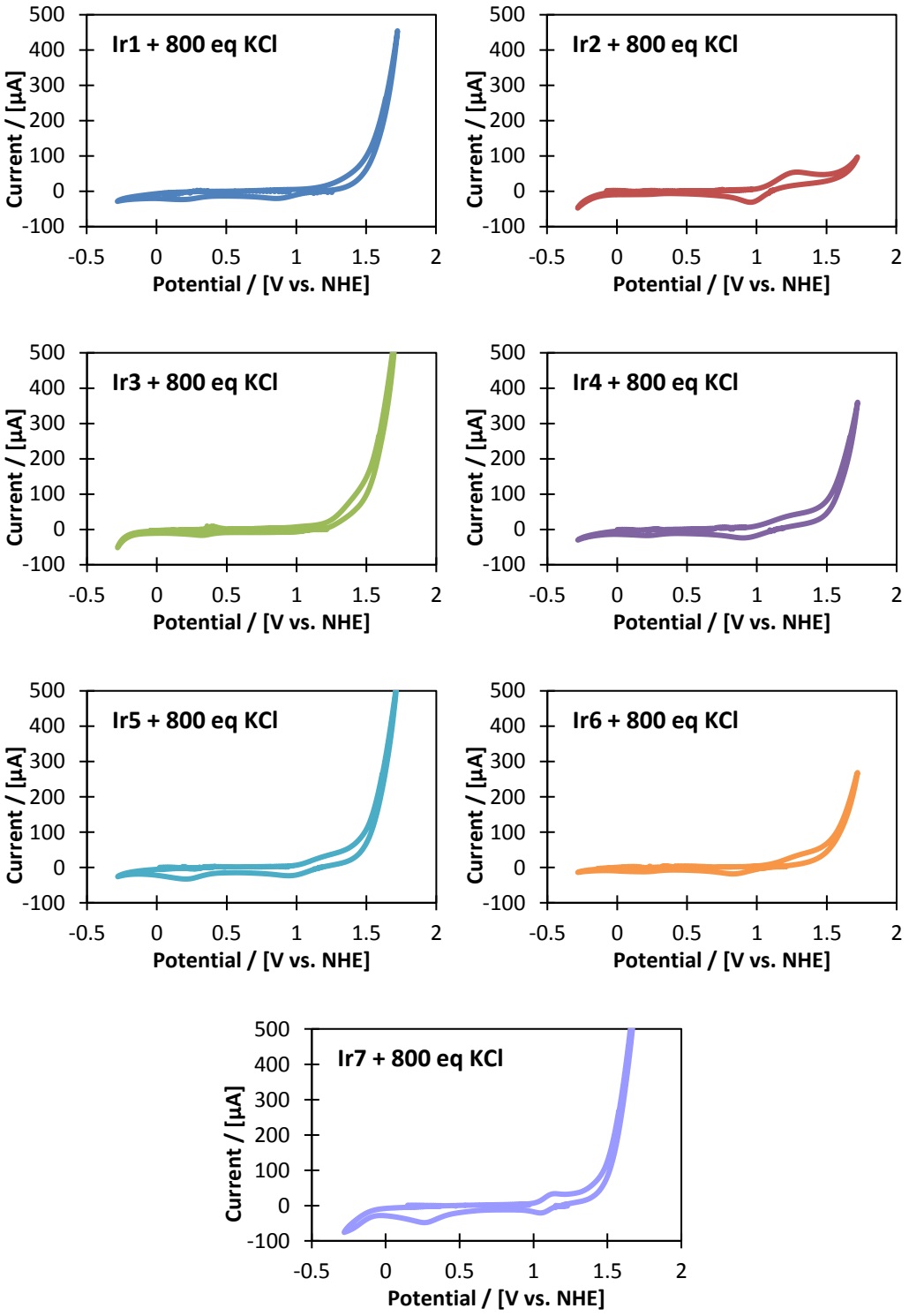

Figure 2.11. *Cyclic voltamograms of precatalsts **Ir1**-**Ir7** with 800 equivalents KCl. 0.45 mM in 0.1 M KNO_3 in 4:1 H_2O/tBuOH, scan rate 250 mVs^{-1} and room temperature, WE: 1 cm^2 FTO glass, RE: Ag/AgCl, CE: Pt wire*

The CV response in excess chloride varied greatly between precatalysts, with some precatalysts showing apparent reversible redox features (**Ir2** and **Ir7** at 1.1 V and 1.0 V vs. NHE), others showing a single quasi reversible redox event (**Ir4**, **Ir5** and **Ir6**), and some showing no oxidation at all (**Ir1** and **Ir3**).

Ir2 showed an E_{mid} of 1.06 V vs NHE with excess KCl; the same as without KCl although with a clearer defined oxidation peak. As with the KCl titration followed by UV-vis (Figure 2.7), addition of KCl had little effect on the CV data, confirming that **Ir2** exists in aqueous solution as ^{6}Ir-Cl.

Complexes **Ir4** and **Ir6**, which previously showed noticeable double redox peaks, both demonstrated a single quasi-reversible redox feature with excess KCl; again mirroring the trends observed in the UV-vis titrations where **Ir4** and **Ir6** exhibited the largest changes upon excess KCl.

Complexes **Ir3** and **Ir1** do not exhibit an oxidation peak in aqueous solution with excess KCl. The CVs of **Ir3** and **Ir1** in H_2O/^{t}BuOH with KNO_3 electrolyte did show redox events, with E_{mid} values of 1.02 and 0.95 V vs NHE respectively, but with peak to peak separation of 45 mV and -13 mV. **Ir3** in particular showed significant deposition onto the FTO electrode (Figure 2.10), with the CV response recorded after **Ir3** with the same electrode in electrolyte retaining the redox feature. Therefore, the redox peaks seen for **Ir1** and **Ir3** previously must be due to a surface bound Ir species.

The working electrodes were investigated for adsorption of Ir onto the FTO in the presence of excess KCl. After collecting CVs in catalyst solution, the working electrodes were washed with distilled water and re-tested in a solution containing only electrolyte and no iridium.

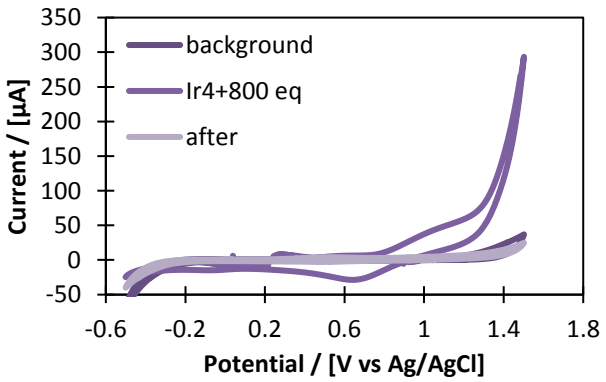

Figure 2.12. *CV data of an FTO working electrode before, during and after cycling in a solution of 0.45 mM* ***Ir4*** *with 800 equivalents of KCl in 4:1 H_2O/ ^{t}BuOH at a scan rate of 250 mvs^{-1}*

Unlike the CVs collected without excess KCl, no deposition on to the working electrode was observed. The presence of surplus chloride therefore must prevent binding of the Ir onto the surface. Although **Ir4** and **Ir6** no longer show double redox peaks, meaningful analysis of the E_{mid} potentials for **Ir1-Ir7** could not be obtained. **Ir1** and **Ir3** show no redox features, and the redox peaks for catalysts **Ir4-Ir6** are not reversible. Furthermore, it can also be seen from the CVs in Figure 2.11, that the multi-electron oxidation wave above 1.4 V vs. NHE is enhanced with the presence of KCl for all complexes except **Ir2**. This could be due to chloride oxidation, but nevertheless further complicates determination of the position of the oxidation peak.

Complicated though the aqueous CV experiments are, several conclusions can be made:

1. In agreement with the UV-vis titration data, more than one [Ir] species is present in solution,
2. The presence of excess Cl^- prevents surface binding of the complexes to FTO.

Despite attempts to simplify the experiments with additional KCl, the $E_{1/2}$ data, which was the original reason for collecting CVs of the precatalysts, was still not definitively obtained. Multiple solution species, deposition on to the FTO electrode and activation of the precatalysts in aqueous solution complicated the analysis, such that a quantitative comparison of the mid-point potentials for **Ir1-Ir7** was inaccessible. Therefore, attempts were made to obtain CVs under non-aqueous, anaerobic conditions.

2.4.3 Electrolyte

Non-aqueous electrochemistry is often performed with $[NBu_4][PF_6]$ (tetrabutyl ammonium hexaflurophosphate) as the supporting electrolyte, but the highly oxidising nature of the precatalysts necessitated an electrolyte with less readily oxidisable C-H bonds. Ionic liquids (ILs), effectively room temperature molten salts, are widely used in electrochemical applications. With high stability and conductivity, and wide working potential ranges, ionic liquids are now being used as electrolytes for battery storage, CO_2 reduction and even water oxidation, either through a hydrated IL as the solvent/electrolyte or by using ILs to electrodeposit effective water oxidation catalysts[18–22]

Given the wide potential ranges and the high conductivity, a novel ionic liquid was synthesised for use as an electrolyte to investigate the non-aqueous CVs of precatalysts **Ir1**-**Ir7** in DCM. Imidazolium derivatives are commonly used as the cation in ionic liquids due to their low viscosity, tunability and cathodic stability. Anion choice is largely dominated by bis((trifluoromethyl)sulfonyl) amide ($[NTf_2]$) or bis(fluorosulphonyl)imide ([FSI]), due to high stability and good conductivity. Consequently, a novel ionic liquid-type electrolyte 1,2,3-trimethyl-1H-benzimidazol-3-ium bis((trifluoromethyl)sulfonyl) amide $[tmbim][NTf_2]$ was synthesised (Figure 2.13).

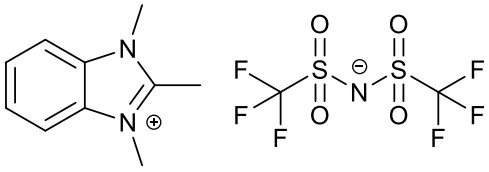

***Figure 2.13**. Trimethyl-benzimidazolium bis((trifluoromethyl)sulfonyl) amide [tmbim][NTf_2] ionic liquid synthesised for use as a non-aqueous electrolyte*

Reaction of 2-methylbenzoimidazole with methyl iodide according to previously published procedures yielded the trimethyl-benzo-imidazolium iodide salt. Initial attempts at salt metathesis with the $Li[NTf_2]$ salt followed by halide abstraction with $Ag[BF_4]$ resulted in residual silver peaks in the CVs of the electrolyte (Figure 2.14a), requiring repeated recrystallisations from ethanol.

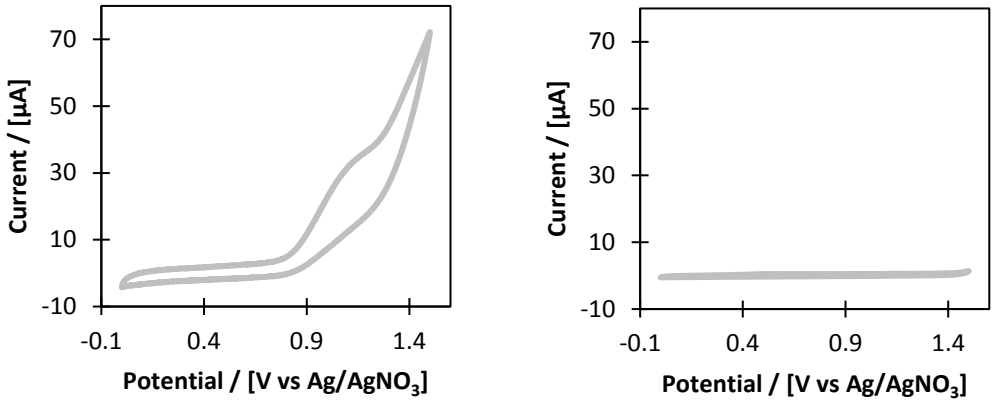

Figure 2.14 *CVs of 0.05 M [tmbim][NTf_2] electrolyte in DCM at room temperature with WE: GC, RE: Ag/$AgNO_3$, CE: Pt wire at 100 mVs^{-1}* ***a)*** *before purification* ***b)*** *after purification by repeated recrystallisation from ethanol*

Recrystallisation of the iodide starting material from ethanol and an addition of excess $LiNTf_2$ followed by repeated recrystallisation with ethanol eventually yielded a pure ionic liquid-type, dichloromethane (DCM) soluble electrolyte suitable for non-aqueous CVs (Figure 2.14b).

2.4.4 Non-aqueous cyclic voltammograms

Using a three-electrode set up, newly synthesised electrolyte, DCM, non-aqueous CVs were collected for precatalysts **Ir1**-**Ir7** (Figure 2.15)

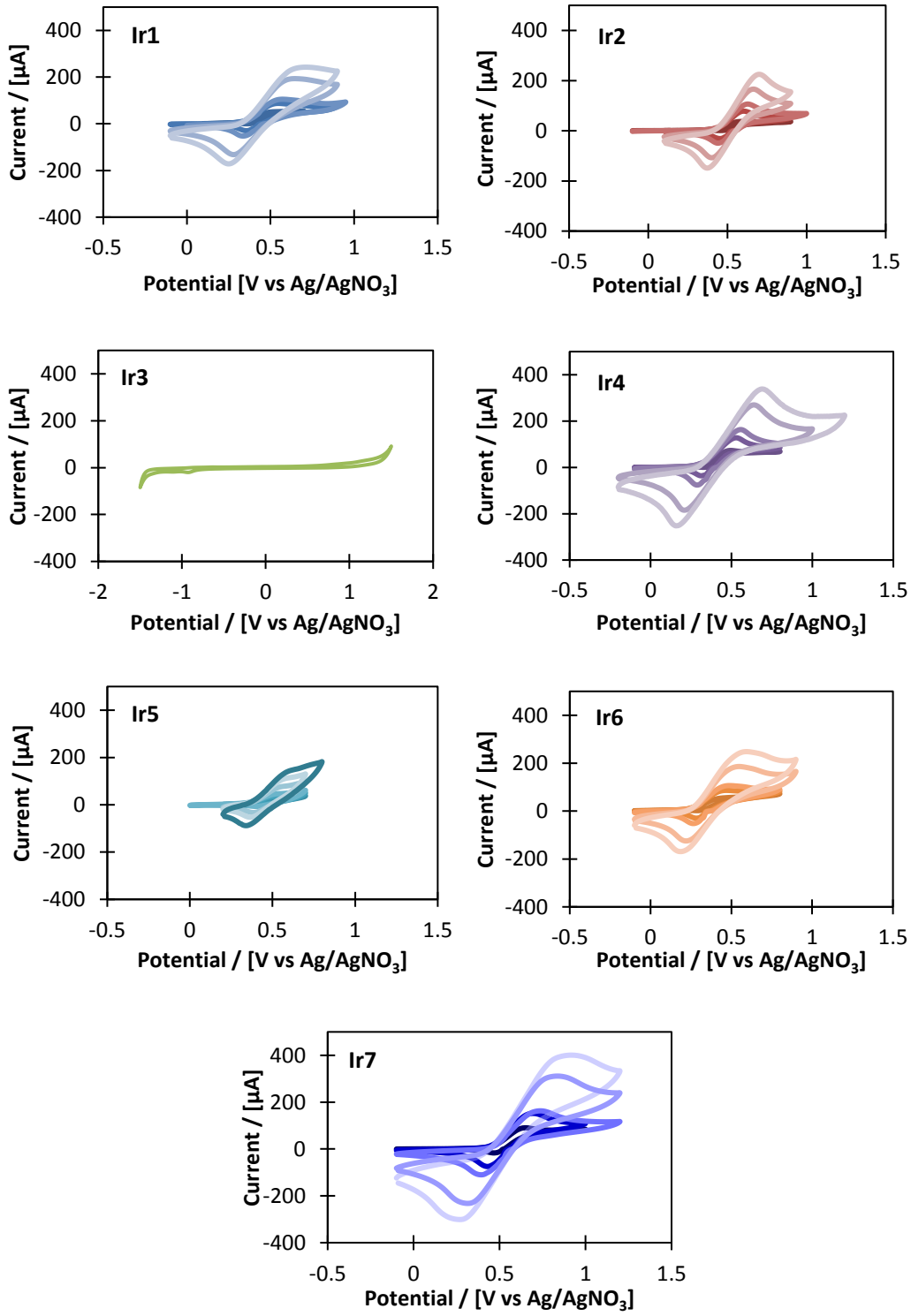

Figure 2.15. *CVs of precatalysts* ***Ir1***-***Ir7*** *under glove box conditions with 10mM [Ir], 0.15 M [tmbim][NTf$_2$] electrolyte, DCM (degassed via freeze pump thawing), WE: GC, RE: Ag/AgNO$_3$, CE: Pt wire, 100 mVs^{-1} scan rate*

All of the neutral complexes (**Ir1**, **Ir2**, **Ir4-Ir7**) showed a clearly defined, quasi-reversible feature assigned to the $Ir^{III/IV}$ redox couple, with the position of the couple, and the peak currents, varying significantly depending on the supporting ligand. Further details of the recorded scans will be discussed as follows:

a. lack of redox features for cationic **Ir3**,
b. E_{mid} analysis and
c. reversibility indicators.

Notably the cationic species **Ir3** did not show redox features even upon extended potential ranges. The inert atmosphere precludes the complexes accessing the $^{6}Ir\text{-}OH_2$ or $^{6}Ir\text{-}OH$ species previously described, and as such, only the $^{6}Ir\text{-}Cl$ and $^{5}Ir^{+}$ species are accessible. For **Ir3**, the bulky bis-^{t}butyl groups prevent formation of the $^{6}Ir\text{-}Cl$ species. Therefore, within the potential window of up to 1.5 V vs. NHE, the $^{5}Ir^{+}$ species is not oxidisable.

In order to confirm the theory that the cationic species is redox inactive up to 1.5 V, the equivalent cationic version of the pyridine dimethyl complex was synthesised[9] and the corresponding CV was recorded (Figure 2.16). As for **Ir3**, **Ir1**$^{+}$ showed no reversible redox features.

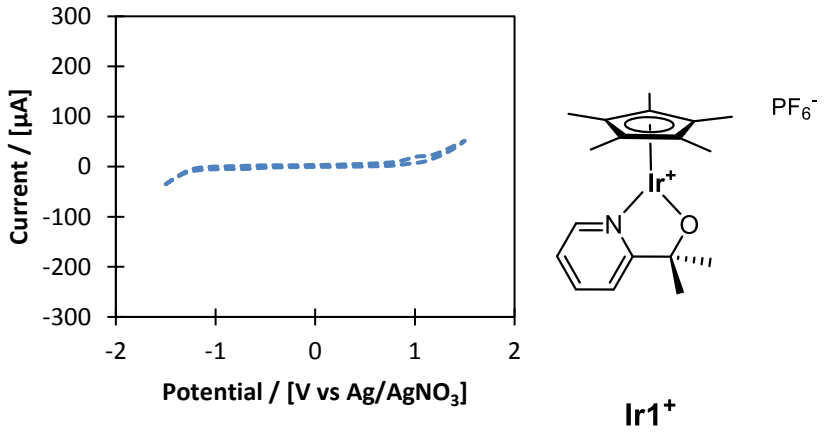

Figure 2.16. *CV of cationic version of* ***Ir1*** *under glove box conditions with 10mM [Ir], 0.15 M [tmbim][NTf$_2$] electrolyte, DCM (degassed, freeze pump thawed), WE: GC, RE: Ag/AgNO$_3$, CE: Pt wire, 100 mVs^{-1} scan rate*

With suitable redox features in the CVs, E_{mid} values could be obtained, therefore giving an indication of the effect of the ligands on the formal redox potential of the $Ir^{III/IV}$ couple (Figure 2.17, numerical values in Table 2.2). E_{mid} values were calculated in the first instance by assessing the potential at the peak current at 100 mVs^{-1}.

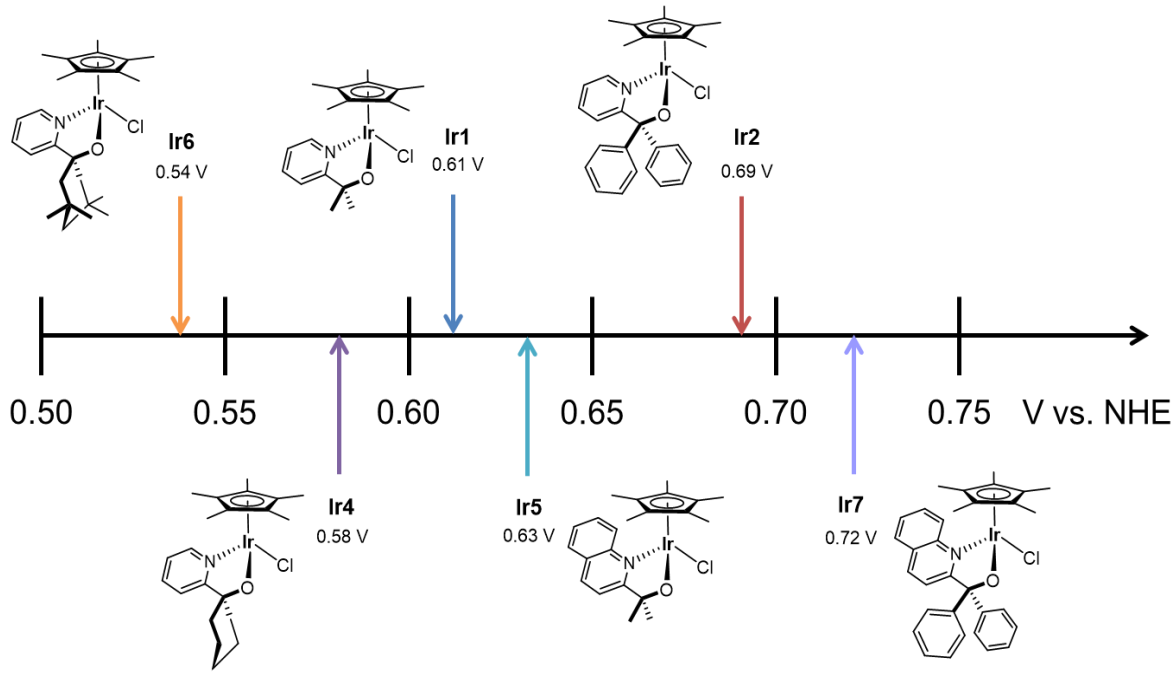

Figure 2.17. *Formal potentials of the $Ir^{III/IV}$ couple for precatalysts **Ir1**, **Ir2**, **Ir4**-**Ir7** shown as potential vs NHE in V. Obtained from mid-point values from cyclic voltammograms at 100 mVs^{-1} (Figure 2.16)*

Table 2.2. *Peak potentials, mid-point potential and peak to peak separation data for precatalysts **Ir1**-**Ir7** from the 100 mVs^{-1} CV shown in Figure 2.16*

	E_{ox} vs NHE / V	E_{red} vs NHE / V	ΔE / V	E_{mid} vs NHE ± 0.1 / V[a]
Ir1	0.77	0.54	0.23	0.61
Ir2	0.83	0.64	0.19	0.69
Ir4	0.75	0.49	0.27	0.58
Ir5	0.73	0.60	0.13	0.63
Ir6	0.68	0.46	0.22	0.54
Ir7	0.93	0.59	0.34	0.72

[a] E_{mid} value reported calculated from average of E_{mid} values at different scan rates vs $Ag/AgNO_3$ and corrected to NHE

The $Ir^{III/IV}$ couple was different for all neutral complexes, varying between 0.54 to 0.72 V vs NHE. In general, the trend correlates to the inductive/withdrawing effects of the N^O ligand, such that the more inductive cyclohexyl groups give a low value for the $Ir^{III/IV}$ couple, whilst the slightly withdrawing phenyl groups give the highest values, suggesting the inductive effects stabilise the Ir^{IV} complex.

As well as mid-point analysis, attempts were made to assess the reversibility of the redox event. As previously discussed, for a redox event to be considered reversible a typical peak to peak separation of 59 mV is expected, and the peak oxidation current = peak reduction current.

Despite the $Ir^{III/IV}$ redox couple expecting to be a chemically reversible event, especially under glove box conditions where no catalytic process should be able to occur, the peak to peak separation of 59 mV was not observed, presumably due to the higher resistivity of the solvent and the glove box itself.[d] A CV of ferrocene, a known one electron redox process, was therefore also recorded under identical conditions, in order to help gauge the measure of reversibility in the precatalysts.

The chemically reversible Fc/Fc^+ couple, the commonly used electrochemical standard, did not show the 59 mV separation, and the E_{ox} and E_{red} peaks change with increasing scan rate (visibly seen in the CVs (Figure 2.18a), such that the system is not considered to be perfectly electrochemically reversible.

[d] Attempts were also made at running these experiments with micro electrodes, as a smaller electrode surface area will also decrease the resistance. However, the background noise detected was greater than the reduced signal current recorded by the micro electrodes (potentially due to the background noise of the glove box itself) and no meaningful data was obtained (Appendix Figure 2.3)

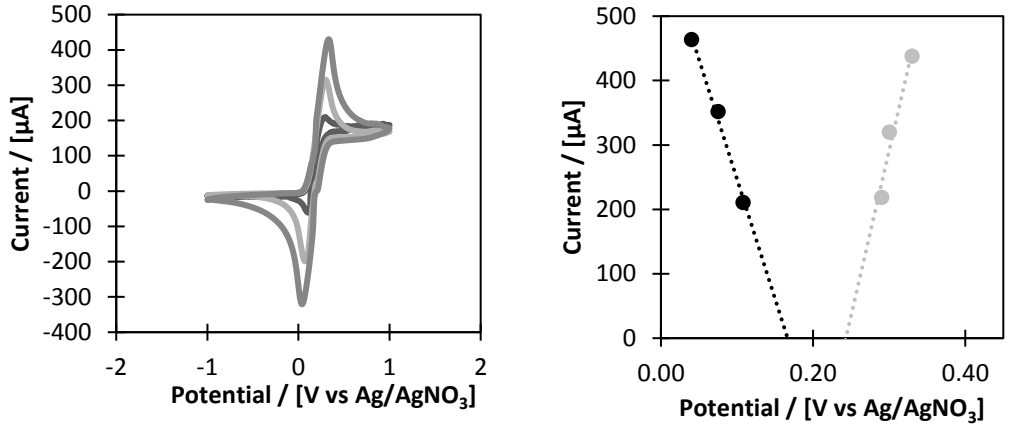

Figure 2.18 a) *CV of ferrocene under glove box conditions with 10mM, 0.15 M [tmbim][NTf$_2$] electrolyte, DCM (degassed, freeze pump thawed), WE: GC, RE: Ag/AgNO$_3$, CE: Pt wire, 100 mVs^{-1} scan rate* ***b)*** *E$_{mid}$ analysis using the peak potential and peak current data for the oxidation (grey) and reduction (black) of ferrocene from a)*

With the high resistivity in mind, additional analysis was undertaken, exploiting the relationship between current, voltage and resistance. By plotting the peak potential vs. the peak current at different scan rates for oxidation and reductions, the data can be extrapolated down to predict an E_{ox} and an E_{red} using the resistance. From here, both the ideal ΔE values can be calculated and an alternative value for $E_{1/2}$. This analysis was performed for all precatalysts **Ir1**-**Ir7** (full graphs Appendix Figure 2.4).

Table 2.3. *Peak oxidation and reduction currents, ratios for ferrocene and precatalysts* ***Ir1***-***Ir7****, mid-point potential and peak to peak separation data calculated from potential vs. current graphs*

	ΔE / mV	**E$_{mid}$ vs NHE / V**	**Peak i$_{ox}$ /µA**	**Peak i$_{red}$ / µA**	**Peak i$_{ox}$ / peak i$_{red}$[a]**
Ferrocene	63	0.39	438	464	0.95
Ir1	94	0.63	107	96	1.11
Ir2	91	0.72	104	95	1.09
Ir4	74	0.61	158	152	1.04
Ir5	80	0.66	45	42	1.06
Ir6	94	0.56	113	113	1
Ir7	94	0.75	173	181	0.96

[a] peak i$_{ox}$ and peak i$_{red}$ values reported here for the 100 mVs^{-1} data

The recalculated E_{mid} values are in good agreement with the previously calculated values, and the ideal ΔE values are much closer to the expected 59 mV. The additional descriptor for chemical reversibility, the peak i_{ox} / peak i_{red} values, were also calculated from the CVs, with all precatalysts giving values of close to unity, indicating chemical reversibility.

Randles-Sevcik analysis was also conducted for all the precatalysts (representative graph Figure 2.19, all others in appendix), revealing a linear relationship between $\sqrt{}$ scan rate and peak current for all complexes, indicating freely diffusing species in solution.

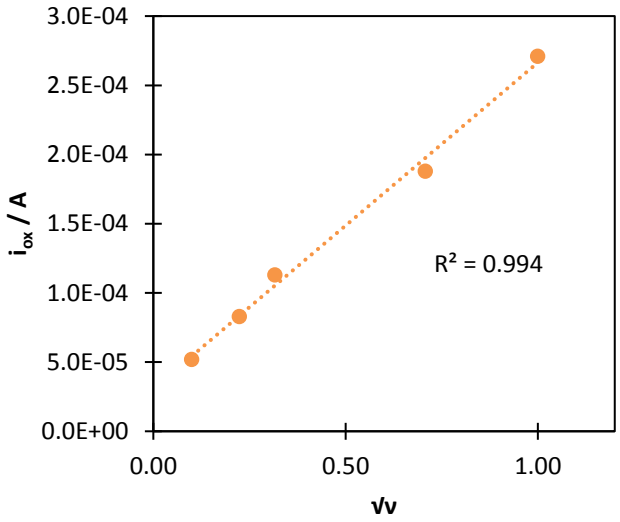

Figure 2.19. *Randles-Sevcik analysis for* ***Ir6*** *from CV data shown in Figure 2.16*

As the CVs collected under aqueous conditions had shown varying levels of deposition onto the electrode surface, scans of the electrolyte were conducted after each catalyst run (Figure 2.20). No deposition was observed between catalyst runs.

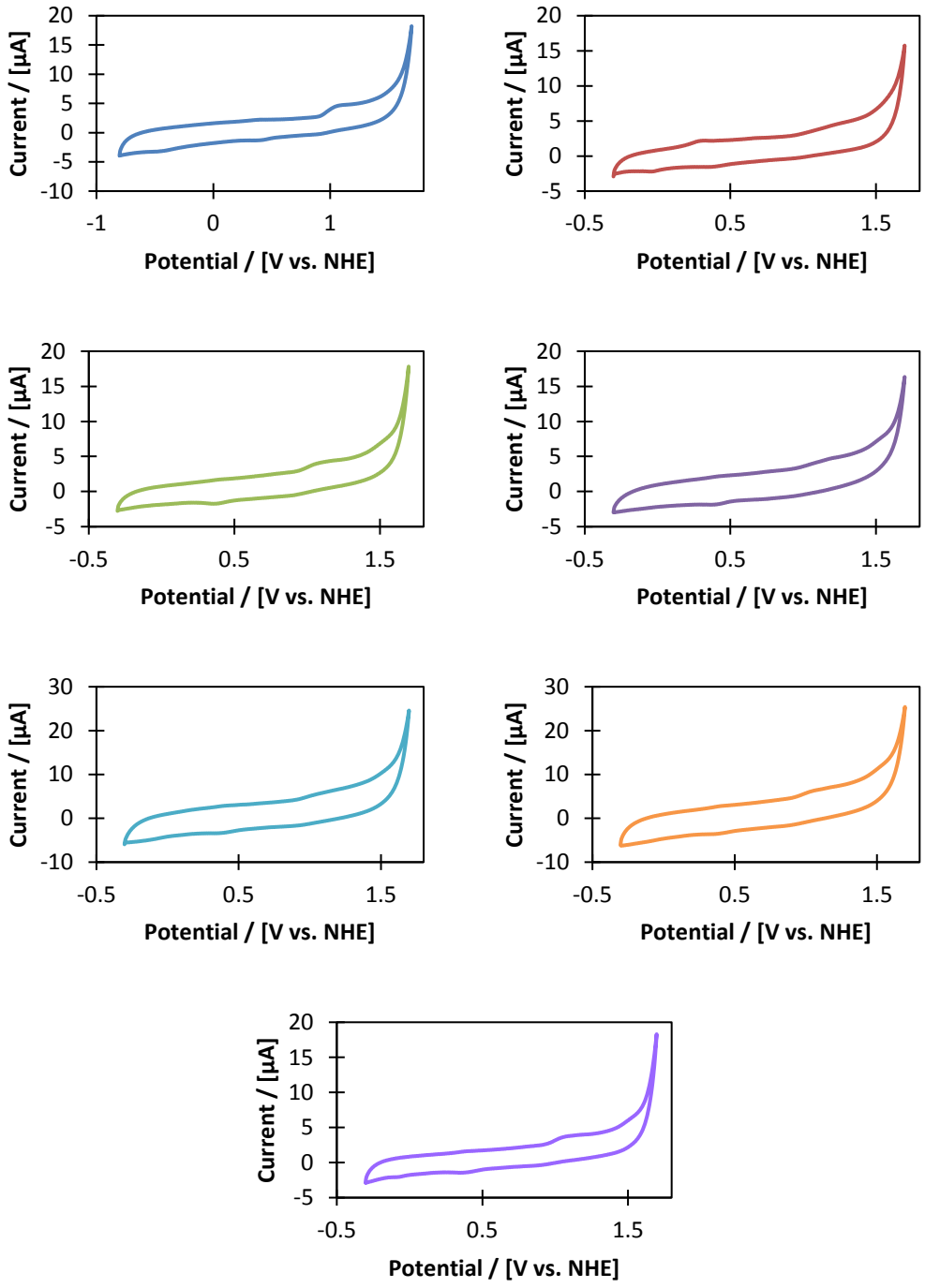

***Figure 2.20**. CVs of fresh electrolyte after each catalyst run showing no deposition was observed in DCM. Glove box conditions. 10mM [Ir], 0.15 M [tmbim][NTf_2] electrolyte, DCM (degassed, freeze pump thawed), WE: glassy carbon, diameter 0.3 cm, RE: $Ag/AgNO_3$, CE: Pt wire, 100 mVs^{-1} scan rate.*

2.5 Chemical Activation

It has been previously shown that the half-sandwich precatalysts undergo oxidative activation with loss of the Cp* ligand, resulting in a deeply blue coloured solution which is attributed to the formation of the active dimeric catalytic species.[23,24]

Scheme 2.5. *Activation of precatalyst by $NaIO_4$*

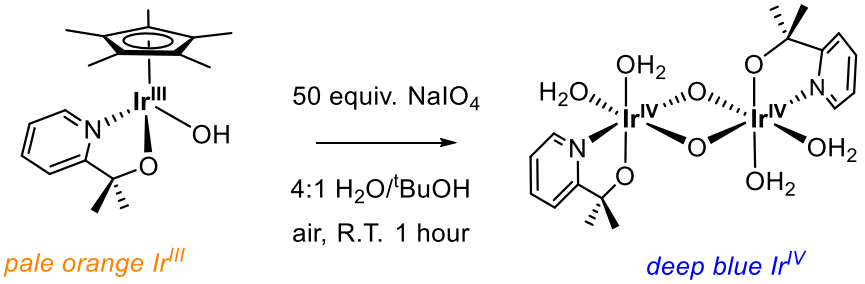

It should be noted at this point that it is assumed that the multiple Ir^{III} species in solution, outlined in the previous section, should have no effect on full activation of the precatalysts to the dimer. The equilibria are considered to be interchanging on a time scale fast enough that it is not limiting for activation.

2.5.1 NMR analysis of precatalyst activation

Investigation of the activation was studied by ^1H NMR to demonstrate the irreversible loss of the bound Cp* ligand. For all the precatalysts, the signal for the Cp* seen at ~1.6 ppm disappeared within the first minute of contact between the precatalyst solution and $NaIO_4$ (Figure 2.21 for representative example for **Ir5**, all other precatalyst activations in Appendix, Figure 2.5).

As previously reported, over the hour experiment there was a build-up of acetate as the main degradation product of the Cp*, as evidenced by the growth of a peak at ~2.0 ppm.[23,25,26] This was observed for all catalysts **Ir1-Ir7**, suggesting that in every case Cp* does not stay bound to the Ir centre in the presence of an oxidant, and is oxidatively degraded.

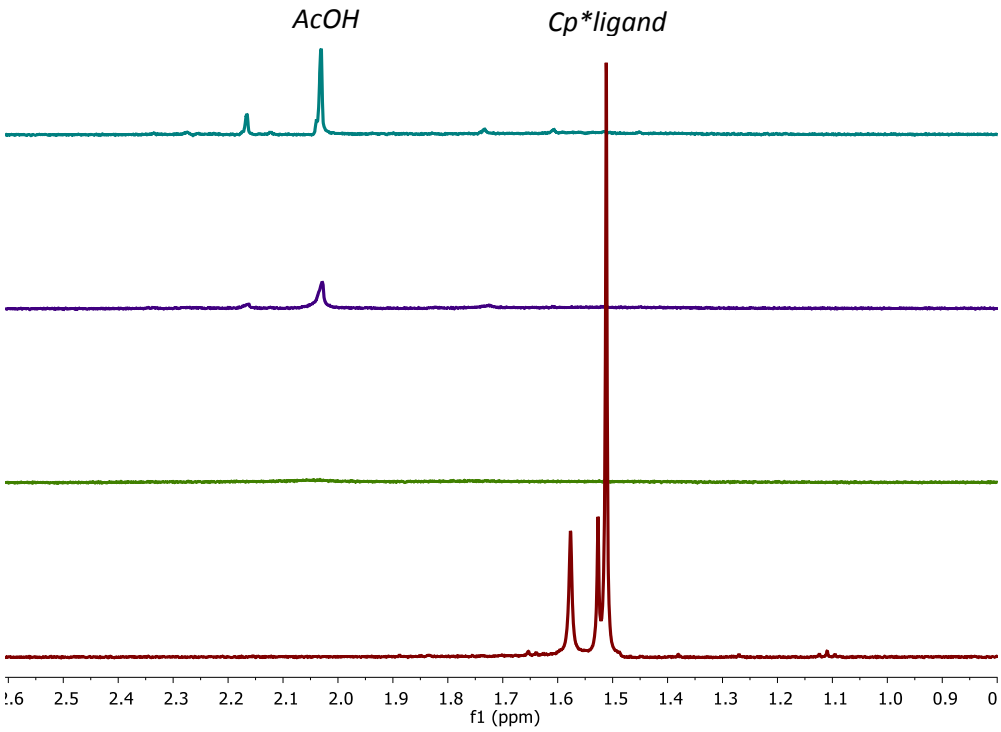

Figure 2.21. *^{1}H NMR data for activation of **Ir5** (0.5 mM) with 50 equivalents of $NaIO_4$ (25 mM) in D_2O (0.5 mL) red) before $NaIO_4$ addition, green) t = 1 min, purple) t = 3 mins and blue) t = 60 mins showing disappearance of Cp* ligand peak (~1.5 ppm) and growth of acetate peak (~2.1 ppm)*

Notably no ligand signals are observed for the activated catalysts. This is attributed to the active catalyst resting in a $Ir^{IV,IV}$ state, which would be expected to be a paramagnetic species. Previous attempts at obtaining electron paramagnetic resonance (EPR) data for activated **Ir1** showed no signal, which was attributed to a polynuclear Ir^{IV} species, with d^5 coupled metal centres.[23]

2.5.2 UV-vis analysis of precatalyst activation

The strong colour change observed upon full precatalyst activation renders the reaction suitable for investigation by UV-vis spectroscopy. With the Cp* ligand shown by NMR to be lost after a minute, any changes in the UV-vis spectra can be ascribed to further structural transformations leading to the formation of the activated resting state of the catalyst.

Whilst previous UV-vis absorption of the parent complex **Ir1** was conducted in neat H_2O, some of the bulkier ligands presented here showed lower solubility and necessitated the addition of an organic co-solvent to aid dissolution. ^{t}Butanol was not seen to have any effect of the activation compared to previous data for compound **Ir1**, apart from a slight shift in the wavelength of the blue band (593 nm to 602 nm) (Appendix, Figure A2.5).

The UV-vis spectra (Figure 2.22) show that changing the bulk of the N^O ligand changes the length of time taken for full activation (as shown in differences in the evolution of the blue band at ~600 nm).

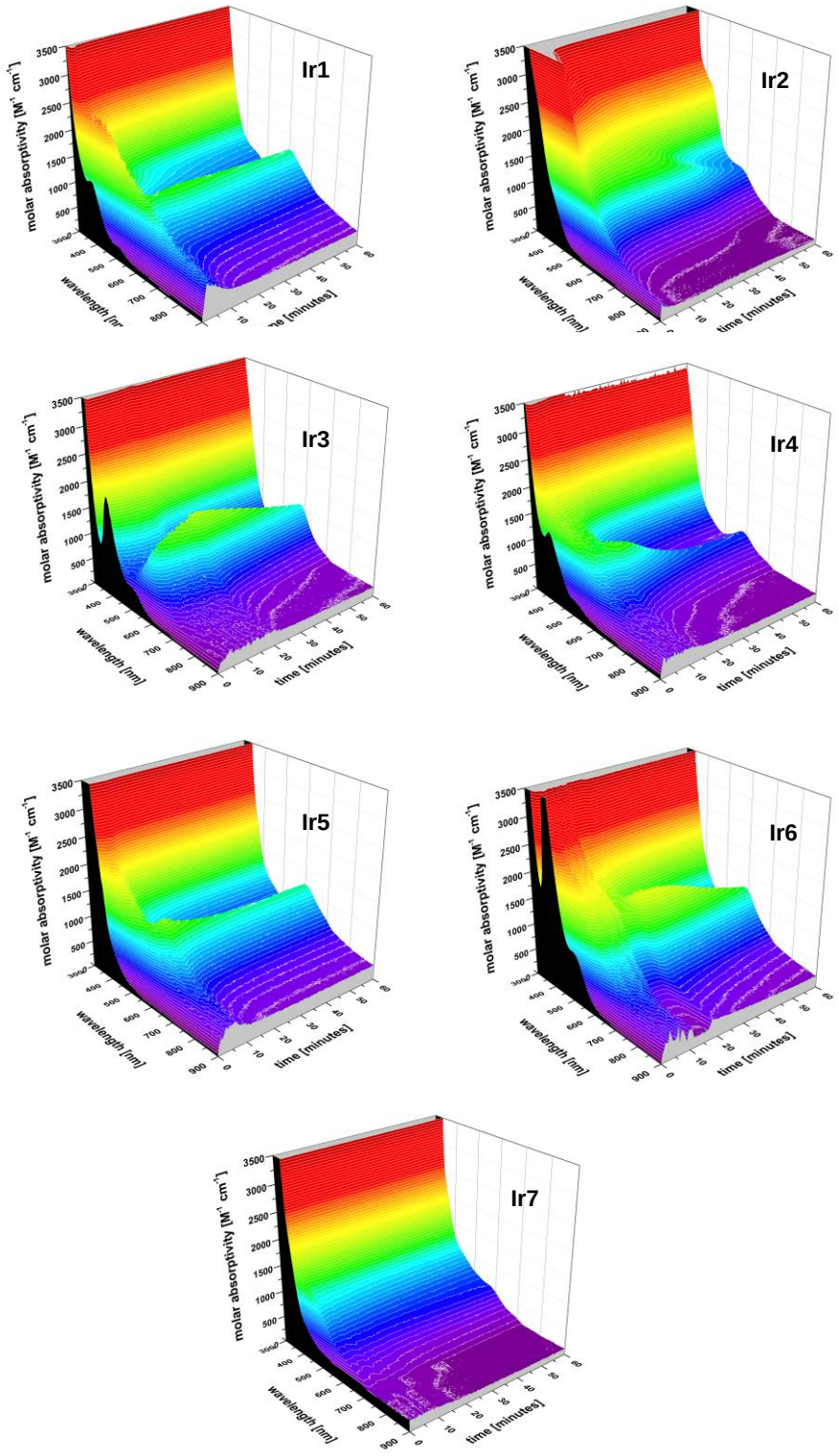

Figure 2.22. *Full scan UV-vis time-courses of the reaction shown in Scheme 2.5 for compounds* ***Ir1***-***Ir7*** *at 0.5 mM [Ir] with 25 mM $NaIO_4$ added after the first scan (black trace) in 4:1 H_2O/ ^tBuOH at room temperature as followed by UV-vis spectroscopy (30 sec intervals).*[e]

[e] UV-vis spectra for Ir2, Ir3, Ir4, Ir5 collected during MRes2; included for comparison.

Under the applied conditions with 50 equivalents of oxidant, all complexes showed some intensity of a blue band around 580 nm attributable to a dimeric Ir^{IV}-O-Ir^{IV} complex.[23] However, significantly different activation kinetics were observed for the precatalysts, as well as variation of the molar absorptivities and λ_{max} (Table 2.4).

Table 2.4. *Activation reaction times, absorption wavelength and intensity of the activated species from* ***Ir1*****-*****Ir7*** *with 50 equiv. $NaIO_4$ in 4:1 H_2O/^{t}BuOH*

Precatalysts	Time / mins [a]	λ_{max} [b]	ε / M^{-1} cm^{-1} [c]
Ir1	2.5 / 15.5	599 nm	1508 / 1354
Ir2	1 / 26.5	568 nm	1562 / 1299
Ir3	22.5	575 nm	1355
Ir4	10	572 nm	1400
Ir5	5.5	602 nm	1772
Ir6	22	573 nm	1623
Ir7	60	571 nm	594

[a] time taken to reach maximum absorbance
[b] wavelength of maximum absorbance
[c] absorbance at λ_{max}.

Slight variation in the Ir^{IV}-O-Ir^{IV} regime of the dimeric species reflect ligand effects on the d(Ir^{IV})π*(Ir-O-Ir) transition at ~580 nm. Changing from a pyridine to a quinoline group (**Ir1** → **Ir5** and **Ir2** → **Ir7**) slightly increased the λ_{max} value. Cyclohexyl complexes **Ir4** and **Ir6** showed very similar λ_{max} values at 572 and 573 nm respectively.

With regards to the time taken to reach λ_{max}, two values are given for **Ir1** and **Ir2**. Bubble formation due to water oxidation complicates the initial values, and for **Ir2** a second absorption at 432 nm partially obscures exact analysis of the feature at 568 nm. The first value reported is therefore the absolute maximum, and the second value is the time taken to reach a stable plateau (Figure 2.23). The absorbance at 432 nm persists for **Ir2** throughout the reaction, whilst a maximum value of λ_{568} is seen upon oxidant addition, but the intensity of the absorbance at 568 nm decays immediately and continues to decay throughout the reaction.

Whilst **Ir1** and **Ir5** show little decay of the ~580 nm absorbance, the intensity of this transition decays over the course of the reaction for **Ir2**, **Ir3**, **Ir4**, **Ir6**.

Ir7 shows a very low molar absorptivity; approximately a third lower than the other precatalysts. The highest ε value is observed after 1 hour, although there is not a large increase in absorbance (570 M^{-1} cm^{-1} at 30 seconds, 594 M^{-1} cm^{-1} after one hour). It is suggested that **Ir7** does not form substantial amounts of a dimeric species which would give rise to a Ir-O-Ir absorbance. However, given that by ^{1}H NMR Cp* loss still occurs within 5 minutes (Appendix, Figure 2.5), activation of **Ir7** must still occur.

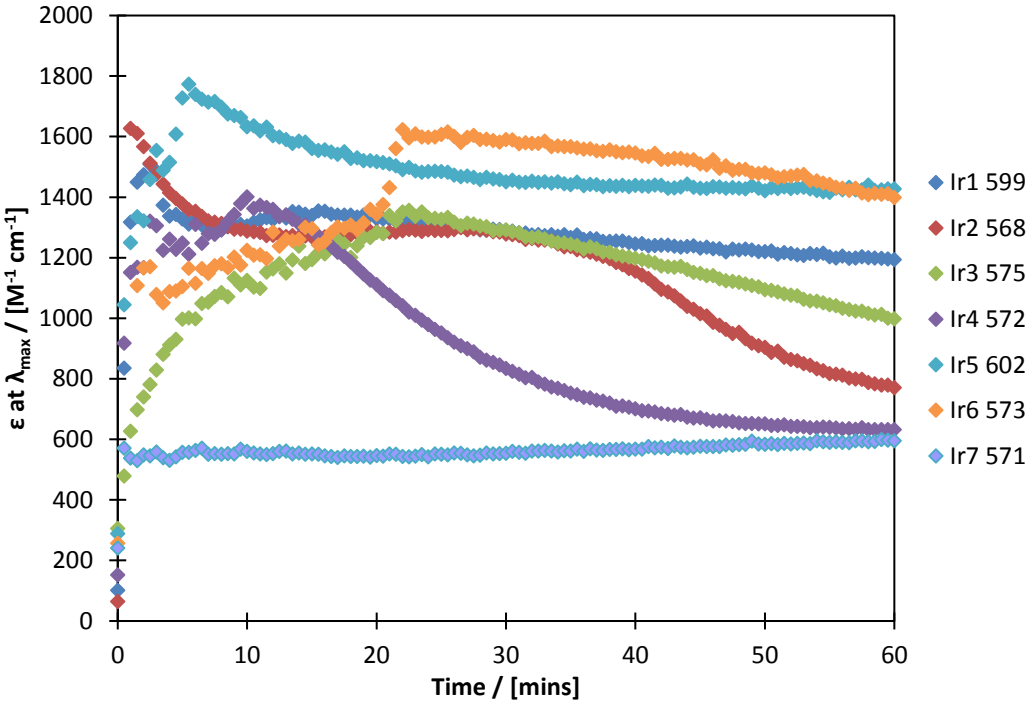

Figure 2.23. *Plot of changing intensities for λ_{max} at ~580nm of **Ir1**-**Ir7** over time*

2.6 Summary

A range of novel Cp* Ir^{III} complexes bearing N^O-type ligands of varying bulk were synthesised and fully characterised.

It was established that the ancillary chloro ligand was labile and that a range of iridium species were therefore present in solution, ranging from ^{6}Ir-Cl -> Ir^{+} -> Ir-OH_2^{+} -> Ir-OH. The position of the species equilibrium in aqueous solution varied depending on the N^O ligand, as evidenced by clear changes upon titrations with KCl (followed by UV-vis spectroscopy) and aqueous electrochemistry.

The complexity of the aqueous electrochemistry, due in part to the solution speciation but also because of precatalyst activation and deposition of [Ir] onto the working electrode, necessitated non-aqueous electrochemistry under glove box conditions to determine meaningful data about the potential of the $Ir^{III/IV}$ redox couple.

The non-aqueous CVs showed clearly defined redox features, from which the $Ir^{III/IV}$ transition could be determined for the Ir-Cl species for **Ir1**-**Ir7** with the exception of **Ir3**, for which the ^{6}Ir-Cl species could not be accessed. In general, the more withdrawing the substituent the higher the E_{mid} value, such that diphenyls **Ir7**, **Ir2** > dimethyls **Ir1**, **Ir5** > cyclohexyls **Ir4**, **Ir6**.

Although the solution speciation data is interesting and somewhat unexpected in terms of the extent to which the ligand affects it, it is not expected to have a significant impact on the catalytic activity of the complexes. The activation time and the E_{mid} values, however, should allow for a more nuanced interpretation of the subsequent oxidative ability of the varying catalysts.

The final investigation of the effect of the ligand under non-catalytic conditions was the precatalyst activation reaction. Analysis of the reaction by ^{1}H NMR kinetics revealed that the Cp* ligand was lost almost immediately for all complexes. However, analogous experiments followed by UV-vis detailed significant variation in the time taken for the fully active catalyst to form, and variation in the λ_{max} depending on the N^O ligand.

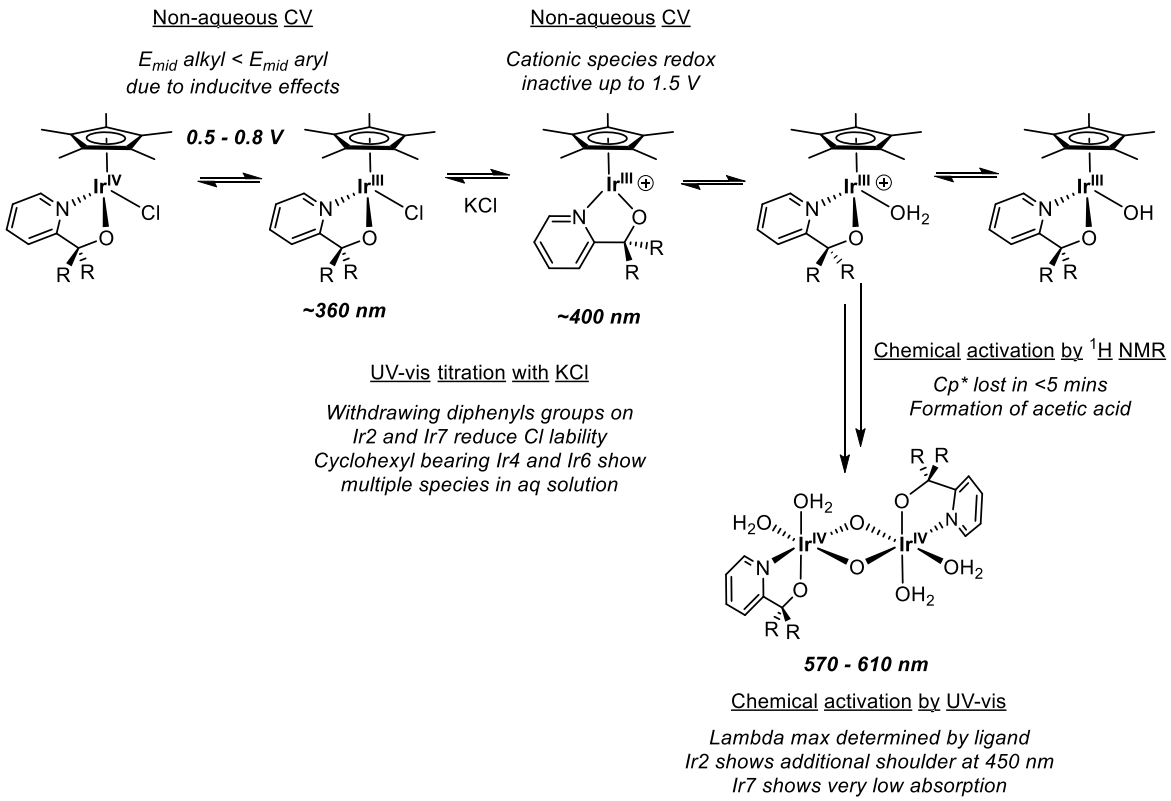

***Figure 2.24**. Summary of key data from Chapter 2*

2.7 Experimental

2.7.1 General

Organic solvents were purified by passing over activated alumina with dry argon. All chemicals were purchased from major commercial suppliers and used as received. Syntheses were performed under an inert atmosphere of dry argon using standard Schlenk techniques. NMR spectra were recorded on either 400 or 500 MHz Bruker Avance spectrometers and referenced to residual protio-solvent signals. The chemical shift δ is reported in units of parts per million (ppm). Elemental analyses were provided by the Science Centre of London Metropolitan University, and mass spectrometry (MS) was performed by the EPSRC UK National Mass Spectrometry Facility at Swansea University. Details of the single crystal X-ray data collections and ligand syntheses can be found in the supporting information. UV-vis spectroscopy was performed on a Varian Cary 50 photospectrometer using 1 cm quartz cuvettes.

2.7.2 Synthesis

2.7.2.1 Ligands

2-(2-Pyridyl)-2-propanol[4], L1

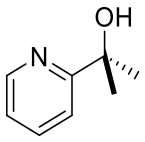

A solution of 2-acetyl pyridine (20 mmol, 2.42g) in diethyl ether (50 mL) was placed in a flame dried round bottom flask and cooled to 0 °C. Methyl magnesium bromide (3 M in diethyl ether, 22 mmol, 7.3 mL) was added dropwise via a dropping funnel and the resultant solution was stirred at room temperature for 1 hour. The reaction was quenched by addition of water (50 mL) and conc. HCl (3 mL). The product was extracted with diethyl ether (3 x 50 mL), the combined organic extracts dried over $MgSO_4$, filtered and dried *in vacuo* to give a pale yellow oil. Upon addition of hexane (5 mL) and storage at -20 ˚C colourless crystals formed, which were collected from their yellow supernatant and dried *in vacuo*.

Yield: 1.70 g (62 %). **^{1}H-NMR** (400 MHz, $CDCl_3$): δ = 8.48 (d, *J* = 4.8 Hz, 1H, H_{arom}), 7.67 (t, *J* = 7.8 Hz, 1H, H_{arom}), 7.36 (d, *J* = 8.0 Hz, 1H, H_{arom}), 7.16 (t, *J* = 6.3 Hz, 1H, H_{arom}), 5.09 (s, 1H, OH), 1.52 (s, 6H, $[CH_3]_2$).

General procedure for L2-L7

2-bromo pyridine or 2-bromo quinoline (20 mmol) was degassed by careful application of vacuum, dissolved in dry THF (40 mL) and the solution cooled to -78°C. n-BuLi (1.6 M in hexanes, 22 mmol) was added via a dropping funnel over 20 mins. The resulting yellow solution was stirred for 1.5 hours at -78°C and a series of colour changes was observed (yellow -> orange -> brown). A solution of the desired ketone (20 mmol) in dry THF (10 mL) was added to the dropping funnel and added to the solution over 10 mins. The solution was left to warm to room temperature and stirred for 18 hours, after which time it had turned dark green. The reaction was quenched by addition of 1 M NaOH (25 mL) and water (25 mL), changing to yellow. The product was extracted with diethyl ether (3 x 50 mL), the combined organic extracts dried over $MgSO_4$, filtered and dried *in vacuo* to afford the crude product as an oil.

Diphenyl(2-pyridyl)methanol[5], L2

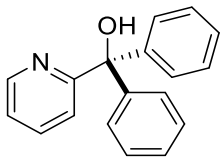

Purification: The crude product (a dark orange oil) was recrystallized from hexane (20 mL) and the yellow supernatant removed. The resulting solid was washed with hexane (2 x 20 mL), giving a creamy white, microcrystalline solid.

Yield: 1.69 g (32 %). **^{1}H-NMR** (400 MHz, $CDCl_3$): δ = 8.60 (d, *J* = 4.9 Hz, 1H, H_{arom}), 7.64 (t, *J* = 7.7 Hz, 1H, H_{arom}), 7.29 (s + m, 11H, H_{arom} + CH_{phenyl}), 7.12 (d, *J* = 9.7 Hz, 1H, H_{arom}), 6.30 (s, 1H, OH).

2,2,4,4-Tetramethyl-3-(2-pyridyl)-3-pentanol[27], L3

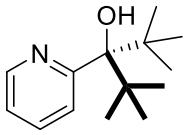

Purification: The crude product (a dark brown oil) was purified via sublimation under high vacuum at 45 ˚C onto a cold finger at -78˚C, yielding colourless crystals.

Yield: 0.53 g (34 %). **^{1}H-NMR** (400 MHz, $CDCl_3$): δ = 8.49 (d, *J* = 5.0 Hz, 1H, H_{arom}), 7.62 (m, 2H, H_{arom}), 7.19 (t, *J* = 5.9 Hz, 1H, H_{arom}), 6.66 (s, 1H, OH), 1.03 (s, 18H, $[CH_3]_6$).

1-(2-Pyridyl)cyclohexanol[28], L4

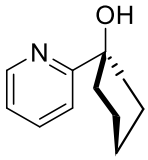

Purification: The crude product (a dark brown oil) was purified via sublimation under high vacuum at 50 ˚C onto a cold finger at -78˚C, yielding a colourless solid.

Yield: 0.77 g (22 %). **^{1}H-NMR** (400 MHz, $CDCl_3$): δ = 8.51 (d, *J* = 4.1 Hz, 1H, H_{arom}), 7.69 (t, *J* = 7.7 Hz, 1H, H_{arom}), 7.39 (d, *J* = 8.1 Hz, 1H, H_{arom}), 7.19 (t, *J* = 6.2 Hz, 1H, H_{arom}), 4.88 (s, 1H, OH), 1.76 (m, 10H, CH_{hexyl}).

2-(2-Quinolyl)-2-propanol[29], L5

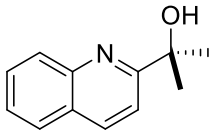

Purification: The product was extracted with diethyl ether (3 x 50 mL), the combined organic extracts dried over $MgSO_4$, filtered and dried *in vacuo* to afford a brown oil that was pure by NMR analysis.

Yield: 0.32 g (72 %). **^{1}H-NMR** (400 MHz, $CDCl_3$): δ = 8.18 (d, *J* = 8.6 Hz, 1H, H_{arom}), 8.06 (d, *J* = 8.5 Hz, 1H, H_{arom}), 7.81 (d, *J* = 8.2 Hz, 1H, H_{arom}), 7.72 (t, *J* = 7.7 Hz, 1H, H_{arom}), 7.54 (t, *J* = 7.5 Hz, 1H, H_{arom}), 7.45 (d, *J* = 8.6 Hz, 1H, H_{arom}), 5.92 (s, 1H, OH), 1.61 (s, 6H, $[CH_3]_2$).

3,3,5,5-Tetramethyl-1-(2-pyridyl)cyclohexanol, L6

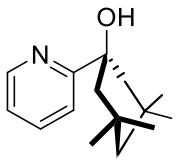

Purification: The crude product (a dark red oil) was recrystallised from cold hexane (20 mL, -78°C) and the supernatant removed to give brown crystals which were dried *in vacuo*.

Yield: 0.65 g (28 %). **^{1}H-NMR** (400 MHz, $CDCl_3$): δ = 8.50 (d, *J* = 4.8 Hz, 1H, H_{arom}), 7.68 (t, *J* = 8.0 Hz, 1H, H_{arom}), 7.40 (d, *J* = 8.0 Hz, 1H, H_{arom}), 7.16 (t, *J* = 8.0 Hz, 1H, H_{arom}), 4.99 (br s, 1H, OH), 1.56 (s, 4H, $H_{cyclohex}$), 1.51 (d, *J* = 13.6 Hz, 2H, $H_{cyclohex}$), 1.34 (s, 6H, $[CH_3]_2$), 0.94 (s, 6H, $[CH_3]_2$); **^{13}C-NMR** (100 MHz, CD_2Cl_2): δ = 166.7 ($C_{pyridine}$), 147.2 ($CH_{pyridine}$), 136.8 ($CH_{pyridine}$), 121.6 ($CH_{pyridine}$), 118.92 ($CH_{pyridine}$), 75.5 (C), 51.8 (CH_2), 49.7 (CH_2), 36.6 (CH_3), 31.7 (C), 28.2 (CH_3); **HR ESI-MS (+)**: m/z calculated for $C_{15}H_{23}NO$: $[M+H]^+$ 234.1849, 235.1882; found 234.1852, 235.1885; **Elemental analysis**: calculated for $C_{15}H_{23}NO$: C 77.21, H 9.94, N 6.00; found: C 77.05, H 10.01, N 6.12.

1,1-Diphenyl-1-(2-quinolyl)methanol, L7

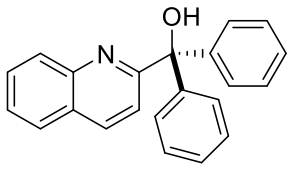

Purification: The product was recrystallised from DCM (5 mL) by addition of hexane (30 mL) and storage at -20°C for 24 hours. The supernatant was removed and the pale yellow solid was dried *in vacuo*.

Yield: 0.13 g (17 %). **^{1}H-NMR** (400 MHz, $CDCl_3$): δ = 8.11 (t, *J* = 8.4 Hz, 2H, H_{arom}), 7.82 (d, *J* = 8.4 Hz, 1H, H_{arom}), 7.75 (t, *J* = 8.0 Hz, 1H, H_{arom}), 7.57 (t, *J* = 8.0 Hz, 1H, H_{arom}), 7.35-7.28 (m, 10H, H_{phenyl}), 7.15 (s, 1H, H_{arom}), 5.30 (s, 1H, OH); **^{13}C-NMR** (100 MHz, CD_2Cl_2): δ = 162.6 ($C_{quinoline}$), 146.1 ($C_{quinoline}$), 145.8 ($C_{quinoline}$), 136.7 (CH_{arom}), 130.1 (CH_{arom}), 129.1 (CH_{arom}), 128.4 (CH_{arom}), 128.1 (CH_{arom}), 127.6 (CH_{arom}), 127.5 (CH_{arom}), 127.3 (CH_{arom}), 127.0 (CH_{arom}), 120.9 ($CH_{quin\text{-}arom}$), 80.9 (C); **HR ESI-MS (+)**: m/z calculated for $C_{22}H_{17}NO$: $[M+H]^+$ 312.1383, 313.1417; found 312.1375, 313.1407; $[M\text{-}H_2O]^+$ 294.1277; found: 294.1273; **Elemental analysis**: calculated for $C_{22}H_{17}NO$: C 84.86, H 5.50, N 4.50; found: C 84.78, H 5.42, N, 4.41.

2.7.2.2 Ir complexes

$[Cp^*IrCl_2]_2$[30]

$IrCl_3.3H_2O$ (2.84 mmol, 1.00 g) was added to a 20 mL microwave flask with methanol (10 mL) and water (1 mL). The solution was degassed by bubbling with argon with stirring for 5 mins. Under a continuous stream of argon, pentamethylcyclopentadiene (3.67 mmol, 0.5 g) was added and the mixture was stirred for a further 2 mins. The flask was sealed, put into a microwave reactor and heated to 140 °C for 20 mins. The reaction was quenched with ice and a red/orange precipitate formed. The mixture was filtered under vacuum using a fritted funnel, and the solid residue extracted with DCM (20 mL). The product was recrystallised from DCM (3 mL) by addition of Et_2O (20 mL). Removal of the supernatant and drying *in vacuo* yielded a microcrystalline red/orange powder.

Yield: 686 mg (61%). **^{1}H-NMR** (400 MHz, $CDCl_3$): δ = 1.57 (s, 15H, $[CH_3]_5$).

$[\eta^5(C_5Me_5)Ir^{III}\{2\text{-}(2\text{-pyridyl})\text{-}2\text{-propanolate-}\kappa O,\kappa N\}Cl]$, Ir1[31]

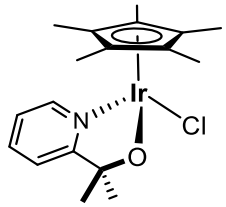

$[Cp^*IrCl_2]_2$ (0.1 mmol, 79.8 mg), dimethyl(2-pyridyl)methanol (0.2 mmol, 27.4 mg) and Na_2CO_3 (0.8 mmol, 84.8 mg) were dissolved in acetone (15 mL). The resulting orange solution was stirred for 6 hours at 50 °C, after which time the solution had turned yellow. $MgSO_4$ was added, and after stirring for 10 minutes the solution was filtered and the solvent removed *in vacuo* to afford an orange-red solid. The product was re-crystallised from DCM by the addition of diethyl ether (5 mL). The yellow supernatant was removed, and the powder dried *in vacuo* to give yellow-orange microcrystals.

Yield: 0.036 g (72 %). **^{1}H-NMR** (400 MHz, $CDCl_3$): δ = 8.53 (d, J = 5.7 Hz, 1H, H_{arom}), 7.66 (t, J = 7.8 Hz, 1H, H_{arom}), 7.14 (m, 2H, H_{arom}), 1.69 (s, 15H, $[CH_3]_5$), 1.53 (s, 6H, $[CH_3]_2$).

[η^5(C$_5$Me$_5$)Ir^{III}\{diphenyl(2-pyridyl)methanolate-κO,κN\}Cl], Ir2

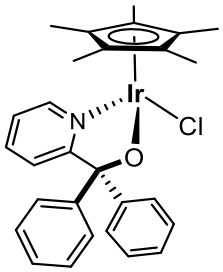

[Cp*IrCl$_2$]$_2$ (0.089 mmol, 70.0 mg), diphenyl(2-pyridyl)methanol (0.194 mmol, 50.7 mg) and Na_2CO_3 (0.704 mmol, 74.6 mg) were dissolved in acetone (20 mL). The resulting orange solution was stirred for 4 hours at 50 °C, after which time the solution had turned yellow. $MgSO_4$ was added, and after stirring for 10 minutes the solution was filtered and the solvent removed *in vacuo* to afford a yellow oil. The product was washed with diethyl ether (2 x 5 mL). The yellow supernatant was removed, and the powder dried *in vacuo* to give an orange-yellow powder. Single crystals suitable for X-ray diffraction analysis were grown by solvent evaporation ($CDCl_3$) at room temperature.

Yield: 0.0447 g (81 %). **^{1}H-NMR** (400 MHz, $CDCl_3$): δ = 8.63 (d, J = 5.7 Hz, 1H, H_{arom}), 7.56 (t, J = 7.7 Hz, 1H, H_{arom}), 7.25 (s, 20H, H_{arom} + CH_{phenyl}), 6.82 (d, J = 7.9 Hz, 1H, H_{arom}), 1.40 (s, 15H, $[CH_3]_5$); **^{13}C-NMR** (100 MHz, $CDCl_3$): δ = 173.2 (C_{arom}), 150.1 ($CH_{pyridine}$), 136.2 ($CH_{pyridine}$), 129.6 (CH_{phenyl}), 128.3 (CH_{phenyl}), 127.6 (CH_{phenyl}), 126.8 (CH_{phenyl}), 125.7 (CH_{phenyl}), 124.0 (CH_{phenyl}), 94.6 (C), 84.3 (C_{Cp*}), 8.8 ($CH_{3\ Cp*}$); **HR ESI-MS (+)**: m/z calculated for $C_{28}H_{29}ClIrNO$: $[M-H]^+$ 622.1476, 620.1460; found 622.1474, 620.1455; $[M-Cl]^+$ 588.1873, 586.1850; found: 588.1866, 586.1848; **Elemental Analysis**: calcd (%) for $C_{28}H_{29}ClIrNO$: C 53.96, H 4.69, N 2.25; found: C 53.96, H 4.74, N 2.34; **Crystal data [CCDC no. 1413039]:** $C_{30}H_{31}Cl_7IrNO$ (**Ir2** + 2 $CHCl_3$), M = 861.91, monoclinic, P $2_{1/}$n, a = 12.3236(2) Å, b = 16.4094(3) Å, c = 16.4100(3) Å, β = 92.2863(11)°, V = 3315.84(10) Å^3, Z = 4, d_{calc} = 1.727 g/cm^3, T = 150 K, 66209 reflections collected, 7585 independent reflections (R_{int} = 0.1312), final R_1 = 0.0422, final wR_2 = 0.0898, GoF = 1.010.

[η^5(C_5Me_5)Ir^{III}\{2,2,4,4-tetramethyl-3-(2-pyridyl)-3-pentanolate-κO,κN\}] hexafluoroantimonate, Ir3

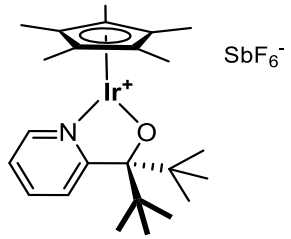

$[Cp^*IrCl_2]_2$ (0.1 mmol, 79.8 mg), 2,2,4,4-tetramethyl-3-(2-pyridyl)-3-pentanol, (0.22 mmol, 48.7 mg) and Na_2CO_3 (0.8 mmol, 84.8 mg) were dissolved in acetone (20 mL). The resulting orange solution was stirred for 20 hours at 50 °C, without observing any colour changes. $AgSbF_6$ (0.22 mmol, 0.0756 g) and acetonitrile were therefore added (2 mL), and the mixture stirred for a further 23 hours after which time the solution had turned yellow and a fine, colourless solid was observed. The solution was filtered through a 0.2 µm Teflon syringe filter and the solvent removed *in vacuo*. The resulting red-brown residue was dissolved in dichloromethane (2 mL) and diethyl ether (30 mL) added, causing the precipitation of a red solid. The supernatant was removed and the product dried to afford a fine dark red powder. Single crystals suitable for X-ray diffraction analysis were grown by diffusion of hexane into a DCM solution at room temperature.

Yield: 0.036 g (46 %). **^{1}H-NMR** (400 MHz, $CDCl_3$): δ = 9.15 (d, J = 5.9 Hz, 1H, H_{arom}), 8.00 (d, J = 8.26 Hz, 1H, H_{arom}), 7.91 (t, J = 7.4 Hz, 1H, H_{arom}), 7.65 (t, J = 6.7 Hz, 1H, H_{arom}), 1.88 (s, 15H, $[CH_3]_5$), 1.90 (s, 18H, $[CH_3]_6$); **^{13}C-NMR** (100 MHz, $CDCl_3$): δ = 178.2 ($C_{pyridine}$), 152.4 ($CH_{pyridine}$), 138.0 ($CH_{pyridine}$), 125.4 ($CH_{pyridine}$), 123.4 ($CH_{pyridine}$), 103.9 (C), 88.9 (C_{Cp^*}), 41.2 ($C_{t\text{-butyl}}$), 28.9 ($CH_{3\ t\text{-butyl}}$), 9.8 ($CH_{3\ Cp^*}$); **ESI-MS (+)**: m/z calculated for $C_{27}H_{45}F_6IrNOSb$: $[M\text{- }SbF_6]^+$: 548.2500, 546.2476; found: 548.2493, 546.2472; **Elemental Analysis**: calcd (%) for $C_{27}H_{45}F_6IrNOSb$: C 36.79, H 4.76, N 1.79, found: C 36.70, H 4.83, N 1.77; **Crystal data [CCDC no. 1413040]:** $C_{24}H_{37}F_6IrNOSb$ (**3**), M = 783.49, triclinic, P-1, a = 10.9884(2) Å, b = 11.9229(2) Å, c = 12.9393(2) Å, α = 113.6957(8)°, β = 114.4785(7)°, γ = 91.0354(7)°, V = 1377.69(4) Å^3, Z = 2, d_{calc} = 1.889 g/cm^3, T = 150 K, 25636 reflections collected, 7937 independent reflections (R_{int} = 0.1343), final R_1 = 0.0710, final wR_2 = 0.1787, GoF = 1.014.

[η^5(C$_5$Me$_5$)Ir^{III}{1-(2-pyridyl)cyclohexanolate-κO,κN}Cl], Ir4

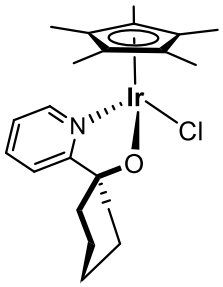

[Cp*IrCl$_2$]$_2$ (0.2 mmol, 160 mg), 1-(2-pyridyl)cyclohexanol (0.3 mmol, 62.0 mg) and Na_2CO_3 (0.8 mmol, 84.8 g) were dissolved in acetone (20 mL). The resulting orange solution was stirred for 5 hours at 50 °C, after which time the solution had turned yellow. $MgSO_4$ was added, and after stirring for 10 minutes the solution was filtered and the solvent removed *in vacuo* to afford an orange-yellow oil. The product was washed with diethyl ether (20 mL). The yellow supernatant was removed, and the powder dried *in vacuo* to give an orange powder. Single crystals suitable for X-ray diffraction analysis were grown by diffusion of hexane into a DCM solution at room temperature.

Yield: 0.0581 g (54 %). **^{1}H-NMR** (400 MHz, $CDCl_3$): δ = 8.49 (d, J = 5.1 Hz, 1H, H_{arom}), 7.63 (t, J = 7.9 Hz, 1H, H_{arom}), 7.12 (m, 2H, H_{arom}), 1.66 (s, 15H, $[CH_3]_5$) 2.06 (m, 2H, CH_{hexyl}), 1.81 (m, 1H, CH_{hexyl}), 1.52 (m, 3H, CH_{hexyl}), 1.38 (m, 2H, CH_{hexyl}), 1.17 (m, 2H, CH_{hexyl}); **^{13}C-NMR** (100 MHz, $CDCl_3$): δ = 178.2 ($C_{pyridine}$), 149.7 ($CH_{pyridine}$), 137.1 ($CH_{pyridine}$), 123.5 ($CH_{pyridine}$), 122.2 ($CH_{pyridine}$), 84.6 (C), 83.9 (C_{Cp*}), 40.9 (CH_2), 26.3 (CH_2), 22.1 (CH_2), 9.1 ($CH_{3\ Cp*}$); **ESI-MS (+)**: m/z calculated for $C_{21}H_{30}ClIrNO$: $[M+H]^+$: 540.1632, 538.1616; found: 540.1626, 538.1609; $[M-Cl]^+$: 504.1878, 502.1855; found: 504.1865, 502.1845; **Elemental Analysis:** calcd (%) for $C_{21}H_{30}ClIrNO$: C 46.78, H 5.42, N 2.60; found: C 46.69, H 5.41, N 2.6; **Crystal data [CCDC no. 1413041]:** $C_{21}H_{31}ClIrNO_2$ (**4** + H_2O), M = 557.12, monoclinic, P $2_1/c$, a = 17.3755(4) Å, b = 15.3635(3) Å, c = 15.7991(3) Å, β = 90.789(2)°, V = 4217.15(15) Å^3, Z = 8, d_{calc} = 1.755 g/cm^3, T = 150 K, 18642 reflections collected, 18642 independent reflections (R_{int} = 0.0513), final R_1 = 0.0559, final wR_2 = 0.1496, GoF = 1.056.

[η^5(C$_5$Me$_5$)Ir^{III}}{2-(2-quinolyl)-2-propanolate-κO,κN}Cl], Ir5

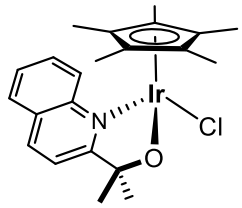

$[Cp^*IrCl_2]_2$ (0.214 mmol, 165 mg), 2-(2-quinolyl)-2-propanol (0.6 mmol, 127 mg) and Na_2CO_3 (1.8 mmol, 190 mg) were dissolved in acetone (20 mL). The resulting orange solution was stirred for 3.5 hours at 50 °C, after which time the solution had turned yellow. $MgSO_4$ was added, and after stirring for 10 minutes the solution was filtered and the solvent removed *in vacuo* to afford a brown oil. The product dissolved in DCM (5 mL) and hexane was added (25 mL). Upon storage at -20 °C a precipitate formed. The clear orange supernatant was removed and the solid dried *in vacuo* to give a dark orange powder. Single crystals suitable for X-ray diffraction analysis were grown by solvent evaporation (DCM) at room temperature.

Yield: 78.9 mg (68 %). **^{1}H-NMR** (400 MHz, $CDCl_3$): δ = 8.51 (d, J = 8.2 Hz, 1H, H_{arom}), 8.09 (d, J = 8.7 Hz, 1H, H_{arom}), 7.80 (d, J = 7.9 Hz, 1H, H_{arom}), 7.78 (t, J = 7.8 Hz, 1H, H_{arom}), 7.56 (t, J = 7.7 Hz, 1H, H_{arom}), 7.19 (d, J = 8.5 Hz, 1H, H_{arom}), 1.61 (s, 21H, $[CCH_3]_5$ + $[CH_3]_2$); **^{13}C-NMR** (100 MHz, $CDCl_3$): δ = 179.7 ($C_{quinoline}$), 144.6 ($C_{quinoline}$) 137.2 ($CH_{quinoline}$), 132.8 ($CH_{quinoline}$), 130.5 ($CH_{quinoline}$), 128.6 ($C_{quinoline}$), 127.7 ($CH_{quinoline}$), 127.0 ($CH_{quinoline}$), 119.2 ($CH_{quinoline}$), 86.6 (C), 84.4 (C_{Cp^*}), 35.2 (CH_3), 33.1 (CH_3), 9.4 ($CH_{3\ Cp^*}$); **ESI-MS (+)**: m/z calculated for $C_{22}H_{27}ClIrNO$: $[M+H]^+$: 550.1475, 548.1460; found: 550.1470, 548.1453; $[M-Cl]^+$: 514.1722, 512.1699; found: 514.1710, 512.1689; **Elemental Analysis**: calcd (%) for $C_{22}H_{27}ClIrNO$: C 48.12, H 4.96, N 2.55, found: C 47.89, H 4.96, N 2.59; **Crystal data [CCDC no. 1413043]:** $C_{22}H_{29}ClIrNO_2$ (**5** + H_2O), M = 567.11, monoclinic, P 2_1, a = 7.8422(3) Å, b = 13.7658(4) Å, c = 10.3658(4) Å, β = 106.632(4)°, V = 1072.22(7) Å^3, Z = 2, d_{calc} = 1.757 g/cm^3, T = 150 K, 12281 reflections collected, 4980 independent reflections (R_{int} = 0.0407), final R_1 = 0.0277, final wR_2 = 0.0465, GoF = 1.000.

[η^5(C$_5$Me$_5$)Ir^{III}\{3,3,5,5-tetramethyl-1-(2-pyridyl)cyclohexanolate-κO,κN\}Cl], Ir6

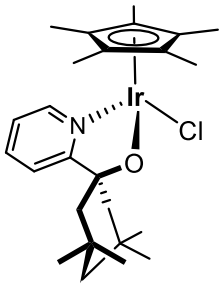

[Cp*IrCl$_2$]$_2$ (0.1 mmol, 79.3 mg), 3,3,5,5-tetramethyl-1-(2-pyridyl)cyclohexanol (0.24 mmol, 58.3 mg) and Na$_2$CO$_3$ (0.8 mmol, 84.8 g) were dissolved in acetone (15 mL). The resulting orange solution was stirred at 50 °C for 36 hours, after which time the solution had turned yellow. MgSO$_4$ was added, and after stirring for 10 minutes the solution was filtered and the solvent removed *in vacuo* to afford a brown oil. The product recrystallised from DCM (1 mL) upon addition of diethyl ether (20 mL) to give a light brown powder. Single crystals suitable for X-ray diffraction analysis were grown by solvent evaporation (DCM) at room temperature.

Yield: 45.5 mg (76 %). **^{1}H-NMR** (400 MHz, CDCl$_3$): δ = 8.51 (d, J = 5.2 Hz, 1H, H$_{arom}$), 7.59 (t, J = 8.0 Hz, 1H, H$_{arom}$), 7.08 (m, 2H, H$_{arom}$), 1.83 (m, 6H, H$_{cyclohexyl}$), 1.67 (s, 15H, [CCH$_3$]$_5$), 1.45 (s, 6H, [CH$_3$]$_2$), 0.87 (s, 6H, [CH$_3$]$_2$); **^{13}C-NMR** (100 MHz, CDCl$_3$): δ = 181.6 (C$_{pyridine}$), 148.9 (CH$_{pyridine}$), 136.2 (CH$_{pyridine}$), 123.1 (CH$_{pyridine}$), 122.7 (CH$_{pyridine}$), 89.1 (C), 83.3 (C$_{Cp*}$), 53.3 (CH$_2$), 52.8 (CH$_2$), 36.9 (CH$_3$), 31.9 (C), 29.1 (CH$_3$), 8.7 (CH$_{3\ Cp*}$); **ESI-MS (+)**: m/z calculated for C$_{25}$H$_{37}$ClIrNO: [M-Cl]$^+$: 558.2476, 560.2500; found: 558.2484, 560.2501; **Elemental Analysis**: calcd (%) for C$_{25}$H$_{37}$ClIrNO: C 50.45, H 6.27, N 2.35; found: C 50.41, H 6.14, N, 2.42; **Crystal data [CCDC no. 1413044]:** C$_{25}$H$_{37}$ClIrNO (**6**), M = 595.20, monoclinic, P 2$_1$/c, a = 16.6537(5) Å, b = 16.6270(10) Å, c = 9.0691(5) Å, β = 96.446(4)°, V = 2495.4(2) Å^3, Z = 4, d$_{calc}$ = 1.584 g/cm^3, T = 150 K, 10408 reflections collected, 5604 independent reflections (R$_{int}$ = 0.0458), final R$_1$ = 0.0411, final wR$_2$ = 0.0527, GoF = 0.980.

[η^5(C$_5$Me$_5$)Ir^{III}\{diphenyl(2-quinolyl)methanolate-κO,κN\}Cl], Ir7

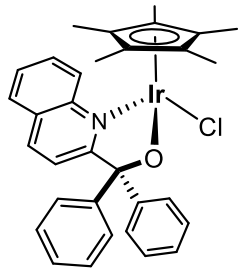

$[Cp^*IrCl_2]_2$ (0.1 mmol, 79.3 mg), diphenyl(2-quinolyl)methanol (0.24 mmol, 74.7 mg) and Na_2CO_3 (0.8 mmol, 84.8 mg) were dissolved in acetone (15 mL). The resulting orange solution was stirred at 50 °C for 36 hours, after which time the solution had turned yellow. $MgSO_4$ was added, and after stirring for 10 minutes the solution was filtered and the solvent removed *in vacuo* to afford an orange oil. The product was dissolved in DCM (1 mL) and diethyl ether was added (20 mL). Upon storage at -20 °C a precipitate formed. The supernatant was removed and the solid dried *in vacuo* to give an orange powder. Single crystals suitable for X-ray diffraction analysis were grown by solvent evaporation (toluene) at room temperature.

Yield: 50.1 mg (74 %). **^{1}H-NMR** (400 MHz, $CDCl_3$): δ = 8.63 (d, J = 8.8 Hz, 1H, H_{arom}), 7.96 (d, J = 8.8 Hz, 1H, H_{arom}), 7.79 (m, 2H, H_{arom}), 7.60 (t, J = 7.8 Hz, 1H, H_{arom}), 7.48 (d, J = 8.0 Hz, 2H, H_{phenyl}), 7.40 (d, J = 8.0 Hz, 2H, H_{phenyl}), 7.32 (m, 3H, H_{phenyl}), 7.14 (m, 3H, H_{phenyl}), 6.98 (d, J = 8.4 Hz, 1H, H_{arom}), 1.61 (s, 15H, $[CH_3]_5$); **^{13}C-NMR** (100 MHz, $CDCl_3$): δ = 174.9 ($C_{quinoline}$), 151.8 (C_{arom}), 150.0 (C_{arom}), 144.5 (C_{arom}), 135.6 (CH_{arom}), 132.8 (CH_{arom}), 130.5 (CH_{arom}), 129.7 (CH_{arom}), 128.8 (CH_{arom}), 127.9 (CH_{arom}), 127.6 (CH_{arom}), 127.4 (CH_{arom}), 127.1 (CH_{arom}), 126.6 (CH_{arom}), 123.4 (CH_{arom}), 97.1 (C), 84.7 (C_{Cp^*}), 9.2 ($CH_{3\ Cp^*}$); **ESI-MS (+)**: m/z calculated for $C_{32}H_{31}ClIrNO$: $[M\text{-}Cl]^+$: 636.2006, 638.2031; found: 636.2009, 638.2025; **Elemental Analysis**: calcd (%) for $C_{32}H_{31}ClIrNO$: C 57.09, H 4.64, N 2.08; found: C 57.18, H 4.49, N 2.23; **Crystal data [CCDC no. 1413042]:** $C_{71}H_{70}Cl_2$**Ir2**N_2O_2 (**7** + 0.5 toluene), M = 1438.59, monoclinic, P 2_1/c, a = 20.7893(4) Å, b = 9.41350(10) Å, c = 15.8988(3) Å, β = 109.826(2)°, V = 2926.97(9) Å^3, Z = 2, d_{calc} = 1.632 g/cm^3, T = 150 K, 21626 reflections collected, 6988 independent reflections (R_{int} = 0.0328), final R_1 = 0.0236, final wR_2 = 0.0487, GoF = 1.023.

2.7.2.3 Electrolyte

1,2,3-trimethyl-1H-benzimidazol-3-ium iodide ([tmbim][I])

According to previously published procedures[32], under an inert atmosphere, 2-methyl-1H-benzimidazole (12 mmol, 1.59 g) was dissolved in anhydrous acetonitrile (20 mL) and methyl iodide was added dropwise (15 mmol, 2.13 g, 0.93 mL). After heating at 80 ˚C for 3 days, the resulting solution was cooled, and the precipitate filtered, washed in THF and dried in vacuo. A subsequent recrystallisation from ethanol yielded 1,2,3-trimethyl-1H-benzimidazol-3-ium iodide ([tmbim][I]) as a white solid (8.4 mmols, 2.41 g, 70 %).

1,2,3-trimethyl-1H-benzimidazol-3-ium bis((trifluoromethyl)sulfonyl) amide

([tmbim][NTf_2])

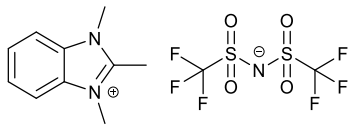

[tmbim][I] (8.4 mmol, 2.41 g) was dissolved in DCM (40 mL) and $LiNTf_2$ (9 mmol, 2.58 g) was dissolved in H_2O. The solutions were combined in a separating funnel and the organic phase was collected. The organic phase was rewashed with H_2O (40 mL x 3). The aqueous phase was washed with DCM (40 mL x 3). All organic phases were collected, dried over $MgSO_4$, and the DCM removed *in vacuo*. The white/yellow solid was recrystallised from hot ethanol and precipitated by cooling to 0 °C, resulting in a yellow solution and white crystals. The white crystals were filtered, washed with cold H_2O and recrystallised a further 2 times. **Yield**: 1.7 g, 3.85 mmol, 48%. **^{1}H NMR** (400 MHz $CDCl_3$): δ = 7.62 (m, 4H, $4H_{arom}$), 3.97 (s, 6H, $[NCH_3]_2$), 2.88 (s, 3H, $[CH_3]$).

2.7.3 Titration with KCl

After a pure solvent background scan, a solution of 0.5 mM [Ir] in 4:1 H_2O/ ^{t}BuOH (2.5 mL) was added to the cuvette and a spectrum acquired (every 30 seconds for 1 hour, 300-900 nm spectral range, 1 nm resolution, 2400 nm/min scan rate). The solution in the cuvette was removed and added to a small vial with pre-weighed KCl. Once the KCl had dissolved the solution was returned to the cuvette and a new spectrum taken. This procedure was repeated for 50, 100, 200, 400 and 800 equivalents of KCl (75 µmol, 150 µmol, 0.3 mmol 0.6 mmol and 1.2 mmol, respectively).

2.7.4 Electrochemistry

2.7.4.1 Aqueous CVs

Electrochemical experiments were all performed using standard three-electrode measurements carried out on an Invium Technologies CompactStat. All electrodes were purchased from Bioanalytical Systems, Inc. in all cases the reference electrode used was Ag/AgCl in 3 M KCl, potentials were reported vs NHE according to the following:

$$E_{NHE} = E_{Ag/AgCl} + 0.205$$

Cyclic voltammetry data was collected using a three-electrode system; WE: defined 1 cm^2 FTO glass (using silicone); RE: Ag/AgCl; CE: platinum wire. All experiments were done in an electrolyte solution of 0.1M KNO_3 in ^{t}BuOH/H_2O (4:1) between -0.5 V and 1.5 V. A range of scan rates were collected for all precatalysts (10, 50, 100, 250, 500, 1000, 2000, 5000 mvs^{-1}). A background scan was run prior to addition of [Ir], which was added as a 5 M solution (0.5 mL) to give a solution of 0.45 mM [Ir] in electrolyte.

2.7.4.2 Aqueous CVs with KCl

Cyclic voltammetry data was collected using the same three electrode system; WE: defined 1 cm^2 FTO glass (using silicone); RE: Ag/AgCl; CE: platinum wire. Background data were collected in a solution mixture of 4:1 H_2O/^{t}BuOH with KCl as the electrolyte (0.24 M). After the background data was recorded the solution used for UV-vis KCl titration was analysed by CV between -0.5 V and 1.5 V vs Ag/AgCl. A range of scan rates were collected for all precatalysts (100, 250, 500 mvs^{-1}).

2.7.4.3 Non-aqueous CVs

Electrochemical experiments were all performed using standard three-electrode measurements carried out on an Invium Technologies CompactStat. All electrodes were purchased from Bioanalytical Systems, Inc. in all cases the reference electrode used was $Ag/AgNO_3$ in acetonitrile, potentials were reported vs NHE according to the following[33]:

$$E_{NHE} = E_{Ag/AgNO3} + 0.197$$

The working electrode used was glassy carbon (0.3 cm diameter, 0.07 cm^2 surface area). Counter electrodes was platinum wire. Before use, carbon electrodes were thoroughly polished with alumina paste (1.0 µm and 0.3 µm), briefly sonicated (10 seconds) and rinsed extensively with Milli-Q water and dried under a stream of Argon.

Inert atmosphere: Cyclic voltammograms were collected under glove box conditions, with 10mM [Ir], 0.15 M [tmbim][NTf_2] electrolyte in DCM (degassed, freeze pump thawed) at a variety of scan rates. Three scans were collected, and the second scan was reported.

2.7.5 Chemical Activation

Activation studies followed by UV-vis

After a pure solvent background scan, a solution of 0.75 mM [Ir] in 4:1 H_2O/^{t}BuOH (2.5 mL) was added to a quartz cuvette containing a small magnetic stirrer bar. The solution was stirred, and automatic acquisition of spectra was started (every 30 seconds for 1 hour, 300-900 nm spectral range, 1 nm resolution, 2400 nm/min scan rate). After the first scan $NaIO_4$ (0.15 M, 0.5 mL in H_2O) was added and the reaction left to proceed while continuing spectra acquisition. Single wavelength kinetic runs were performed using the same protocol but following intensity at a selected wavelength with 0.1 Hz resolution.

Activation studies followed by ^{1}H NMR

A solution of 0.5 mM [Ir] in 4:1 D_2O (0.5 mL) was placed in an NMR tube and a ^{1}H NMR spectrum was recorded. $NaIO_4$ (50 equivalents, 25 mM, 12.5 µmol, 2.7 mg) was added as a solid and the tube shaken vigorously for 1 minute, when another spectrum was recorded. Further spectra were recorded after 3 minutes and after 1 hour.

2.8 References

1. T. J. Collins, *Acc. Chem. Res.*, 1994, **27**, 279–285.
2. R. H. Crabtree, *J. Organomet. Chem.*, 2014, **751**, 174–180.
3. T. K. Michaelos, D. Y. Shopov, S. B. Sinha, L. S. Sharninghausen, K. J. Fisher, H. M. C. Lant, R. H. Crabtree, and G. W. Brudvig, *Acc. Chem. Res.*, 2017, **50**, 952–959.
4. Y. Wong, Q. Yang, Z. Zhou, H. K. Lee, T. C. W. Mak, and D. K. P. Ng, *New J. Chem.*, 2001, **25**, 353–357.
5. DOW Global Tecnhologies LLC, M. Christianson, T. De Vries, R. Froese, M. Ober, J. Patton, D. Romer, G. Roof, L. Sun, E. Szuromi, C. Theriault, D. Welsh, T. Wenzel, and P. Moran, 2012.
6. U. Hintermair, T. P. Brewster, L. M. Pratt, N. D. Schley, and R. H. Crabtree, *ACS Catal.*, 2014, **4**, 99–108.
7. J. Campos, U. Hintermair, T. P. Brewster, M. K. Takase, and R. H. Crabtree, *ACS Catal.*, 2014, **4**, 973–985.
8. C. White, A. Yates, P. M. Maitlis, and D. M. Heinekey, in *Inorganic Synthesis*, 1992, pp. 228–234.
9. N. D. Schley, S. Halbert, C. Raynaud, O. Eisenstein, and R. H. Crabtree, *Inorg. Chem.*, 2012, **51**, 12313–12323.
10. D. S. Glueck, J. Wu, F. J. Hollander, and R. G. Bergman, *J. Am. Chem. Soc.*, 1991, **113**, 2041–2054.
11. R. Noyori, M. Yamakawa, and S. Hashiguchi, *J. Org. Chem.*, 2001, **66**, 7931–7944.
12. J. M. Mayer, *Inorg. Chem.*, 1988, **27**, 3899–3903.
13. N. Elgrishi, K. J. Rountree, B. D. McCarthy, E. S. Rountree, T. T. Eisenhart, and J. L. Dempsey, *J. Chem. Educ.*, 2018, **95**, 197–206.
14. A. Lever, *J. Chem. Inf. Model.*, 1989, **53**, 160–160.
15. A. J. . L. R. F. Bard, *Electrochemical Methods*, 2000, vol. ISBN 0-471.
16. J. M. Thomsen, L. Que Jr., S. M. Hashmi, J. Campos, U. Hintermair, R. H. Crabtree, and G. W. Brudvig, *J. Am. Chem. Soc.*, 2014, **136**, 13826–13834.
17. S. W. Sheehan, J. M. Thomsen, U. Hintermair, R. H. Crabtree, G. W. Brudvig, and C. A. Schmuttenmaer, *Nat. Commun.*, 2015, **6**, 6469–6478.
18. M. Armand, F. Endres, D. R. MacFarlane, H. Ohno, and B. Scrosati, *Nat. Mater.*, 2009, **8**, 621–629.
19. S. Zein El Abedin, K. S. Ryder, O. Höfft, and H. K. Farag, *Int. J. Electrochem.*, 2012, **2012**, 1–2.

20. M. C. Buzzeo, C. Hardacre, and R. G. Compton, *ChemPhysChem*, 2006, **7**, 176–180.

21. S. A. Forsyth and D. R. MacFarlane, *J. Mater. Chem.*, 2003, **13**, 2451–2456.

22. D. R. Macfarlane, M. Forsyth, P. C. Howlett, J. M. Pringle, J. Sun, G. Annat, W. Neil, and E. I. Izgorodina, *Acc. Chem. Res.*, 2007, **40**, 1165–1173.

23. U. Hintermair, S. W. Sheehan, A. R. Parent, D. H. Ess, D. T. Richens, P. H. Vaccaro, G. W. Brudvig, and R. H. Crabtree, *J. Am. Chem. Soc.*, 2013, **135**, 10837–10851.

24. D. B. Grotjahn, D. B. Brown, J. K. Martin, D. C. Marelius, M. Abadjian, H. N. Tran, G. Kalyuzhny, K. S. Vecchio, Z. G. Specht, S. A. Cortes-llamas, V. Miranda-soto, V. Niekerk, C. E. Moore, and A. L. Rheingold, *J. Am. Chem. Soc.*, 2011, **133**, 19024–19027.

25. A. Savini, P. Belanzoni, G. Bellachioma, C. Zuccaccia, D. Zuccaccia, and A. MacChioni, *Green Chem.*, 2011, **13**, 3360–3374.

26. C. Zuccaccia, G. Bellachioma, S. Bolaño, L. Rocchigiani, A. Savini, and A. MacChioni, *Eur. J. Inorg. Chem.*, 2012, **9**, 1462–1468.

27. P. Gros, Y. Fort, and P. Caubère, *J. Chem. Soc. - Perkin Trans. 1*, 1997, **24**, 3597–3600.

28. J. S. Lomas, A. Adenier, and C. Cordier, *J. Phys. Org. Chem.*, 2006, **19**, 295–307.

29. A. Murti, K. Bhandari, S. Ram, Y. S. Prabhakar, A. K. Saxena, P. C. Jain, A. K. Gulati, R. C. Srimal, B. N. Dhawan, S. Nityanand, and N. Anand, *Indian J. Chem*, 1989, **28**, 934–942.

30. J. F. Hull, D. Balcells, J. D. Blakemore, C. D. Incarvito, O. Eisenstein, G. W. Brudvig, and R. H. Crabtree, *J. Am. Chem. Soc.*, 2009, **131**, 8730–8731.

31. N. D. Schley, J. D. Blakemore, N. K. Subbaiyan, C. D. Incarvito, F. Dsouza, R. H. Crabtree, and G. W. Brudvig, *J. Am. Chem. Soc.*, 2011, **133**, 10473–10481.

32. W. C. Chen, J. S. Shen, T. Jurca, C. J. Peng, Y. H. Lin, Y. P. Wang, W. C. Shih, G. P. A. Yap, and T. G. Ong, *Angew. Chemie - Int. Ed.*, 2015, **54**, 15207–15212.

33. B. Kratochvil, E. Lorah, and C. Garber, *Anal. Chem.*, 1969, **41**, 1793–1796.

CHAPTER 3

CHEMICALLY DRIVEN WATER OXIDATION

This chapter is based on the following publication:

*Electrochemical and Kinetic Insights into Molecular Water Oxidation Catalysts Derived from Cp*Ir(pyridine-alkoxide) Complexes*, E. Sackville, F. Marken, U. Hintermair, *ChemCatChem*, accepted

3. Chemically Driven Water Oxidation

3.1 Introduction

Water oxidation catalysts are developed with the end goal of being functional in fuel cells to improve efficiency of hydrogen production. Whilst heterogeneous or immobilised water oxidation catalysts (WOCs) provide greater current collection when bound to an anode, molecular systems allow for easier characterisation and the opportunity for catalyst design and tuning.

Evaluation of a molecular catalyst's water oxidation performance can be conducted electrochemically, under similar conditions to a functioning electrochemical cell. However, as will be seen in Chapter 5, this can be problematic, requiring electrochemically well-behaved systems and an often complicated set up.

Molecular WOCs are therefore typically investigated with a sacrificial oxidant in the first instance, allowing catalysts to be screened quickly and under varying conditions (Scheme 3.1).[1] The reactions can also be performed in bulk, such that suitably large amounts of oxygen are produced that can be detected directly.[1] Unlike with most electrochemical methods where the turnover numbers (TONs) or turnover frequencies (TOFs) must be inferred from the data via calculation, direct measurement of the oxygen produced allows these properties to be measured explicitly. Furthermore, testing with chemical oxidants provides direct evidence of product formation; current detected during electrochemical testing can often be due to formation of side products and is not selective.

Scheme 3.1 *General reaction of water oxidation using a WOC and driven with a sacrificial single electron oxidant*

$$4Ox^{+} + 2H_2O \xrightarrow{WOC} O_2 + 4H^{+} + 4Ox$$

3.1.1 Chemical oxidants

One of the key disadvantages to using chemical oxidants is that the reaction conditions are not entirely representative of the conditions in an electrochemical cell. In order to circumvent this, a wide range of sacrificial oxidants have been employed in the investigation of WOCs with attendant drawbacks and benefits to each.

In order for a compound to be successful as a sacrificial oxidant, it must have a reduction potential sufficiently high enough to oxidise water with the catalyst under investigation. However, the potential of water oxidation and proton reduction changes with pH. This relationship can be described with a Pourbaix diagram, relating the pH to the potential of the water oxidation reaction.

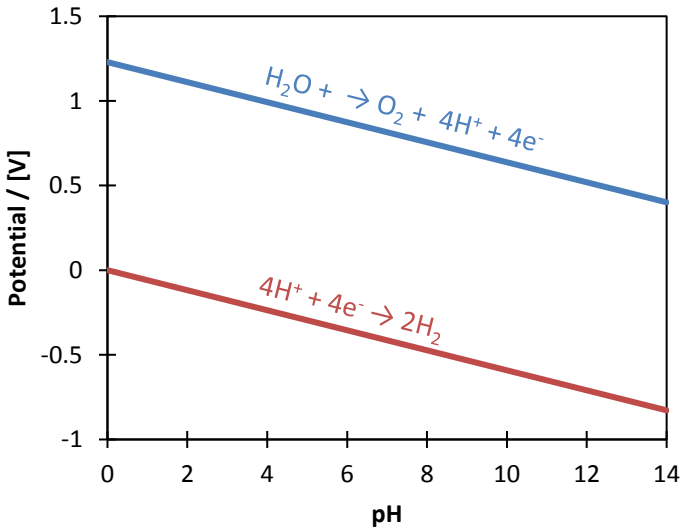

Figure 3.1. *Pourbaix diagram of water oxidation and proton reduction*

Therefore, for a sacrificial oxidant to drive water oxidation, its reduction potential must lie above the thermodynamic value for water denoted in the Pourbaix diagram. Commonly used oxidants, cerium^{IV} (usually as cerium^{IV} ammonium nitrate (CAN)), potassium peroxymonosulphate (Oxone) and sodium periodate. The reduction potentials for these oxidants are schematically represented in Figure 3.2.

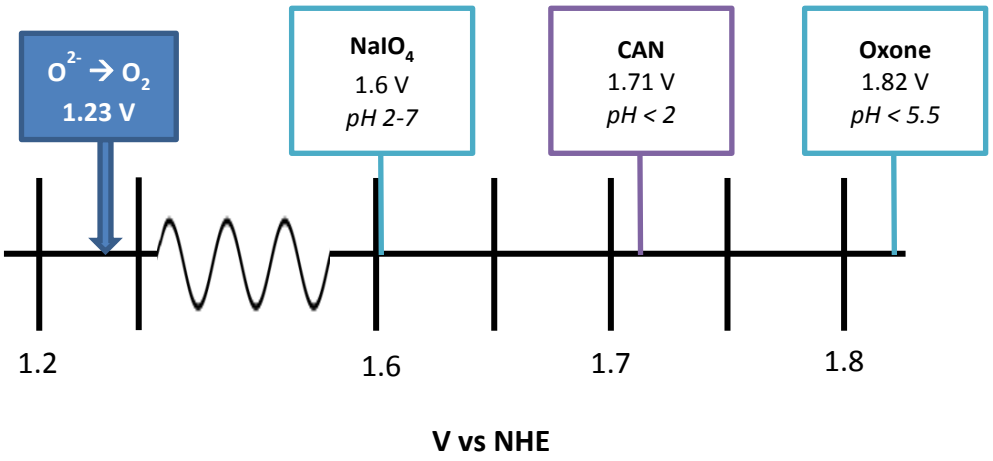

Figure 3.2. *Schematic of the relative oxidising potentials of commonly used oxidants. The pH stability range is indicated. One electron oxidants are in purple and two electron oxidants are in blue.*

All the oxidants represented above are either one electron (purple box) or two electron (blue box) oxidants; the WOC is driven either in four single electron transfer steps or by two double electron transfers. One electron oxidants are considered closest to the functioning of a photoelectrochemical cell or the photosynthetic PSII complex found in plants.[1]

Key advantages and disadvantages of the above oxidants are discussed in Table 3.1.

Table 3.1. *A summary of the benefits and drawbacks of commonly used sacrificial oxidants*[1]

Oxidant	Key advantage	Key disadvantage
CAN	– Powerful, single electron oxidant – Readily commercially available – Stable in solution over long periods of time – Easily trackable by UV-vis due to Ce^{III} vs Ce^{IV} absorbance – Historically many WOCs that perform well with CAN also perform water oxidation electrochemically	– Stable only at very low pH so can only be used with acid stable catalysts – Known to form insoluble $CeOx^2$ which can cause background heterogenous WO activity[3] – High reduction potential will oxidise other side reactions and can degrade the catalyst – Implicated in WOC pathways by oxygen exchange[4]
Oxone	– Compatible 1st row transition metals (TMs) as it can drive water oxidation in two electron steps and avoid unstable single electron species [5] – Higher pH stability than CAN	– Can serve as an oxo-transfer agent (but ^{18}O studies allow for determination of O_2 source) – Less successful with 2nd and 3rd row TM WOCs
$NaIO_4$	– Successful with 2nd and 3rd row TM WOCs – Middling reduction potential so less likely to degrade catalysts – High pH stability up to pH 8	– Also serves as oxo transfer agent but oxygen groups are labile and exchange with water to form a bis aqua adduct ($IO_4^- \leftrightarrow H_2IO_6^-$) complicating O^{18} studies[6] – Slow self-decomposition in solution

3.1.2 Clark electrode

First developed in the 1960s by Leland Clark, the polarographic electrode (or Clark electrode) was initially produced as a more accurate method of investigating the oxygenation level of blood during surgery.[7,8] The modern Clark electrode consists of an oxygen permeable Teflon membrane over Pt cathode connected to a silver anode via a spacer paper soaked in KCl electrolyte (Figure 3.3). Applying a voltage of around 700 mV across the electrodes causes oxygen to be reduced at the cathode. The resultant current is stoichiometrically related to the amount of oxygen in solution such that increasing oxygen concentration results in increasing current, and therefore the rate of O_2 evolution can be detected.

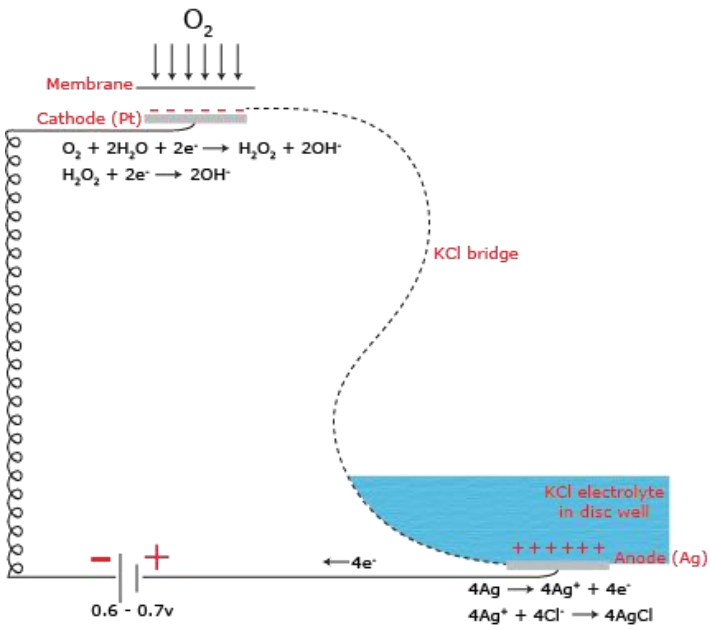

Figure 3.3. *Schematic of the functioning of a Clark electrode. Copied from Hansatech.*

It is worth noting that the Clark electrode only measures oxygen dissolved in solution. The measurements are therefore very accurate at low concentrations, but if large amounts of oxygen are produced then they will not be detected, and a plateau current will be reached. The reactions must also be performed under temperature control as O_2 solubility varies with temperature.

This chapter will describe the investigations of precatalysts **Ir1**-**Ir7** using sacrificial chemical oxidants and a Clark electrode. The WOCs will be investigated with varying oxidants and under varying pH and solvent conditions. The presence of a H/D kinetic isotope effect (KIE) has also been investigation, along with graphical rate analysis in order to explore the order in iridium of each of the catalysts.

3.2 Chemical water oxidation with periodate

3.2.1 Complexes Ir1-Ir7 for water oxidation

In the first instance, precatalysts **Ir1**-**Ir7** were investigated for their activity in the water oxidation reaction, with $NaIO_4$ as the oxidant, by measuring oxygen evolution over time with a Clark electrode (Figure 3.4).

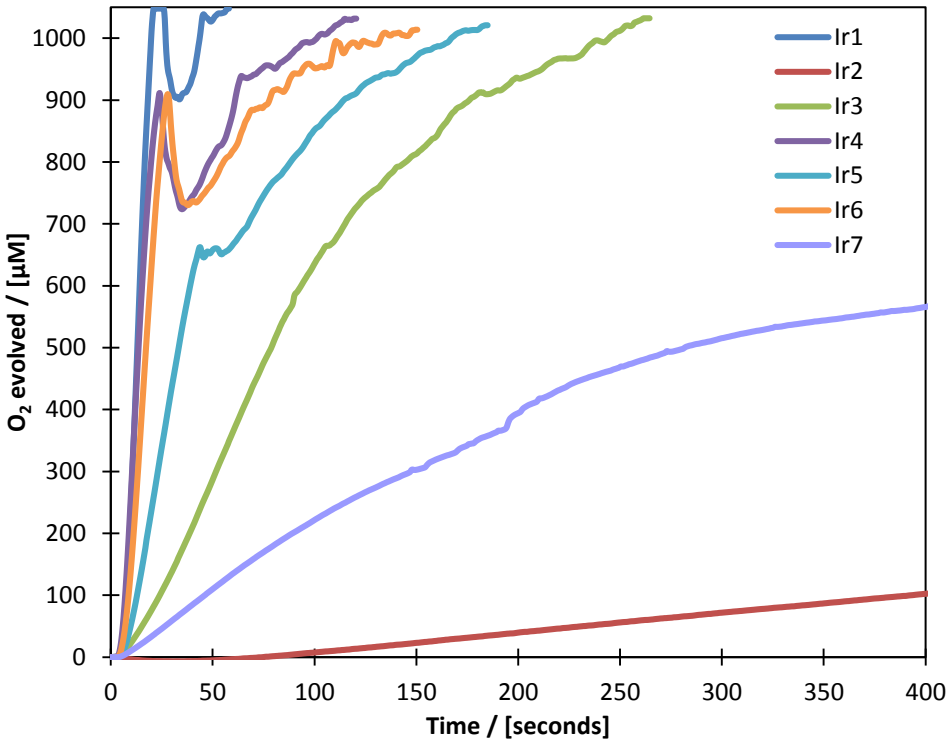

Figure 3.4. *Oxygen evolution traces of precatalysts **Ir1**–**Ir7** at 100 µM [Ir] with 100 mM $NaIO_4$ in H_2O (native pH 5.6) at 25 °C using a calibrated Clark electrode with stirring (fluctuations due to O_2 bubble formation causing localised saturation). Triplicate data in the Appendix Figure A3.1*

All compounds evolved oxygen, but the rate of evolution was markedly different between the precatalysts. The aryl substituted compounds **Ir2** and **Ir7** were particularly slow for water oxidation. The comparatively less bulky alkyl substituted complexes **Ir1**, **Ir4**, and **Ir6** showed the fastest rates of oxygen evolution, with little variation between their initial rates (Figure 3.5a); the large fluctuations seen particularly clearly for these faster precatalysts are due to the rapid evolution of oxygen resulting in gas bubbles, which perturb the Clark electrode reading. The pyridine diphenyl compound **Ir2** also showed a significant induction period where oxygen was consumed from solution (Figure 3.5b), which may be attributed to precatalyst activation.

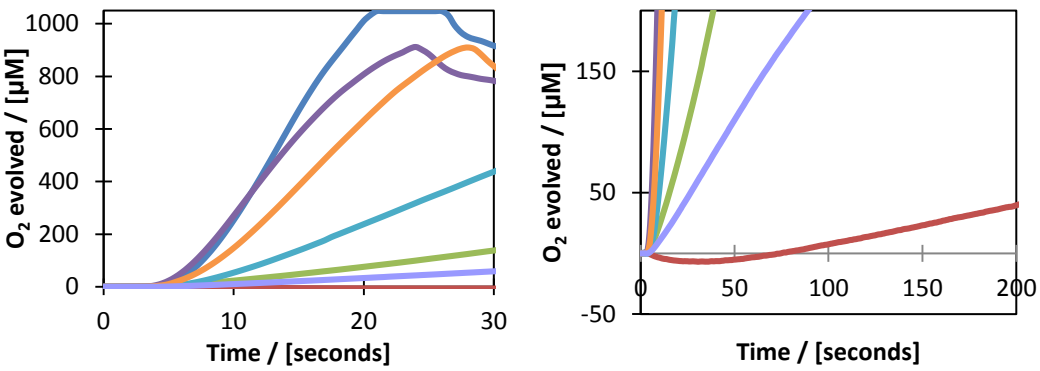

Figure 3.5.a) *Fast initial rates for alkyl complexes* ***Ir1****,* ***Ir4*** *and* ***Ir6*** ***b)*** *Induction period of* ***Ir2*** *from Figure 3.4.*

A comparison between the order of catalyst activity for water oxidation and the E_{mid} value observed during cyclic voltammetry experiments can also be made. From the electrochemical analysis, strong electronic ligand effects were observed. **Ir6** which bears the most electron donating alkyl group, has the lowest reduction potential (0.54 V vs. NHE), and **Ir2** and **Ir7** with electron withdrawing diphenyl groups having the highest (0.69 and 0.72 V vs. NHE respectively). Assuming an Ir^{IV} state must be reached in order for water oxidation, the E_{mid} values indicate that **Ir6** is electronically the easiest catalyst to undergo turnover with $NaIO_4$, and aryl complexes **Ir2** and **Ir7** the hardest. Although complexes **Ir1** and **Ir4** have higher $Ir^{III/IV}$ potentials, they surpass **Ir6** for water oxidation activity (see Table 3.2 for specific rates), presumably due to the increased steric bulk of **Ir6**.

3.2.2 pH variation with Ir1

Investigations into the effect of pH on the rate of water oxidation with $NaIO_4$ were conducted with complex **Ir1** and $NaIO_4$ (Figure 3.6).

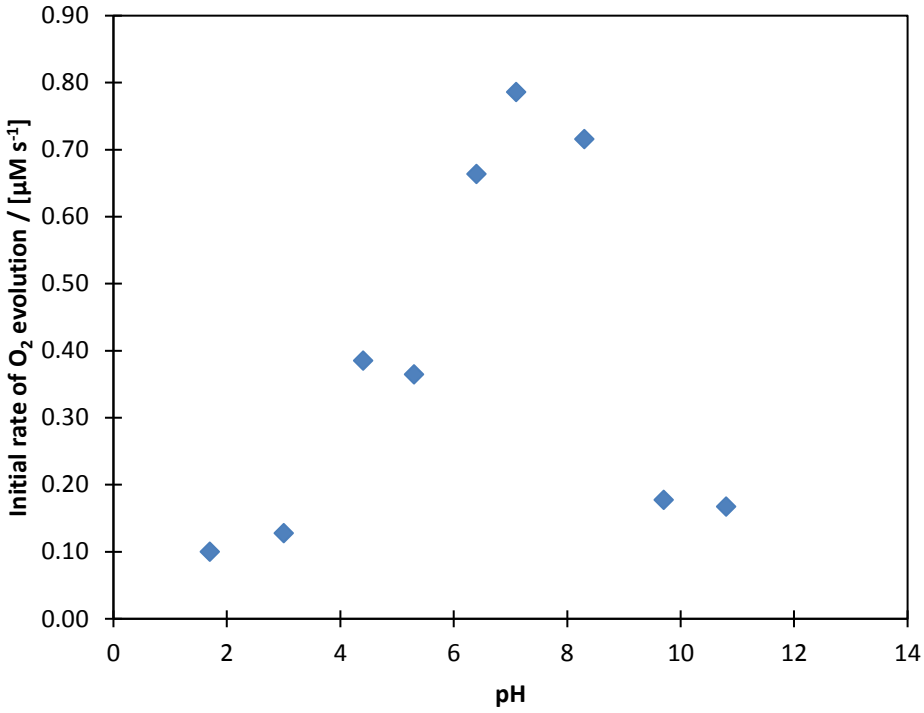

Figure 3.5. *Oxygen evolution traces of the complex* ***Ir1*** *at 10 mM $NaIO_4$ in H_2O, 1 µM [Ir] at 25 °C, using a calibrated Clark electrode with stirring with varying pH (adjusted with KOH and KNO_3).*

A clear dependence on pH was seen when using **Ir1** and $NaIO_4$, with the fastest rate observed under neutral conditions. Although this experiment was undertaken initially with the aim of investigating the behaviour of the Ir complex at different pHs, the observed dependence is more likely due to the pH dependence of the $NaIO_4$ oxidant rather than the catalyst. Periodate is stable from approximately pH 2 to pH 7.5[1], so the sharp decrease in rate after pH ~8 is likely due to breakdown of the oxidant.

3.2.3 Solvent variation

As seen in Chapter 2, the bulky R groups for compounds **Ir3** and **Ir7** necessitated the addition of an oxidation-resistant organic co-solvent. Oxygen assays with $NaIO_4$ were therefore repeated in a 20% ^{t}butanol/water mixture as the solvent in order to assess the effect of the solvent on the water oxidation reaction (Figure 3.6).

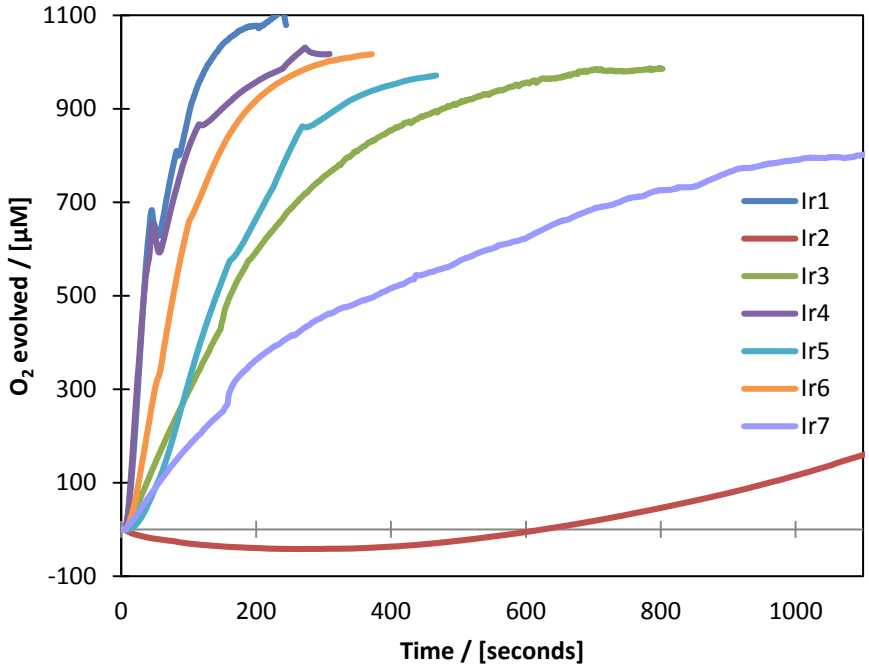

Figure 3.6. *Oxygen evolution traces of precatalysts **Ir1**–**Ir7** at 100 µM [Ir] with 100 mM $NaIO_4$ in 4:1 H_2O/^{t}BuOH (native pH 5.4) at 25 °C using a calibrated Clark electrode with stirring. Triplicate data in Appendix Figure A3.2*

For all precatalysts investigated the rate of water oxidation was suppressed by the addition of ^{t}BuOH. Alkyl complexes **Ir1**, **Ir3**-**Ir6** were all approximately 3-4 times slower in the presence of 20% ^{t}BuOH compared to 100% H_2O. Aryl substituted compounds **Ir2** and **Ir7** showed little difference upon addition of ^{t}BuOH, although this is potentially due to the already slow water oxidation rate. The effect of ^{t}BuOH as a co-solvent becomes particularly relevant when considered with the C-H Oxidation data (Chapter 4) and will be discussed further at that juncture.

Table 3.2. *Initial rates of oxygen evolution of precatalysts* ***Ir1****−7 with $NaIO_4$ in pure water and with 20% ^tBuOH*

Precatalyst	Initial k_{obs}[(a)] in pure H_2O / mM min^{-1}[b]	Initial k_{obs}[(a)] in 4:1 $H_2O/^tBuOH$ / mM min^{-1}[b]	Relative rate Reduction[c]
Ir1	4.60 ± 0.053	1.26 ± 0.008	3.6
Ir2	0.02 ± 0.001	0.02 ± 0.002	0
Ir3	0.41 ± 0.015	0.16 ± 0.025	2.7
Ir4	3.61 ± 0.020	1.25 ± 0.026	2.9
Ir5	1.23 ± 0.057	0.18 ± 0.022	6.8
Ir6	2.88 ± 0.029	0.92 ± 0.076	3.2
Ir7	0.14 ± 0.0078	0.13 ± 0.007	1.1

[a] Calculated from initial gradient of O_2 formation over time as the average value from triplicates.

[b] General errors calculated from standard deviation of rate over repeat runs

[c] Relative rate reduction calculated from initial rate in H_2O / initial rate with 20% ^tBuOH

3.3 Chemical water oxidation with cerium^{IV}

As detailed previously, different oxidants have different advantages and disadvantages, along with differing operating conditions. To explore the effect of oxidant on the water oxidation activity of the precatalysts, oxygen evolution assays were also investigated using Ceric Ammonium Nitrate (CAN) as an alternative sacrificial oxidant (Figure 3.7).

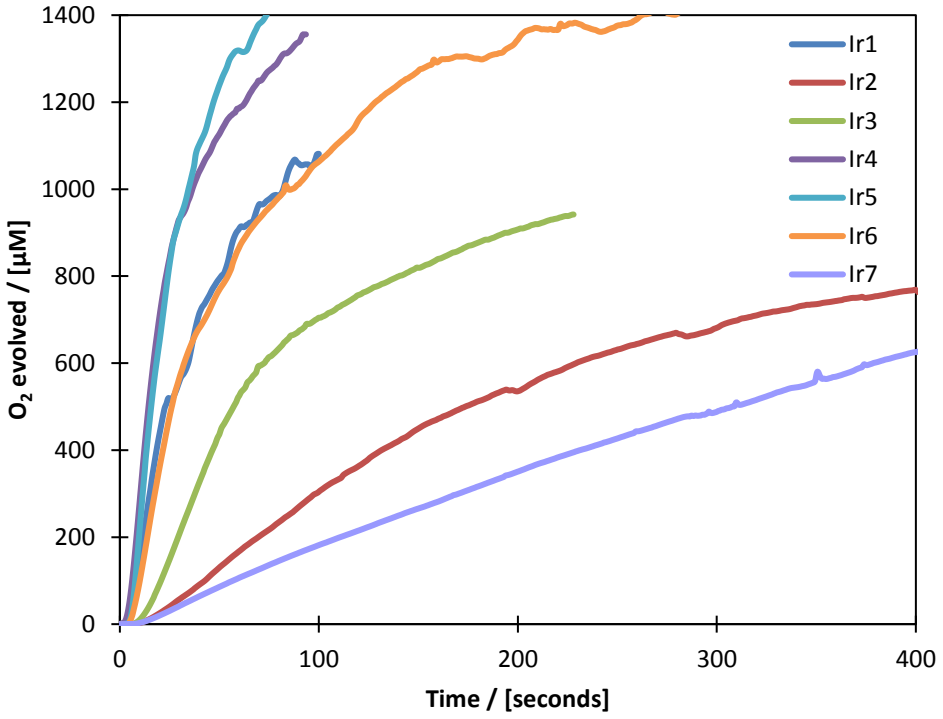

Figure 3.7. *Oxygen evolution traces of precatalysts* ***Ir1****–7 at 100 µM [Ir] with 200 mM CAN in 0.1 M* HNO_3 *in* H_2O *(pH 1.5) at 25 °C using a calibrated Clark electrode with stirring. Triplicate data in Appendix Figure A3.3*

Although CAN is a stronger electron oxidant than $NaIO_4$, it performs single electron transfer steps and is only stable at low pH values, thus double the concentration was used compared to the assays with periodate, and the reactions were conducted at pH 1.5 in 0.1M HNO_3. All precatalysts showed activity for water oxidation driven by CAN, but displayed significant variation in rate for complexes **Ir1**, **Ir2**, **Ir4** and **Ir6** (Table 3.3) compared to the $NaIO_4$ data.

Table 3.3. *Differences in initial rates of oxygen evolution of precatalysts **Ir1**–**Ir7** with $NaIO_4$ and CAN from Figures 3.3 and 3.7.*

Precatalyst	Initial k_{obs}[(a)] with $NaIO_4$ / mM min^{-1}	Catalyst TOF[(b)] with $NaIO_4$ / h^{-1}	Initial k_{obs}[(a)] with CAN / mM min^{-1}	Catalyst TOF[(b)] with CAN / h^{-1}
Ir1	4.60 ± 0.053	2739 ± 32	1.84 ± 0.126	1105 ± 75
Ir2	0.02 ± 0.001	11 ± 1	0.22 ± 0.050	133 ± 30
Ir3	0.41 ± 0.015	248 ± 9	0.44 ± 0.049	266 ± 29
Ir4	3.61 ± 0.020	2167 ± 11	1.88 ± 0.185	1087 ± 111
Ir5	1.23 ± 0.057	738 ± 34	1.22 ± 0.054	709 ± 33
Ir6	2.88 ± 0.029	1728 ± 17	1.12 ± 0.072	644 ± 43
Ir7	0.14 ± 0.008	83 ± 5	0.09 ± 0.004	54 ± 2

[a] Calculated from initial gradient of O_2 formation over time as the average value from triplicates.
[b] Initial rate divided by [Ir] concentration.
Errors calculated from standard deviation of rate over repeat runs (appendix)

The less bulky alkyl compounds **Ir1**, **Ir4** and **Ir6** gave the highest rate of water oxidation when driven by periodate, but were approximately 2-3 times slower in terms of initial rate with CAN (Table 3.3). Although little change was observed for the rate of oxygen evolution for **Ir3**, **Ir5** and **Ir7**, **Ir2** showed markedly higher activity with CAN as compared to $NaIO_4$.

Significant variation between catalyst activity under different reaction conditions has been well documented and cannot be overstated, especially in the case of the multi-electron water oxidation reaction, where a number of charge sensitive transfer events occur.[9] It is, therefore, not unexpected that a different oxidant at a different pH would affect the catalyst activity. Despite these local changes in rate, the overall trend remains broadly the same, such that complexes bearing alkyl R groups (**Ir1**, **Ir3**, **Ir4**, **Ir5**, **Ir6**) performed water oxidation at a faster rate than those bearing aryl R groups (**Ir2**, **Ir7**).

3.4 Kinetic isotope studies

In order to gain further mechanistic insight into the operation of these catalysts, the H/D kinetic isotope effect (KIE) for O_2 evolution was measured for both $NaIO_4$ and CAN. It has previously been detailed that the varying ligands affect rate of formation of the blue dimeric species (Section 2.5), the $Ir^{III/IV}$ reduction potential (Section 2.4) and the rate of water oxidation (Section 3.2). Investigations into the H/D KIE are therefore expected to highlight whether the ligand variation also impacts the rate determining step for water oxidation.[10]

Previous investigations into the KIE for Cp* Ir^{III} catalysts have typically shown values of >1.0 for water oxidation.[11] This indicates a primary KIE, whereby the rate determining step (RDS) involves formation of a high valent metal oxo intermediate (i.e. M-OH → M=O).[10] Crucially, nanoparticulate iridium oxides (IrOx NPs) display a KIE of unity; O-H bond cleavage is not involved in the RDS.[12] Instead, for water oxidation with IrOx NPs, the RDS is assumed to be oxidation of the catalyst by an outer sphere oxidant (e.g. Ir^{III} → Ir^{IV}).[12] Research was conducted by Crabtree and co-workers into the KIE of complex **Ir1** by which had been pre-activated to the blue dimeric species (denoted **Ir1***). When the water oxidation was driven electrochemically, a KIE value of 2.06 was obtained.[11,13]

3.4.1 Kinetic isotope effects with periodate

The KIE was investigated for precatalysts **Ir1**-**Ir7** using $NaIO_4$ (Figure 3.8, Table 3.4)

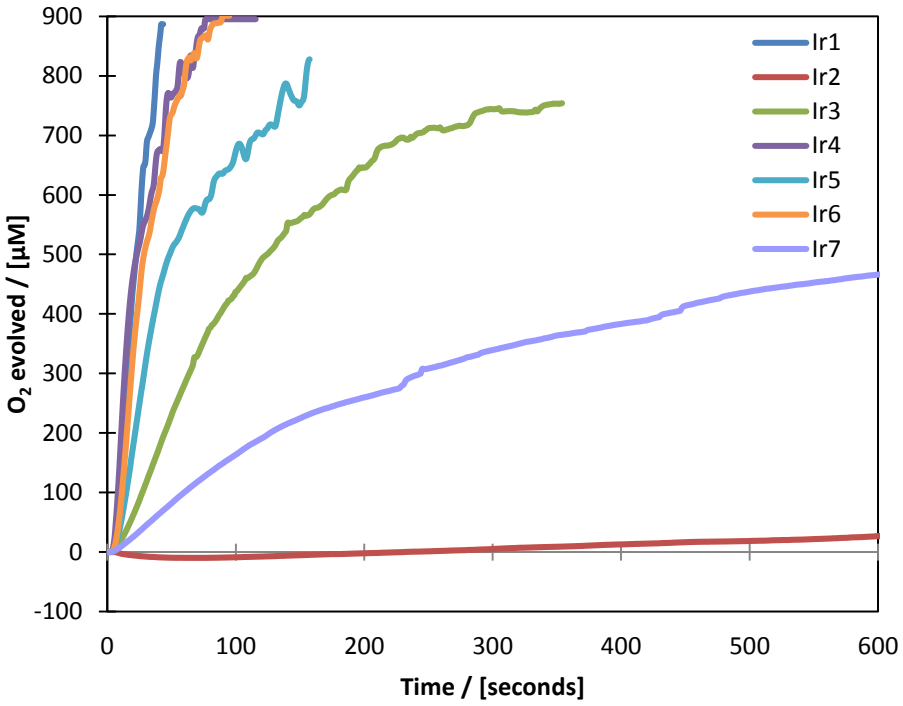

Figure 3.8. *Oxygen evolution traces of the precatalysts **Ir1**–**Ir7** at 100 mM $NaIO_4$ in D_2O, 100 µM [Ir], 25 °C, using a calibrated Clark electrode with stirring. Triplicate data in Appendix Figure A3.4*

Table 3.4. *Kinetic H/D isotope effects of oxygen evolution with precatalysts **Ir1**–**Ir7** and $NaIO_4$ in 100% H_2O or 100% D_2O at 25˚C.*

Precatalyst	Initial k_{obs} [a] in H_2O / mM min^{-1} [c]	Initial k_{obs} [a] in D_2O / mM min^{-1} [c]	KIE [b][c]
Ir1	4.60 ± 0.053	2.14 ± 0.107	2.15± 0.17
Ir2	0.02 ± 0.001	0.01 ± 0.001	2.50 ± 0.34
Ir3	0.41 ± 0.015	0.32 ± 0.010	1.28 ± 0.07
Ir4	3.61 ± 0.020	1.88 ± 0.114	1.92 ± 0.16
Ir5	1.23 ± 0.057	0.71 ± 0.061	1.73 ± 0.19
Ir6	2.88 ± 0.029	1.46 ± 0.143	1.97 ± 0.18
Ir7	0.14 ± 0.008	0.11 ± 0.011	1.27 ± 0.16

[a] Calculated from initial rate of O_2 formation over time as the average value from triplicates

[b] Calculated as initial k_{obs} in H_2O / initial k_{obs} in D_2O.

[c] General errors calculated from standard deviation of rate over repeat runs (appendix)

[d] KIE error calculated from standard deviation of upper and lower limits of KIE (max rate H_2O/min rate D_2O and min rate H_2O/max rate D_2O)

All precatalyst **Ir1**-**Ir7** showed a H/D KIE of >1, indicating a primary isotope effect where the RDS directly involves cleavage of an O-H bond.[10] As water is both solvent and substrate in this reaction, and solvent binding with oxidant and catalyst is fast, solvent effects are assumed to be negligible, with all observed differences in KIE attributed to changes in the ligand environment.

The KIE of 2.15 ± 0.17 found for **Ir1** is comparable to the previously reported value of 2.01 for electrochemical water oxidation[11] with complexes **Ir4** and **Ir6** showing similar values of 1.92 ± 0.16 and 1.97 ± 0.18 respectively. The KIE for **Ir5** was slightly lower than that for **Ir1**, at 1.73 ± 0.19. **Ir3** and **Ir7** show lower KIEs of 1.28 ± 0.07 and 1.27 ± 0.16 respectively. The highest KIE was observed for **Ir2** at 2.50 ±0.34.

Assuming the activated catalyst exists as a dimeric Ir^{IV} species in the stable resting state (as shown for **Ir1***[11]), the RDS is proposed to be a proton coupled electron transfer (PCET) of Ir^{V}-OH to an Ir^{V}-O (Figure 3.9). The varying electronics and H-bonding ability imparted on the catalysts by the different pyalk ligands thus gives rise to the different magnitudes for the H/D KIE observed in the crucial proton transfer step.

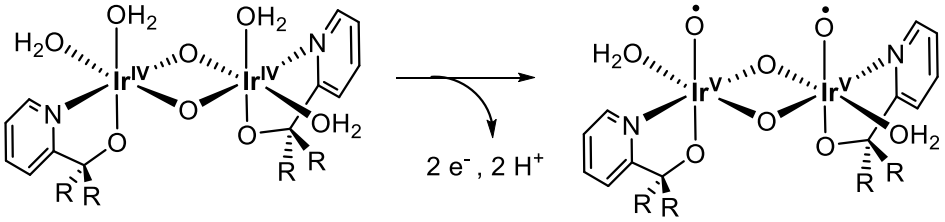

Figure 3.9. *Proposed RDS involving proton coupled electron transfer of Ir^{V}-OH to and Ir^{V}-O species from H/D KIE data for **Ir1**-**Ir7** with $NaIO_4$*

Despite differences in the KIE between complexes, all are distinct from the H/D KIE of 1.0-1.1 seen for IrOx nanoparticles, where the RDS does not involve O-H cleavage.[12] This further supports previous work suggesting that the active species is homogeneous and that no IrOx NPS are formed during the water oxidation reaction.[12,14]

3.4.2 Kinetic isotope effects with cerium^{IV}

Given the variation between KIEs seen for periodate driven water oxidation, and the significant differences observed for CAN as a sacrificial oxidant, H/D KIE analysis was repeated for CAN driven water oxidation.

H/D effects have been investigated in CAN for a similar Cp* Ir^{III} complex bearing a bipyridine ligand in place of the pyridine alkoxide ligand by the Crabtree group in 2010.[15] However, the reported KIE varied significantly with oxidant concentration. At lower oxidant loadings (8 mM CAN), an inverse KIE of 0.65 was observed, data which were attributed to the rate determining step involving the transition of Ir^{IV} → Ir^{V}. Crabtree and co-workers suggested that the transition state for this oxidation occurs via Ce^{IV} bound to the Ir^{IV} via a bridging OH. In this situation, the strong OD bond stabilises the transition state, such that the reaction in D_2O occurs faster than in H_2O, and an inverse KIE is observed. At higher oxidant concentrations (243 mM CAN), a KIE of 1.2 was seen, consistent with the previous suggestion that the RDS involves O-H bond cleavage.[15]

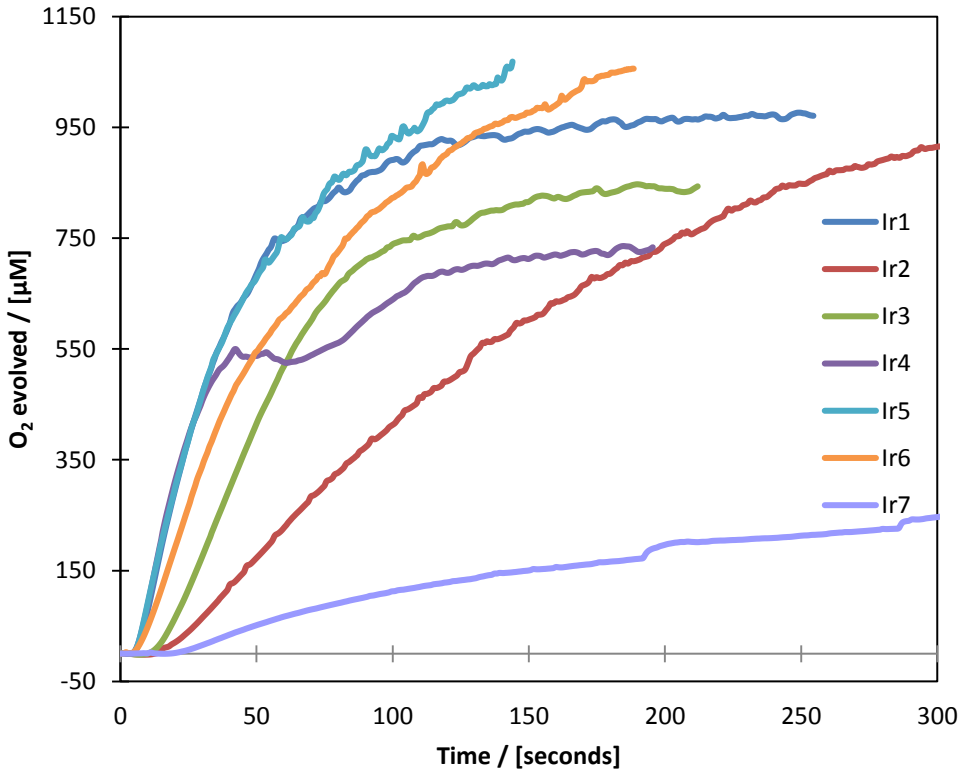

Figure 3.10. *Oxygen evolution traces of the precatalysts* ***Ir1****–7 at 200 mM CAN in D_2O, 100 µM [Ir], 25 °C, using a calibrated Clark electrode. Triplicate data in the Appendix Figure A3.5*

Table 3.5. *Kinetic H/D isotope effects of oxygen evolution with precatalysts **Ir1**–**Ir7** and CAN at 25˚C.*

Precatalyst	Initial k_{obs}[a] with CAN / mM min^{-1} [c]	Initial k_{obs}[a] with CAN in D_2O / mM min^{-1} [c]	KIE [b][d]
Ir1	1.84 ± 0.126	1.31 ± 0.100	1.40 ± 0.17
Ir2	0.22 ± 0.050	0.28 ± 0.041	0.79 ± 0.25
Ir3	0.44 ± 0.049	0.61 ± 0.053	0.73 ±0.12
Ir4	1.89 ± 0.185	1.22 ± 0.075	1.55 ± 0.20
Ir5	1.22 ± 0.054	1.19 ± 0.079	1.03 ± 0.09
Ir6	1.12 ± 0.072	0.89 ± 0.082	1.26 ± 0.16
Ir7	0.09 ± 0.004	0.10 ± 0.0267	0.88 ± 0.23

[a] Calculated from initial gradient of O_2 formation over time

[b] Calculated as initial k_{obs} in H_2O / initial k_{obs} in D_2O.

[c] General errors calculated from standard deviation of rate over repeat runs

[d] KIE error calculated from standard deviation of upper and lower limits of KIE (max rate H_2O/min rate D_2O and min rate H_2O/max rate D_2O)

The KIEs recorded using CAN for precatalysts **Ir1**-**Ir7** are all lower than the KIEs reported with $NaIO_4$, and some inverse KIEs are evidenced. Before in-depth analysis and discussion of these values are undertaken it is worth noting the following:

- Firstly, that in addition to oxidant variation, the pH stability requirements of CAN necessitate that the reactions are done at several pH units lower than that for $NaIO_4$; for a process involving proton coupled electron transfer events, pH variation thus makes direct comparison difficult.
- Secondly, the errors for all the CAN data are higher than those observed for $NaIO_4$; presumably due to the effect on the Clark electrode of sustained and repeated experiments at highly acidic pH.
- Thirdly, additional protons will have been introduced with the addition of HNO_3 required to lower the pH for the CAN experiments, thereby adding additional ions and increasing the H/D ratio.

As with the KIEs for $NaIO_4$, precatalysts **Ir1**, **Ir4** and **Ir6** show the highest KIEs, with values greater than one, indicating an RDS involving O-H bond cleavage.

Precatalysts **Ir2**, **Ir3** and **Ir7** all show inverse KIEs of less than 1, which could suggest an RDS involving an O-D stabilised transition state with CAN as previously proposed.[15] Notably **Ir3** and **Ir7** again show the lowest KIEs; a trend also seen for the $NaIO_4$ experiments.

The diphenyl complex **Ir2** has the greatest variation between the KIEs for the different oxidants. **Ir2** had the greatest H/D KIE when driven with $NaIO_4$ (2.50 ± 0.34), but one of the lowest KIEs in CAN (0.79 ± 0.25). Given the fact that **Ir2** evolved oxygen at a factor of ten faster in CAN than periodate, and regardless of the potential error, water oxidation driven by complex **Ir2** must proceed via a different mechanism in CAN to $NaIO_4$.

3.5 Kinetics of oxygen evolution

Along with the acquisition of the KIE data, further mechanistic investigation was sought with regards to the kinetics of the water oxidation reaction with **Ir1**-**Ir7**. Kinetic investigations by means of initial rate analysis have previously been reported for Cp* Ir based water oxidation complexes, but with CAN as the oxidant.[15]

Typically when CAN is used in kinetic studies, the reaction is monitored by CAN consumption via UV-vis spectroscopy.[16] However, it has been shown that around 20-30 equivalents of CAN are consumed during precatalyst activation, thus the observed consumption cannot wholly be attributed to the oxidation reaction. Furthermore, CAN and its reduced forms have been known to interfere with the water oxidation cycle[4] and to form ceria nanoparticles. These nanoparticles can cause degradation of catalyst and undergo heterogeneous background oxygen evolution.[3] Additionally, as seen with the KIE experiments, the strongly acidic media required to keep CAN stable can cause additional complications. Experiments to determine the order in Ir during oxygen evolution were therefore undertaken with $NaIO_4$, which operates under milder conditions. By measuring the production of oxygen via a Clark electrode, rather than oxidant consumption, a direct correlation of the effect of [Ir] on reaction rate can be made.

3.5.1 Fundamentals of graphical rate analysis

Although initial rate analysis has proven successful in other analogous systems,[15] a large number of experiments are often required to produce the log/log plots. As the rate data are only considered for the initial (and therefore fastest) part of the temporal concentration graph, complexities in the mechanism, such as changes in order changes in order throughout the experiment, can be lost.

Reaction Progress Kinetic Analysis (RPKA), first described by Blackmond[17], uses a graphical comparison of rate data to identify reaction order using the full dataset. In this case we use a variation of RPKA detailed by Bures: Variable Time Normalised Analysis (VTNA). [18,19]

This technique allows for a visual comparison of the entire temporal concentration profiles by normalising the time axis using the catalyst concentration to a power (α), whereby α is the order in catalyst. All profiles with varying catalyst loading are plotted on the same graph and the value of α is then iteratively changed until a clear visual overlap is observed (Figure 3.10).

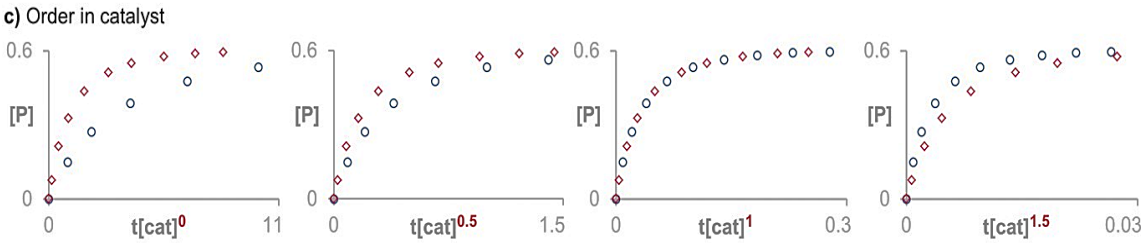

Figure 3.11. *Representation of iterative overlap for VTNA to determine catalyst order. Reproduced from Bures 2016*[19]

Data analysed by VTNA produces mathematically identical results to the RPKA method, but with the advantage of being able to use concentration data, rather than rate data. Therefore, concentration data can be taken directly from the Clark electrode oxygen assay, without the need to convert to rate data.

3.5.2 Saturation Regime

In the first instance, VTNA was attempted for precatalysts **Ir1**-**Ir7** at high concentrations of precatalyst (50-200 μM) and relatively low concentrations of oxidant (10 mM). Surprisingly, a zeroth order of catalyst was observed (Figure 3.12), suggesting that catalyst concentration had no effect on the rate of the reaction.

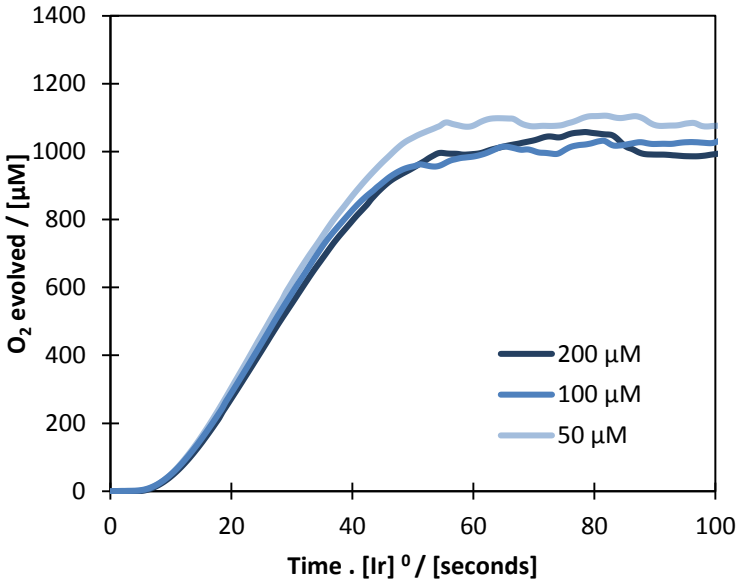

Figure 3.12. *Oxygen evolution with VTNA applied at 10 mM $NaIO_4$ in H_2O, 200 μM, 100 μM, 50 μM of precatalyst* ***Ir1*** *with best fit at α = 0 at native pH, 25 °C, using a calibrated Clark electrode*

At these concentrations of iridium, it appeared that the reaction was occurring under saturation conditions, whereby there was such a high level of active catalyst available, the relatively small variation between catalyst concentrations did not impact the rate. Alternatively, it could be considered that with a lower [Ir]:[oxidant] ratio, precatalyst activation and not oxygen evolution, was the limiting factor. Previous kinetic studies of the activation of **Ir1** followed by UV-vis spectroscopy showed zero order dependence on [Ir].[20]

In order to try and move the conditions out of the saturation regime, the oxidant loading was increased by 10-fold, with the same iridium concentrations, and the VTNA was repeated (Figure 3.13).

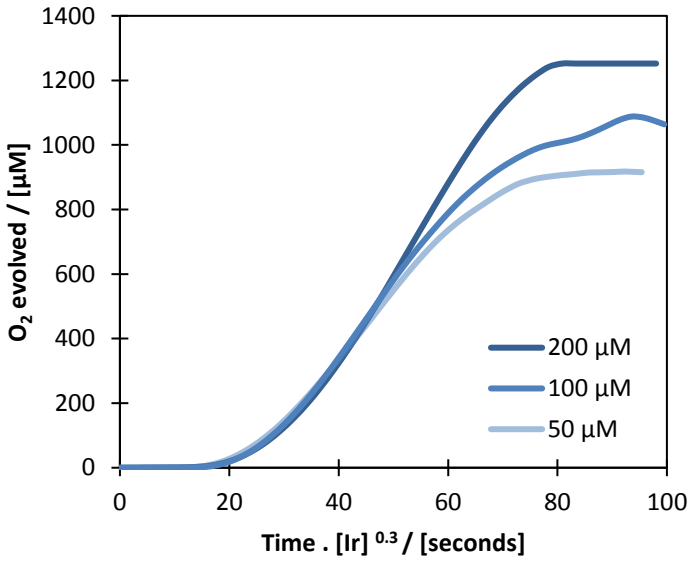

Figure 3.13. *Oxygen evolution with VTNA applied at 100 mM $NaIO_4$ in H_2O, 200 µM, 100 µM, 50 µM of precatalyst 1 with best fit at α = 0.3 at native pH, 25 °C, using a calibrated Clark electrode*

Under these conditions the VTNA revealed an order in catalyst of 0.3, but with poor overlap towards the end of the reaction profiles. It appeared that the reaction was still operating on the edge of the saturation regime, and thus the catalyst concentration was also decreased in order to attempt to obtain clearer data (Figure 3.14).

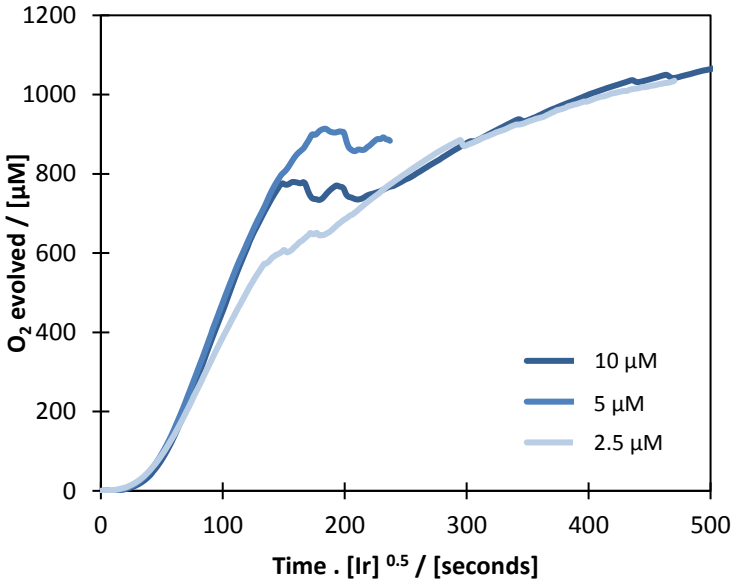

Figure 3.14. *Oxygen evolution with VTNA applied at 10 mM $NaIO_4$ in H_2O, 10 µM, 5 µM, 2.5 µM of precatalyst* ***Ir1*** *with best fit at α = 0.5 at native pH, 25 °C, using a calibrated Clark electrode*

In this case VTNA showed a reaction order of 0.5. The same ratio of [catalyst]:[oxidant] was investigated with increased concentrations. The reason for this was two-fold. Firstly, the reaction seen in Figure 3.14 took 10 mins with the fastest water oxidation catalyst **Ir1**. It was considered that under these conditions the reaction with **Ir2** and **Ir7** would be too slow to accurately monitor; reactions with the Clark electrode that take longer than 2 hours are prone to signal drift. Secondly, in order to ensure that the 'saturation regime' previously observed was due to excess catalyst and not an effect of the oxidant.

These conditions also produced a reaction order of 0.5 by VTNA, and thus full investigation for all precatalysts was undertaken at these conditions (full analysis by VTNA in section 3.5.3). The range of conditions tested by VTNA and the resulting catalyst order can be seen in Table 3.6.

Table 3.6. *Varying order in [Ir] with varying oxidation and [Ir] conditions*

Concentration of $NaIO_4$	Concentration of Ir	Order in [Ir] by VTNA
10 mM	200 µM, 100 µM, 50 µM	0
100 mM	200 µM, 100 µM, 50 µM	0.3
10 mM	10 µM, 5 µM, 2.5 µM	0.5
100 mM	20 µM, 10 µM, 5 µM	0.5

With a wide range of catalysts data available, a ln(k_{obs}) vs ln([Ir]) plots were constructed for the reaction carried out with 100 mM $NaIO_4$ (Figure 3.14). Gradient analysis revealed an order in catalyst of 0.54, consistent with the value obtained by VTNA.

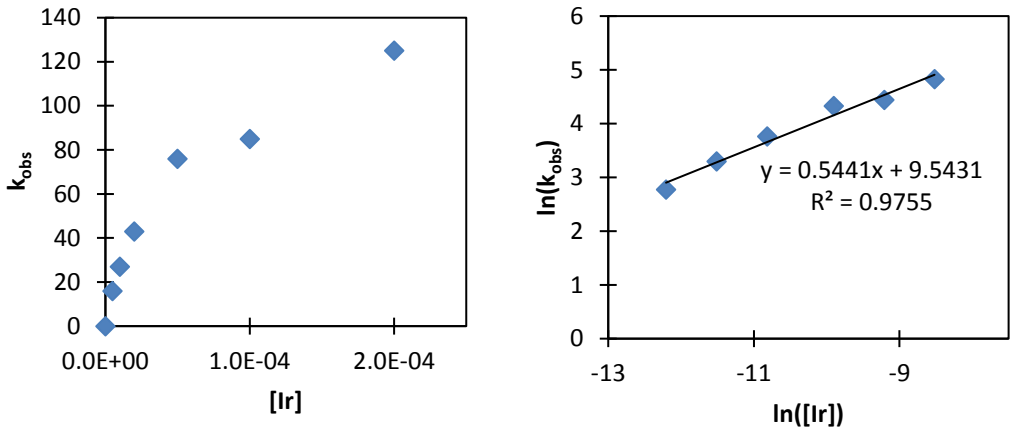

Figure 3.14. *ln(k_{obs}) / ln([Ir]) plots for $NaIO_4$ 100 mM,* ***Ir1*** *at 5, 10, 20, 50, 100, 200 µM in H_2O at 25 °C. Data for plot is in the Appendix (Figure A3.7)*

3.5.4 Variable time normalised analysis for catalyst order

The results of applying VTNA to varying concentrations of precatalysts **Ir1**-**Ir7** are shown in Figure 3.15. For **Ir1**, the iterative process is included, indicating the closest fit values either side of the chosen value.

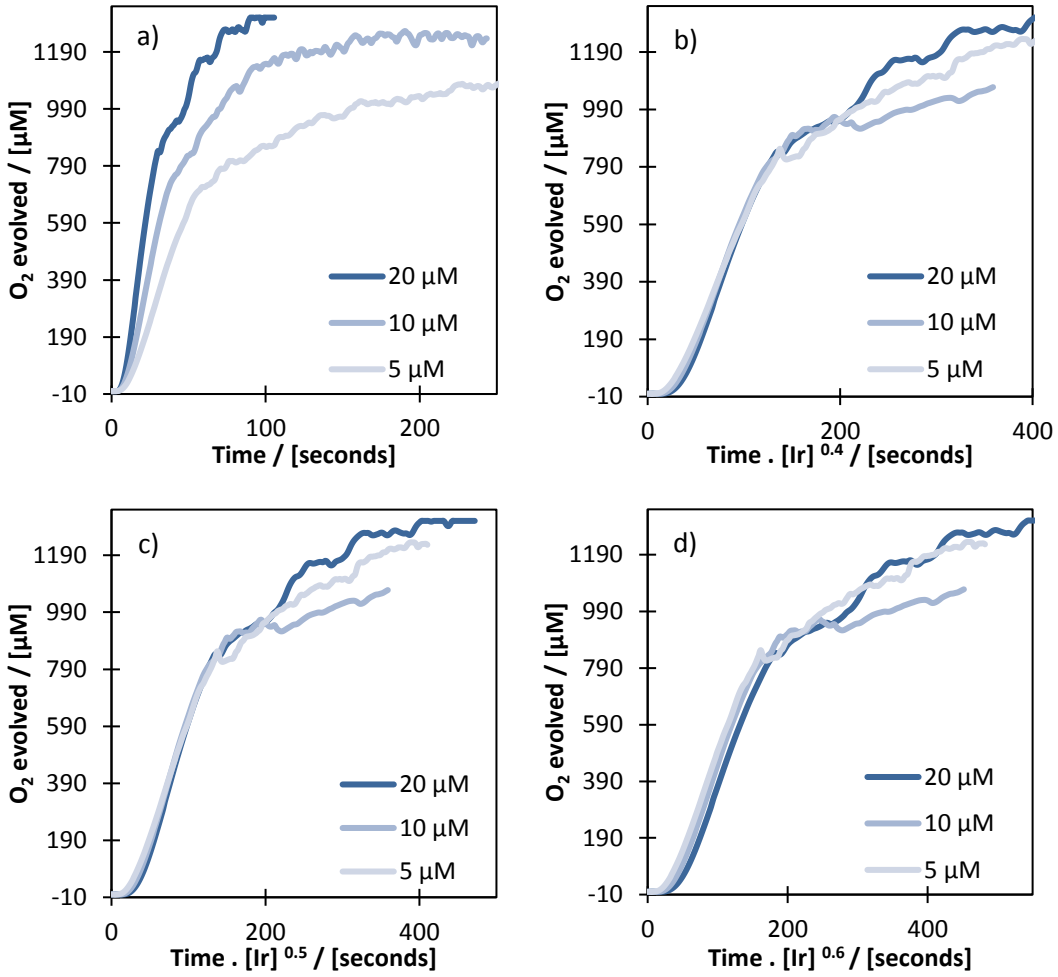

Figure 3.15. *Oxygen evolution traces of precatalysts **Ir1** at 100 mM $NaIO_4$ in H_2O, with varying **Ir1** (20 µM, 10 µM, 5 µM), at 25 °C, using a calibrated Clark electrode right) the same trace with VTNA applied to the x axis, where the factor has been iteratively changed to give the best overlap a) no VTNA applied, b) α = 0.4, c) α = 0.5, d) α = 0.6*

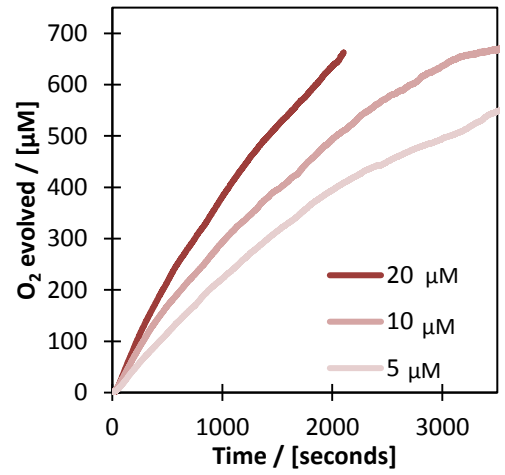
O2 evolved / [µM]
Time / [seconds]
20 µM
10 µM
5 µM

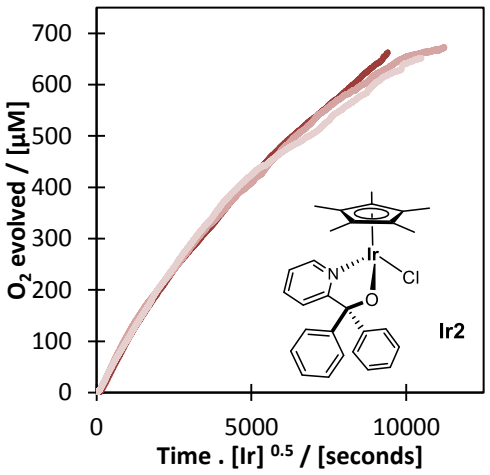
O2 evolved / [µM]
Time . [Ir] 0.5 / [seconds]
Ir2

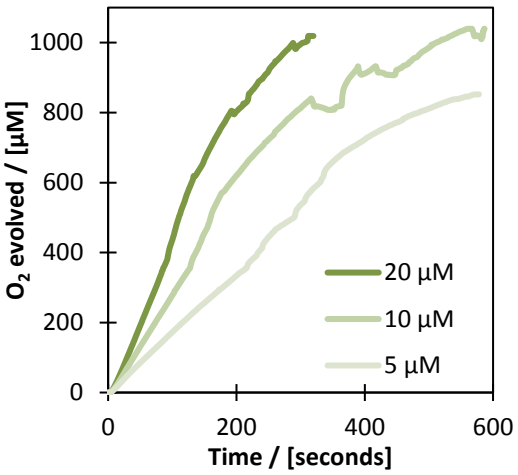
O2 evolved / [µM]
Time / [seconds]
20 µM
10 µM
5 µM

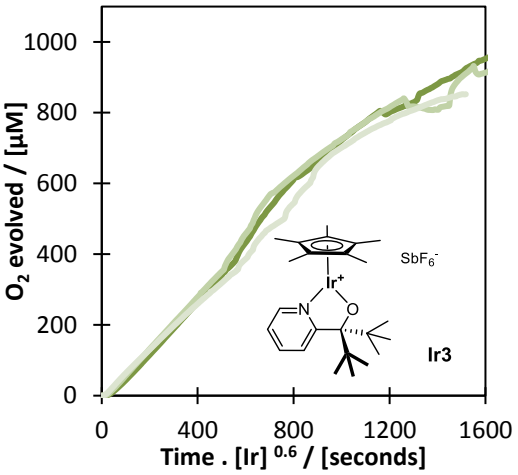
O2 evolved / [µM]
Time . [Ir] 0.6 / [seconds]
Ir3

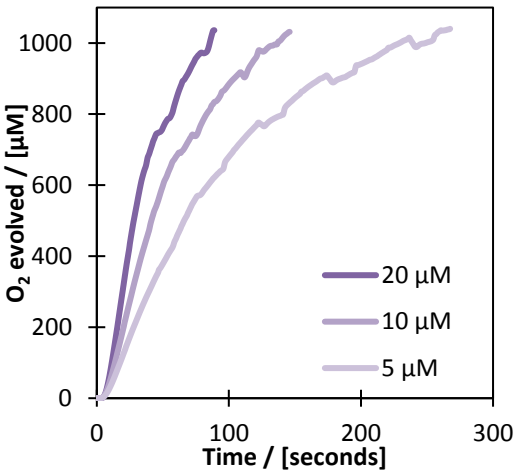
O2 evolved / [µM]
Time / [seconds]
20 µM
10 µM
5 µM

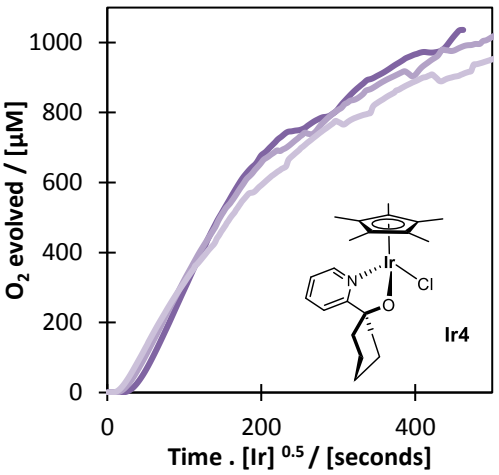
O2 evolved / [µM]
Time . [Ir] 0.5 / [seconds]
Ir4

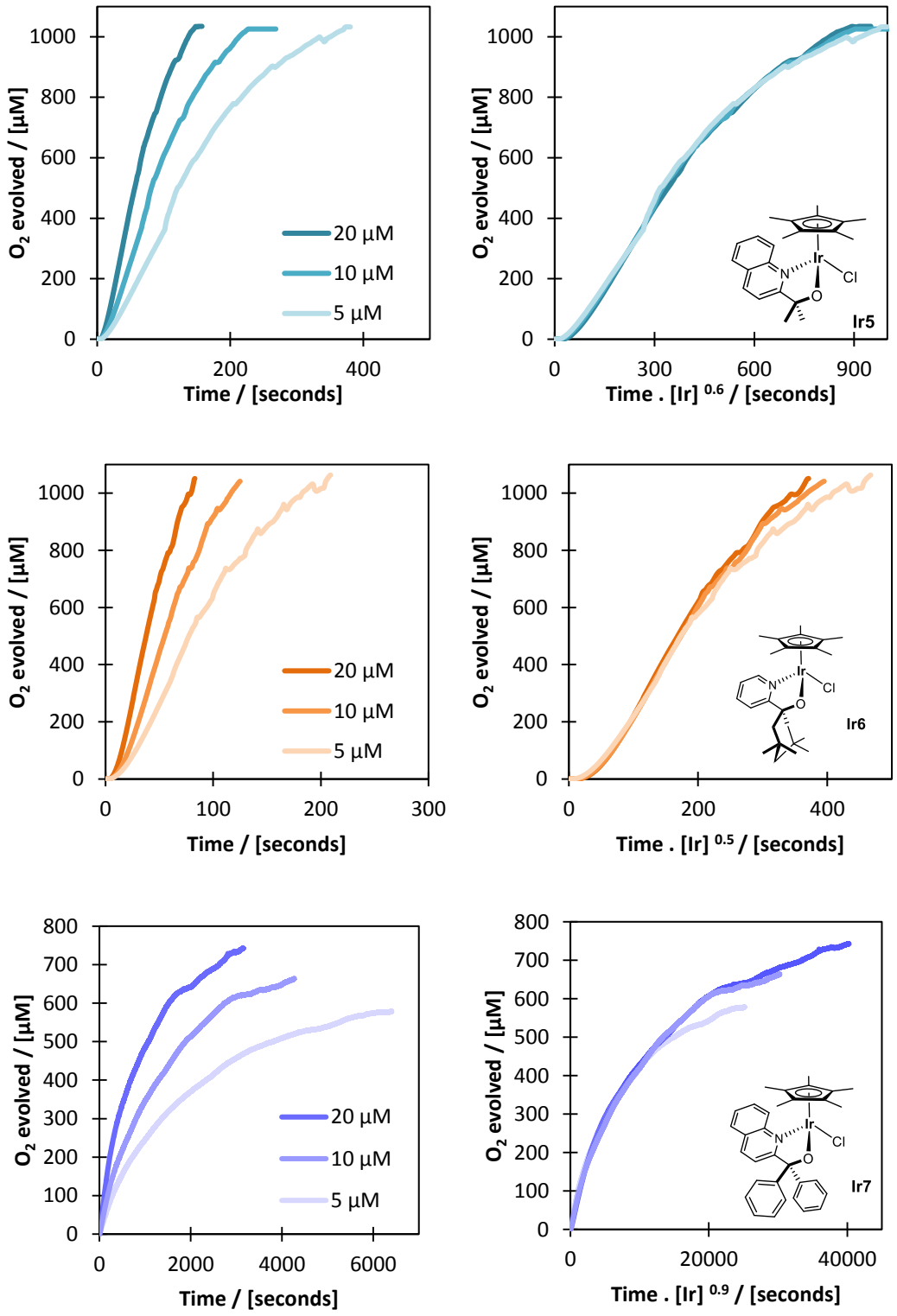

Figure 3.16. *Oxygen evolution traces of precatalysts* ***Ir1*****–*****Ir7*** *at various [Ir] concentrations with 100 mM $NaIO_4$ in H_2O (native pH 5.6) at 25 °C using a calibrated Clark electrode with stirring as measured (left; fluctuations caused by O_2 bubble formation), and with variable time normalisation applied (right).*

Notably, precatalysts **Ir1**-**Ir6** all show an order in Ir of 0.5-0.6, with very good fit throughout the course of the entire reaction. Minor deviation was observed at longer reactions times (particularly for the faster catalysts **Ir1**, **Ir4** and **Ir6**) which could be due to catalyst deactivation, or oxygen escaping detection due to the fast rates of oxidation. It is worth noting that measurements with Clark electrode become less accurate at higher O_2 concentrations and longer reaction times, due to saturation of oxygen in solution. Intriguingly, **Ir7** shows a clear deviation from this 0.5-0.6 value, with an apparently order in Ir of 0.9, discussion of which will be made in section 3.5.3.

The fact that one reaction order is pervasive for all complexes **Ir1**-**Ir6** (within experimental error) is indicative of no significant mechanistic changes in the RDS during the reaction. Crucially, indicators for nanoparticle formation such as orders in Ir of greater than one, or rate acceleration, were not observed with any of the complexes.[12]

The half order in [Ir] reported here is particularly interesting when considering the mechanistic implications, as it implies that two [Ir] metal centres are involved in the formation of oxygen in the RDS. Explanation for this interpretation can be seen in Figure 3.17, where n iridium centres form a multinuclear species which performs the water oxidation. When considering the rate of product formation, the order of iridium involved in the reaction is therefore 1/n.

$$n\ x\ [Ir] \longrightarrow 1/n\ [Ir]_n \begin{array}{l} \curvearrowright\ 2H_2O + 4Ox^+ \\ \curvearrowright\ O_2 + 4H^+ + 4Ox \end{array}$$

$$\frac{d[O_2]}{dt} = k\,.\,[Ir]^{1/n}$$

Figure 3.17. *Schematic to explain the observed half order in iridium obtained by VTNA of water oxidation of complexes* ***Ir1***-***Ir6***

A dimeric Ir^{IV} complex has been previously postulated to be the active catalyst in these Cp^*Ir^{III} complexes[20], a hypothesis recently corroborated by the synthesis of a range of stable model complexes based on μ-oxo iridium dimers.[21–28] The persistent half order in iridium seen for VTNA suggests that this dimeric structure is retained throughout the catalytic cycle, and would allow for the four electron transfers required for water oxidation to be spread over two metal centres.

Several studies have recently been conducted using RPKA to study the oxygen evolution kinetics of complex **Ir1** under varying conditions (Table 3.7).

***Table 3.7**. Comparison of previously reported literature on **Ir1** by graphical rate analysis*

	Technique	[Ir]	Oxidant	[ox]	Order in Ir
Reek[16]	RPKA by UV-vis of oxidant consumption	1-5 μM	CAN	1.5 mM	1.7
Macchioni[29]	RPKA by O_2 formation by manometer	1-10 μM	$NaIO_4$	20 mM	0.89
This work	VTNA by O_2 formation by Clark electrode	5-20 μM	$NaIO_4$	100 mM	0.5

In the study by Reek and co-workers, the reaction order was determined by assessing consumption of CAN over the course of the reaction by UV-vis spectroscopy.[16] Aside from the previously described difficulties with using CAN, the method of measuring oxidant consumption and not product formation complicates the order obtained. CAN is a single electron oxidant, and therefore four moles of CAN are required to produce one mole of O_2. Reek and co-worked reported an order of [Ir] of 1.7, taking the stoichiometry into account as described in Figure 3.17, the order becomes 0.43; a value not too dissimilar to the 0.5 reported herein. Even without manipulation of stoichiometry, determining the order of iridium by CAN consumption is difficult because the observed reduction of CAN is not wholly due to production of oxygen. Activation of the Cp* Ir complex and loss of CAN due to formation of ceria nanoparticles could also explain the different iridium order.

One of the compounds investigated by Hetterscheid and Reek, $[Cp^*Ir(NHC)(OH)_2]$, was investigated previously with $NaIO_4$. In this case the oxygen production was recorded by Clark electrode, and initial rate analysis was performed revealing an order in Ir of 0.65, again a value similar to the 0.5 - 0.6 values reported herein.[30]

The Macchioni study reported last year was performed under very similar conditions to the experiments described herein, with $NaIO_4$ used as the oxidant and O_2 evolution recorded by manometry. An order in iridium of 0.89 was obtained for **Ir1**. However, the analysis was performed at the "point of maximum rate", suggesting non-uniform rate behaviour throughout the reaction, and not via RPKA of the full reaction profiles, which could lead to a higher order in Ir than expected.[29]

3.6 A discussion of Ir7

Whilst complexes **Ir1**-**Ir6** all showed an order in iridium of 0.5 by VTNA, **Ir7** showed an order of 0.9, which persisted throughout the reaction. From the data described in Chapter 2, **Ir7** also showed the highest E_{mid} potential, 0.72 V vs. NHE (Section 2.4) and a very low ε value for the Ir-O-Ir absorbance by UV-vis (Section 2.5), although no Cp* ligand was observed by ^{1}H NMR after 5 mins (Section 2.5).

Additionally, for the water oxidation data detailed here under varying conditions, **Ir7** showed very little variation, regardless of conditions. A slow rate of oxidation evolution was maintained, regardless of solvent or oxidant, ranging between 0.09 mM min^{-1} to 0.14 mM min^{-1}. There is even an argument to be made that the KIE for **Ir7** is the same for both $NaIO_4$ and CAN within experimental error (lower limit KIE in $NaIO_4$ is 1.1, upper limit KIE in CAN is 1.1). If the KIE for **Ir7** is taken at its lowest value of 1.1 (1.3 ± 0.2) in $NaIO_4$, the RDS could be different to the proposed deprotonation of Ir^{IV}-OH to Ir^{V}=O. However, the relatively large error of ± 0.2 in the KIE value could also support an RDS of deprotonation of Ir^{IV}-OH to Ir^{V}=O, and so determining the RDS with certainty is challenging at this point.

It was initially suggested that the explanation for these data was due to the solution equilibrium outlined in Section 2.3. If **Ir7** was predominantly in solution as ^{6}Ir-Cl, and conversion to **Ir7**$^{+}$ was difficult due to a combination of the enhanced sterics and the electron withdrawing phenyl groups, then activation of the Cp* complex by hydroxyl attack on the Cp* ring[31] would not take place. However, activation followed by ^{1}H NMR indicated full loss of the Cp* ring and acetate formation. Furthermore, the cationic **Ir7**$^{+}$ complex was synthesised Cl^{-} free and tested for water oxidation, but slower rates were observed.

As part of the initial investigation into the identity of the blue species by Crabtree and co-workers, computational modelling was undertaken to determine the probable absorptions for a dimeric Ir^{IV} species by UV-vis, which was shown to have an absorption of 580 nm. The UV-vis spectrum was also modelled for a mononuclear $[Ir^{IV}(pyalk)(H_2O)_3(O)]^{+}$ complex (Figure 3.18b reproduced from Hintermair *et al* 2013)[20]. The major contributions to the modelled UV-vis spectrum from this species were absorptions at 334 nm and 473 nm, and a weak absorption at 587 nm. The activation of **Ir7** was therefore reconsidered in relation to the modelled UV-vis spectrum (Figure 3.18a).

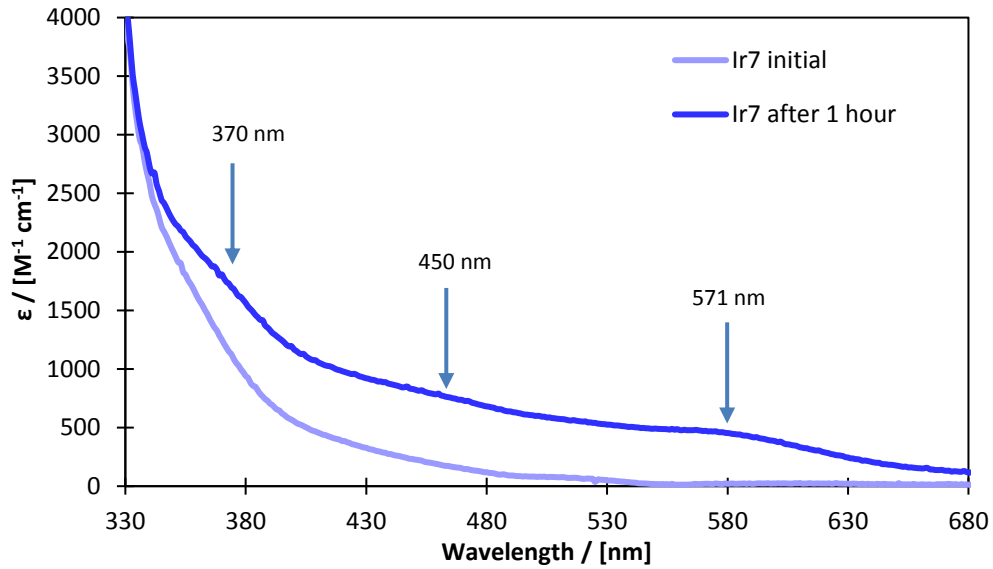

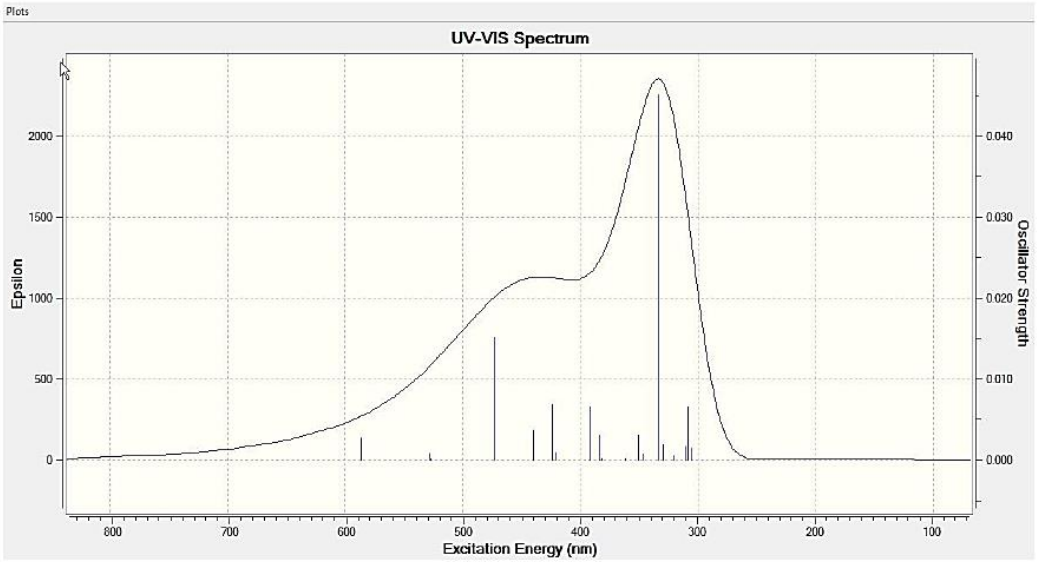

Figure 3.18. a) *UV-vis spectra of activation of Ir7 (0.5 mM) with $NaIO_4$ (25 mM) at t = 0 (pale purple) and t = 60 min (dark purple)* ***b)*** *modelled spectrum of a monomeric $[Ir^{IV}(pyalk)(H_2O)_3O]$ species reproduced from Hintermair et al*[20]

Collating the data described above and the apparent order of 0.9 in Ir by VTNA, it is therefore likely that the active form of **Ir7** is a mononuclear species. This species could then perform water oxidation by water nucleophilic attack by a single [Ir] centre, rather than radical oxyl coupling by a dimeric species as proposed in Figure 3.19.

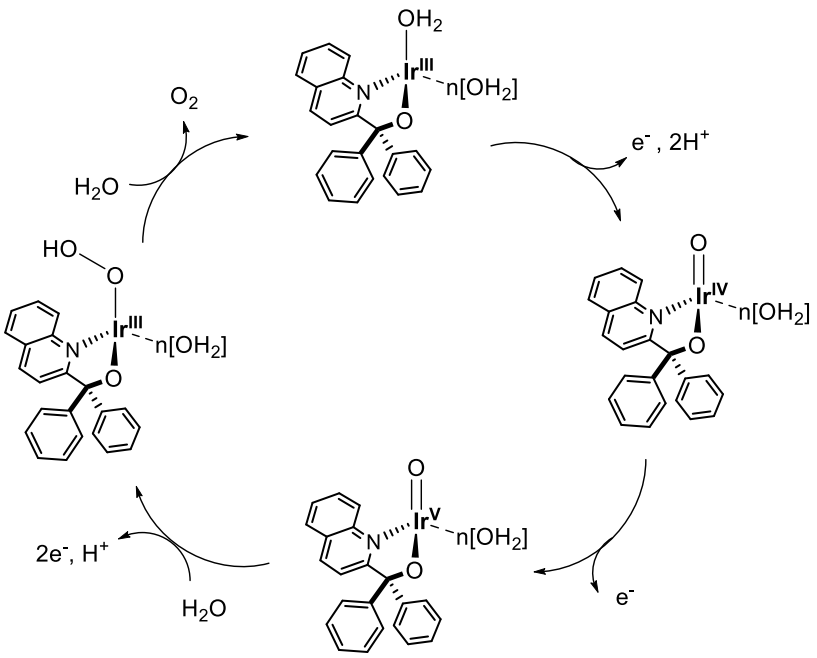

Figure 3.19. *A proposed alternative catalytic cycle for a monomeric **Ir7** species as the active catalyst*

The proposed monomeric mechanism for **Ir7** would account for:

- The low absorbance of the Ir-O-Ir species for **Ir7** by UV-vis during activation (ε of 594 M^{-1} cm^{-1} compared to >1350 M^{-1} cm^{-1} for **Ir1**-**Ir6**)
- The low KIEs observed for **Ir7** with both $NaIO_4$ and CAN, if the RDS is electron transfer of Ir^{III} → Ir^{IV}. This is also supported by the high $Ir^{III/IV}$ reduction potential of **Ir7** observed in non-aqueous CVs
- The apparent order in Ir of 0.9 for **Ir7** during water oxidation by VTNA.

3.7 Summary

The chemically driven water oxidation activity of complexes **Ir1**-**Ir7** was investigated under varying conditions using a Clark electrode. Solvent, pH and choice of oxidant were all shown to affect the rate of oxygen evolution; in general terms the alkyl complexes showed faster rates of water oxidation than the aryl counterparts. A summary of the key effects on **Ir1**-**Ir7** for water oxidation are shown in Figure 3.20.

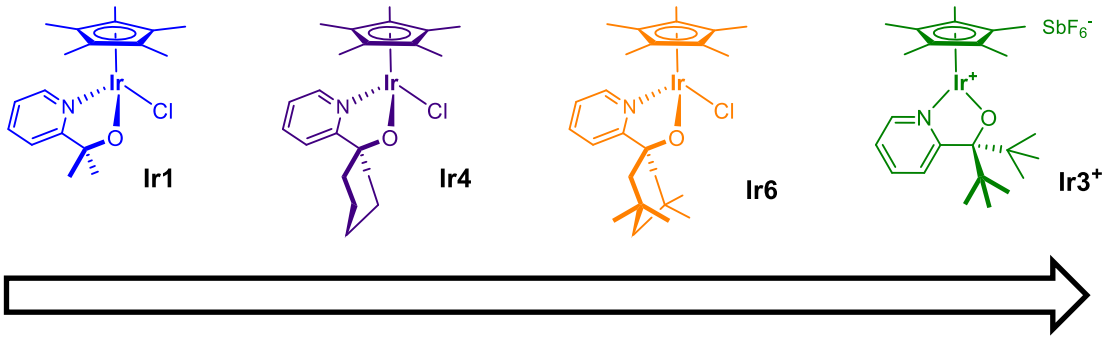

Increasing steric bulk
Decreasing rates of water oxidation with both $NaIO_4$ and CAN
Rates of water oxidation 2/3 times slower with 20% ^tBuOH

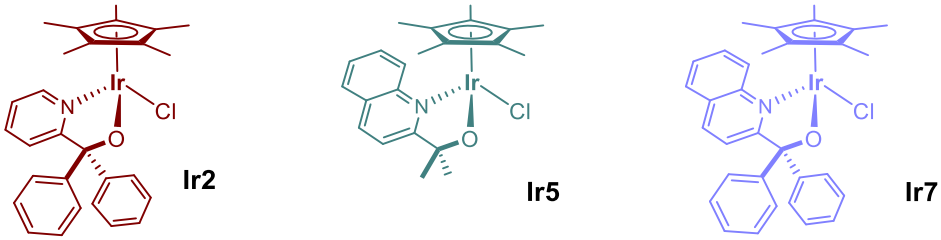

Ir2	Ir5	Ir7
Rate not affected by 20% ^tBuOH	*Quinoline ring reduces rate compared to **Ir1***	*Rate not affected by 20% ^tBuOH*
Rate 10 times faster with CAN than $NaIO_4$	*Rate 7 times slower in 20% ^tBuOH*	*Rate not affected by oxidant*

Figure 3.20. *A summary of the key effects of different conditions on the rate of water oxidation with complexes **Ir1**-**Ir7***

The relative ease of data acquisition for water oxidation assays by Clark electrode also allowed for a range of kinetic investigations to be undertaken, namely KIE studies and determination of the order in catalyst by graphical kinetic analysis.

Primary KIEs of 1.3 – 2.5 were observed for all complexes with $NaIO_4$, indicating cleavage of an O-H bond in the RDS. KIE analysis with CAN yielded very different data, with inverse KIEs seen for several catalysts (**Ir2**, **Ir3** and **Ir7**). Notable amongst the different KIEs was that for **Ir2**, which had the strongest KIE in $NaIO_4$, but a large inverse KIE in CAN, indicating a change in mechanism for this complex depending on oxidant.

Analysis of the reaction order in [Ir] of the complexes was performed using Variable Time Normalised Analysis, and a reaction order of 0.5-0.6 was observed for precatalysts **Ir1**-**Ir6**, indicating the presence of a dimer, consistent with previous hypotheses.[20] The correlation of the KIE and the VTNA data is depicted in the catalytic cycle proposed *vide infra*.

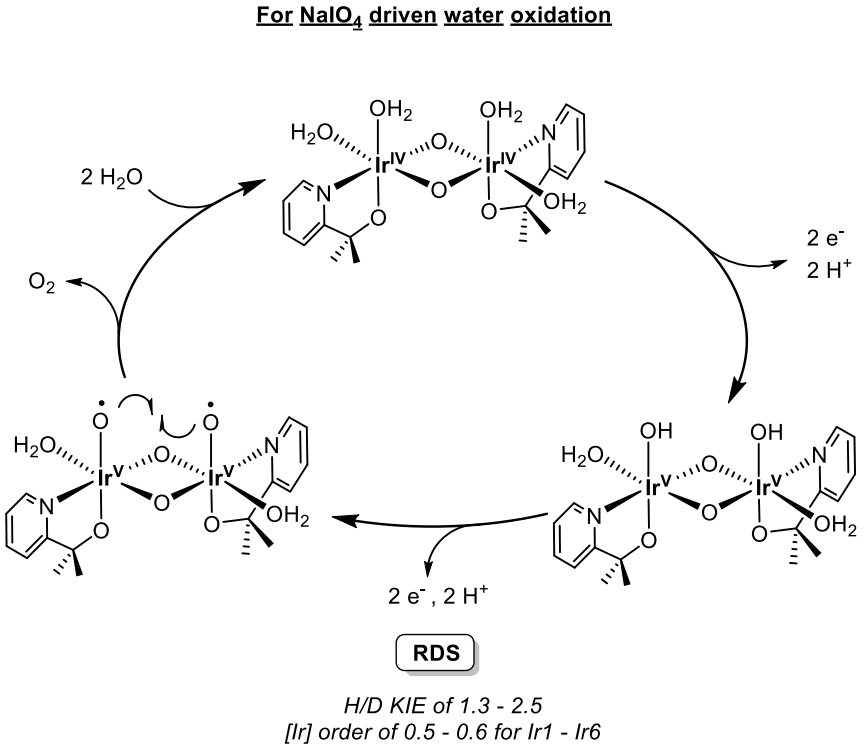

Figure 3.21. *A proposed catalytic cycle for the oxidation of water with complexes **Ir1**-**Ir6** driven by $NaIO_4$ in aqueous solution*

Complex **Ir7** showed a different order in [Ir] for the VTNA and maintained a similarly slow rate of oxygen evolution under the wide range of conditions tested. In combination with data from Chapter 2, an alternative mechanism involving a monomeric active species was proposed for **Ir7** (Figure 3.19), proving yet again that simple ligand variation in these complicated iridium systems can have a significant impact on the catalytic activity.

3.8 Experimental

General

Precatalysts were synthesised according to procedures outlined in Chapter 2. Other chemicals were used as purchased. High-purity Milli-Q water was used in all experiments.

In situ oxygen evolution data were collected using a Hansatech Oxygraph Plus system with a DW2/2 Clark-type electrode chamber (with temperature control and magnetic stirring) measuring dissolved O_2 in solution. The electrode was prepared with 2 M KCl electrolyte under a PTFE membrane and spacer paper, and the instrument was zeroed with the appropriate background solution depending on the reaction (e.g. 100 mM $NaIO_4$ solution in H_2O (2 mL) or 200 mM CAN solution in H_2O (2 mL) etc) thoroughly degassed with argon. Solution pHs were measured with a 913 Metrohm pH meter.

In all cases the reactions were initiated by addition of Ir, but the Clark electrode was set to collect data for 1 minute prior to addition to ensure a flat base line. The first minute of data was discarded, and the oxygen evolution data normalised by subtraction of the baseline value just before catalyst addition. The reactions were conducted in triplicate with the exception of testing of the saturation regime for the VTNA data; data can be found in the appendix.

Standard conditions

A solution of 100 mM $NaIO_4$ in H_2O (2 mL) was added to the Clark electrode chamber and the reaction started with the addition of Ir (100 µM, 40 µL of a 5 mM stock solution in $H_2O/^tBuOH$ (4:1)).

pH Variation

A solution of 10 mM $NaIO_4$ (2mL) at native pH (5.3) was added to the Clark electrode chamber and the reaction started by addition of **Ir1** (1µM, 40 µL of a 50 µM solution in H_2O). The pH of the $NaIO_4$ solution was adjusted as desired with KOH and HNO_3 (pH measured at 1.7, 3.0, 4.4, 6.4, 7.3, 8.3, 11.8 and 13.0).

Oxidant variation

A solution of 200 mM CAN in 0.1 M HNO_3 in H_2O (pH 1.5) (2 mL) was added to the Clark electrode chamber. The reaction was started with the addition of Ir (100 µM, 40 µL of a 5 mM stock solution in $H_2O/^tBuOH$ 4:1).

KIE studies

Reactions were performed as described in 'Standard conditions' ($NaIO_4$) and 'Oxidant variation' (CAN) but the oxidant solutions were made up in D_2O rather than H_2O.

Solvent effects

A solution of 100 mM $NaIO_4$ in 20% ^tBuOH in H_2O (2 mL) was added to the Clark electrode chamber. The reaction was started with the addition of Ir (100 µM, 40 µL of a 5 mM stock solution of the desired Ir catalyst in $H_2O/^tBuOH$ 4:1).

VTNA data

A solution of 100 mM $NaIO_4$ in H_2O (2 mL) was added to the Clark electrode chamber. The reaction was started by the appropriate addition of [Ir] from 5 mM stock solution in $H_2O/^tBuOH$ 4:1. For 50 µM [Ir] final concentration, 20 µL of [Ir] stock solution was added; for 100 µM [Ir] final concentration, 40 µL of [Ir] stock solution was added; and for 200 µM [Ir] final concentration, 80 µL of [Ir] stock solution was added.

3.9 References

1. A. R. Parent, R. H. Crabtree, and G. W. Brudvig, *Chem. Soc. Rev.*, 2013, **42**, 2247–2252.
2. S. A. Hayes, P. Yu, T. J. O'Keefe, M. J. O'Keefe, and J. O. Stoffer, *J. Electrochem. Soc.*, 2002, **149**, 623–630.
3. D. B. Grotjahn, D. B. Brown, J. K. Martin, D. C. Marelius, M. Abadjian, H. N. Tran, G. Kalyuzhny, K. S. Vecchio, Z. G. Specht, S. A. Cortes-llamas, V. Miranda-soto, V. Niekerk, C. E. Moore, and A. L. Rheingold, *J. Am. Chem. Soc.*, 2011, **133**, 19024–19027.
4. D. J. Wasylenko, C. Ganesamoorthy, M. A. Henderson, B. D. Koivisto, H. D. Osthoff, and C. P. Berlinguette, *J. Am. Chem. Soc.*, 2010, **132**, 16094–16106.
5. J. Limburg, J. S. Vrettos, H. Chen, J. C. De Paula, R. H. Crabtree, and G. W. Brudvig, *J. Am. Chem. Soc.*, 2001, **123**, 423–430.
6. I. Pecht and Z. Luz, *J. Am. Chem. Soc.*, 1965, **87**, 4068–4072.
7. L. Clark, F. Gollan, and V. Gupta, *Science.*, 1950, **111**, 85–87.
8. J. W. Severinghaus, *Anesthesiology*, 2002, **97**, 253–256.
9. R. Pokhrel, M. K. Goetz, S. E. Shaner, X. Wu, and S. S. Stahl, *J. Am. Chem. Soc.*, 2015, **137**, 8384–8387.
10. M. Gómez-Gallego and M. A. Sierra, *Chem. Rev.*, 2011, **111**, 4857–4963.
11. J. M. Thomsen, L. Que Jr., S. M. Hashmi, J. Campos, U. Hintermair, R. H. Crabtree, and G. W. Brudvig, *J. Am. Chem. Soc.*, 2014, **136**, 13826–13834.
12. N. D. Morris, M. Suzuki, and T. E. Mallouk, *J. Phys. Chem. A*, 2004, **108**, 9115–9119.
13. S. W. Sheehan, J. M. Thomsen, U. Hintermair, R. H. Crabtree, G. W. Brudvig, and C. A. Schmuttenmaer, *Nat. Commun.*, 2015, **6**, 6469–6478.
14. U. Hintermair, S. M. Hashmi, M. Elimelech, and R. H. Crabtree, *J. Am. Chem. Soc.*, 2012, **134**, 9785–9795.
15. J. D. Blakemore, N. D. Schley, D. Balcells, J. F. Hull, G. W. Olack, C. D. Incarvito, O. Eisenstein, G. W. Brudvig, and R. H. Crabtree, *J. Am. Chem. Soc.*, 2010, **132**, 16017–16029.
16. J. M. Koelewijn, M. Lutz, W. I. Dzik, R. J. Detz, and J. N. H. Reek, *ACS Catal.*, 2016, **6**, 3418–3427.
17. D. G. Blackmond, *Angew. Chemie - Int. Ed.*, 2005, **44**, 4302–4320.
18. J. Burés, *Angew. Chemie - Int. Ed.*, 2016, **55**, 2028–2031.
19. J. Burés, *Angew. Chemie - Int. Ed.*, 2016, **55**, 16084–16087.
20. U. Hintermair, S. W. Sheehan, A. R. Parent, D. H. Ess, D. T. Richens, P. H. Vaccaro, G. W.

Brudvig, and R. H. Crabtree, *J. Am. Chem. Soc.*, 2013, **135**, 10837–10851.

21. D. Y. Shopov, L. S. Sharninghausen, S. B. Sinha, B. Q. Mercado, D. Balcells, G. W. Brudvig, and R. H. Crabtree, *Inorg. Chem.*, 2018, **57**, 5684–5691.

22. P. Steegstra, M. Busch, I. Panas, and E. Ahlberg, *J. Phys. Chem. C*, 2013, **117**, 20975–20981.

23. M. C. Lehman, D. R. Pahls, J. M. Meredith, R. D. Sommer, D. M. Heinekey, T. R. Cundari, and E. A. Ison, *J. Am. Chem. Soc.*, 2015, **137**, 3574–3584.

24. L. S. Sharninghausen, S. B. Sinha, D. Y. Shopov, B. Choi, B. Q. Mercado, X. Roy, D. Balcells, G. W. Brudvig, and R. H. Crabtree, *J. Am. Chem. Soc.*, 2016, **138**, 15917–15926.

25. L. S. Sharninghausen, S. B. Sinha, D. Y. Shopov, B. Q. Mercado, D. Balcells, G. W. Brudvig, and R. H. Crabtree, *Angew. Chemie - Int. Ed.*, 2017, **56**, 13047–13051.

26. S. B. Sinha, D. Y. Shopov, L. S. Sharninghausen, C. J. Stein, B. Q. Mercado, D. Balcells, T. B. Pedersen, M. Reiher, G. W. Brudvig, and R. H. Crabtree, *J. Am. Chem. Soc.*, 2017, **139**, 9672–9683.

27. D. Y. Shopov, B. Rudshteyn, J. Campos, D. J. Vinyard, V. S. Batista, G. W. Brudvig, and R. H. Crabtree, *Chem. Sci.*, 2017, **8**, 1642–1652.

28. D. Y. Shopov, B. Rudshteyn, J. Campos, V. S. Batista, R. H. Crabtree, and G. W. Brudvig, *J. Am. Chem. Soc.*, 2015, **137**, 7243–7250.

29. G. Menendez Rodriguez, G. Gatto, C. Zuccaccia, and A. Macchioni, *ChemSusChem*, 2017, **10**, 4503–4509.

30. D. G. H. Hetterscheid and J. N. H. Reek, *Eur. J. Inorg. Chem.*, 2014, **4**, 742–749.

31. A. Savini, P. Belanzoni, G. Bellachioma, C. Zuccaccia, D. Zuccaccia, and A. MacChioni, *Green Chem.*, 2011, **13**, 3360–3374.

CHAPTER 4

OXIDATION OF C-H BONDS

This chapter is based on the following publication:

*Ligand Tuning in Pyridine-Alkoxide Ligated Cp*Ir^{III} Oxidation Catalysts*, E. Sackville, G. Kociok-Köhn, U. Hintermair, *Organometallics*, 2017, **36**, 3578-3588

4. Iridium Catalysed Oxidation of C-H bonds

As detailed in Chapter 1, the ubiquity of C-H bonds, and the challenges of selectively functionalising them, makes C-H oxidation an important area of research. Although developed initially for water oxidation, the highly active Cp^*Ir^{III} catalysts first reported by Crabtree and co-workers have also been shown to perform selective oxidation of C-H bonds.[1,2] The importance of the oxidatively resistant pyalk ligand becomes even more important in C-H oxidation, as IrOx NPs resulting from catalyst degradation are not able to oxidise C-H bonds, despite being active water oxidation catalysts.[3]

Thus, the C-H oxidation activity of complexes **Ir1**-**Ir7** will be described herein, focussing on the effects of ligand variation on C-H oxidation with a model substrate, the effect of a co-solvent, and the capabilities of the complexes for more challenging terpene-based compounds.

4.1 Investigations with model substrate

The oxidation of ethyl benzene sulphonate (EBS) has been successfully used by Crabtree and co-workers to investigate its C-H oxidation by **Ir1**.[2,4] The solubilising sulphonate group allows for study in aqueous solution, and the aromatic protons provided a handle for ^{1}H NMR analysis of the direct conversion to the product.[2] The reaction typically proceeds with clean and selective oxidation of the methylene group to the ketone, without aromatic oxygenation; an unwanted reaction sometimes reported for ruthenium based catalyst systems driven by $NaIO_4$.[5]

Scheme 4.1. *Oxidation of ethyl benzene sulphonate by [Ir] and $NaIO_4$*

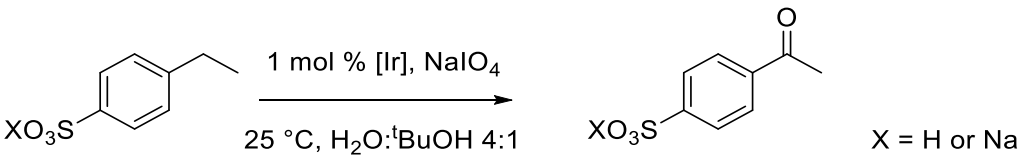

4.1.1 C-H oxidation with varying solvents

A range of oxidatively resistant, water miscible organic co-solvents were tested for their effect on the EBS oxidation reaction. The bulky R-groups, particularly for **Ir2**, **Ir3** and **Ir7**, necessitated the addition of a co-solvent to aid dissolution. Although co-solvents such as ^{t}BuOH,[1] acetonitrile (MeCN)[6] and hexafluoroisopropanol (HFIP)[2] have been used for investigation of C-H oxidation reactions with various Cp*Ir^{III} complexes, a direct comparison has not been made. Additionally, most real-world organic substrates are unlikely to be as water soluble as the ionic model compound. A comparison of the C-H oxidation reaction profile for EBS oxidation with **Ir1** with a range of co-solvents is seen in Figure 4.1.

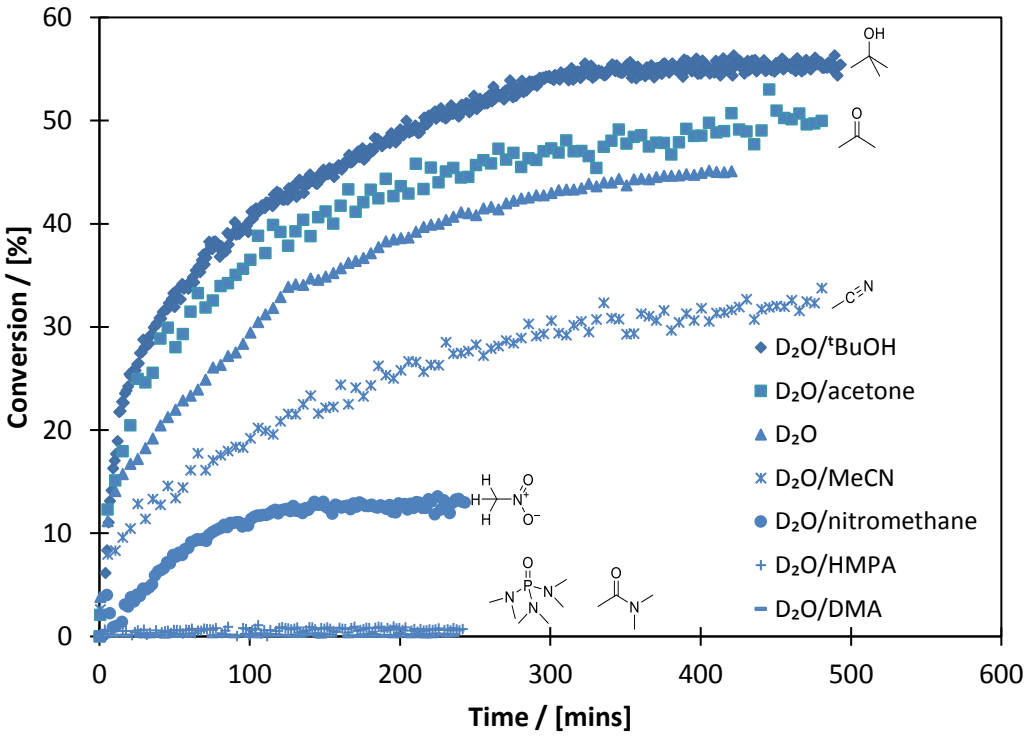

Figure 4.1. *The effect of cosolvent on oxidation of EBS. ^{1}H NMR time course of the oxidation of EBS with* ***Ir1*** *at 0.04 mmol EBS, 0.2 mmol $NaIO_4$, 0.2 µmol, 1 mol % [Ir] at pH 7, 25 °C in 4:1 D_2O/cosolvent mixtures*

Kinetic analysis indicated although the initial rates were similar for ^{t}BuOH/D_2O, acetone/D_2O and pure D_2O, the addition of ^{t}BuOH and acetone improved the overall C-H conversion compared to pure D_2O. The addition of nitrogen containing co-solvents appeared to reduce both the initial rate and the conversion of EBS. Two of the solvents tested (hexamethylphosphoramide (HMPA) and dimethylacetamide (DMA)) showed no C-H conversion at all. Analysis of the NMR data showed additional peaks suggesting that the

solvents themselves were oxidised under the reactions conditions.[7] The solvent trends observed could be due to the effects on the active catalytic species or due to changing potential of the chemical oxidant.[8] Given the enhanced conversion of C-H product with 20% ^{t}BuOH, this solvent system was used for all subsequent investigations of EBS oxidation.

4.1.2 C-H oxidation with varying pH

Investigation into the effect of pH on the reaction was briefly conducted by taking aliquots of reactions at different pH values. ^{1}H NMR analysis showed that highest C-H conversions were seen at neutral pH, with very low conversions under acidic and basic conditions (Figure 4.2)

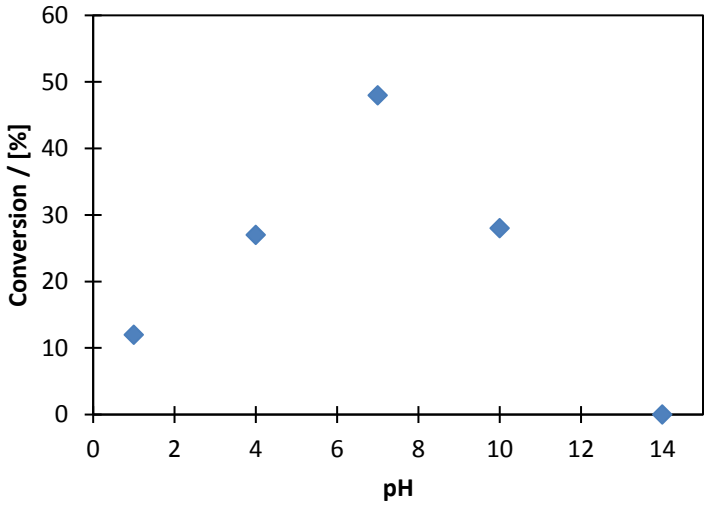

Figure 4.2. *The effect of pH on oxidation of EBS with compound* ***Ir1*** *at 0.04 mmol EBS, 0.2 mmol $NaIO_4$, 0.2 µmol, 1 mol % [Ir] at pH 7, 25 °C in 4:1 D_2O/ ^{t}BuOH solvent mixture for 10 min*

The strong correlation between the C-H conversion date and the water oxidation rates at varying pH (Chapter 3) suggests that the pH dependence is due to the stability of the oxidant as previously described[9], rather than any inherent functionality of the catalyst.

4.2 C-H oxidation kinetics with iridium complexes

With suitable conditions established, complexes **Ir1** – **Ir7** were evaluated for their C-H oxidative ability using the model substrate EBS and comparing the reaction profiles through the use of *in situ* ^{1}H NMR data (Figure 4.3).

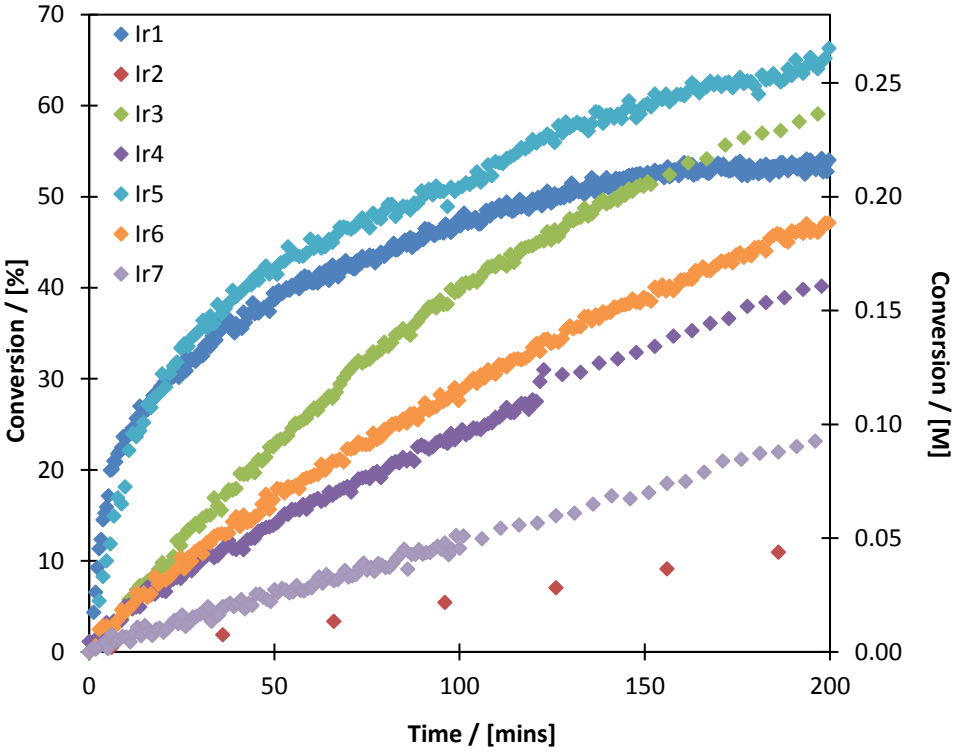

Figure 4.3. *Initial ^{1}H NMR time course data of the oxidation of EBS (Scheme 4.1) with complexes **Ir1**-7 at 40 mM EBS, 200 mM $NaIO_4$, 0.4 mM (1 mol%) [Ir] at pH 7, 25 °C in 4:1 H_2O/ ^{t}BuOH.*

In the absence of iridium, no conversion was observed, but all catalysts were active for the oxidation of EBS under these conditions with 100% selectivity to the para-sulphonated acetophenone product. However, complexes **Ir1**-**Ir7** varied greatly in terms of both the initial rates and the final C-H conversions. Table 4.1 summarises key performance data under the conditions applied.

Dimethyl complexes **Ir1** and **Ir5** showed the fastest initial rates by far (1.61 mM min^{-1} and 0.99 mM min^{-1} respectively); approximately an order of magnitude greater than the next fastest complex **Ir3** (0.19 mM min^{-1}). By contrast, and as seen with the water oxidation data, the diphenyl complexes **Ir2** and **Ir7** were the slowest, again by an order of magnitude (0.03 mM min^{-1} and 0.05 mM min^{-1} respectively).

When the full reaction profile is considered, it can be seen that the reaction conversions plateaued at different levels for the different complexes (Figure 4.4), despite the use of a 5-fold excess of oxidant over substrate in all cases.

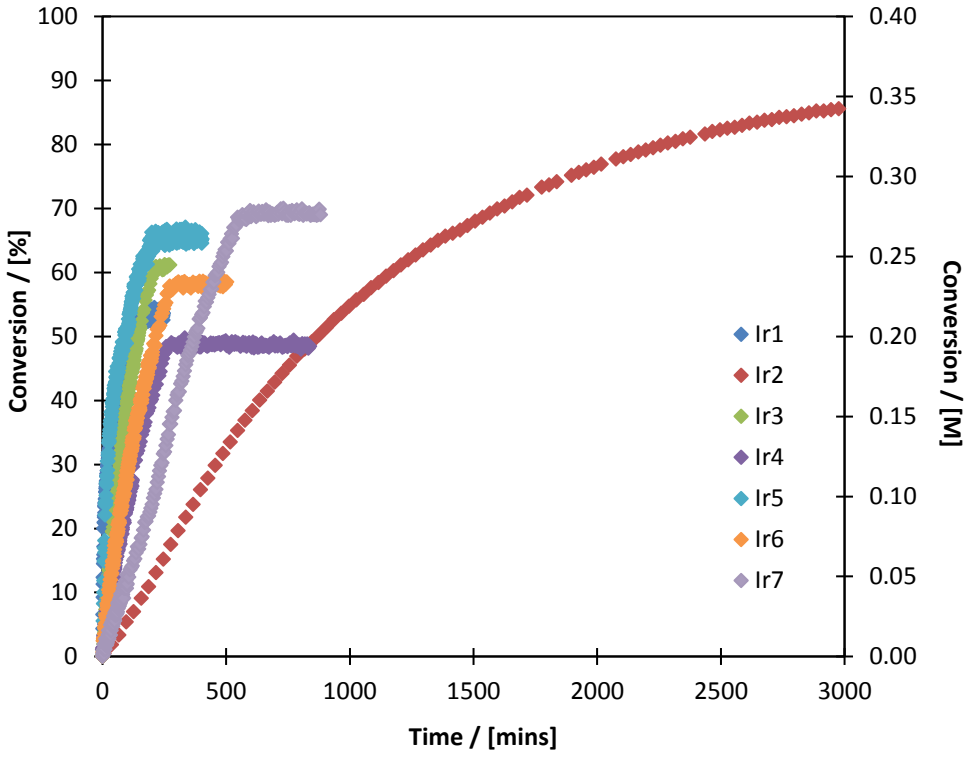

Figure 4.4. *Full ^{1}H NMR time course data of the oxidation of EBS (Scheme 4.2) with* ***Ir1****-****Ir7*** *at 40 mM EBS, 200 mM $NaIO_4$, 0.4 mM (1 mol%) [Ir] at pH 7, 25 °C in 4:1 H_2O/ ^{t}BuOH.*

Despite being the slowest to perform the C-H oxidation reaction, **Ir2** gave the highest conversion plateau, reaching almost 90% conversion of C-H substrate over 60 hours. The other diphenyl complex **Ir7** gave the next highest conversion plateau (70%) and was the second slowest both in terms of initial rate, and the time take to reach the plateau (9 hours). It would therefore be tempting to correlate C-H conversion with rate, but the fast complex **Ir5** gave a relatively high conversion of ~70%, and the lowest conversion plateau was seen for **Ir4** which had one of the slower middling rates. Numerical values for the initial rates and the corresponding plateau conversions can be seen in Table 4.2.

***Table 4.1**. Initial rates, final conversion values and time taken to final conversion of the reaction profiles shown.*

Complex	Initial k_{obs} / mM min^{-1} [a]	TOF / $hour^{-1}$ [b]	Conversion plateau [c]	Time to reach plateau / hour
Ir1	1.61	242	55%	2.6
Ir2	0.03	4	88%	60
Ir3	0.19	29	65%	3.3
Ir4	0.13	20	52%	4.3
Ir5	0.99	149	68%	3.2
Ir6	0.14	21	60%	4.5
Ir7	0.05	8	70%	9.0

[a] calculated from initial gradient of product concentration over time
[b] initial reaction rate divided by catalyst concentration
[c] averaged value over plateau

To test whether catalyst deactivation was responsible for the limited conversion values, a second portion of oxidant was added to a catalytic run with **Ir5** after conversion had stalled at 3.5 hours (Figure 4.5).

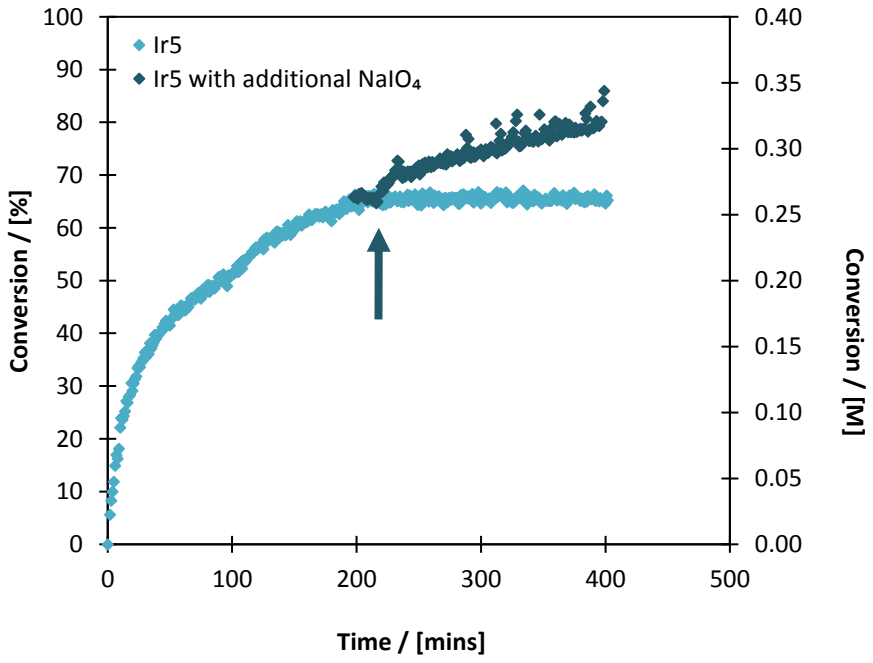

***Figure 4.5.** ^{1}H NMR time course of the oxidation of EBS (Scheme 4.2) with complex **Ir5** with a second addition of $NaIO_4$ at 40 mM EBS, 200 mM $NaIO_4$ (initial), 0.4 mM (1 mol%) [Ir] at pH 7, 25 °C in 4:1 H_2O/ ^{t}BuOH.*

After the re-addition of oxidant, catalysis immediately resumed with a stable rate, accurately extrapolating the initial reaction profile, proving that the catalyst remained active. The varying conversion plateaus seen for **Ir1**-**Ir7** are therefore ascribed to the consumption of oxidant by the concurrent water oxidation reaction, which cannot be observed by NMR. These different C-H oxidation plateaus are thus indicative of the individual C-H vs. O-H oxidation selectivity (i.e. a branching ratio).

With such a clear definition between complexes in the branching ratios of water and C-H oxidation, it appears that the N^O ligand has a direct impact, such that there is scope for molecular control based purely on ligand design.

4.2.1 Investigation of water oxidation in the presence of C-H substrate

In order to attempt to correlate the water oxidation activity with the C-H oxidation kinetics, oxygen evolution experiments, as described in Chapter 3, were undertaken in the presence of EBS, under the same reaction conditions (Figure 4.6).

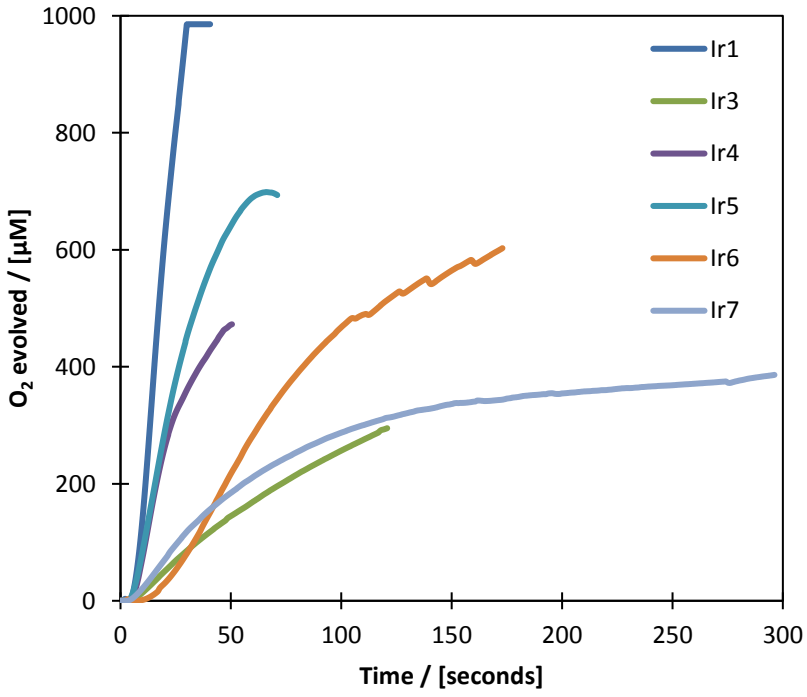

Figure 4.6. *Oxygen evolution traces of the complexes **Ir1** and **Ir3**-**Ir7** during C-H oxidation catalysis at 40 mM EBS, 200 mM $NaIO_4$, 0.4 mM (1 mol%) [Ir] at pH 7, 25 °C in 4:1 H_2O/ ^tBuOH using a calibrated Clark electrode.*

***Table 4.2**. Activation times and initial rates of the O_2 evolution profiles shown in Figure 4.6*

Complex	Initial k_{obs} CH / mM min^{-1} [a]	Conversion plateau	Initial k_{obs} WO with EBS/ mM min^{-1} [b]	Catalyst TOF for WO with EBS / hour^{-1}[c]
Ir1	1.61	55%	2.98	448
Ir2	0.03	88%	0	0
Ir3	0.19	65%	0.21	32
Ir4	0.13	52%	0.89	134
Ir5	0.99	68%	1.26	188
Ir6	0.14	60%	0.25	38
Ir7	0.05	70%	0.28	43

[a] calculated from initial gradient of product concentration over time

[b] calculated from initial gradient of product concentration over time (average from triplicates)

[c] initial reaction rate divided by catalyst concentration

Complexes **Ir1** and **Ir3**-**Ir7** evolved oxygen in the presence of C-H substrate. As observed previously with for water oxidation without EBS, the relative order of catalyst activity for the pyridine alkoxide complexes decreased **Ir1** > **Ir4** > **Ir6** > **Ir3**. However, absolute comparison to the previous water oxidation data cannot be made due to differences in catalyst and oxidant concentration.

As seen in Table 4.2, the initial rates of water and C-H oxidation were of the same order of magnitude, but the timescale of the EBS oxidation was much longer than that of the water oxidation. The higher excess of water compared to EBS suggests that the water oxidation reaction occurs before EBS oxidation, even though water is thermodynamically more challenging as a substrate. Thus, water is only oxidised in the early stages of the reaction where there is still plentiful oxidant and therefore a high solution potential. Once oxidant concentration has depleted sufficiently, EBS oxidation can start to occur and compete with the water oxidation reaction.

A plot of initial rate of O_2 evolution against C-H oxidation efficiency (as determined by the plateau conversion) (Figure 4.7), shows that the competition between these reactions is a function of the oxidising power of the catalysts. Thus, the electron withdrawing aryl substituent in **Ir2** makes for a less oxidising catalyst which slowly oxidises the EBS substrate.

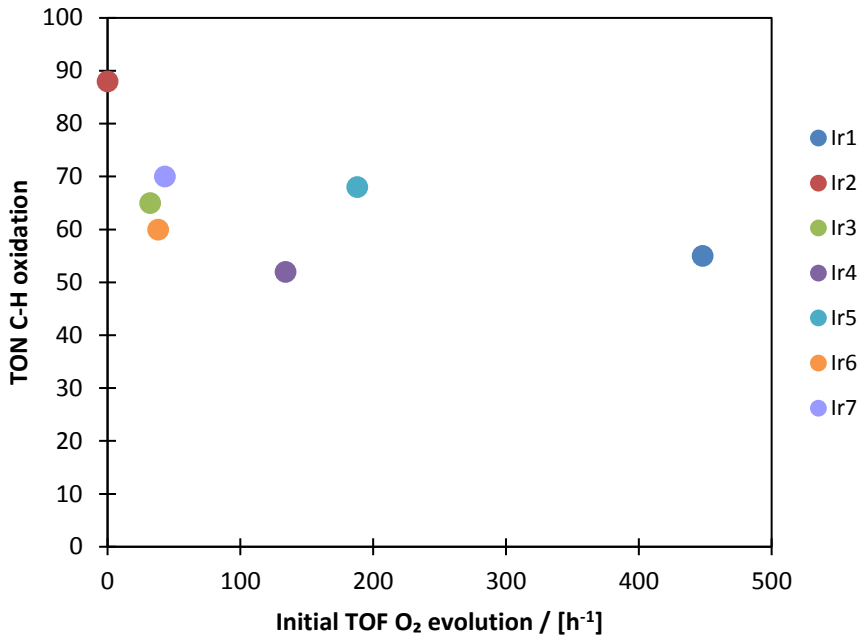

Figure 4.7. *Correlation of initial O_2 evolution rates with final EBS oxidation yields catalysed by **Ir1**-**Ir7** (40 mM EBS, 200 mM $NaIO_4$, 0.4 mM (1 mol%) [Ir] at pH 7, 25 °C in 4:1 H_2O/ ^tBuOH.*[10]

Despite there being no clear link between the varying catalysts when analysed this way, comparing the ligand sets does show some interesting trends.

1. Extending the pyridine ring to a quinoline increases the C-H selectivity with alkyl substituents (**Ir1** vs **Ir5**) but decreases it with aryl substituents (**Ir2** vs **Ir7**)
2. Increasing the bulk of the alkoxide ligand decreases the rate of water oxidation and slightly increases the C-H selectivity (**Ir1** → **Ir4**, **Ir6** and **Ir3**)
3. Changing the alkyl groups to aryls (**Ir1** → **Ir2**) substantially decreases the rate of water oxidation but greatly increases the selectivity towards C-H oxidation.

4.2.2 Water oxidation in the presence of C-H substrate for Ir2

Notably absent from Figure 4.6, is the water oxidation competition trace for **Ir2**. This is due to the fact that on the time scale of the experiment (<8 min), **Ir2** evolved no oxygen. In actual fact, as seen below, **Ir2** *consumes* oxygen during the competition reaction with EBS. This is highly interesting in conjunction with the previous data (Figure 4.4) in which **Ir2** showed the highest conversion of EBS.

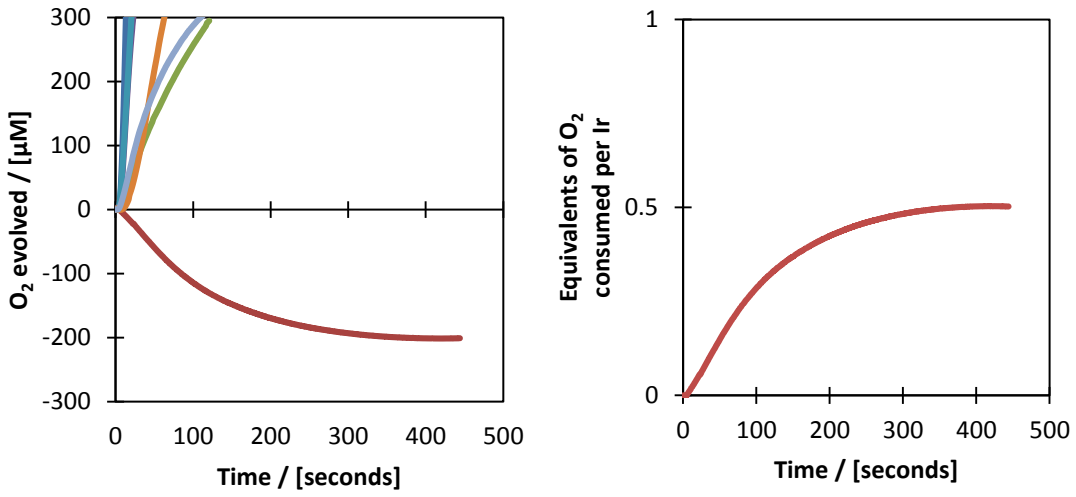

Figure 4.8a) *Oxygen evolution traces of the complexes* ***Ir1****-****Ir7*** *during C-H oxidation catalysis at 40 mM EBS, 200 mM $NaIO_4$, 0.4 mM (1 mol%) [Ir] at pH 7, 25 °C in 4:1 H_2O/ ^tBuOH using a calibrated Clark electrode showing oxygen consumption by* ***Ir2*** *b) the consumed oxygen plotted against equivalents of* ***Ir2***

In the first instance, it was suggested that the reason for this oxygen consumption was due to **Ir2** performing C-H oxidation aerobically. However, the oxygen consumption plateaus after approximately 6 minutes; if catalytic aerobic oxidation was occurring, the consumption of oxygen would increase with increasing C-H oxidation. Furthermore, a plot of O_2 consumed against [Ir] revealed that 0.5 O_2 molecules are consumed per iridium metal, i.e. one oxygen per [Ir]. The different time scales for the reactions mean that corresponding C-H oxidation data for this oxygen consumption phase cannot be correlated (the first C-H oxidation data point was collected at 6 minutes). Similar induction phases were also seen for **Ir2** during water oxidation (Figure 3.4 and Figure 3.6). The observed oxygen consumption is therefore attributed to catalyst activation, not aerobic C-H oxidation.

Nevertheless, none of the other complexes display such a pronounced induction period, and **Ir2** does not show a sharp plateau for C-H oxidation; water oxidation is completely suppressed in the presence of a C-H substrate. The oxidant is also unlikely to remain stable in solution for the longer reaction time of EBS oxidation with **Ir2**. Clearly, further work in to the mechanism of **Ir2** C-H oxidation is warranted, and investigations into the effect of performing the reaction with and without oxygen would be beneficial.

4.2.3. Effect of butanol on C-H oxidation

It was noted in Chapter 2 that activation of **Ir2** with $NaIO_4$ revealed an additional absorbance at 480 nm in the UV-vis spectrum of the activated complex. Given the high selectivity of **Ir2** for C-H oxidation, it was postulated that the species responsible for the absorption at 480 nm was also responsible for the C-H oxidation activity of **Ir2**.

An observation that the water oxidation reaction with **Ir2** yielded a blue solution, but the C-H oxidation reaction resulted in a pale pink solution, occasioned in a re-investigation into the effect of ^{t}BuOH on the activation of **Ir2**. The effect of ^{t}BuOH on activation had been shown to be negligible for **Ir1** (Appendix, Figure A2.5), but the activation of **Ir2** was repeated in 100% H_2O and compared to the activation in a 20% ^{t}BuOH co-solvent mixture (Figure 4.9).

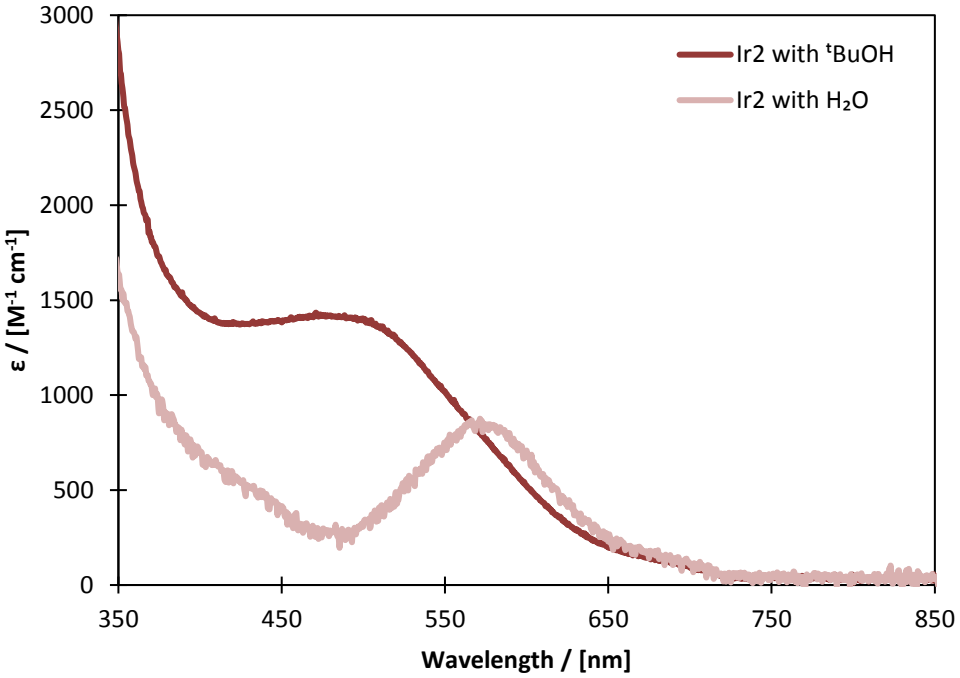

Figure 4.9. *Comparison of the UV-vis traces of* ***Ir2*** *(0.5 mM) activated with $NaIO_4$ (25 mM) after 1 hour with (dark red) and without (pale red) 20% ^{t}BuOH at room temperature*

After one hour, the UV-vis spectrum of the activation **Ir2** in the presence of ^{t}BuOH shows an absorption at 493 nm, but in 100% H_2O the main absorption is at 574 nm. As with the previously detailed UV-vis experiments, the 574 nm absorption is attributed to an $d(Ir^{IV})\pi^*$ transition corresponding to a dimeric bridging μ- oxo species, but interestingly in the presence of 20% ^{t}BuOH, the predominant peak of the activated form of **Ir2** is now the absorption at 493 nm.

As previously described in Chapter 3 (Section 3.5.3), when detailed spectroscopic analysis was undertaken into the activated form of **Ir1**, computational modelling was performed to predict UV-vis spectra. The dimeric Ir^{IV} species was predicted to have an absorbance of 580 nm due to Ir^{IV}-O-Ir^{IV}, and a mononuclear Ir^{IV}-oxo species was shown to have a main absorbance at 334 nm. The group also reported the key absorbances from a Ir^{IV}-OH species, which was proposed to have formed from hydrolytic cleavage of the bis-μ-oxo dimer (Figure 4.10 reproduced from Hintermair *et al*[4]). The major contribution to the modelled UV-vis spectrum from this species was an absorption at 488 nm. The varying species and their modelled absorbances are shown in Figure 4.10.

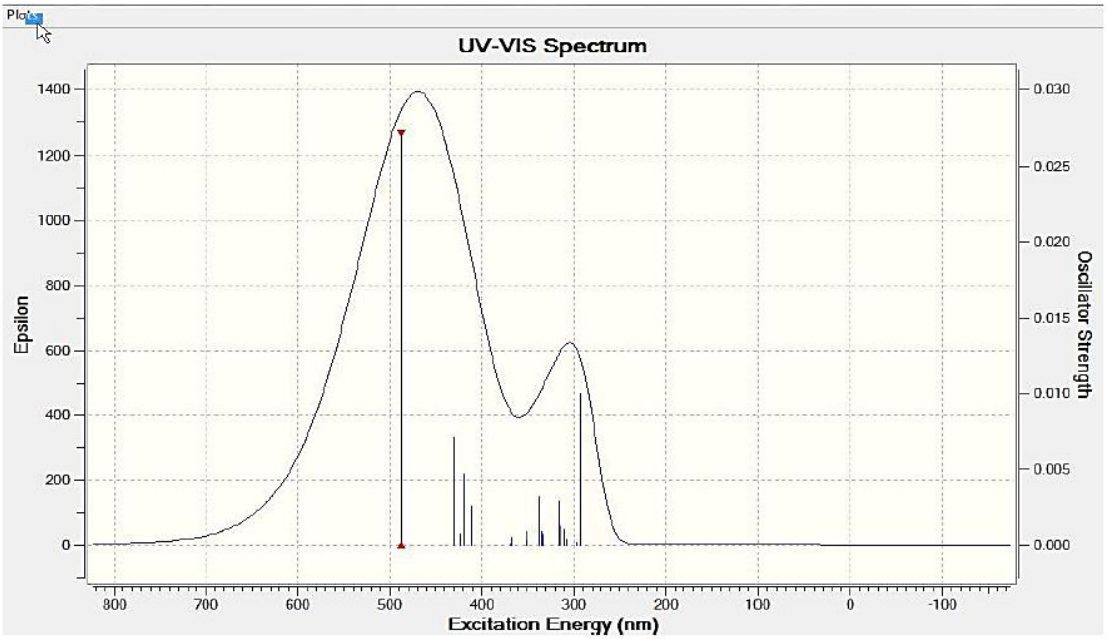

***Figure 4.10**. A modelled UV-vis spectrum of a monomeric Ir^{IV}-OH species. Reproduced from supporting information from Hintermair et al 2013*[4]

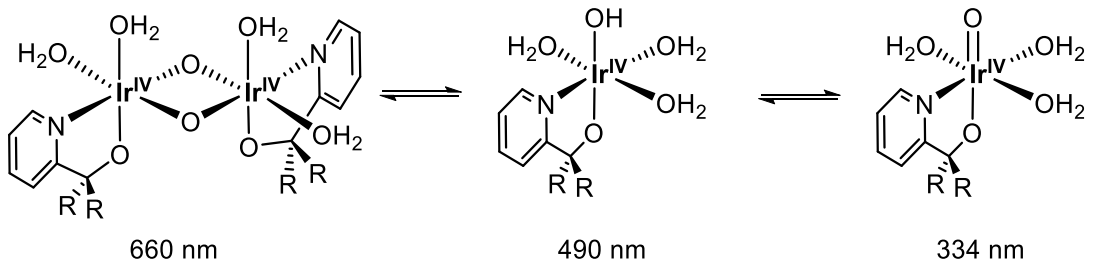

***Figure 4.11.** Possible dimeric and monomeric Ir^{IV} species with the main UV-vis absorbances as modelled by Hintermair et al*[4]

The observed absorption at 493 nm in the spectrum of **Ir2** when activated in the presence of ^{t}BuOH can therefore be assigned to a monomeric Ir^{IV}-OR species, where OR is $O^{t}Bu^{-}$ (Scheme 4.2). It is proposed that this species could be accessed either by hydrolytic cleavage of the bis-μ-oxo dimer (route A), or during catalyst activation (route B).

Scheme 4.2. *A proposed alternative catalyst activation pathway where ^{t}BuOH blocks a hydroxyl site on the active dimeric species*

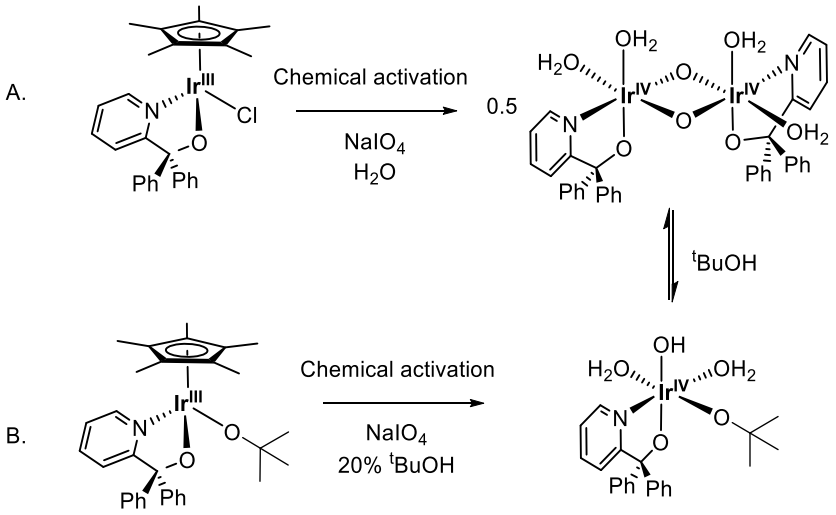

Given the UV-vis spectra for **Ir2** activated in the presence of 20% ^{t}BuOH, and the corresponding high C-H oxidation ability, it is further proposed that the monomeric Ir^{IV}-OR species is responsible for C-H oxidation (Figure 4.12).

Figure 4.12. *Proposed delineation between a dimeric water oxidation catalyst and a monomeric Ir^{IV}-OR C-H oxidation catalyst*

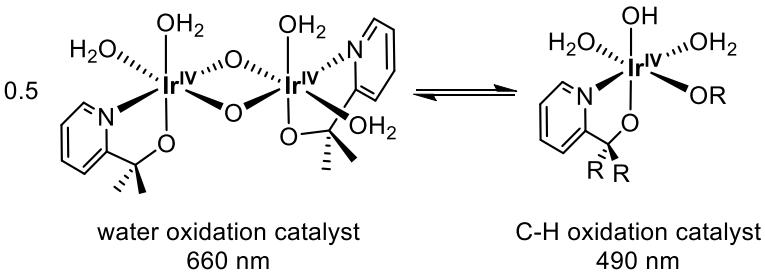

The enhanced C-H oxidative ability of **Ir2** can therefore be explained by the proposed equilibrium. For **Ir2** which exists as the monomeric Ir^{IV}-OR when activated in 20% ^{t}BuOH (UV-vis spectrum Figure 4.10), no water oxidation is observed at all in the presence of C-H substrate. It is suggested that the electron withdrawing phenyl groups promote binding of the $^{t}BuO^{-}$ ligand.

It is interesting to note that in the absence of ^{t}BuOH, the UV-vis of **Ir2** has an absorption band of 583 nm, assigned to the Ir-O-Ir dimer. Without ^{t}BuOH or C-H substrate, **Ir2** performs water oxidation, albeit at a slow rate, presumably due to exclusive formation of the active water oxidation dimer (Figure 3.4). In the presence of ^{t}BuOH *and* C-H substrate, no water oxidation is observed at all (Figure 4.8), due to the predominance of the O^{t}Bu monomeric species.

Complex **Ir7** also gave very high C-H conversions with EBS (70%). It was proposed in Chapter 3 that **Ir7** does not form a dimeric Ir^{IV} species but rather forms a monomeric Ir^{IV}=O complex as the active catalyst (small absorbance in UV-vis for Ir^{IV}-O-Ir^{IV} (Figure 3.16); the order in iridium for **Ir7** was 0.9 for water oxidation by VTNA (Figure 3.16). The high C-H conversion observed with **Ir7** is consistent with this theory; the already monomeric **Ir7** can perform both water and C-H oxidation, but lack of the highly active dimeric species leads to slower rates of water oxidation and an enhanced selectivity for C-H oxidation.

An active Ir^{IV}-OR monomer as the C-H oxidation catalyst also explains the solvent data trends previously observed in Section 4.2.1 and Section 3.2. Enhanced C-H oxidation selectivity with **Ir1** was observed for ^{t}BuOH compared to 100% D_2O (55% conversion with 20% ^{t}BuOH, 45% conversion in 100% D_2O). The presence of ^{t}BuOH promotes the formation of the Ir^{IV}-OR thus enhancing the C-H oxidation selectivity. In Chapter 3 (Figure 3.2 Table 3.2) it was also observed that the rate of water oxidation was reduced for **Ir1**-**Ir6** with the addition of 20% ^{t}BuOH. If the presence of ^{t}BuOH reduces the amount of the active water oxidation dimer, then the rates of water oxidation are also concurrently lower. By contrast, **Ir7**, which is proposed to perform water oxidation with a monomeric Ir^{IV}=O complex, does not show a decrease in rate of water oxidation with the addition of 20% ^{t}BuOH.

***Table 4.3**. Comparison of rates for C-H and water oxidation with and without 20% ^{t}BuOH co-solvent*

Water Oxidation		**C-H Oxidation**	
k_{obs} with 100% H_2O	k_{obs} with 20% ^{t}BuOH	k_{obs} with 100% H_2O	k_{obs} with 20% ^{t}BuOH
46 min^{-1}	12.6 min^{-1}	14.7 min^{-1} (45% conv.)	1.72 min^{-1} (55% conv.)

4.2.4. C-H oxidation with pre-activated Ir

The EBS reaction profile was also collected for preactivated **Ir1*-Ir7*** where the complexes were reacted with 50 equivalents of oxidant in 100% H_2O and stirred for 12 hours at room temperature. This activated catalyst solution was then added to the EBS/$NaIO_4$ reaction mixture and monitored by ^1H NMR (Figure 4.13, Table 4.4).

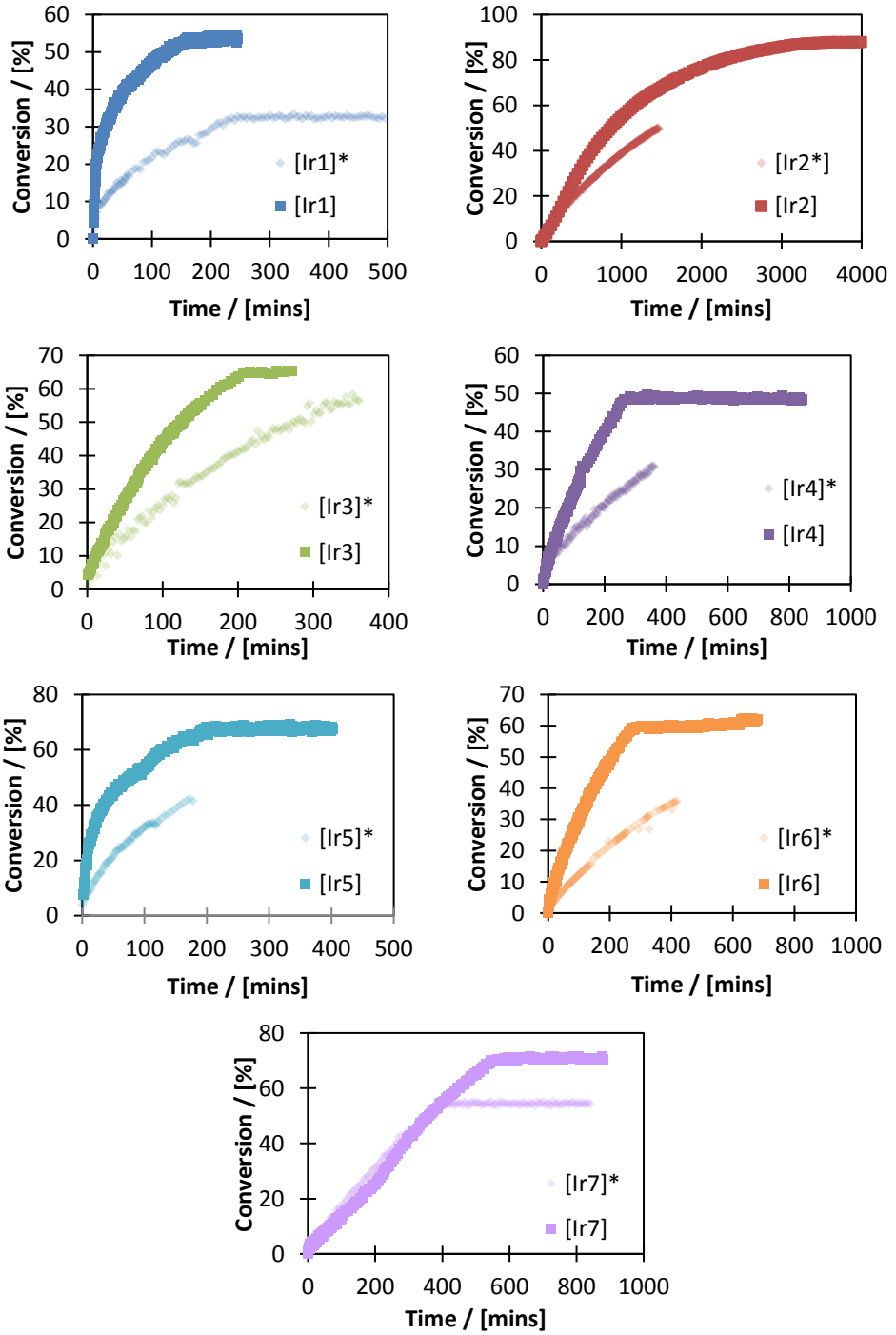

Figure 4.13. *Full ^1H NMR time course data of the oxidation of EBS with preactivated complexes **Ir1-Ir7** at 40 mM EBS, 200 mM $NaIO_4$, 0.4 mM (1 mol%) [Ir] at pH 7, 25 °C in 4:1 H_2O/^{t}BuOH.*

Table 4.4. *Observed initial rates with C-H oxidation of EBS with complexes **Ir1**-**Ir7** with and without preactivation of the Ir complex*

Complex	Initial k_{obs} with Cp* complex / mM min^{-1}[a]	Initial k_{obs} with preactivated Ir / mM min^{-1}[a]
Ir1	16.1	4.23
Ir2	0.03	0.02
Ir3	0.19	0.11
Ir4	0.13	0.12
Ir5	0.99	0.17
Ir6	0.14	0.06
Ir7	0.05	0.06

[a] calculated from initial gradient of product concentration over time

For complexes **Ir1**-**Ir6**, the rate of C-H oxidation with the preactivated catalyst was slower than with the Cp* complex. Although plateau conversions were not reached for all complexes, the plateau conversion for **Ir1** and **Ir7** was lower with the preactivated complex than with the Cp* complex (32% vs 52% conversion for **Ir1**; 54% vs 71% conversion for **Ir7**). No reduction in C-H oxidation rate was observed with **Ir7**.

In the paper reported last year by Huang *et al*, a similar experiment was performed with **Ir1**, in which the C-H oxidation rates were reported with and without preactivation (procedure B and A respectively, Figure 4.14).

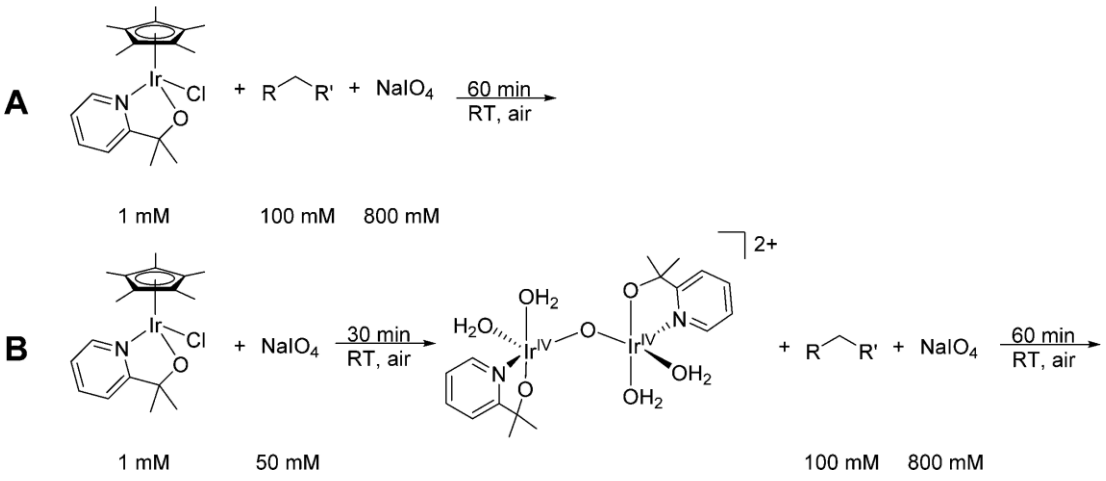

Figure 4.14. *The two varying reaction procedures for C-H oxidation by **Ir1**. Reproduced from Huang et al 2017*[6]

The group reported a decrease in yield of EBS product when using protocol B, where the Ir complex was added after preactivation. Interestingly, they also noted an absorbance by UV-vis spectroscopy of 485 nm for **Ir1** during C-H oxidation, and from here assigned the active C-H oxidation catalyst to be a monomeric Ir^{IV} species, where the Cp* ligand is retained, but the labile chloro ligand is substituted for an oxygen containing ligand (Figure 4.15).[6]

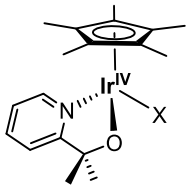

where X = H_2O, ^-OH, IO_3^-, acetate

Figure 4.15. *Cp* mononuclear species proposed to be the active C-H oxidation catalyst*[6]

Although the results reported show a similar reduction in yield of C-H product with preactivated **Ir1**, the conclusion of an active species with the Cp* ligand retained seems implausible given the groups previously described data of activation of **Ir1**. The ^1H NMR data for activation of **Ir1** shows loss of the Cp* ligand (reported here in Section 2.5 and in earlier work[4,11,12]).

One alternative suggestion is that the lower C-H conversion with preactivated [Ir] is due to the monomer/dimer equilibrium described above. When the complexes are preactivated without the presence of C-H substrate, the dimeric Ir-O-Ir species is formed, and thus the rate of C-H oxidation is slower because the dimer must convert to the monomer to perform C-H oxidation. This is also consistent with the result that **Ir7** performs C-H oxidation at the same rate regardless of whether an activation step is included. In Chapter 3 it was proposed that **Ir7** already activates to a monomeric species and thus conversion is not required.

4.2.5 Kinetic isotope effects for C-H oxidation

A brief investigation into the solvent effects between H_2O and D_2O (with 20% ^tBuOH as a co-solvent) was conducted for complexes **Ir1**, **Ir2** and **Ir5** (Figure 4.16). A sub-set of catalysts was selected as they were considered to be representative of the varying ligands.

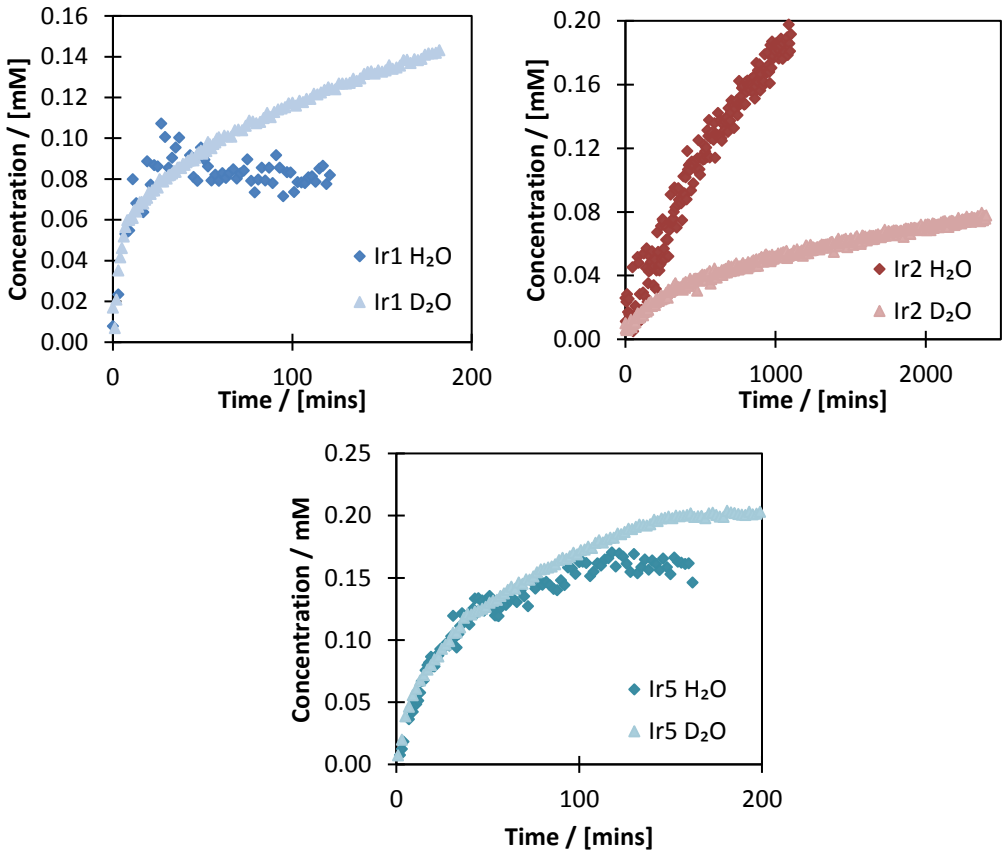

Figure 4.16. *Full ^1H NMR time course data of the oxidation of EBS with activated complexes **Ir1**, **Ir2** and **Ir5** at 40 mM EBS, 200 mM $NaIO_4$, 0.4 mM (1 mol%) [Ir] at pH 7, 25 °C in 4:1 $D_2O/^tBuOH$ (pale) compared to 4:1 $H_2O/^tBuOH$.*

Table 4.5. *Comparison of initial rates of* C-H oxidation *in $D_2O/^tBuOH$ 4:1 and $H_2O/^tBuOH$ 4:1 and subsequent solvent KIE*

	k_{obs} in D_2O / mM min^{-1}[a]	k_{obs} in H_2O / mM min^{-1}[a]	Solvent KIE[b]
Ir1	4.0×10^{-3}	3.4×10^{-3}	0.9
Ir2	7.9×10^{-5}	16.5×10^{-5}	2.1
Ir5	5.1×10^{-3}	4.5×10^{-3}	0.9

[a] calculated from initial gradient of product concentration over time
[b] KIE calculated from k_{obs} in D_2O / k_{obs} in H_2O

Noticeably, **Ir1** and **Ir5** showed no H/D solvent dependence in initial rate, with a KIE value of 0.9 reported for both complexes. **Ir2**, however, showed a KIE of 2.1, with the oxidation of EBS proceeding at twice the rate in H_2O as D_2O. This could be attributed to a primary KIE, where breaking of an O-H bond is involved in the RDS of EBS catalysed by **Ir2**. By contrast, the KIE value of 0.9 for **Ir1** and **Ir5** indicates that O-H bond cleavage is not involved in the RDS. If the KIE for **Ir2** is a primary KIE, it could be proposed that the RDS is deprotonation of the monomeric Ir^{IV}-OH species to an active Ir^{V}=O species (Figure 4.17). By contrast the RDS for **Ir1** and **Ir5** would be the C-H oxidation.

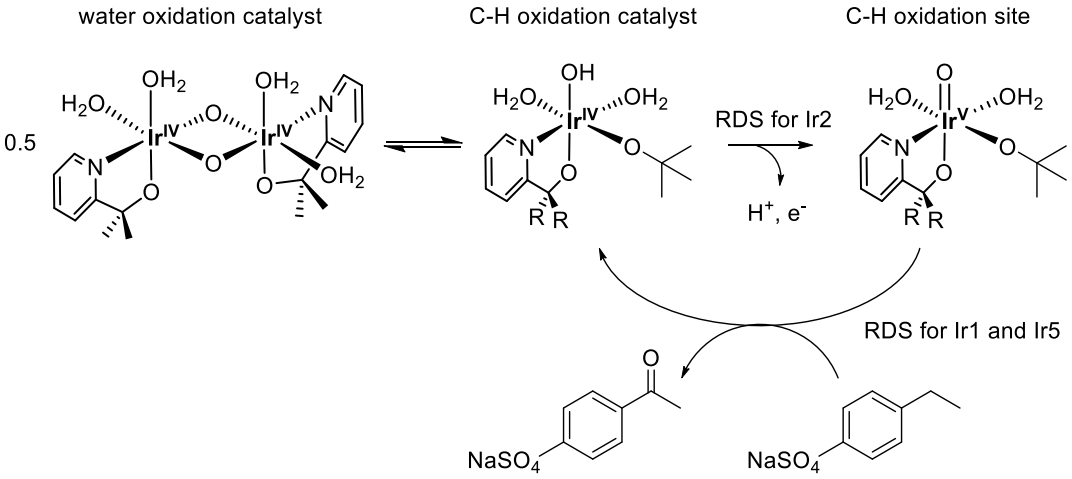

Figure 4.17. *Proposed differences in RDS for **Ir1** and **Ir5**, and **Ir2** based on the H/D KIE data for C-H oxidation performed in H_2O or D_2O.*

Prior investigations into the KIE of ethyl benzene oxidised by [Cp*Ir(bypy)Cl] and CAN by Zhou *et al* determined a large KIE of 15.4 ± 0.8 and attributed the RDS to the oxidation of ethyl benzene to phenyl alcohol.[13] The higher KIE observed for **Ir2** could therefore also be due to solvent effects, and further H/D experiments with deuterated EBS would be required to fully determine whether the variations in RDS proposed in Figure 4.17 are correct.

4.3 Terpene oxidation

With successful data from the model substrate EBS for precatalyst **Ir1**-**Ir7**, the substrate scope was expanded to terpene-based compounds. Terpenes and terpene type structures are secondary metabolites found in plants bearing an isoprene (C_5H_8) unit. The ubiquity and relative cheapness of common terpenes such as limonene and pinene means that they are attractive alternative feedstock chemicals in place of fossil fuel derived compounds, but selectively functionalising them can be challenging due to the multiple potential sites for reactivity.[14]

4.3.1 Eucalyptol oxidation

The complexes were subsequently tested for the selective oxidation of eucalyptol, a terpene derived (and therefore biorenewable) feedstock. Eucalyptol was chosen in the first instance as it contains multiple oxidisable C-H bonds, and there was the potential for the varying ligand bulk to affect the selectivity of the catalyst.

Scheme 4.3. *Oxidation of eucalyptol by [Ir] and $NaIO_4$*

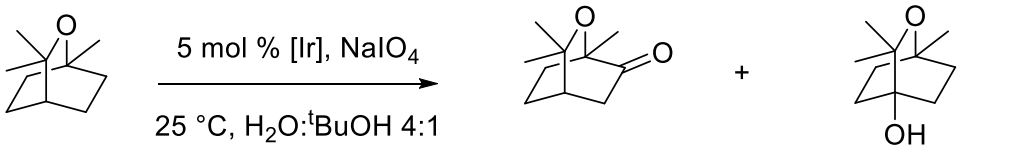

Methylene oxidation product

Methine oxidation product

Despite the higher reactivity of the tertiary methine bond, all reactions yielded the methylene oxidation product regardless of the complex used. This is believed in part to be due to the inherent sterics of the substrate itself, where the more reactive tertiary site is too hindered for facile oxidation.[15]

The product distribution was determined by gas chromatography mass spectrometry (GC-MS), as analysis by ^{1}H NMR spectroscopy proved an impractical tool due to lack of distinct product peaks. Although GC-MS is highly sensitive and a suitable technique for mixtures of similar compounds, structural information is entirely absent from the analysis. Thus, despite knowing that the ketone product was the major one, the exact position of the double bond is not determinable by GC-MS. Purification of the product by column chromatography and

analysis by NMR showed the oxidation product exclusively as shown in Scheme 4.3 (Appendix Figure A4.1)

After 2 hours, the conversions profiles were similar for all complexes, although there was some variation similar to pattern observed with the initial C-H oxidation reaction rates seen with EBS. Complexes **Ir2** and **Ir7** show the lowest conversion after 2 hours, whilst dimethyl and cyclohexyl complexes have the highest conversion. After 120 hours, the two diphenyl complexes obtained the highest conversions.

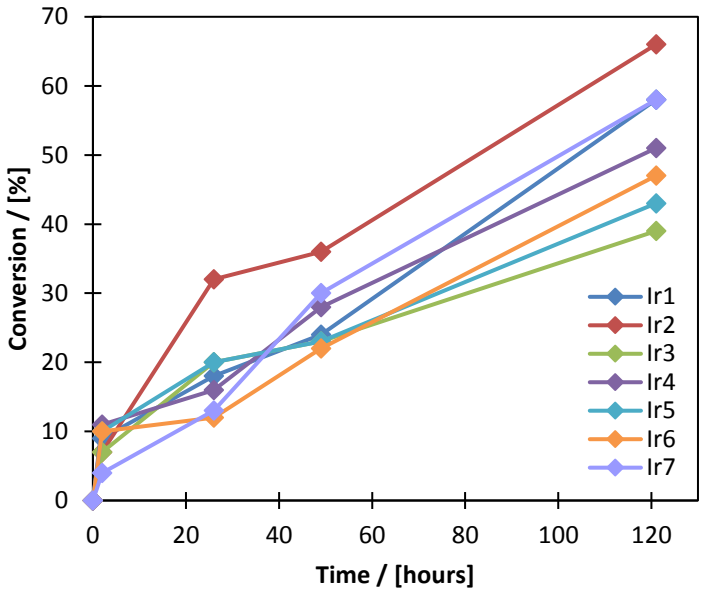

Figure 4.18. *Graphical representation of data in Table 4.6 of eucalyptol oxidation by* ***Ir1****-****Ir7*** *at 5 mol % [Ir], 20 mmol substrate, 400 mmol $NaIO_4$ at 25 °C in a 4:1 H_2O/^tBuOH mixture at native pH. Lines are drawn to guide the eye.*

Table 4.6. *Oxidation of eucalyptol with [Ir] complexes*

Precatalyst	Conversion 2 hours	Conversion 26 hours	Conversion 49 hours	Conversion 121 hours
Ir1	9%	18%	24%	58%
Ir2	7%	32%	36%	66%
Ir3	7%	20%	23%	39%
Ir4	11%	16%	28%	51%
Ir5	10%	20%	23%	43%
Ir6	10%	12%	22%	47%
Ir7	4%	14%	30%	58%

Conversion calculated by GC-MS by peak area integration extrapolated from eucalyptol calibration based on material recovered in a catalyst free control sample

Eucalyptol is a more challenging substrate to oxidise than EBS and different experimental conditions were used. However, diphenyl complex **Ir2** still gave the highest overall conversion after 5 days. A similar pattern was observed for **Ir7**. Although the patterns seen for EBS oxidation were not entirely replicated in the eucalyptol reactions, the oxidative ability of these catalysts is seen in the relatively high conversions of selectively oxidising a challenging bio-renewable substrate in water at room temperature.

4.3.2 Additional terpene substrates

In order to further expand the scope of the C-H oxidation reaction for the complexes, additional terpene substrates were investigated: limonene and β-elemene. In these cases, the complexes were restricted to **Ir1**, **Ir2**, **Ir5** and on occasion **Ir7**. These were the catalysts that had shown high C-H oxidation activity, or were particularly relevant for comparison purposes. In all experiments the work should be considered preliminary data, as work up and characterisation were not fully optimised. Additional complications arose from the fact that as with eucalyptol, the terpenes present a range of oxidisable sites and thus give rise to a range of products that are difficult to fully analyse without extensive purification.[a]

4.3.2.1 Limonene oxidation

Attempts were made to oxidise limonene with **Ir1**, **Ir2**, **Ir5** and **Ir7** using both periodate and hydrogen peroxide as the terminal oxidant. Hydrogen peroxide was investigated because there was the potential for these reactions to be performed in flow. The by-products form from the reduced $NaIO_4$ are less desirable than H_2O produced when H_2O_2 is used as the oxidant. The potential products from limonene oxidation can be seen in Scheme 4.4.

Scheme 4.4. *Reaction conditions and potential products for limonene oxidation*

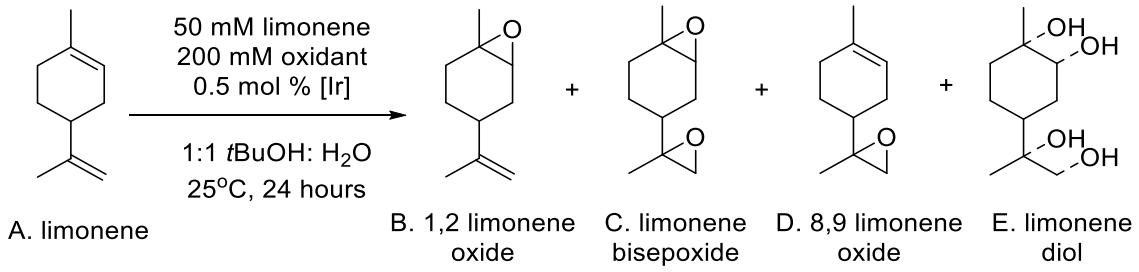

[a] Work on limonene and β-elemene was done in collaboration with Kasia Smug

The resulting product mixture from the experiments were analysed by GC-MS after a single extraction with toluene. No standard was included thus the reported percentages are calculated from the total area of the integratable peaks; absolute values are not reported but rather the product distribution relative to the recovered starting material for the different conditions is shown in Table 4.7.

Table 4.7. *Product distributions for limonene oxidation with range of Ir catalysts and different oxidants determined by ratio of integratable peak areas by GC-MS*

Precatalyst	Oxidant	% A	% B	% C	% E
Ir1	$NaIO_4$	70.1	9.4	20.5	-
Ir1	H_2O_2	-	-	-	-
Ir2	$NaIO_4$	83.0	-	16.9	-
Ir2	H_2O_2	-	-	-	-
Ir5	$NaIO_4$	47.9	12.2	39.8	-
Ir5	H_2O_2	79.3	4.4	-	16.3
Ir7	$NaIO_4$	82.7	3.5	13.8	-
Ir7	H_2O_2	84.3	-	-	15.7
none	$NaIO_4$	93.0	-	7.0	-
none	H_2O_2	-	-	-	-

With this preliminary data, there are some key observations. Notably, that in all cases periodate was a superior oxidant to hydrogen peroxide; in most cases the latter showed no detectable product. No 8,9-epoxide product was observed, in the cases where mono epoxidation had occurred it was exclusively to the 1,2- product. All complexes showed some formation of the bis-epoxide, but there was a peak present for the bis-epoxide reaction with periodate in the absence of catalyst so there is a possibility that some or all of its formation is due to the presence of the periodate. Conversely, peroxide showed no reaction without [Ir] catalyst. Although the pyridine complexes **Ir1** and **Ir2** showed no reaction with H_2O_2, both quinoline compounds did show some activity. Interestingly, in these cases a diol product was observed, presumably due to opening of the epoxide ring. **Ir5** appears to show the highest conversion by these data, but it also had the lowest reported total peak area; this could be due to missing material during the work up process.

4.3.2.2 β-Elemene

β-elemene was also investigated as a C-H oxidation substrate, in this case only with complexes **Ir1**, **Ir2** and **Ir5** but with $NaIO_4$ as the oxidant (Scheme 4.5).

Scheme 4.5. *β-elemene reaction conditions and potential product distribution*

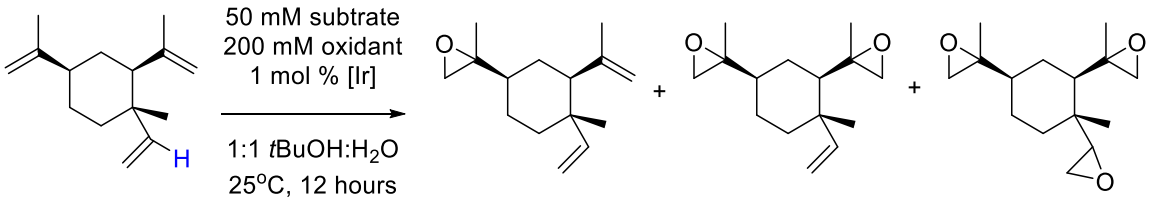

In this case the analysis was conducted with ^1H NMR, by integration of the alkene peaks against the peak at 5.8 ppm, which corresponds to the C-H on the bottom double bond, which is the final double bond to react (denoted with as a blue H in Scheme 4.5). From this an estimate of double bond conversion can be made from the alkene peaks at 4.5 – 5.0 ppm, and an estimate of product formation by comparison to the epoxy peaks at around 2.5 ppm (Table 4.8). Figure 4.19 demonstrates the ^1H NMR analysis, the peaks at 5.8 ppm for the C-H proton set as the standard are highlighted in yellow, the alkene groups corresponding to β-elemene starting material are in blue, and the epoxy product peaks are highlighted in pink.

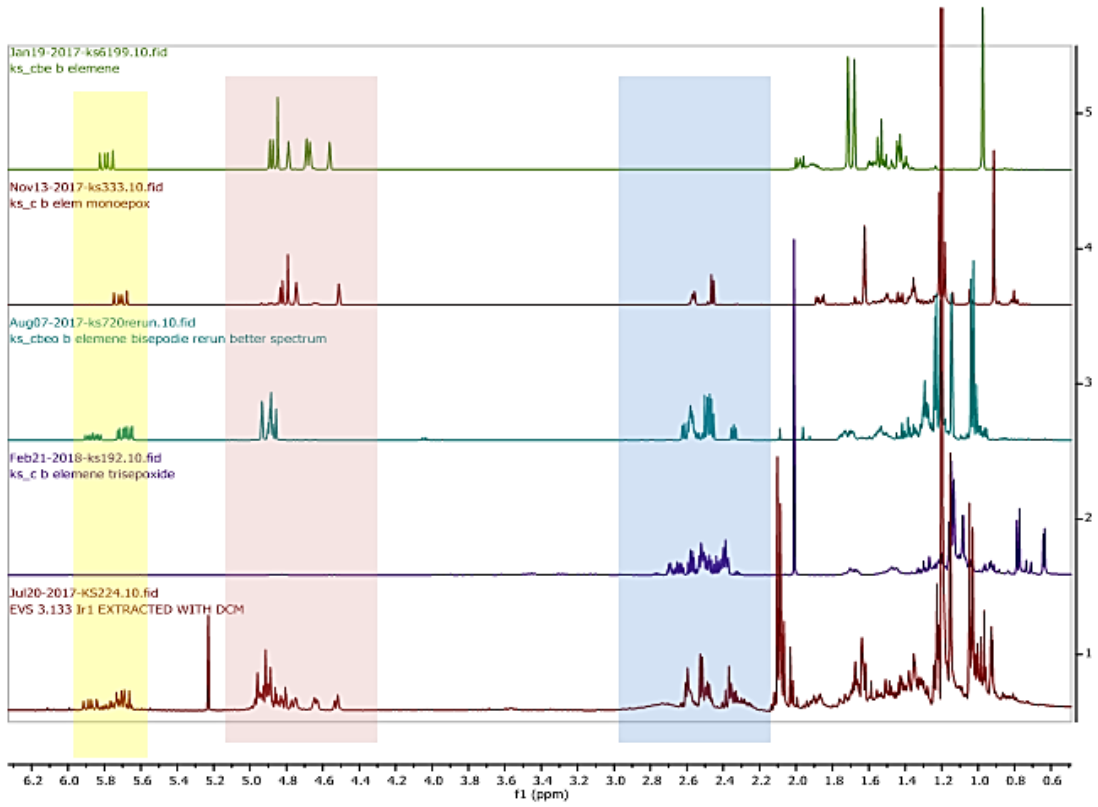

Figure 4.19. *^{1}H NMR spectra of possible products from β-elemene oxidation. Yellow band shows the peak at 5.8 ppm which is set as the standard integration, pink band denotes the alkene groups for β-elemene starting material, and blue band shows the epoxy product region.* ***Ir1*** *shown here, ^{1}H NMRs for* ***Ir2*** *and* ***Ir5*** *are in the Appendix (Figure A4.2)*

Table 4.8. *Product conversion for complexes* ***Ir1****,* ***Ir2*** *and* ***Ir5*** *with β-elemene*

	Conversion of starting material	Selectivity to epoxy products
Ir1	55%	85%
Ir2	13%	45%
Ir5	61%	72%

A single extraction with DCM of the reaction mixture was made for NMR analysis, but a significant amount of precipitate was observed in all the reactions. Attempts at identifying this solid by dissolution in D_2O, $CDCl_3$ revealed no peaks by NMR, and it was therefore attributed to insoluble periodate oxidation products. The organic product mixture was a combination of mono and bis-epoxy products, with **Ir5** showing some apparent conversion to a diol, as observed for limonene.

4.4 Summary

Complexes **Ir1**-**Ir7** were investigated for their ability to oxidise C-H bonds, by reaction with EBS and a variety of terpene-based compounds. Initial investigations with varying pH and the effect of a co-solvent revealed highest conversion of C-H substrate at neutral pH and with ^{t}BuOH as a co-solvent.

Kinetic profiles were collected for the oxidation of EBS, as investigated by ^{1}H NMR, but sharp plateaus were observed in the C-H conversion data. The plateau conversions varied greatly between complexes, with **Ir4** giving the lowest conversion of 52%, and **Ir2** the highest, turning over 88% of the C-H substrate. Addition of further oxidant restarted the C-H oxidation, and as such the plateau was attributed to the competition of C-H vs. water oxidation. The C-H selectivity of the varying complexes depended on the ligand.

UV-vis data of the activation of **Ir2** showed a change in the active complex depending on the presence of ^{t}BuOH. Without ^{t}BuOH, an absorbance at 583 nm was observed attributed to the dimeric active catalyst previously described (Chapter 2 and Chapter 3). However, with 20% ^{t}BuOH as a co-solvent, the main absorbance was seen at 493 nm. This band was assigned to a monomeric Ir^{IV}-OR species[4,6], which could be formed either from hydrolytic cleavage of the Ir^{IV}-O-Ir^{IV} dimer[4], or directly from the Cp* precursor. The high selectivity of **Ir2** was correlated to the presence of this monomeric species, which is proposed to be the active C-H oxidation catalyst. This is summarised in Figure 4.20.

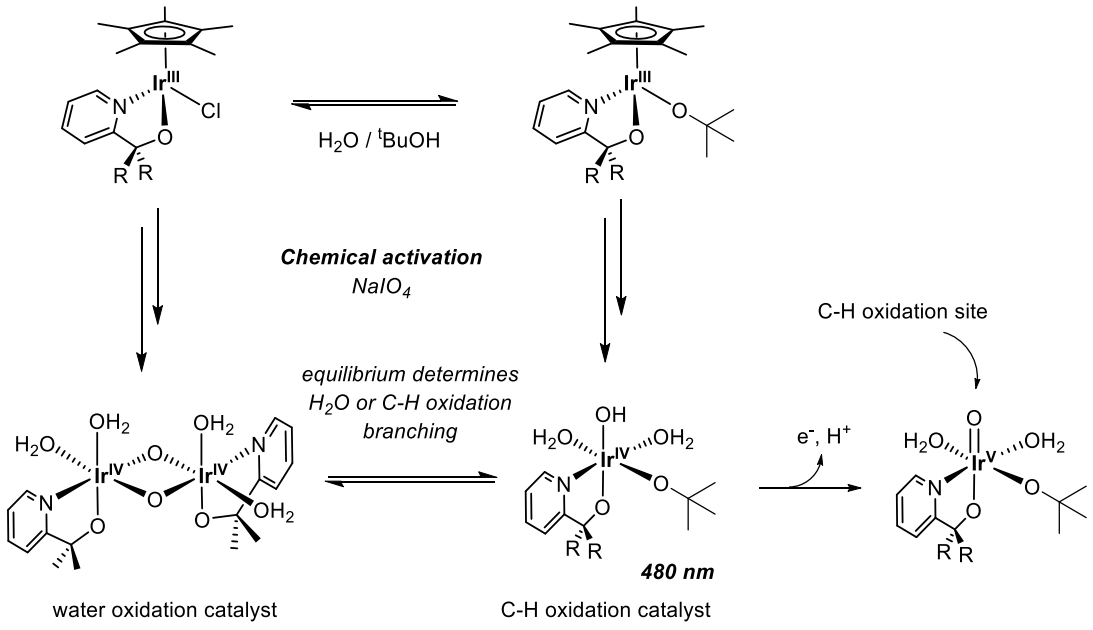

Figure 4.20. *Proposed formation of active monomeric Ir^{IV}-OR species responsible for C-H oxidation*

This proposal explains the enhanced rate of C-H selectivity in ^{t}BuOH compared to water; the sterics of ^{t}BuO^{-} ligand promote formation of the monomeric species. It is also consistent with the branching ratios of the complexes for water vs C-H oxidation. Complexes bearing electron withdrawing R-groups (**Ir2** and **Ir7**) preferentially form the monomeric species and as such selectively catalyse C-H bonds rather than water. Complexes bearing small alkyl groups (**Ir1** and **Ir4**) preferentially form the dimeric species, which undergoes water oxidation and competes with C-H oxidation.

Whilst this proposal is consistent with the current data, further experiments are required. The effect of ^{t}BuOH on the proposed monomer/dimer equilibrium needs to be explored, for example by UV-vis titration experiments with increasing ratios of ^{t}BuOH. Furthermore, as conducted for water oxidation, kinetic studies to determine the order in [Ir] during C-H oxidation would be beneficial for determining if a monomeric or a dimeric species is involved in the RDS.

Initial scoping of the activity of **Ir1**-**Ir7** for more challenging C-H substrates was conducted with a range of terpene-based compounds. Oxidation of eucalyptol proceeded slowly but with regioselectivity which did not vary between complexes. Although no conclusive trends can be drawn, aryl complexes **Ir2** and **Ir7** again gave high conversion of C-H oxidation product. Initial exploration into the activity with other terpenes, limonene, and β-elemene was also undertaken. Some oxidation of starting material was observed, but absolute quantification and product determination is still required.

Regardless of the exact mechanism, the C-H oxidation experiments described further highlight the extraordinary scope for these complexes and the robustness of the pyalk ligands. Variation in ligand modulates the selectivity of the catalysts, thus providing molecular control over these oxidising iridium complexes and widening the scope for further ligand design.

4.5 Experimental

Complexes were synthesised according to procedures outlined in Chapter 2. Otherwise chemicals were used as purchased. High-purity Milli-Q water was used in all experiments. ^{1}H NMR data were obtained on 500 MHz Bruker instrument. GC-MS analyses were conducted on an Agilent 7890A GCMS with a HP-PLOT/Q, 30 m long, and 0.320 mm diameter column.

pH dependence

A solution of ethylbenzene sulphonic acid and NaOH (0.1 mM in H_2O, 2 mL, pH adjusted to the desired value as measured by multi-indicator paper strips) was added to a [Ir] solution (5 mM in 4:1 H_2O/ ^{t}BuOH, 0.4 mL) in a screw-cap vial and stirred at 25 °C (temperature maintained in an oil bath). A further 1 mL H_2O and 1 mL ^{t}BuOH were added to give a total volume of 4.4 mL. The reaction was initiated by the addition a solution of $NaIO_4$ (1 mL, 0.1 mM in H_2O). The reaction was quenched after 5 mins by addition of $NaHSO_3$ (1 M, 2 mL). An aliquot of the solution was taken, D_2O added and analysed by ^{1}H NMR spectroscopy to give conversion by peak area integration of the CH_{arom} of starting material (400 MHz, D_2O: δ = 7.63, 7.61, 7.32, 7.30) and product (400 MHz, D_2O: δ = 8.02, 8.00, 7.84, 7.82) as in the literature.[13]

Solvent variation

$NaIO_4$ (200 mM, 0.1 mmol) in D_2O, 40 mM EBS (0.2 ml in D_2O, 0.02 mmol) and the desired cosolvent (0.1 mL) were added to the NMR tube. A background scan was taken and [Ir] was subsequently added (1 mol %, 2 µmol) and the kinetic programme started. The time between the addition of [Ir] and the first scan was recorded and incorporated into the kinetic data. Co-solvents tested included ^{t}BuOH, acetone, MeCN, nitromethane, HMPA, DMA. In the case where no cosolvent was added a further 0.1 ml of D_2O was used.

Precatalyst variation

$NaIO_4$ (200 mM, 0.1 mmol) in H_2O, 40 mM EBS (0.2 ml in H_2O, 0.02 mmol) and ^{t}BuOH (0.1 mL) were added to the NMR tube. A background scan was taken and [Ir] was subsequently added (1 mol %, 2 µmol) and the kinetic programme started. The time between the addition of [Ir] and the first scan was recorded and incorporated into the kinetic data.

Additional $NaIO_4$

Initial reaction carried out at 0.04 mmol EBS, 0.2 mmol $NaIO_4$, 0.2 µmol, 1 mol % [**Ir5**] at pH 7, 25 °C in 4:1 H_2O/tBuOH solvent mixture and the NMR tube left at room temperature for

200 mins. ^{1}H kinetic data were recorded to check the reaction had plateaued, before a second addition of $NaIO_4$ was made. After second addition of $NaIO_4$ (a further 0.2 ml of a 1 M solution such that a further 0.2 mmol was added) 0.04 mmol EBS at pH 7, 0.4 mmol $NaIO_4$, 1 mol % [Ir] at 25 °C in 0.52 mL 4:1 H_2O/^{t}BuOH.

Oxidation with preactivated [Ir]

Kinetic data recorded under the same reaction condiditons as for precatalyst variation but the [Ir] solution used was preactivated with 30 equivalents of $NaIO_4$ (added as a solid to maintain the concentration) and the solution stirred at room temperature overnight. Complete colour change was observed for all complexes, denoting full activation.

Water Oxidation with EBS substrate

In-situ oxygen evolution data was collected using a Hansatech Oxygraph Plus system with a DW2/2 Clark-type electrode chamber (with temperature control and magnetic stirring) measuring dissolved O_2 in solution. The electrode was prepared with 0.1 M KCl electrolyte under a PTFE membrane and spacer paper, and the instrument zeroed with 10 µM $NaIO_4$ solution in H_2O (2 mL) thoroughly degassed with Argon. Oxygen evolution data were collected under identical conditions as the C-H oxidation (200 mM $NaIO_4$, 40 mM EBS, 1 mol% [Ir] in ^{t}BuOH/H_2O/D_2O (1:2:2), with initiation by addition of [Ir] (120 µL of a 5 mM solution of [Ir] in H_2O/20% ^{t}BuOH).

Eucalyptol oxidation

Eucalyptol (1 mL, 0.1 mM solution in H_2O) and [Ir] (1 mL, 5 mM solution in 4:1 H_2O/ ^{t}BuOH) were added to screw-cap vial and stirred continuously at 25 °C, with a further 0.2 mL H_2O and 0.8 mL ^{t}BuOH. The reaction was started by adding $NaIO_4$ (2 mL, 0.1 mM in H_2O). The final volume of the reaction was 5 mL with concentrations as follows: 1 mM [Ir], 20 mM eucalyptol, 400 mM $NaIO_4$. A catalyst free sample was also run at the same time in order to calculate conversions.

At the required time point, an aliquot of the reaction mixture was taken (0.5 mL) and quenched with IPA (2 mL). $MgSO_4$ was added to the solutions to remove the water to yield a solution suitable for analysis by GCMS. Conversion calculated using a substrate calibration graph and based on the amount of material recovered from the catalyst free $NaIO_4$ sample. Product yields were calculated assuming identical response factors.

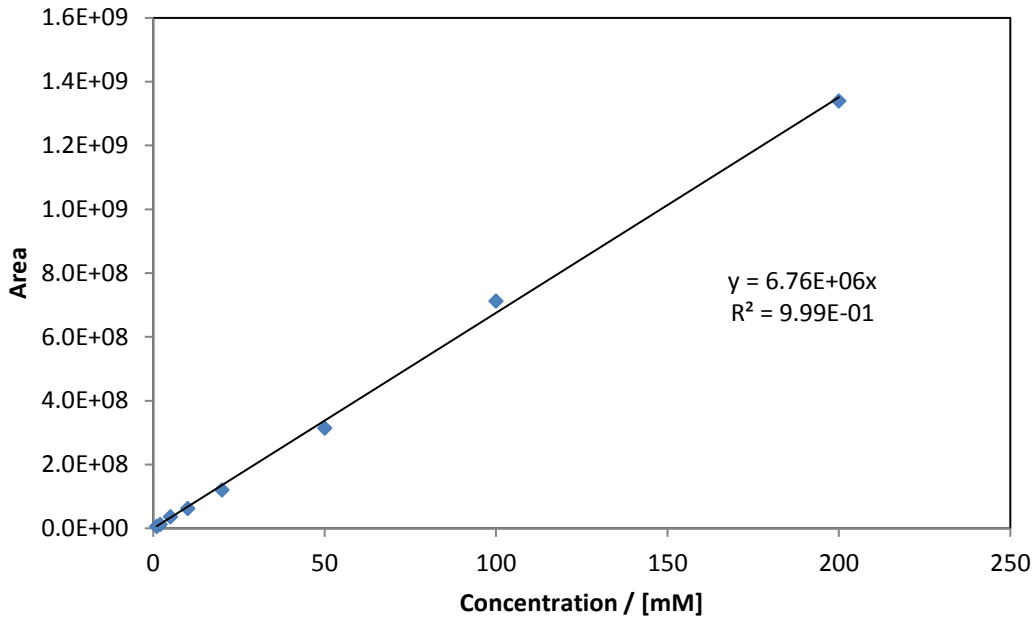

For identification of the ketone stereochemistry all the reaction solutions were collected, and the solvent removed *in vacuo.* The product was purified by column chromatography with silica gel (23 cm by 3.5 cm) using a solvent mixture of 5:1 hexane:ethyl acetate and the stereochemistry determined by ^{13}C NMR.

^{13}C-NMR (100 MHz, $CDCl_3$): δ = 213.2, 73.6, 51.9, 49.1, 30.4, 29.6, 26.9, 26.3, 21.0, 18.3 [16]

Terpene oxidation

Reactions were made up in 30 mL screw cap vials with 50 mM subtrate (limonene, β-elemene, α-pinene, β-pinene) and 200 mM oxidant (H_2O_2, $NaIO_4$) in 5 mL total 1:1 ^{t}BuOH/H_2O, with 1 mol% of [Ir] added from a stock solution (5 mM in 4:1 ^{t}BuOH/H_2O). β-elemene was extracted with DCM and analysed by ^{1}H NMR. Limonene and both pinene derivatives were extracted with toluene and analysed by GC-MS.

4.6 References

1. M. Zhou, N. D. Schley, and R. H. Crabtree, *J. Am. Chem. Soc.*, 2010, **132**, 12550–12551.
2. M. Zhou, U. Hintermair, B. G. Hashiguchi, A. R. Parent, S. M. Hashmi, M. Elimelech, R. A. Periana, G. W. Brudvig, and R. H. Crabtree, *Organometallics*, 2013, **32**, 957–965.
3. U. Hintermair, S. M. Hashmi, M. Elimelech, and R. H. Crabtree, *J. Am. Chem. Soc.*, 2012, **134**, 9785–9795.
4. U. Hintermair, S. W. Sheehan, A. R. Parent, D. H. Ess, D. T. Richens, P. H. Vaccaro, G. W. Brudvig, and R. H. Crabtree, *J. Am. Chem. Soc.*, 2013, **135**, 10837–10851.
5. B. Plietker, *Synthesis (Stuttg).*, 2005, **15**, 2453–2472.
6. D. L. Huang, D. J. Vinyard, J. D. Blakemore, S. M. Hashmi, and R. H. Crabtree, *Organometallics*, 2017, **36**, 199–206.
7. C. Della Pina and E. Falletta, *Catal. Sci. Technol.*, 2011, **1**, 1564–1571.
8. N. G. Connelly and W. E. Geiger, *Chem. Rev.*, 1996, **96**, 877–910.
9. A. R. Parent, R. H. Crabtree, and G. W. Brudvig, *Chem. Soc. Rev.*, 2013, **42**, 2247–2252.
10. E. V. Sackville, G. Kociok-Köhn, and U. Hintermair, *Organometallics*, 2017, **36**, 3578–3588.
11. A. Savini, A. Bucci, G. Bellachioma, L. Rocchigiani, C. Zuccaccia, A. Llobet, and A. Macchioni, *Eur. J. Inorg. Chem.*, 2014, 690–697.
12. C. Zuccaccia, G. Bellachioma, S. Bolaño, L. Rocchigiani, A. Savini, and A. MacChioni, *Eur. J. Inorg. Chem.*, 2012, **9**, 1462–1468.
13. M. Zhou, D. Balcells, A. R. Parent, R. H. Crabtree, and O. Eisenstein, *ACS Catal.*, 2012, **2**, 208–218.
14. M. C. White, *Science (80-.).*, 2012, **335**, 807–809.
15. T. Newhouse and P. S. Baran, *Angew. Chemie - Int. Ed.*, 2011, **50**, 3362–3374.
16. A. J. Farlow, P. V. Bernhardt, and J. J. De Voss, *Tetrahedron Asymmetry*, 2013, **24**, 324–333.

CHAPTER 5

APPLIED ELECTROCHEMISTRY

This chapter is based in part on the following publication:

*Electrochemical and Kinetic Insights into Molecular Water Oxidation Catalysts Derived from Cp*Ir(pyridine-alkoxide) Complexes*, E. Sackville, F. Marken, U. Hintermair, *ChemCatChem*, accepted

5. Applied Electrochemistry

5.1 Introduction

Chemically driven catalysis of both water and C-H oxidation has been demonstrated with complexes **Ir1**-**Ir7**. However, the use of chemical oxidants, whilst useful for initial benchmarking and screening of water oxidation catalysts, is not representative of the electrochemical behaviour. Therefore, if a WOC is to be truly applicable for renewable energy storage, a rigorous assessment of their electrocatalytic activity needs to be undertaken.

In addition to the electrochemical performance, immobilisation of homogeneous WOCs is also important when considering the end application. Despite the high activity displayed by molecular WOCs, long term stability of these compounds is often reduced at continued exposure to high potentials. Therefore, depositing the highly active molecular catalyst onto a suitable electrode surface, whilst retaining the activity, is an important long-term goal for application of WOCs.

This chapter will explore the behaviour of the precatalysts for water oxidation when driven by voltage as opposed to a chemical oxidant, a brief foray into the deposition and subsequent activity of some of the catalysts onto an electrode surface, and finally application of a technique called Fourier Transform Alternating Current Cyclic Voltammetry (FTAC CV), to attempt to elucidate further mechanistic information during the electrocatalysis.

5.2 Electrochemically driven water oxidation

5.2.1 Methods of determining electrocatalytic water oxidation

When attempting to quantify electrochemical activity of an electrocatalyst, analysis of the CV is usually undertaken in the first instance. However, the lack of electrochemical performance data for water oxidation catalysts is often due to the difficulties arising from accurately interpreting the resulting CV traces.[1]

Considering the case where a metal species P can be reversibly oxidised to Q, which can then go on to perform an irreversible chemical reaction, regenerating P, the electrochemical mechanism can be described as EC' (where E is the electrochemical step and C' is a catalytic chemical step) (Scheme 5.1).

Scheme 5.1 *An electrochemical – chemical coupled reaction EC' where P is the reduced form of Q, A is the substrate, and B is the product*

$$P \leftrightarrow ne^- + Q$$

$$Q + A \xrightarrow{k_{obs}} P + B$$

The mathematical solutions for the CV responses for this EC' have been mapped out and described by Saveant and co-workers for a one-electron, one-substrate model. When there is no substrate present, the CV response is the typical 'duck' shaped trace previously described (D in Figure 5.1). Increasing the substrate concentration will change the shape of the CV, until the system is no longer under diffusion control, but it instead governed by the kinetics of the system, i.e. the C' reaction described in Scheme 5.1. Under full kinetic control, the plateau current can be extracted, and a value of k_{obs} can be acquired for the system being tested (KS in Figure 5.1).[2]

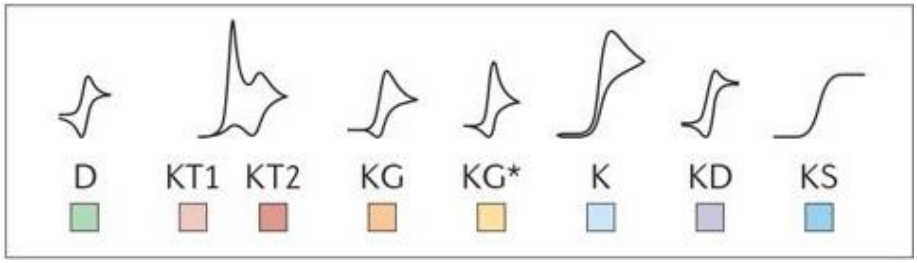

Figure 5.1 *A scheme of the various CV shapes resulting from an EC' mechanism, with increasing substrate from D to KS. Reproduced from Lee et al 2017.*[2]

In systems that can operate under substrate limited conditions, the catalytic plateau current can be used to determine the k_{obs}. However, in the case of water oxidation the analysis is complicated by the aqueous solution, where the substrate i.e. water, is in excess and cannot be limited.

In the cases where a suitable catalytic plateau current is inaccessible (and KS cannot be reached), for example due to catalyst deactivation or side reactions, an alternative method called Foot-of-the-Wave-Analysis (FOWA) can be used.[2–4] In this case kinetic information is determined from the part of the CV just prior to the catalytic wave, where minimal catalytic current has flowed. A plot of the ratio of peak current with and without substrate against a potential term results in a graph where the rate of water oxidation, k_{obs}, can be extrapolated from the gradient of the linear regime. Similar to the limitations in initial rate analysis, FOWA only considers the first part of the catalytic reaction and takes the data where the rate is greatest; data calculated from FOWA therefore typically over-estimates the catalyst performance.[2–4] This analysis requires approximate knowledge of the catalytic mechanism, and a suitably reversible redox feature (i.e. a clear reversible transition from P → Q described in Scheme 5.1) prior to the catalytic wave in order to plot the potential term.

FOWA has been used to analyse water oxidation catalysts previously, and the equations manipulated by Llobet and co-workers, to determine the mechanism under which water oxidation is occurring.[3] Figure 5.2 shows the CV obtained suitable for FOWA. Well defined reversible redox events were seen at 1.1 V and 0.5 V which allowed for the rate to be extracted. Manipulation of the original FOWA equations described by Saveant[4] allowed for a comparison of the two possible pathways for water oxidation as described in Chapter 1, water nucleophilic attack (Figure 5.2 orange) or radical oxyl coupling (Figure 5.2 purple). Repeated CVs at different concentration of [Ru] catalyst and extraction of k_{obs} showed that the mechanism under operation was WNA.[3]

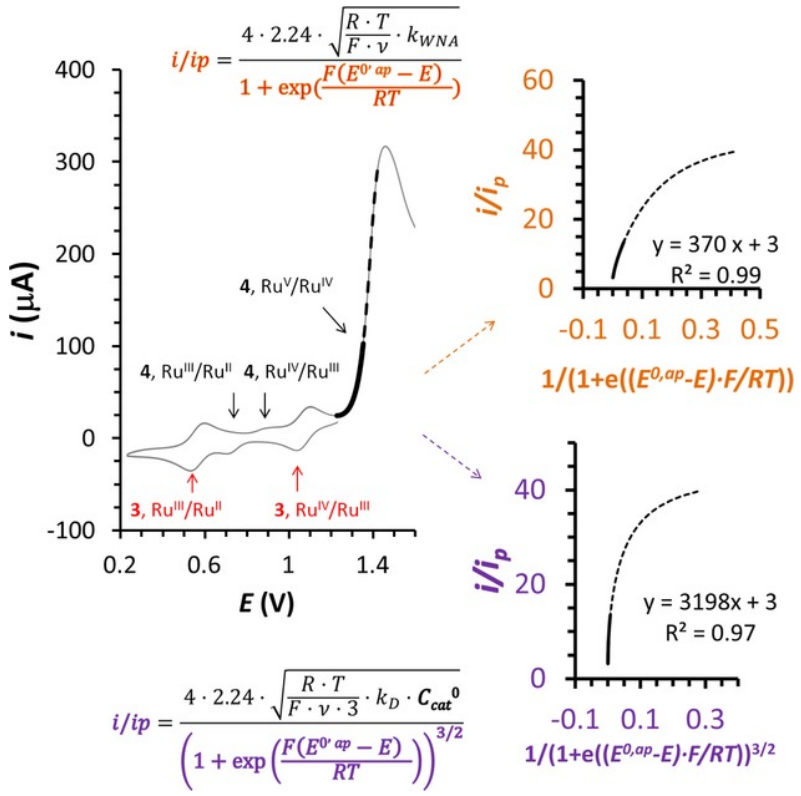

Figure 5.2. *Foot of the Wave analysis undertaken by Llobet and co-workers with Ru based water oxidation catalysts to determine whether the mechanism was water nucleophilic attack (WNA, orange) or radical oxyl coupling (ROC, purple) Reproduced from Matheu et al 2016.*[3]

CVs of aqueous solutions with pre-activated **Ir1*-Ir7*** were collected in the hope of applying FOWA and comparing the intrinsic catalytic rates (Figure 5.3). Although an apparent catalytic wave was observed for all catalysts, the observed redox features were not suitable for FOWA. A potential oxidation peak was seen for all catalysts at ~1.5 V vs RHE, but it was not clearly separable from the catalytic wave and was demonstrably not reversible. A broad catalytic wave occurred at ~1.8 V vs RHE, but again little variation was seen between catalysts.

Due to the fact that the complexes were pre-activated with periodate, there was a concern that the reduced form of periodate, iodate (IO_3^-) was responsible for the observed redox features. A control experiment with $NaIO_3$ was therefore undertaken, and the resulting CV showed similar features to the catalyst CVs. This therefore further complicated the assignment of the observed redox events. Although a few slight differences were seen between catalysts, the absence of any clearly defined pre-catalytic redox feature of the catalyst obscured evaluation of electrocatalytic performance by purely electrochemical techniques.

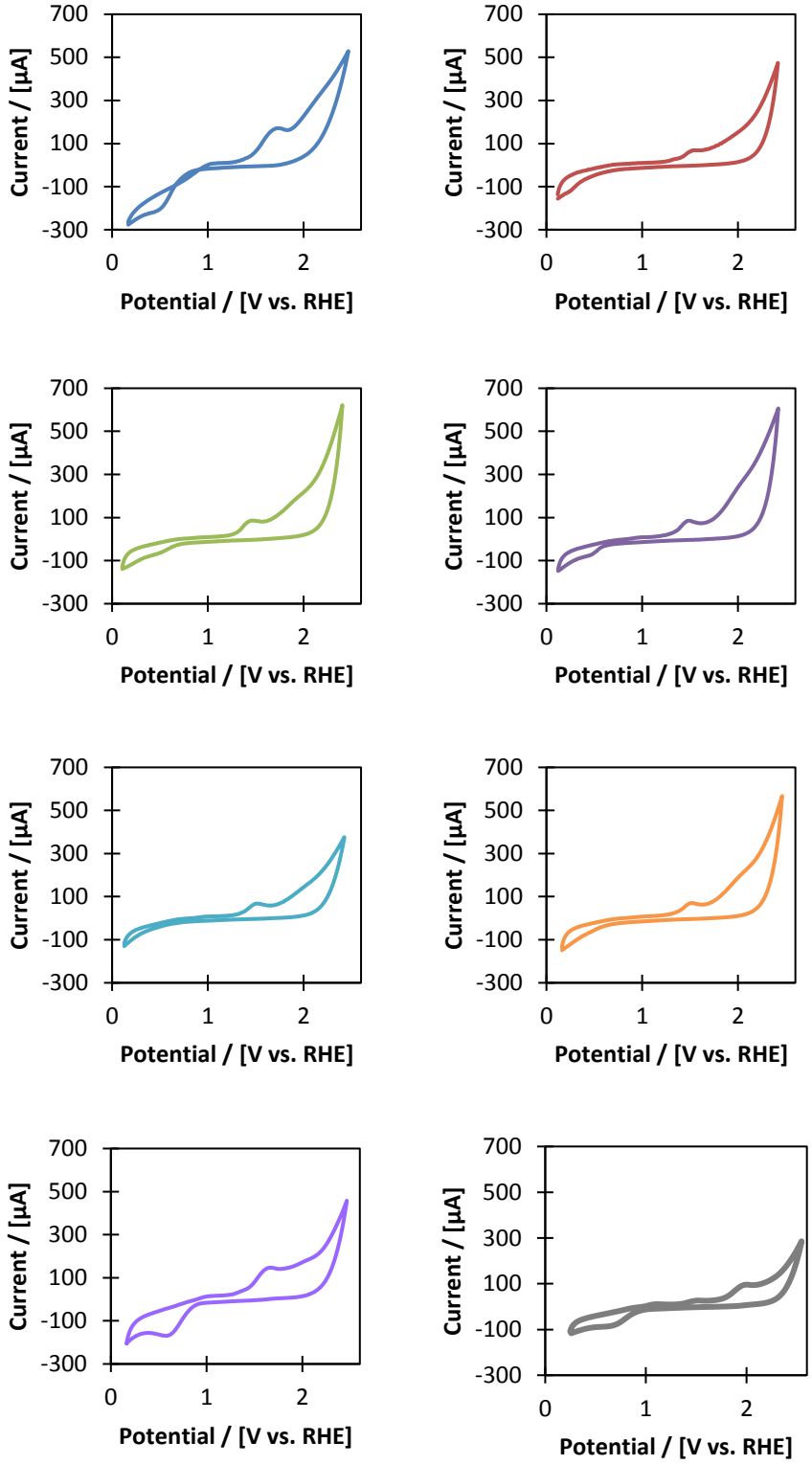

Figure 5.3. *Cyclic voltammograms of complexes* ***Ir1*-Ir7**** *preactivated with 50 equivalents of $NaIO_4$ for 24 hours in water. 1 mM [Ir], 0.1 M $NaNO_3$, H_2O, glassy carbon working electrode, diameter 0.3 cm, Ag/AgCl reference electrode, Pt wire counter electrode, 100 mVs^{-1} scan rate at pH ~6.*

5.2.2 Direct electrochemical measurement

With complex CVs, and unlimited substrate in the form of solvent, the typical methods for determining electrocatalytic performance for **Ir1***-**Ir7*** were not suitable. Direct measurement of electrochemically driven oxygen evolution was therefore attempted with concurrent chronoamperometry and Clark electrode experiments by inserting the electrodes into the opening of the Clark electrode (Figure 5.4).

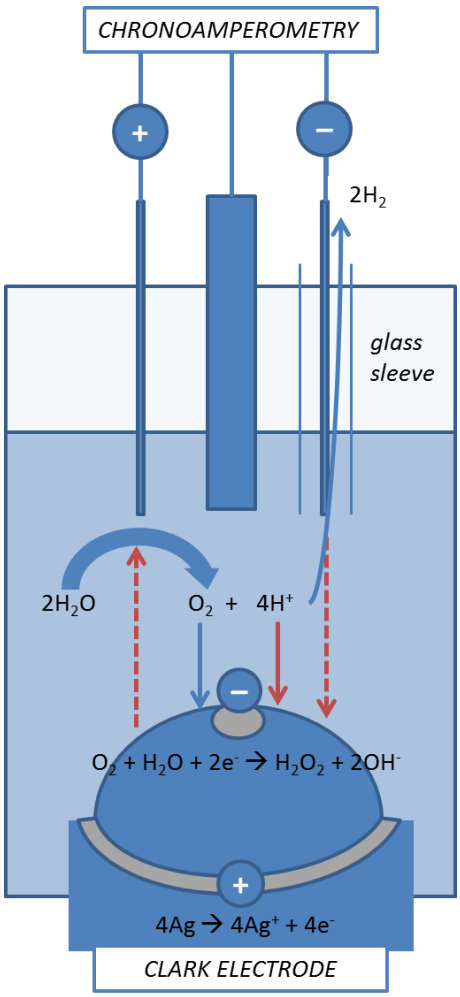

Figure 5.4. *Schematic to represent the set up for direct measurement of electrochemically driven water oxidation. Blue arrows indicate the desired routes and electrochemical transfers, and red arrows the undesired side reactions. Dashed lines indicate current*

One downside of this method is that there is no guarantee that all the oxygen produced during electrolysis will be detected by the Clark electrode. However, independently and selectively detecting the water oxidation product *in situ* from electrochemical potential is a

more direct method of testing the true water oxidation ability of a molecular WOC than inferred electrochemical techniques such as FOWA.

Initial testing with a three-electrode set up inserted into the top of the Clark electrode resulted in an overload of the Clark electrode. Within <5 seconds of immersion, the Clark electrode gave the maximum value of oxygen evolution, indicating full saturation of oxygen in solution, *before any potential had been applied* (Figure 5.5).

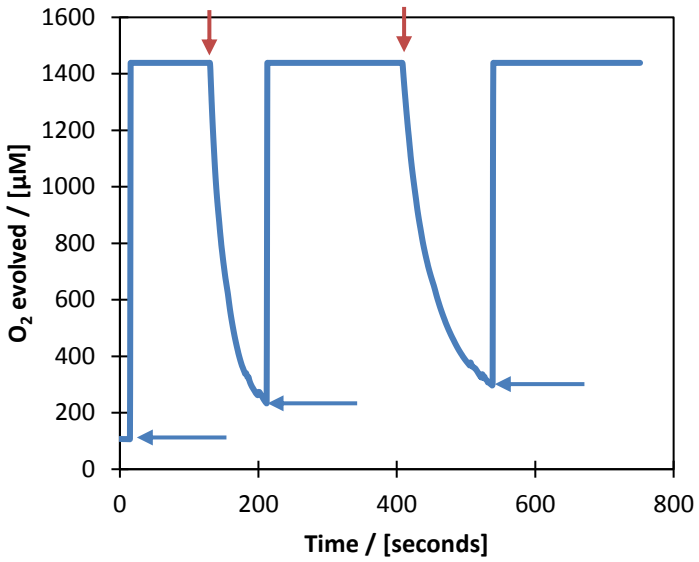

Figure 5.5. *Oxygen evolution trace indicating saturation of the Clark electrode upon insertion of the electrodes when connected to the potentiostat. Blue arrows indicate immersion, red arrows indicate removal of the electrodes*

Working with two or more electrodes often means that the system is at risk of cross currents where one electrode picks up the current response from the other, but moving the electrodes around within the Clark electrode chamber such that they were further away from the Clark electrode itself had no effect on reducing the cross currents. After varying different tests, it was suggested that this response was due to cross currents between the working electrode and the Clark electrode, as a result of both systems being powered by the mains. However, moving one of the electrode systems to being battery powered negated this particular problem; the potentiostat was plugged into a laptop and powered from this external battery source.

A secondary concern was envisaged with the possibility that hydrogen produced at the counter electrode could also be registered by the Clark electrode. As such the Pt counter electrode was encased in a glass sleeve such that any hydrogen produced would be separated from the rest of the solution and therefore would not interfere with the oxygen measurement.

5.2.3 Initial attempts

Once the initial set up had been optimised a concomitant chronoamperometry and water oxygen evolution experiment was attempted. Most of the previous CV data was collected with a glassy carbon electrode, but the relatively narrow width of the Clark electrode chamber opening (<1 cm^2) resulted in restriction in the combination of electrodes that could be used. To circumvent this, a Pt mesh working electrode, a Pt wire counter electrode and a standard Ag/AgCl reference were used. With a suitable combination of electrodes, an experiment was run with a chemically pre-activated solution of **Ir1*** (Figure 5.6).

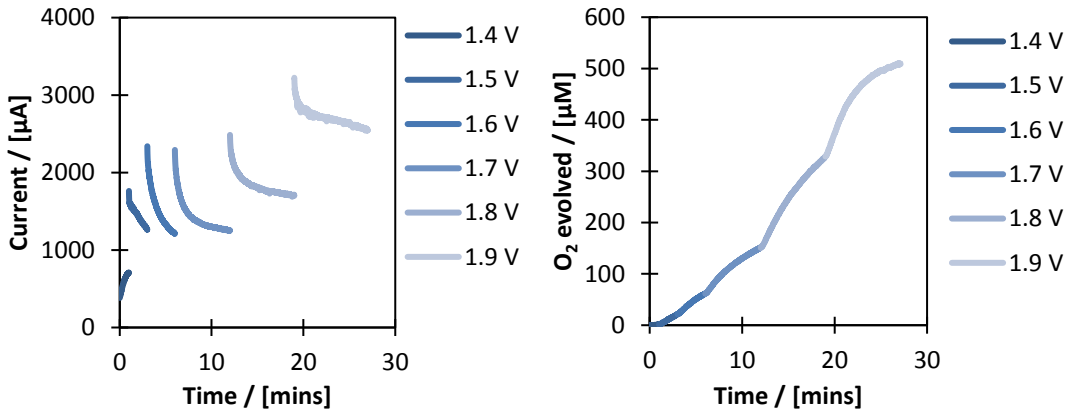

Figure 5.6. *Chronoamperometry (left) and oxygen evolution (right) traces for electrochemically driven water oxidation using **Ir1***. WE: Pt mesh, CE: Pt wire, RE: Ag/AgCl, 0.5 mM **Ir1***, 25mM $NaIO_3$, 0.1 M $NaNO_3$ electrolyte*

Although the initial data looked promising, platinum is known to perform water oxidation, and so a check of the Pt mesh electrode in a blank electrolyte solution was conducted (Figure 5.7). High water oxidation activity was observed, even without the iridium catalyst, necessitating an alternative electrode combination.

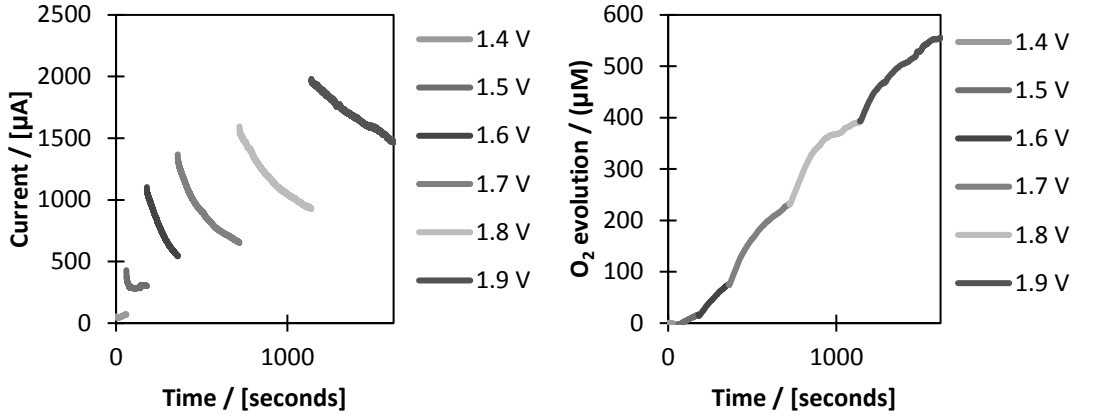

Figure 5.7. *Chronoamperometry (left) and oxygen evolution (right) traces for a blank electrolyte solution (0.1 M $NaNO_3$) with a Pt mesh WE and a Pt wire CE. Chronoamperometry experiments were done at 1.4, 1.5, 1.6, 1.7, 1.8 and 1.9 V for 1, 2, 3, 6, 7, 8 minutes respectively.*

Boron Doped Diamond (BDD) has been shown to have a large working potential window for water oxidation[5,6] and unlike glassy carbon, does not show catalyst deposition. In a solution of just electrolyte ($NaIO_3$), very little water oxidation was observed (Figure 5.8), such that it was considered appropriate for further investigation.

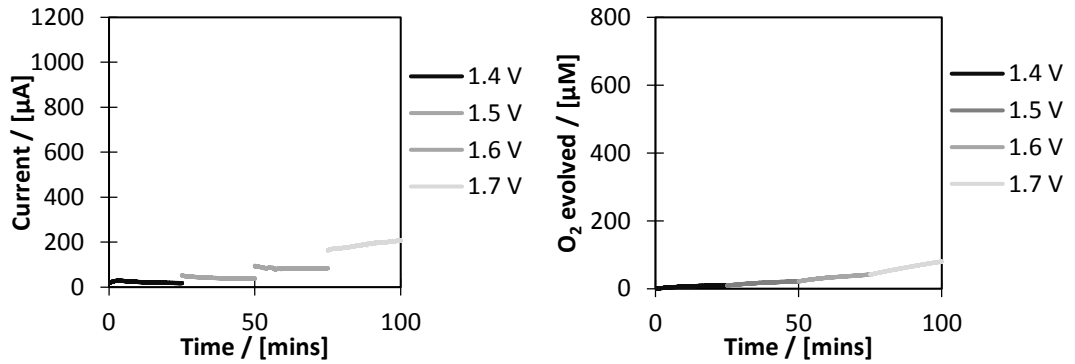

Figure 5.8. *Chronoamperometry (left) and oxygen evolution (right) traces for a blank electrolyte solution (0.5 M $NaIO_3$) with a BDD plate WE and a Pt wire CE. Chronoamperometry experiments were done at 1.4, 1.5, 1.6 and 1.7 V for 25 minutes each.*

5.2.4 Activity with iridium catalysts

With a suitably inert working electrode, solutions of activated **Ir1***-**Ir7*** were made and tested for electrochemical water oxidation. As the water oxidation reaction produces protons as a by-product, there was concern that prolonged water oxidation would increase the solution pH, and thus cause a drift in the applied potential. The [Ir] solutions were therefore adjusted down to a pH of ~4 in order to attempt to negate this effect. However, initial studies with **Ir1*** showed little oxygen evolution at pH 4. The solution pH was therefore varied, and the electrochemical water oxidation experiments repeated (Figure 5.9).

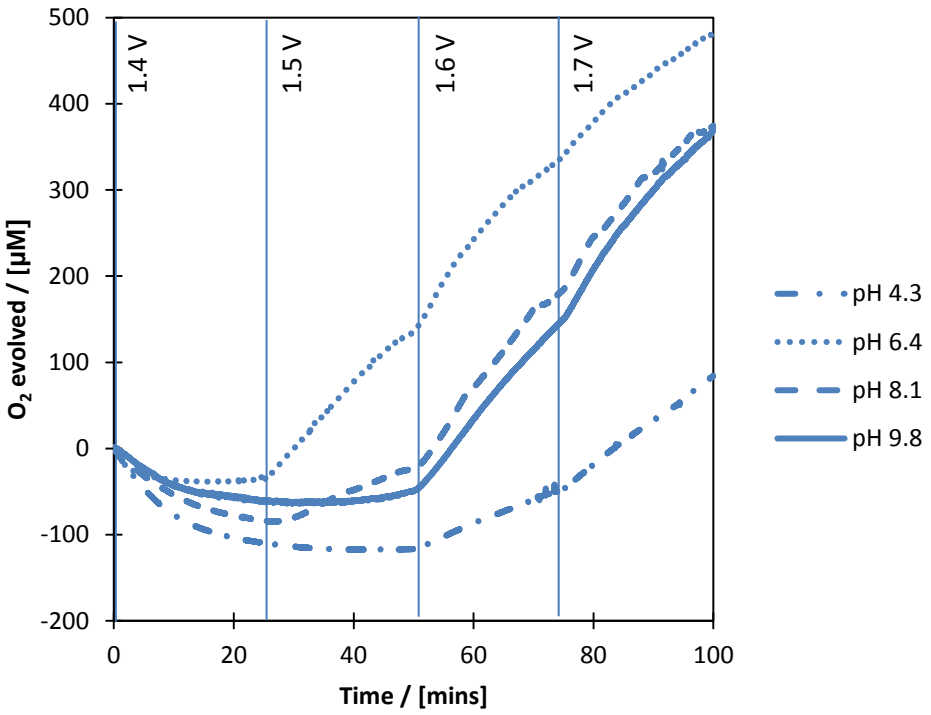

Figure 5.9. *Water oxidation traces for preactivated complex 1 (5 mM, 50 equivalents of $NaIO_4$ for 24 hours, 250 mM $NaIO_3$) at varying pHs (adjusted with NaOH and HNO_3) as driven by electrochemical potential (1.4-1.7 V held for 25 mins. WE: BDD plate 1cm^2, CE: Pt wire, RE: Ag/AgCl*

Although there is little difference observed in the measured current between the pHs, the amount of oxygen evolved is markedly different, with pH ~6 giving the most oxygen. This pH dependence is similar to that observed with chemically driven water oxidation with **Ir1** (Chapter 3, Figure 3.5).

With the conditions optimised, all [Ir*] solutions were adjusted to pH ~6 using ~HNO_3 and NaOH. Between each catalyst reaction a repeat was conducted in a solution of electrolyte to ensure there was no deposition (Appendix, Figure A5.1).

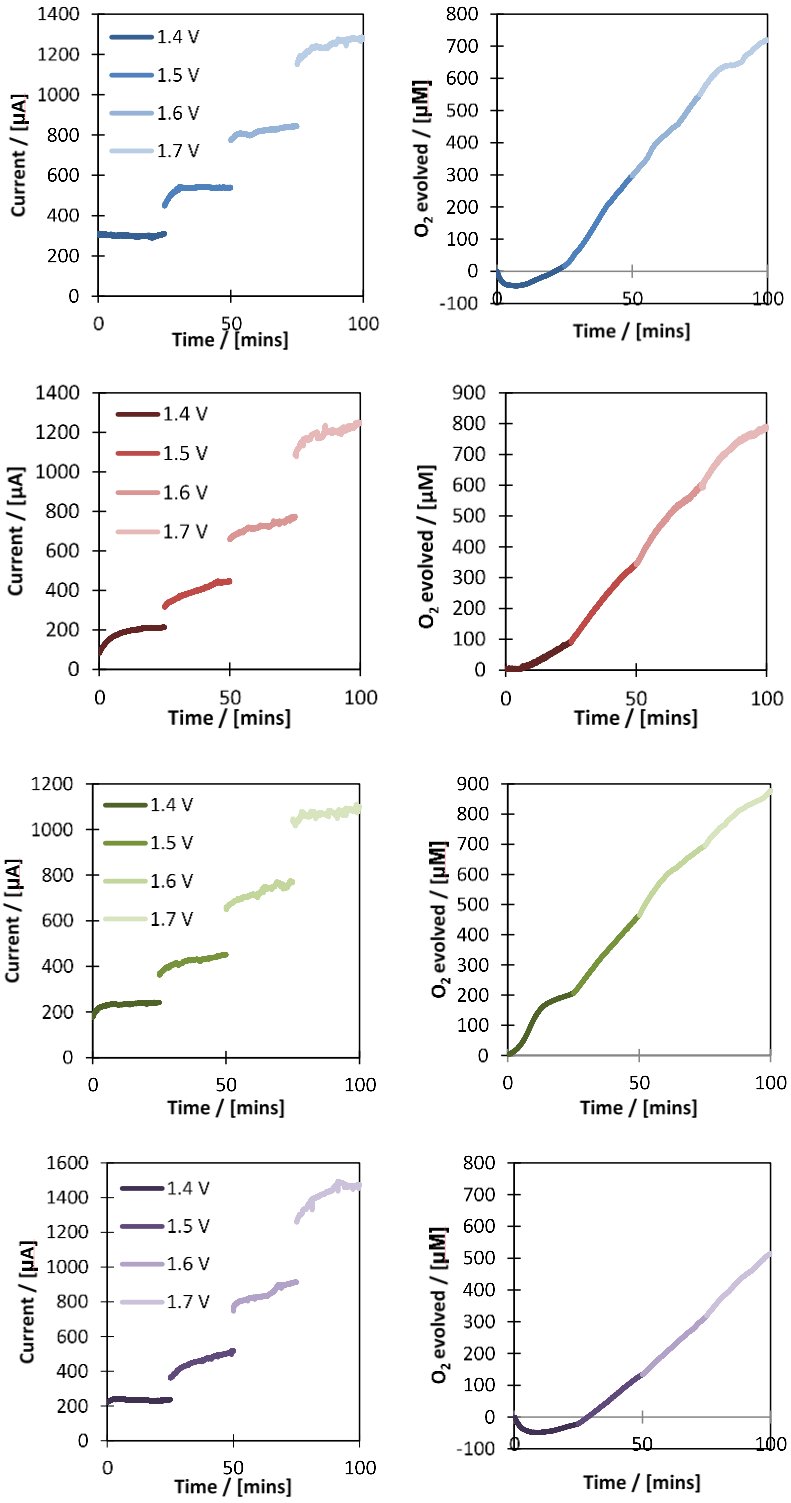

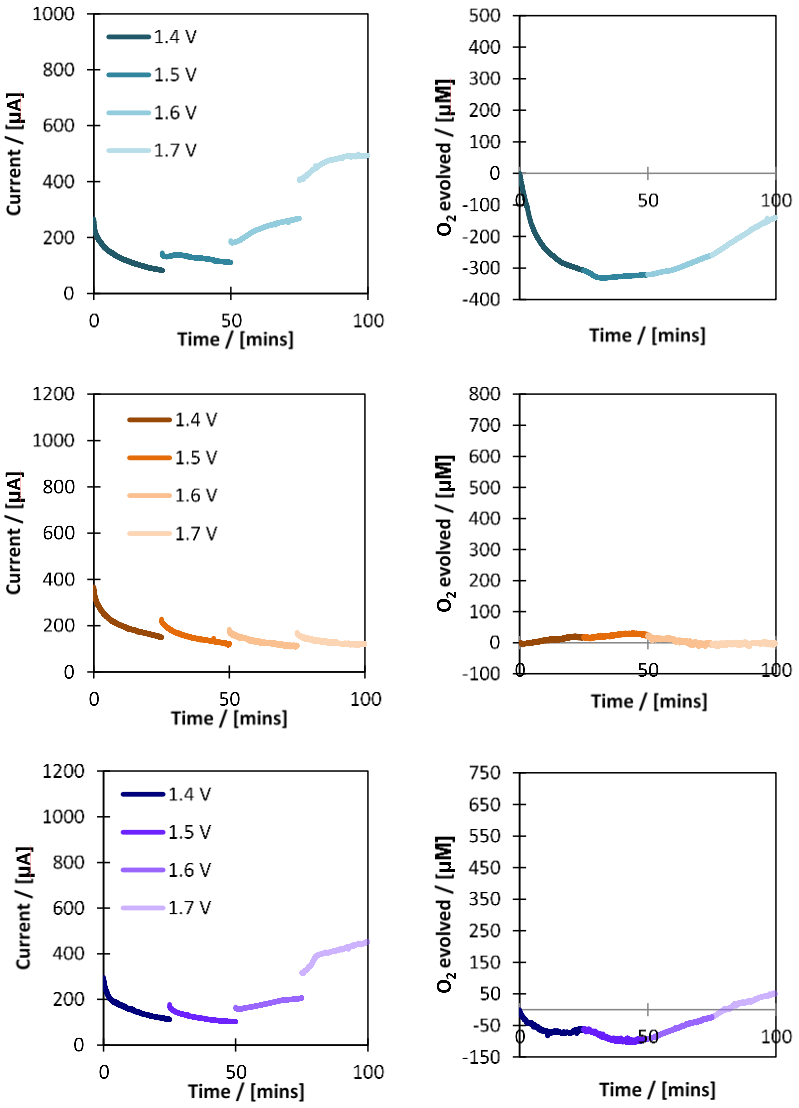

Figure 5.10. *Chronoamperometry (left) and oxygen evolution (right) traces for electrochemically driven water oxidation using complexes **Ir1*-Ir7*** chemically activated with 100 equivalents of $NaIO_4$ for 24 hours. All solutions were adjusted to a pH of ~6 with NaOH and HNO_3 WE: BDD plate 0.25 cm^2, CE: Pt wire, RE: Ag/AgCl, 2.5 mM [**Ir1**], 250mM $NaIO_3$. Chronoamperometry experiments were done for 25 mins at 1.4, 1.5, 1.6 and 1.7 V.*

Initial comparison between the catalyst performance indicates that **Ir1***-**Ir4*** show substantial water oxidation, but cata r**5***-**Ir7*** showed no oxygen evolution and reduced currents at the potentials investigated. It is worth noting that no oxygen evolution was seen without catalyst, and that the experiments were not performed in linear order **Ir1***-**Ir7***. Thus, the apparent decrease in activity between **Ir1*** and **Ir7*** is not a function of catalyst

decomposition or solution ageing, but rather a true reflection of the effects on catalyst activity imparted by the ligand.

Notably with the catalysts that did show substantial water oxidation, rate of oxygen evolution did not increase with increasing voltage above 1.5 V, such that the voltage is not rate limiting. This suggests that oxygen produced at voltages above 1.5 V was transport limited.

The potential at which the catalysts started producing oxygen varied. **Ir1*** and **Ir4*** both showed reduced oxygen evolution at a potential of 1.4 V, whereas **Ir2*** and **Ir3*** started to evolve oxygen at 1.4 V, giving them a lower apparent overpotential than **Ir1*** and **Ir3***. Whilst **Ir6*** appeared to have no electrochemical activity for water oxidation at all, the data for **Ir5*** and **Ir7*** suggest that at high enough potentials, they will evolve oxygen.

It is worth mentioning that there is an obvious concern with the residual iodate (IO_3^-) in the solution left over from catalyst activation. Whilst all $NaIO_4$ will have reacted or decomposed in solution, the remaining IO_3^- could feasibly act as a mediator for water oxidation, becoming re-oxidised under the potentials used. In this case the water oxidation behaviour observed would be considered iodate mediated but ultimately still electrochemically driven (Scheme 5.2).

Scheme 5.2. *Iodate mediated electrochemical water oxidation by* ***Ir1****

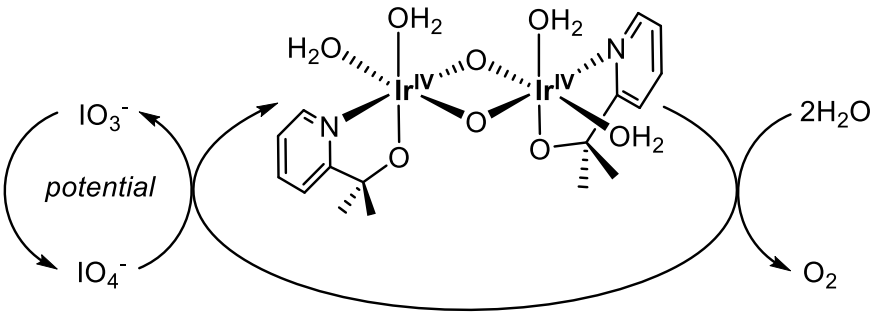

However, if this were true then the resultant pattern in the catalysts activity would be expected to match, at least to some extent, the trends observed in water oxidation with $NaIO_4$, where **Ir1** > **Ir6** > **Ir4** > **Ir5** > **Ir3** > **Ir7** > **Ir2**. Clearly the trend in the electrochemical activity for the catalysts does not follow this pattern, where **Ir3*** > **Ir2*** > **Ir1*** > **Ir4*** > **Ir6*** > **Ir7*** > **Ir5***.

One way to quantify the success of the catalysts for electrochemical catalytic performance is by calculating the Faradaic efficiencies (Fes); namely the ratio between the electrons passed (as determined by the current flow) and the electrons detected (as obtained from the oxygen evolution assays).

$$Faradaic\ Efficiency = \frac{4O_2\ electrons\ detected}{electrons\ passed\ as\ current}\ x\ 100$$

The calculated Faradaic Efficiencies are seen in Table 5.1. Ideally the plateau current would be used but clear plateaus were not observed and thus averages currents were taken from sampling the current data and the calculated FEs are presented as a range. The previously reported Faradaic efficiency for chemically activated **Ir1*** at 1.6 V was 59% with a gold working electrode. The additional current passed that is not detected in product formation could potentially be being lost in side reactions with the residual iodate species.

Table 5.1. *Approximate Faradaic efficiencies for catalysts **Ir1*-Ir7*** at 1.5V*

Catalyst	Faradaic efficiency
Ir1*	23-30%
Ir2*	21-30%
Ir3*	27-31%
Ir4*	15-19%
Ir5*	-
Ir6*	0-4%
Ir7*	-

A plot of current passed against O_2 evolution rate (Figure 5.11) shows another visualisation of the varying catalyst activity.

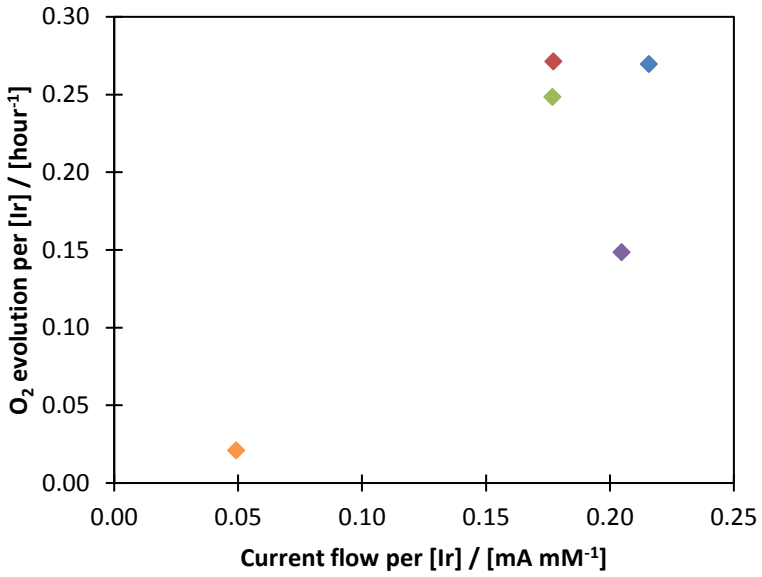

Figure 5.11. *O_2 TOF (calculated from k_{obs} of electrochemically driven water oxidation for catalysts **Ir1*-Ir7***) vs plateau current (in mA divided by catalyst concentration) for 1.5 V*

In terms of the pyridine-based complexes electrochemical activity, the substantial difference in comparative performance is highly interesting but correspondingly complicated. That **Ir2*** and **Ir3*** should outperform **Ir1*** for electrochemical water oxidation, whilst **Ir6*** is completely inactive, is surprising. Interestingly, **Ir2*** was the only precatalyst which showed a substantially faster rate when driven with CAN rather than periodate; the rate was 10 times faster with the single electron oxidant CAN.

It is interesting that both quinoline compounds **Ir5*** and **Ir7*** showed no electrochemical water oxidation at the potentials tested, but there was an apparent lag phase in the oxygen evolution data which could suggest that at higher potentials oxygen evolution would be observed.

The importance of consistent conditions for testing and comparing catalysts is well documented and is a particular plague for comparison of water oxidation catalysts, where the oxidant, pH, potential, solvent can all have a substantial impact on the catalyst activity. For example, an initial screen of the catalysts with periodate would suggest that **Ir6** would be worth investigating, and **Ir2** would be less useful; the electrochemical activity data demonstrates the opposite.

A paper published in 2015 by Stahl and co-workers effectively highlighted this by testing nine different Mn based WOCs.[7] The catalysts were investigated for their water oxidation activity with a chemical oxidant, via photochemical oxidation, and by electrochemical oxidation at different pH values. The relative order of catalyst activity was different for every method, such that a catalyst that showed very low activity when driven with CAN gave one of the highest current densities when driven with electrochemical potential.[7]

This mirrors results described herein, where even oxidant variation gives rise to different catalytic performance (Chapter 3, Section 3.3). It is not surprising that this should be true for multi-electron reactions with charge sensitive transfer events,[7] but these data highlight the importance of consistency within a data set, and the importance of assessing the activity with the end application in mind.

5.3 Catalyst immobilisation

As detailed in Chapter 1, heterogenisation of molecular WOCs onto electroactive surfaces can improve the charge transfer and thus the efficiency of the WOC, as well as improving the stability whilst still retaining the high activity. Binding of fully activated **Ir1*** to an electrode surface has been achieved by self-adherence of the [Ir] complex to a metal oxide film via the hydroxyl groups (Figure 5.12) as reported by Sheehan *et al* in 2015.[8]

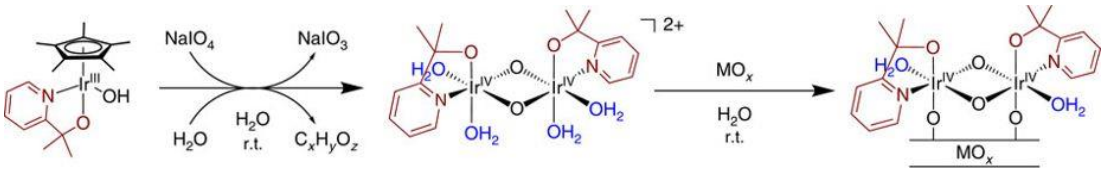

Figure 5.12. *Activation and immobilisation of **Ir1*** onto a metal oxide film. Reproduced from Sheehan et al 2015.*[8]

The metal oxide film used was fluorine-doped tin oxide (FTO) film spin coated with indium tin oxide (ITO) nanoparticles (nanoITO|FTO); an electrode that had previously been shown to bind a Ru WOC via a phosphonate linker[9]. The resulting electrocatalyst is a fully functionalised electrode which retains the pyalk ligand, remains active after repeated use and is highly active for water oxidation.[8] Given the retention of the pyalk ligand during surface binding, and the ligand tuning reported herein, attempts were made at functionalising nanoITO|FTO electrodes with activated **Ir1*-Ir7***.

In the first instance, the literature procedure was repeated for fully activated **Ir1*** in order to attempt to replicate the data reported. The nanoITO|FTO electrode was prepared as previously described[9], by spin coating a suspension of ITO nanoparticles onto an FTO coated glass slide, followed by heating in air and subsequent reduction of the nanoITO by annealing the film under a H_2/N_2 atmosphere. Binding of the [Ir] catalysts was achieved by soaking the spin coated electrode in a solution of pre-activated **Ir1*** for 2 hours. The resulting functionalised electrodes were compared by CV (Figure 5.13) and compared to the unfunctionalised nanoITO|FTO slides.

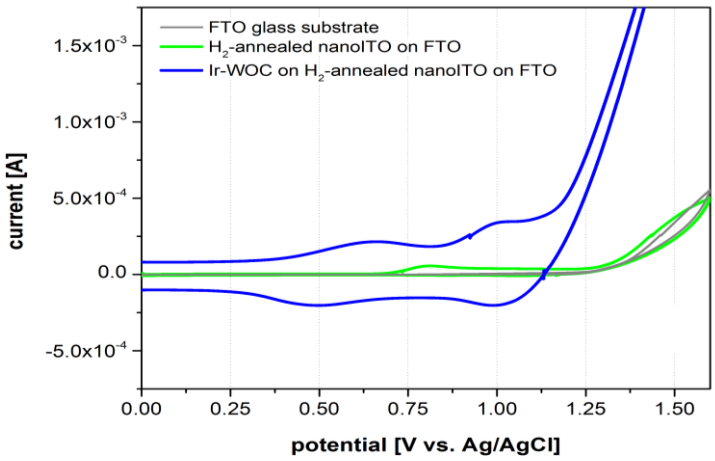

Figure 5.13. *CVs of bare FTO, nanoITO|FTO and functionalised nanoITO|FTO electrodes in 0.1 M KNO3 at pH 3 and a scan rate of at 10 mVs^{-1}. RE: Ag/AgCl, CE: Pt wire*

A clear difference between the bare electrode and the surface functionalised electrode was observed by a reduction in the onset potential of the catalytic water oxidation (from 1.3 V vs. Ag/AgCl to 1.1 V vs. Ag/AgCl), a redox feature at 0.55 V vs. Ag/AgCl assigned to an $Ir^{III} \rightarrow Ir^{IV}$ transition, and a marked increase in current density.

Despite the clear functionalisation of the modified surface, additional peaks in the CV at 1.0 V vs Ag/AgCl were attributed to residual copper from the annealing tubes, and a large peak to peak separation was observed for the $Ir^{III} \rightarrow Ir^{IV}$ redox feature. Attempts were also made to replicate the surface binding profiles reported, whereby the optical density of the films was recorded after immersion in the solution of **Ir1***. However, no usable data was obtained, attributed to over-reduction of the nanoITO during annealing. Analysis of controlled surface binding for fully activated **Ir1***-**Ir7*** was therefore not achieved, but these initial promising results provide scope for further investigation.

Another reason for immobilising WOCs onto electrode materials is to couple the WOC to a photochemical reaction, and thus drive the water oxidation by light rather than by electrochemical potential, as performed by nature during photosynthesis. In collaboration with groups at the University of Loughborough (U.Wijayantha-Kahagala-Gamage) and University of Toronto (G. A. Ozin) attempts were made to immobilise **Ir1*** onto photoanodic materials developed by the respective groups.

Functionalisation of $BiVO_4$ and $ZnFe_2O_4$ were performed by immersion of the electrodes (prepared at Loughborough)[10,11] in a preactivated solution of **Ir1*** and the resulting dark CVs were recorded at Bath (Figure 5.14). For both materials a decrease in the onset potential of water oxidation was observed (1.4 V vs. Ag/AgCl for 1.1 V vs. Ag/AgCl with $BiVO_4$, 1.4 V vs. Ag/AgCl to 1.2 V vs. Ag/AgCl for $ZnFe_2O_4$). The films were returned to Loughborough for corresponding photochemical experiments.

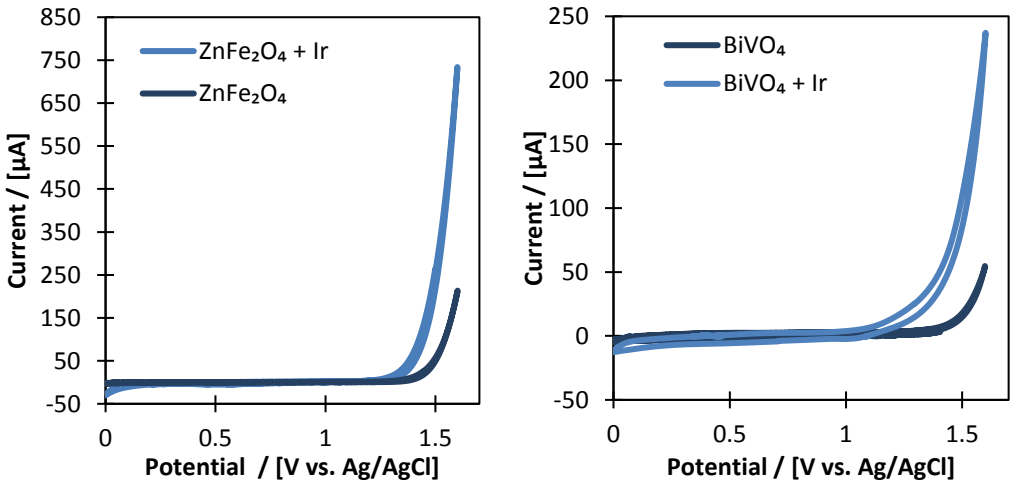

Figure 5.14. *CVs of bare (dark blue) and **Ir1*** functionalised (light blue) electrodes with **Ir1*** with photoanodic materials $BiVO_4$ and $ZnFe_2O_4$ provided by U.Wijayantha-Kahagala-Gamage and co-workers. RE: Ag/AgCl, CE: Pt wire in 0.1 M KNO_3 at 10 mVs^{-1}*

In addition to the photoanode materials described above, haematite (Fe_2O_3) was also investigated with **Ir1*** in collaboration with Prof. Geoff Ozin. Haematite shows several benefits as a photoanode material; it is stable in aqueous media at high pH, is Earth abundant and therefore relatively low cost and low toxicity. However, modification of the Fe_2O_3 structure is required to improve the photoactivity. Two modified Fe_2O_3 films were prepared and modified with the activated **Ir1*** compound by immersion; an air treated film (sample-A) and a hydrogen treat film (sample-H).[a] For both films dark and light CVs were collected, and the addition of the **Ir1*** reduced the overpotential for the water oxidation reaction for both films (Figure 5.15).[12]

[a] Catalyst synthesis and activation and film functionalisation performed at Bath, all other experiments performed by Ozin and co-workers

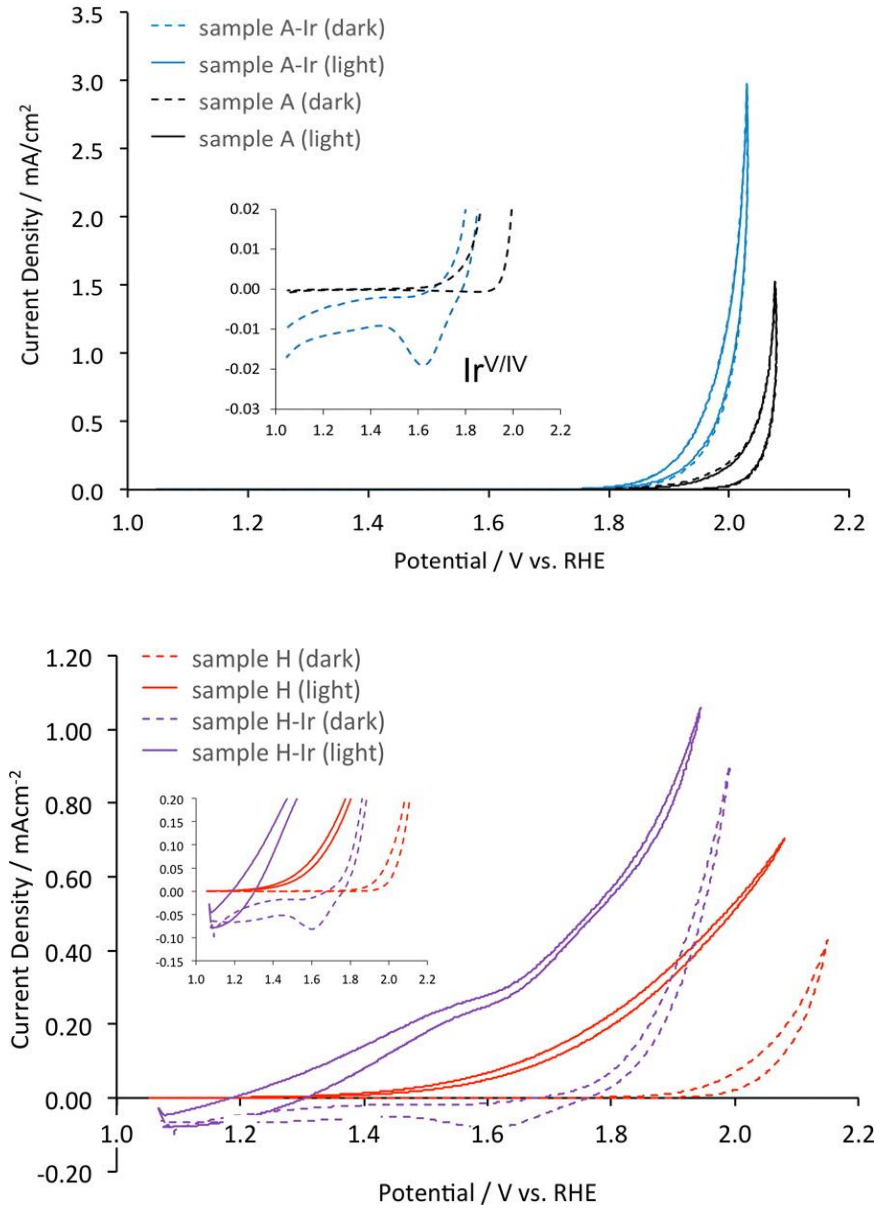

Figure 5.15. *Effect of addition of immobilisation of* ***Ir1**** *onto two different* Fe_2O_3 *films showing a decrease in overpotential with the presence of* ***Ir1****. Reproduced from Moir et al 2016*[12]

5.4 Fourier transform alternating current cyclic voltammetry

5.4.1 Introduction

Traditional CV analysis measures the current response as a result of an applied potential. However, the resulting current can arise from both Faradaic and non-Faradaic processes. Non-Faradaic currents, or capacitive currents, arise due to electro-capacitive charging and discharging of the 'double layer' which builds up at the electrode surface during the experiment. The Faradaic contributions, usually the ones under investigation, stem from typical electron transfer redox reactions, usually of the metal centre under investigation. During an electrocatalytic experiments, these redox events and can be segmented into catalytic and non-catalytic current.[13]

Determining the non-catalytic redox events, in order to assign them to a specific metal oxidation state transition, can be complicated by both capacitive currents and catalytic currents. In the case where the species in question is immobilised on an electrode surface, low surface coverage can result in the non-catalytic contributions being obscured due to large background capacitance.[14–16] Additionally, during a catalytic reactions, the net flow of electrons between the electrode and the substrate results in the catalytic current, which is dependent on the turnover rate of the catalyst in question. Typically, turnover rates are very high, so the corresponding catalytic current is also enhanced relative to the non-catalytic redox events, resulting in catalytic current amplification. As with the capacitive current, amplified catalytic current will also obscure any redox features under the catalytic wave, but any meaningful analysis of the mechanism or kinetics during the electrocatalysis requires comparison of the catalytic and non-catalytic currents. Investigating the complex in question in the absence of substrate can provide information about the non-catalytic features, (as with the non-aqueous CVs of precatalysts **Ir1**-**Ir7** seen in chapter 2) but similar analysis of the catalytic wave is difficult.

A number of alternative techniques have been developed where the applied voltage is modulated as a function of time, in order to separate out the Faradaic and the non-Faradaic current contributions, typically by applying a small amplitude perturbation to the voltage sweep.[14,15] A small amplitude is applied, in part due to the complications in the analysis of the results; the resulting sinusoidal current has the same frequency as the applied frequency.

The non-linearity between applied potential and current (for example the shape of a typical CV plot is non-linear) becomes more prominent when applying a large amplitude perturbation. This means that the frequency of the resulting current is no longer limited to the same as the frequency of the perturbation that was applied. Instead the current has several sinusoidal signals at differing frequencies (n x f), which made analysis complicated.

However, the difficulties in analysing the current response with large amplitudes were concurrently solved in 2000 by Gavaghan and Bond and Engblom, Myland and Oldham, by development of a technique now commonly called Fourier Transform Alternating Current Voltammetry (FTACV).[14–17]

FTACV still uses the typical three-electrode set up, but requires a specialised potentiostat which can apply a sine wave, with frequency f and amplitude Δ E, onto the potential usually applied during a linear voltage sweep (Figure 5.16)

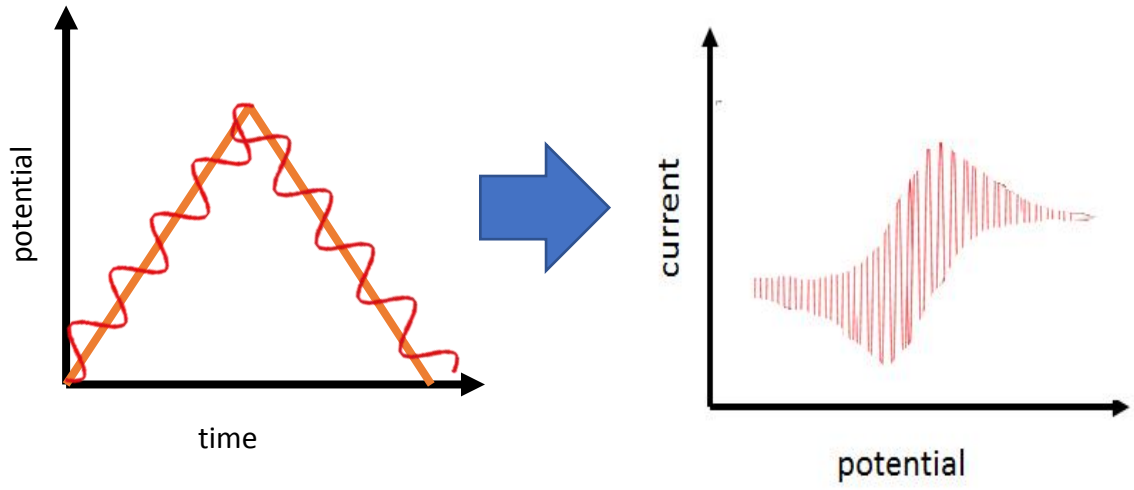

Figure 5.16. *Schematic of the applied perturbation to the potential/time step for a traditional CV and the corresponding CV response*

The applied potential, E_{app}, can therefore be described as the sum of the dc and ac contributions (Equation 5.1), where $\omega = 2\pi f$ is the angular frequency.

$$E_{app} = E_{dc} + \Delta E sin(\omega t)$$

As the total current output is measured as a function of time, a Fourier Transform can be applied to the waveform to get the different frequencies that make up the current contribution; a so-called power spectrum (Figure 5.17) By selecting specific frequencies from the power spectrum, and then inverting the Fourier Transform, certain harmonics can be deconvoluted and viewed as individual spectra.

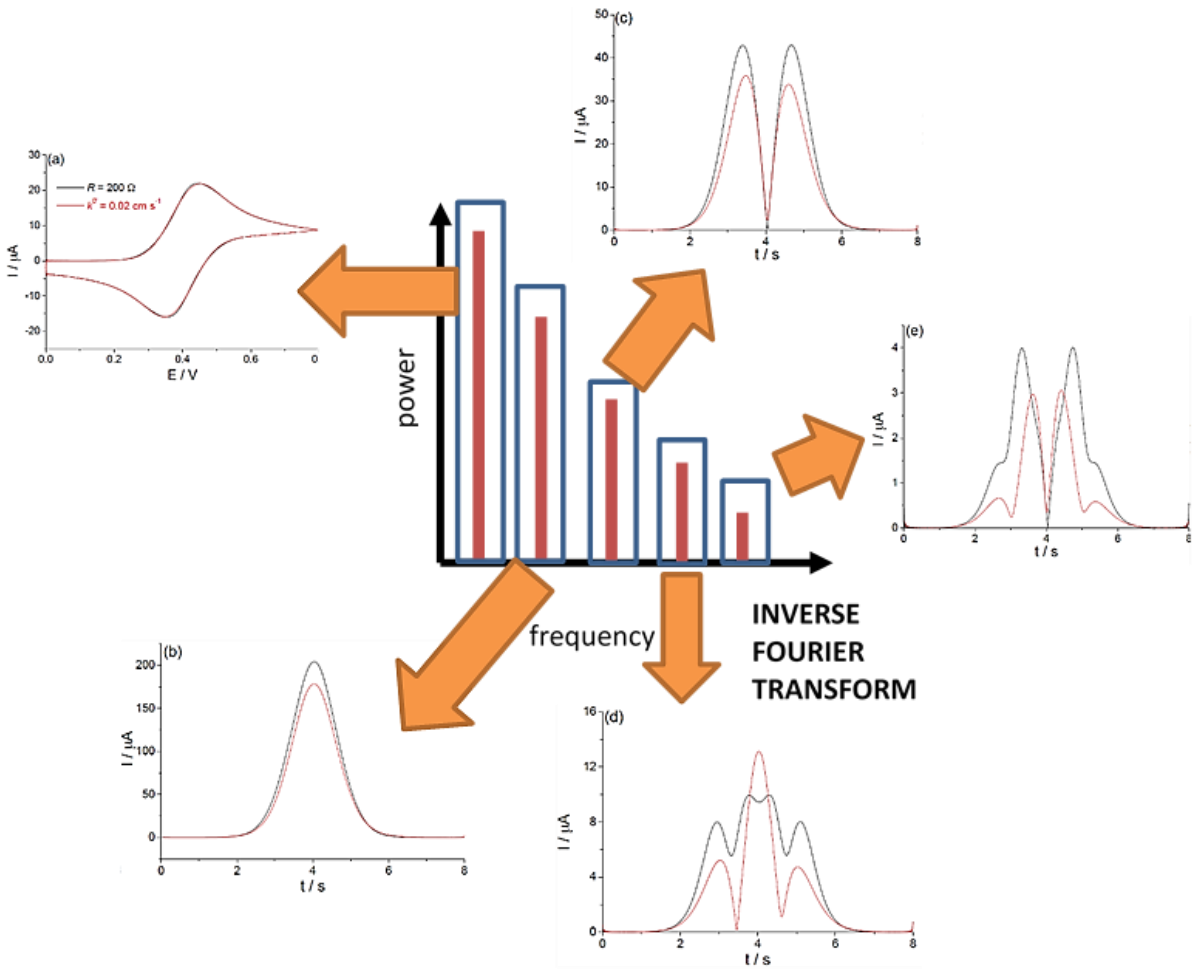

Figure 5.17. *The power spectrum resulting from the Fourier Transform of the sinusoidal components of the CV trace, and the individual inverse Fourier transforms resulting in the various individual harmonic components*[15,16]

At high enough frequencies/harmonics, the capacitive current contribution disappears. As an aside, theoretically the double layer at the electrode surface should behave as a simple capacitor, whereby the capacitive current will increase linearly with potential. In this situation, the resulting frequency would be the same as the input frequency, and no capacitive currents would be observed for the sinusoidal higher frequencies. In reality, the double layer is slightly potential dependent, so some capacitive current will potentially be

seen up to the 3rd/4th harmonics. Therefore, by looking at the higher harmonics, non-catalytic Faradaic currents obscured by non-Faradaic contributions can be elucidated.[14]

A solution was also found to decouple the catalytic and non-catalytic currents, assuming the speed of the electron transfer of the catalytic event is much smaller than the magnitude of the frequency (which is determined by n x f, where n is the harmonic and f is the frequency). Therefore, at high harmonics, and with a high enough frequency experiment, the chemical catalytic contributions to the current become minimal, and the underlying non-catalytic events can be determined.[14,16]

Although the FTACV harmonic traces indicate the presence of a redox event, the exact shape of the harmonic itself is inherently linked to the mechanism and kinetics of the redox reaction and any subsequent chemical processes. Therefore, extensive modelling is usually done to accompany the FTACV experimental data, and to assign the number of electrons transferred in the observed harmonic.

As in Chapter 2, CV analysis of the active water oxidation catalysts in water in inherently complicated by the presence of the substrate, but analysis of the underlying redox events that the metal centre undergo during catalysis is crucial for understanding the observed activity.

With a well-established method for depositing the activated water oxidation catalyst onto an electrode surface, FTAC CV was therefore employed to attempt to elucidate the redox events of the iridium metal centre during electrochemical catalysis, and thus attempt to determine the oxidation state of the active catalyst. This work was undertaken at Monash University with Dr. Jie Zhang and Prof. Alan Bond.

5.4.2 Alternating current voltammetry with ferricyanide

As an introduction to the technique, the DC and FTAC CV responses for ferricyanide, which undergoes a known, reversible, one electron redox event centred around ~0.4 V vs. NHE, can be seen in Figure 5.18.

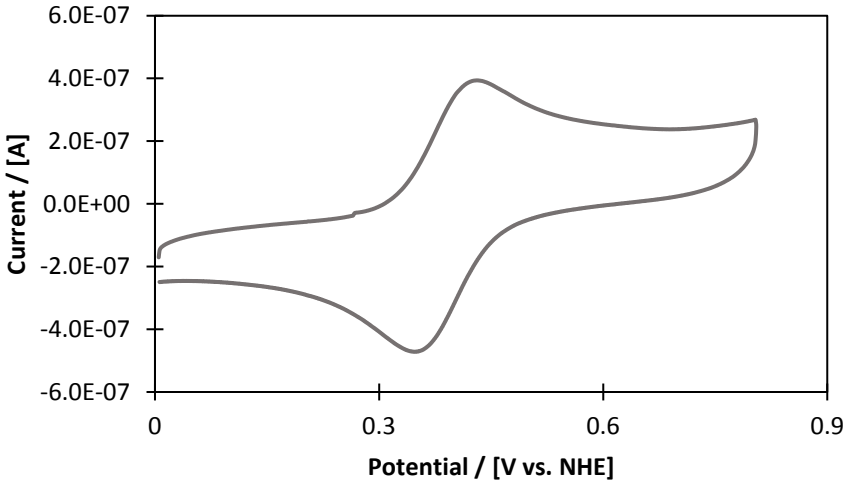

Figure 5.18a. *The dCV response of ferricyanide 30 µM $K_3(FeCN_6)$ in aqueous 0.1 M KNO_3, WE: Graphite, RE: Ag/AgCl, CE: Pt wire, Scan rate: 50 mVs^{-1}*

The typical CV response is seen with a reversible redox peak centred at 0.39 V vs NHE and a peak to peak separation of 80 mV. The redox peak can be clearly seen and not obscured by capacitive currents or catalytic activity, but the corresponding FTACV seen below demonstrates the varying harmonic responses.

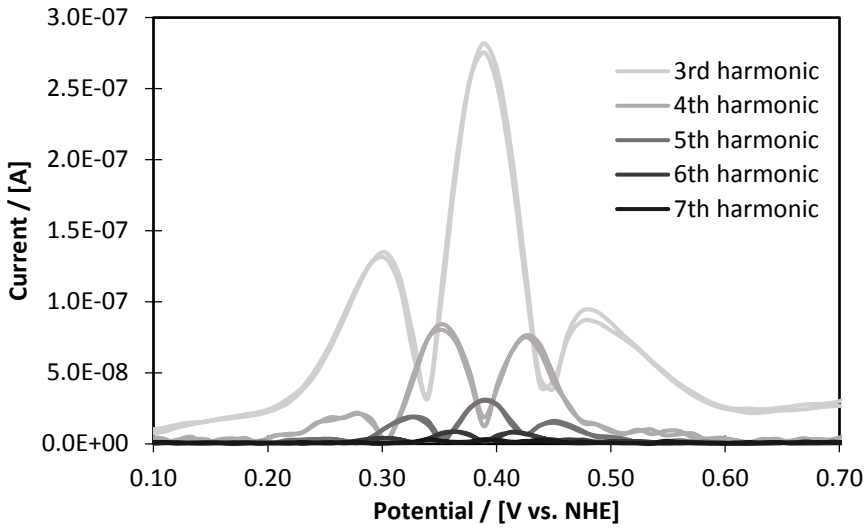

Figure 5.18b. *A standard CV response of ferricyanide 30 µM $K_3(FeCN_6)$ in aqueous 0.1 M KNO_3, WE: Graphite, RE: Ag/AgCl, CE: Pt wire, Scan rate: 50 mVs^{-1}, Harmonic: 3^{rd}- 7^{th}, Amplitude: 120 mV, Frequency: 27 Hz*

The 3^{rd}-7^{th} harmonics are shown here, although higher harmonics (up to 9^{th}) were observable, centred around 0.4 V vs NHE and therefore corresponding to the redox feature seen in the dCV. This is a good representation of the ideal harmonic response for a reversible one-electron process, with clearly delineated peaks for the different harmonics. Noticeably the current response is not perfectly symmetrical around the centre, but the reverse trace completely aligns with the forward oxidation sweep, indicating chemical reversibility as expected. Suffice to say, data of similar clarity was not observed for any other system investigated.

5.4.3 Alternating current voltammetry with ITO|FTO electrodes

In the first instance, the electrodes synthesised according to the published procedure with ITO|FTO[8] were functionalised with **Ir1*** and tested by FTACV (Figure 5.19).

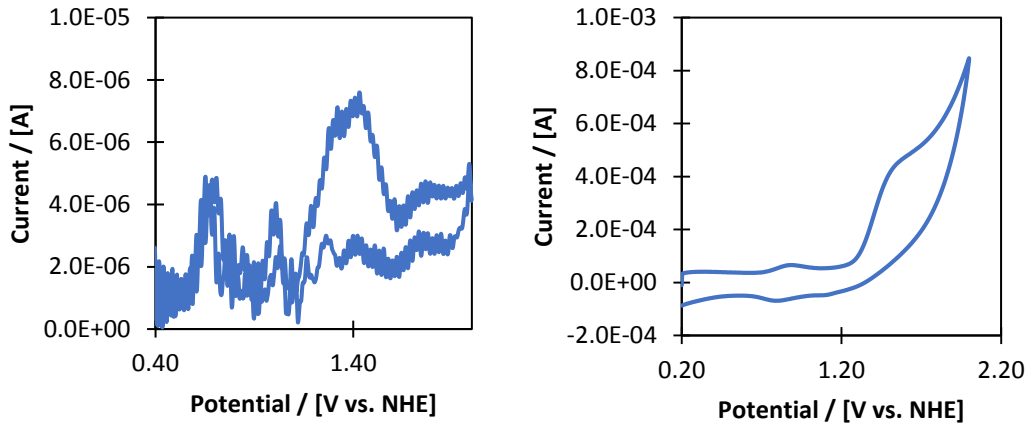

Figure 5.19. *FTAC CV and CV of functionalised ITO|FTO electrode in KNO_3. WE: functionalised ITO|FTO, RE: Ag/AgCl, CE: Pt wire, Scan rate: 50 mVs^{-1}, Harmonic: 3rd, Amplitude: 120 mV, Frequency: 9 Hz, Electrolyte: 0.1 M KNO_3*

The dCV showed a small redox feature at ~0.85 V vs NHE as well as a large catalytic wave attributed to water oxidation, with a potential second oxidation peak at ~1.50 V vs NHE; potentially a remnant from functionalisation or electrode synthesis. The corresponding FTACV data showed no harmonics higher than the 3rd (displayed in Figure 5.19). At this comparatively low frequency, contribution from capacitive current could still be observed, although there is potentially a reversible peak at ~0.7 V vs NHE and the oxidation feature seen in the dCV also appears in the FTACV. Despite these tentative assignments, without the higher harmonics available, limited concrete evidence can be drawn.

It was initially suggested that the lack of response was due to the film being too thin, and therefore not containing enough [Ir] to be produce a clear response, and thus the FTAC CV was re-run with a thicker film (Figure 5.20). The film thickness was not quantified here but was previously shown to be 2.5 µM thick after one spin coating with a solution of ITO nanoparticles.[9] The mesoporous nature of the nanoITO means that successive spin coating can be performed to increase the coverage of [Ir][8]; a thicker film in this case was achieved by three successive spin coatings.

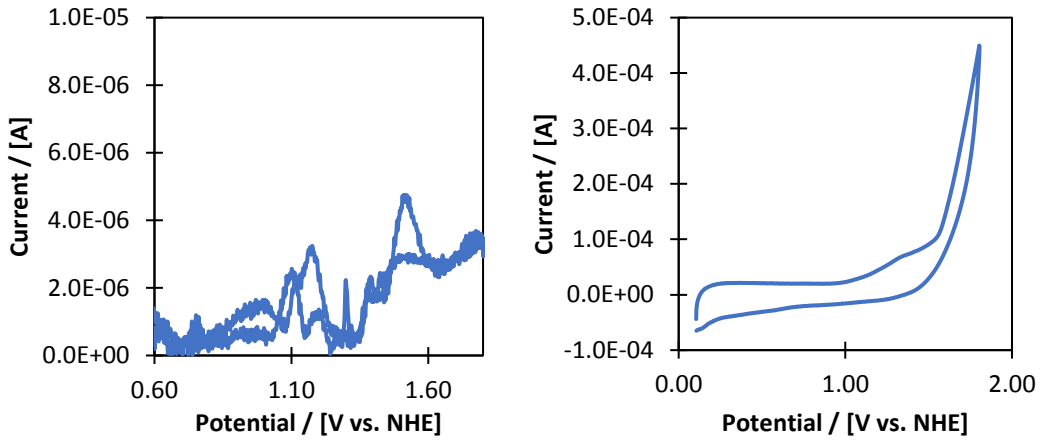

Figure 5.20. *FTAC CV and CV of functionalised ITO|FTO electrode with a thicker layer of ITO 3rd harmonic WE: functionalised ITO|FTO, RE: Ag/AgCl, CE: Pt wire, Scan rate: 50 mVs-1, Harmonic: 3rd Amplitude: Frequency: 9 Hz, Electrolyte: KNO3*

Although cleaner traces were observed in both the dCV and FTACV, again no higher harmonics were seen. A reversible feature at around 1.1 V vs NHE was seen by FTACV and again a single irreversible peak at ~1.5 V vs NHE were observed. However, as with the previous data, the lack of higher harmonics limits the utility of these data.

It was suggested that the supporting electrolyte could influence the bound catalyst and help achieve the higher harmonics. Thus, the functionalised electrode was investigated in K_2SO_4 (Figure 5.21).

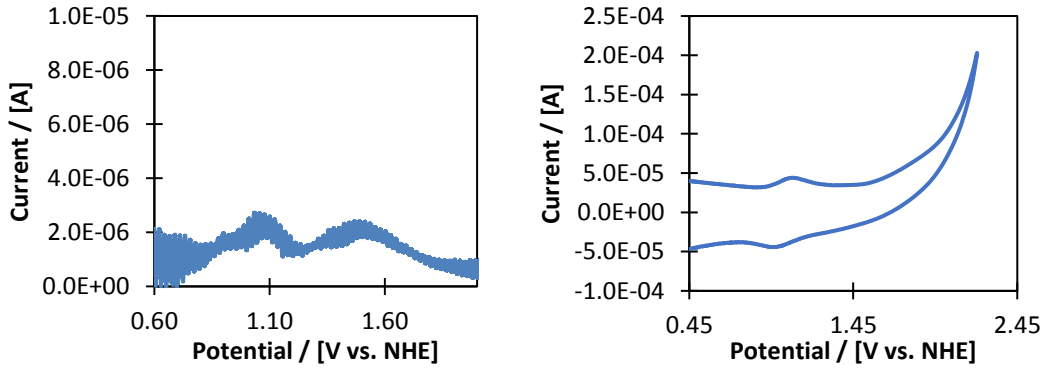

Figure 5.21. *FTAC CV and CV of functionalised ITO|FTO electrode in K_2SO_4 WE: functionalised ITO|FTO, RE: Ag/AgCl, CE: Pt wire, Scan rate: 50 mVs-1, Harmonic: 3rd Amplitude: 120 mV, Frequency: 9 Hz, Electrolyte: K_2SO_4*

Interestingly the resulting dCV showed lower overall current than with KNO_3, but the pre-feature was much sharper and better defined with a sulphate supporting electrolyte. The corresponding FTACV harmonics are also much more cleanly reversible than in KNO_3, with good overlap for the first peak at ~1.1 V vs NHE and a reversible peak for the feature at 1.5 V vs NHE. However, again no harmonics higher than the 4th were detected.

With no higher harmonics observed for the ITO|FTO films despite varying conditions, an unannealed ITO|FTO film was functionalised and tried. ITO is well known to have a so called 'goldilocks zone' for annealing and is particularly susceptible to over oxidation during the annealing process, and thus the lack of high harmonics was thought to be due to over reduction of the ITO. However, with the unannealed ITO|FTO electrode, no harmonic components were observed at all (Figure 5.22).

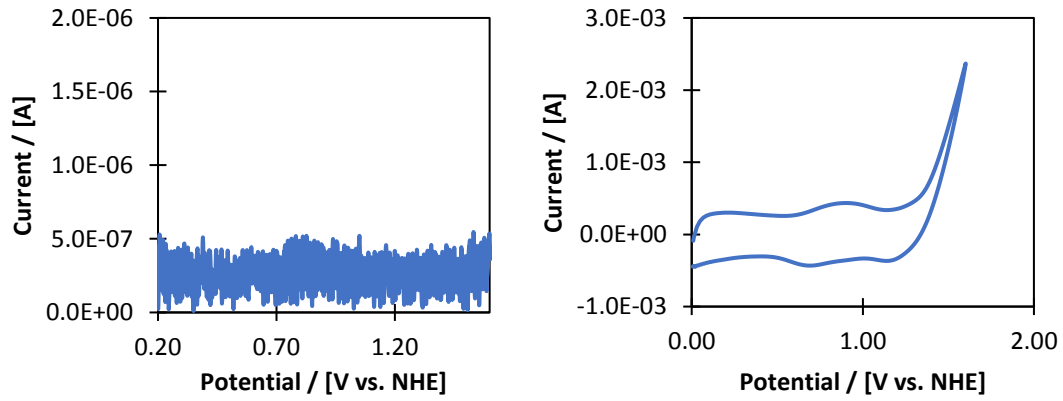

Figure 5.22. *FTAC CV and CV of functionalised ITO|FTO electrode in $NaNO_3$ WE: functionalised ITO|FTO, RE: Ag/AgCl, CE: Pt wire, Scan rate: 10 mVs^{-1}, Harmonic: 3rd, Amplitude: 120 mV, Frequency: 9 Hz, Electrolyte: 0.1 M $NaNO_3$*

5.4.4 Alternating current voltammetry with activated Ir1

Despite multiple attempts at FTAC CV with ITO|FTO electrodes, all proved futile, with no harmonics higher than the 4th observed under a range of different conditions. In order to see the higher harmonics in FTAC CV, the electron transfer kinetics must be extremely fast, and with two interfaces to traverse (**Ir1***|ITO|FTO), it was felt that the inherently slow electron transfer was the reason behind the lack of clear data.

To try and circumvent this, FTAC CV was undertaken with a solution of **Ir1**, which had been preactivated with $NaIO_4$, using a standard issue graphite electrode (Figure 5.23).

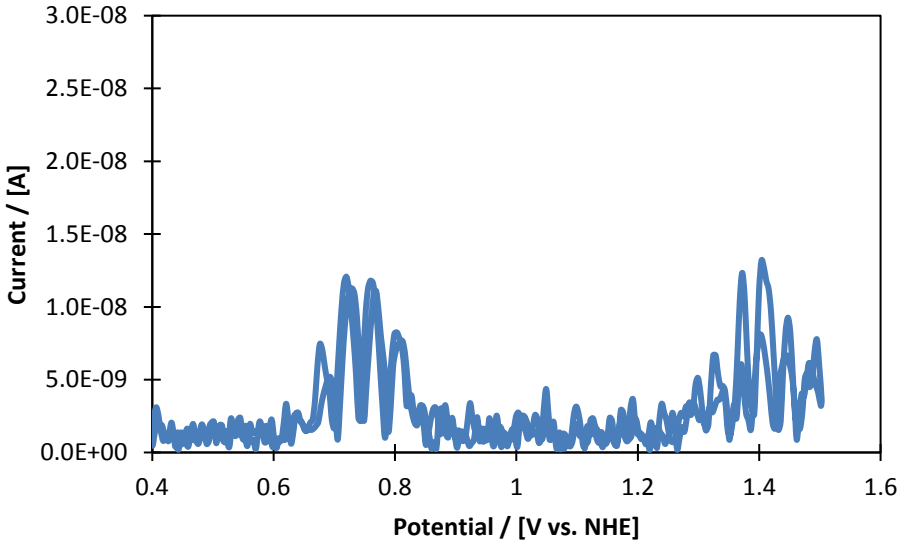

Figure 5.23. *FTACV 9th harmonic graphite electrode in **Ir1*** solution WE: graphite, RE: Ag/AgCl, CE: Pt wire, Scan rate: 100 mVs^{-1}, Harmonic: 9th, Amplitude: 120 mV, Frequency: 27 Hz, Electrolyte: 0.1 M KNO_3 with 0.3 mM **Ir1****

With the standard electrode, clear FTACV data were obtained, the trace above is for the 9th harmonic and shows clearly defined reversible features centred at ~0.7 vs NHE and ~1.4 V vs NHE. Interestingly the peak at 0.7 is at a similar position to the $Ir^{III} \rightarrow Ir^{IV}$ peak observed during the precatalyst CVs. Additionally, although there is a reduction peak at 1.4 V, it is not of equal intensity to the oxidation, suggesting some loss of the oxidised species and a slight lack of reversibility.

Typically, concurrent electrochemical modelling of the system is performed in order to elucidate how many electrons are transferred in the observed FTAC responses. However,

accurate modelling could not be conducted for this system, as the Ir* species was in solution and not immobilised on the electrode surface, and catalyst concentration is required in the model. However, qualitatively speaking, the comparative heights of the two peaks would potentially suggest that both events comprise the same number of electrons being transferred.

The open circuit potential (the resting potential of the solution where no current is flowing) was approximately 0.8 V vs NHE for the activated **Ir1*** solution. It is therefore inferred that at 0.8 V, the solution consists of Ir^{IV}-Ir^{IV}, the resting state of the activated catalyst.

The situation is complicated by the assumption that the activated species is dimeric, thus there is the potential that the two [Ir] metal centres could be in different oxidation states, or that both metal centres are oxidised in a two-electron process. This can be envisioned in Figure 5.24, where the potential oxidation state transfers are described for the case where one electron is transferred (b) and two electrons are transferred (a) at each potential redox event.

Figure 5.24. *Representation of the two possible electron transfer event scenarios for the data shown in Figure 5.21*

a) **0.7 V** Ir^{III}-Ir^{III} → Ir^{IV}-Ir^{IV} **1.4 V** IrIV-Ir^{IV} → Ir^{V}-Ir^{V}

b) **0.7 V** Ir^{III}-Ir^{IV} → Ir^{IV}-Ir^{IV} **1.4 V** Ir^{IV}-Ir^{IV} → Ir^{IV}-Ir^{V}

Last year, Crabtree and co-workers reported a synthetic procedure for an isolatable Ir^{IV}-Ir^{IV} oxo bridged dimer, similar to activated catalysts **Ir1***, although without the oxidative catalytic activity. CV analysis showed a highly reversible feature at 0.99 V vs NHE, which was attributed to the $Ir^{IV,IV}$ to $Ir^{IV,V}$ transition. There was also an irreversible event at 0.7 V vs NHE, which was assigned to $Ir^{III,III}$ to $Ir^{IV,IV}$. Further analysis in non-aqueous solvent revealed another oxidation event at a potential equivalent to 1.9 V vs NHE in DCM, which was again a reversible, one-electron event and was designated as the $Ir^{IV,V}$ to $Ir^{V,V}$ transition.

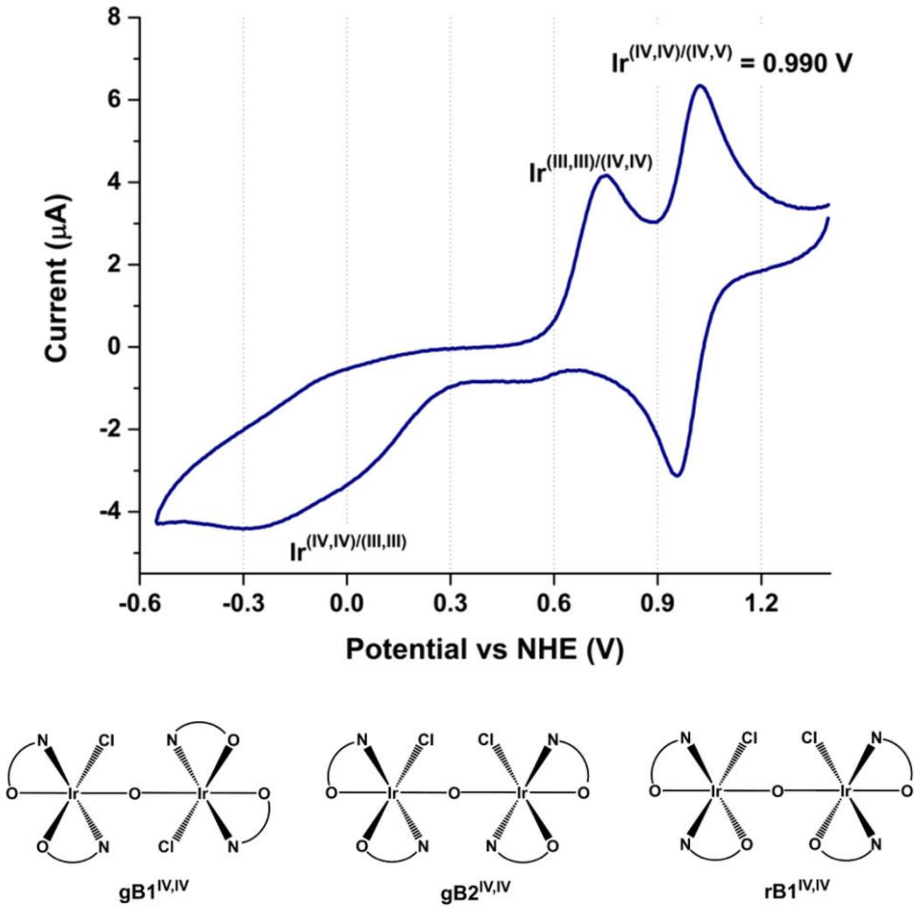

Figure 5.25. *Synthesised dimeric $Ir^{IV,IV}$ species reported by Sinha et al and the corresponding aqueous CV. Reproduced from Sinha et al 2017*[18]

Although these data are not exactly comparable to the system reported here, there are similarities to the FTAC data obtained. The value at 0.7 V can be assigned as the $Ir^{III/III} \rightarrow Ir^{IV/IV}$ transition, which would then suggest that the second event observed by FTAC (also a two-electron transfer) must be the $Ir^{IV/IV} \rightarrow Ir^{V/V}$ transfer.

5.4.5 Alternating current voltammetry with functionalised graphite electrodes

With the previously observed deposition of the activated catalyst onto certain electrode surfaces, the graphite electrode used for the previous experiments was removed, washed thoroughly, and retested in a blank electrolyte solution (Figure 5.26a).

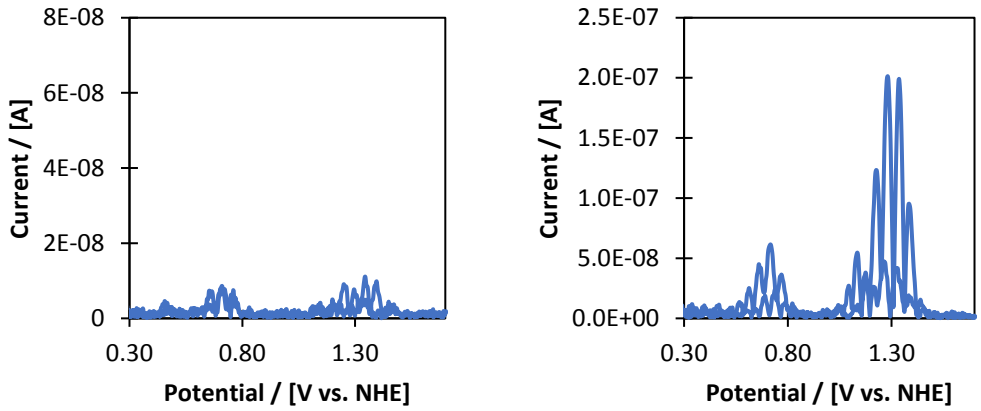

Figure 5.26. *a) after washing the graphite electrode used in the previous experiments b) after cycling the electrode in* ***Ir1**** *solution (cycle 23) WE: graphite, RE: Ag/AgCl, CE: Pt wire, Scan rate: 100 mVs^{-1} Harmonic: 7th, Amplitude: 120 mV, Frequency: 27 Hz, Electrolyte:0.1 M KNO_3 with 0.3 mM* ***Ir1****

Even after washing, remnants of the catalytic response were seen at harmonics as high as the 7th, with the characteristic peaks at 0.7 and 1.4 V vs NHE still noticeable, although at a lower current. It therefore appeared that the catalyst could be deposited onto a graphitic electrode surface, circumventing the need for the use of the sluggish ITO|FTO electrodes. It could also explain the lack of a response with BDD; the catalysts have been seen not to bind to BDD.

The graphite electrode was therefore repeatedly cycled in activated iridium solution in order to fully deposit as much Ir as possible (Figure 5.26b), although little change was seen after about the 11th cycle (Figure 5.27).

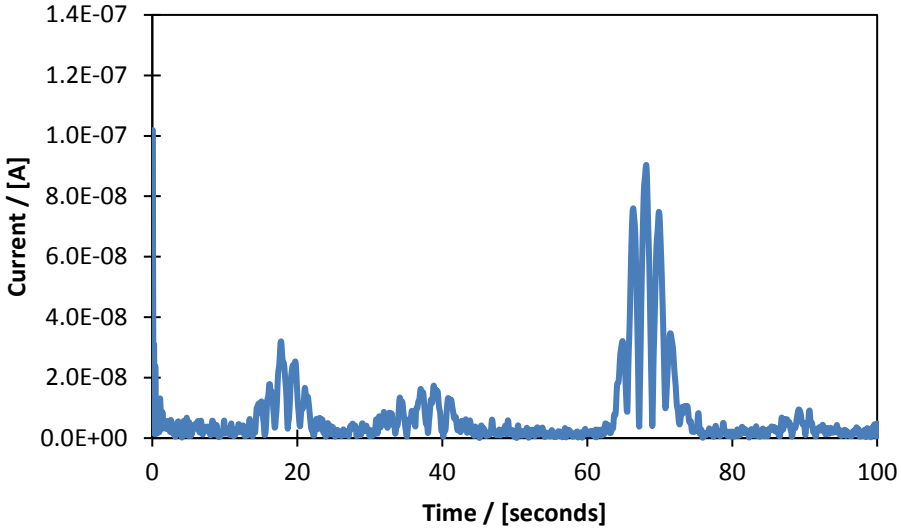

Figure 5.27. *FTAC of functionalised graphite electrode in* ***Ir1**** *solution after the 11th cycle showing current response against time WE: graphite, RE: Ag/AgCl, CE: Pt wire, Scan rate: 100 mVs-1, Harmonic: 7th, Amplitude: 120 mV, Frequency: 27 Hz, Electrolyte: 0.1 M KNO3 with 0.3 mM* ***Ir1****

The same peaks as before were still seen, although the reduction peak for the 1.4 V response was significantly larger than the original oxidation peak, and the reduction of the peak at 0.7 V vs NHE was comparatively smaller.

As has been stressed, concrete modelling of this system was not feasible because the model requires knowledge of the amount of surface bound catalyst. However, a comparison of the one and two electron processes modelled for a dimeric catalyst bound in a monolayer[b] (Figure 5.28) gives an indication of the expected comparitve current responses. A two electron transfer event for a dimeric catalyst would give a current that is approximately four fold greater than a single electron transfer.

[b] Modelling performed by Dr. Jie Zhang on in house software used for FTAC experimentation

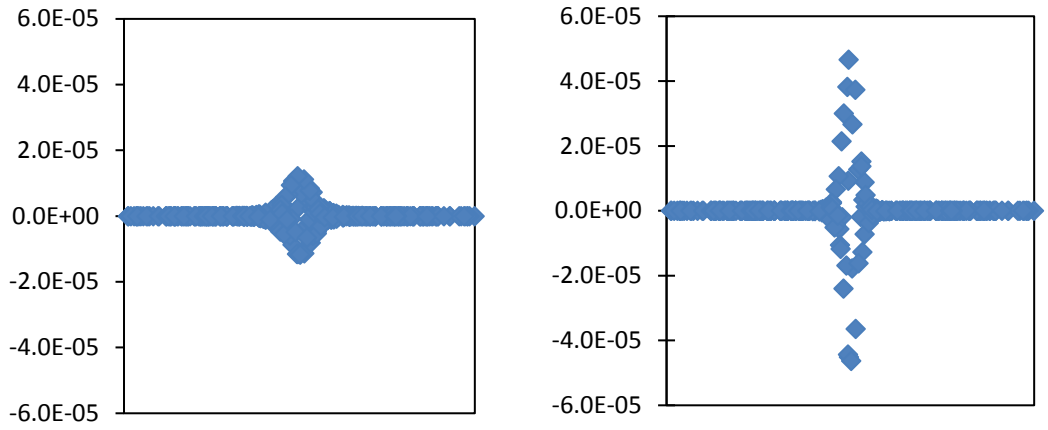

Figure 5.28. *comparitive approximate simulatios for the AC response for a 1 electron (left) and a 2 electron (right) redox event for a dimeric species bound to the surface*

With this in mind it seems likely that the reduction peak observed in involves twice as many electrode as the oxidation peaks, as the comparitive current of the reduction peak is four times greater than the oxidation events (9 x 10^{-8} A and 2.5 x 10^{-8} A respectively). Based on the comparative current responses this could be a function of the reduction peak being for a four- electron reduction, while the oxidation steps are double electron transfers (Figure 5.29).

Figure 5.29. *Potential oxidation events for solution based **Ir1*** after repeated cycling with graphite electrode*

oxidation	**0.7 V** Ir^{III}-Ir^{III} → Ir^{IV}-Ir^{IV}	**1.3 V** Ir^{IV}-Ir^{IV} → Ir^{V}-Ir^{V}
reduction		**1.3 V** Ir^{V}-Ir^{V} → Ir^{III}-Ir^{III}

The experiment was repeated with smaller potential windows to fully explore the reversibility of the individual peaks (Figure 5.30). Restricting the potential window to a single redox event ensures that influences from other events do not impact the reversibility.

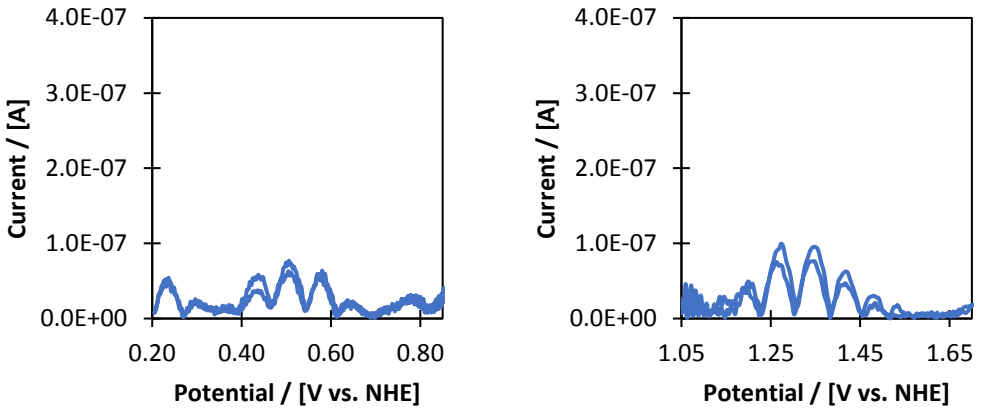

Figure 5.30. *FTAC CV of 'functionalised graphite' in electrolyte with varying potential windows to check reversibility WE: 'functionalised' graphite, RE: Ag/AgCl, CE: Pt wire, Scan rate: 100 mVs^{-1}, Harmonic: 8^{th}, Amplitude: 200 mV, Frequency: 27 Hz, Electrolyte: 0.1 M KNO_3*

There was a slight shift in the position of the lower peak from ~0.7 V to ~0.5 V vs NHE, but both peaks showed better defined harmonics and improved reversibility.

5.4.5.1 pH dependence of water oxidation with functionalised graphite electrode

Part of the initial motivation, for undertaking the FTACV data was to attempt to establish the relationship between [Ir] species and pH, potentially leading to construction of a Pourbaix diagram for the iridium catalysts. As such the pH of the solution was varied and the resulting FTAC harmonics compared (Figure 5.31).

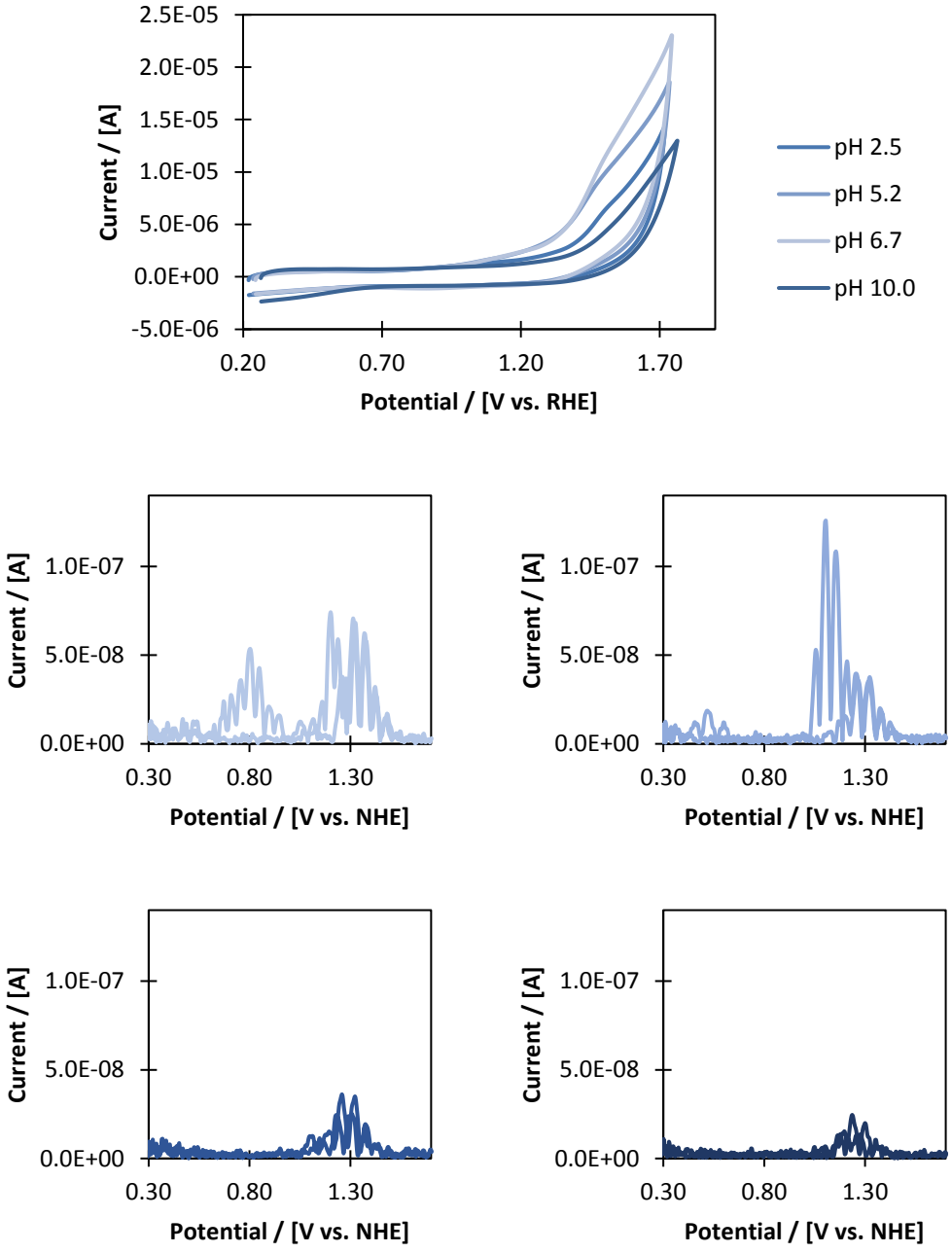

Figure 5.31. *CV and FTAC of functionalised graphite electrode with* ***Ir1**** *at varying pHs WE: 'functionalised' graphite, RE: Ag/AgCl, CE: Pt wire, Scan rate: 100 mVs^{-1}, Harmonic: 7th, Amplitude: 120 mV Frequency: 27 Hz Electrolyte: 0.1 M KNO$_3$*

Firstly, looking at the dCV component of the traces at varying pH it appears that the onset potential of the catalytic wave decreases from 2.5 → 5.2 → 6.7 and the current increases concomitantly. However, the onset potential of the catalytic wave appears to decrease again at pH 10, along with the peak catalytic current; an unexpected trend as the reduction potential of water oxidation decreases with increasing pH. Interestingly, this trend mirrors the previously observed data in Chapter 3, where the peak rate of water oxidation with **Ir1** was seen at pH ~7 and decreased either side.

Turning to the FTACV response traces, a large irreversible oxidation peak at ~1.2 V vs NHE is seen for pH 5.2 and 2.5. This feature is not reversible, not observed above pH 5.2 and is not seen in the solution CVs. It is therefore attributed to a solution artefact and not assigned to an [Ir] oxidation state.

At all pH values there is an apparent reversible peak at ~1.20 V vs RHE, which does shift slightly with increasing pH (Table 5.2), attributable to the $Ir^{IV,IV}$ → $Ir^{V,V}$ transition. The $Ir^{III,III}$ → $Ir^{IV,IV}$ peak at 0.7 V vs NHE, appears to have shifted from 0.8 V vs NHE at pH 2.5, to 0.5 V vs NHE in the pH 5.2 data, but is not seen at higher pHs.

Table 5.2. *peak assignments at varying pH with functionalised graphite electrode from the mid-point of the peak in the FTAC CV data in Figure 5.31 reported as Potential vs NHE*

	2.5	**5.2**	**6.7**	**10.0**
$Ir^{IV,IV}$ → $Ir^{V,V}$	1.36	1.32	1.26	1.24
$Ir^{III,III}$ → $Ir^{IV,IV}$	0.80	(0.52)	-	-

Notably decreased currents were observed for the FTAC traces at higher pH values. One possible explanation, is that binding of the active catalyst to the electrode surface is compromised at higher pHs, leading to a lesser amount of **Ir1*** on the electrode surface.[8]

5.4.6 Alternating current voltammetry with electrochemically activated Ir5*E

After the publication of the electrochemical method for precatalyst activation,[19] attempts were made at preactivating complex **Ir5** electrochemically, **Ir5***E (where the superscript E denotes electrochemical activation), and subsequent assessment of the FTACV response (Figure 5.32). To avoid contamination, a fresh graphite electrode was used in the electrochemically activated **Ir5***E solution. Binding has been shown not to occur for electrochemically activated complexes without the presence of IO_3^-,[8] and so catalyst deposition was not considered to be an issue for these experiments.

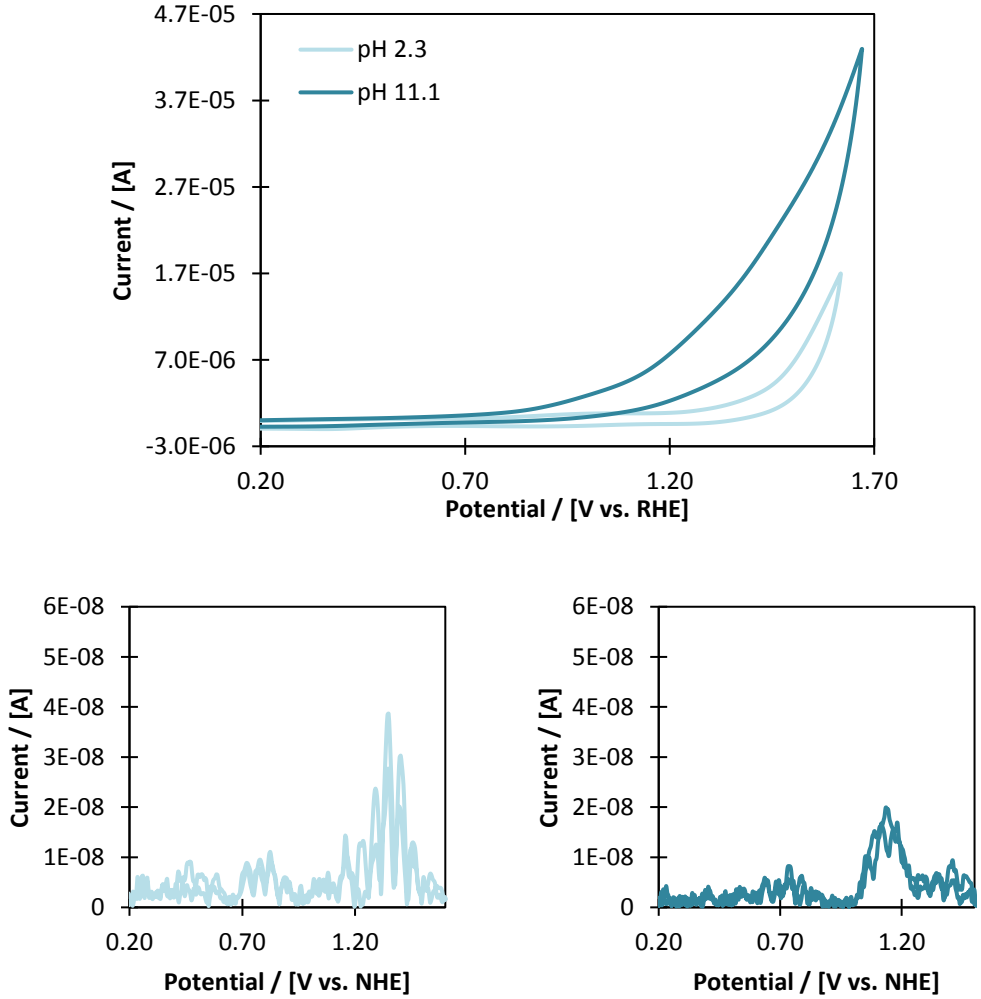

Figure 5.32**. Electrochemically activated **Ir5E at pH 2.3 and 11.1. CV and FTAC data WE: Graphite, RE: Ag/AgCl, CE: Pt wire, Scan rate: 100 mVs^{-1}, Harmonic: 7th, Amplitude: 120 mV, Frequency: 27 Hz, Electrolyte: 0.1 M K_2SO_4*

In this instance, clear differences in the pH response can be seen, with a big shift in the onset potential and a big increase in the catalytic current in the dCV and a shift of the peak at 1.20 V vs. NHE in the FTACV responses.

The ratio between the current of the two observable peaks in the FTAC harmonics is roughly 4:1 (at pH 2.5, the peak at 0.8 V is approximately 0.8 x 10^{-8} A and the peak at 1.4 V is approximately 2.8 x 10^{-8}), indicating that the second peak is a two-electron transfer event, and the first is a single electron event. Thus, the proposed transitions are from $Ir^{III,IV}$ → $Ir^{IV,IV}$ at 0.7 V and $Ir^{IV,IV}$ → $Ir^{V,V}$ at 1.2 V.

Figure 5.33. *Oxidation states assigned to the features observed in the FTAC traces from Figure 2.26*

0.7 V $Ir^{III,IV}$ → $Ir^{IV,IV}$ **1.2 V** $Ir^{IV,IV}$ → $Ir^{V,V}$

Table 5.3. *Peak assignments at varying pH with a graphite electrode in* ***Ir5****^{E} *from the mid-point of the peak in the FTAC CV data in Figure 5.32 reported as Potential vs NHE*

	pH 2.3	**pH 11.1**
$Ir^{IV,IV}$ → $Ir^{V,V}$	1.40	1.14
$Ir^{III,IV}$ → $Ir^{IV,IV}$	0.78	0.73

Although the oxidation state assignments are preliminary and not confirmed by modelling, the FTAC data described is extremely promising. For the first time a clear iridium redox event has been seen for electrocatalytic water oxidation. Although concrete assignment of the transition cannot be made, the initial experiments reported show great potential for further development and further elucidation of the oxidation state for the active catalyst.

5.5 Summary

The electrochemical activity of preactivated catalysts **Ir1***-**Ir7*** was investigated. Complex CVs necessitated direct measurement of oxygen evolution by synchronised chronoamperometry and Clark electrode experiments. Variation in ligands which had previously imparted different WO activity when driven with $NaIO_4$ also gave rise to different electrochemical activity, but with an entirely different relative order in catalyst activity. **Ir6** was the third most active complex for $NaIO_4$ driven water oxidation but was essentially inactive when driven with potential. Conversely the diphenyl complex **Ir2** showed high activity in the electrochemical oxygen evolution experiments; a result made more remarkable by the fact that the precatalyst has one of the highest $Ir^{III/IV}$ redox potentials and was the slowest water oxidation catalyst with chemical oxidants. The significant variation between catalyst performances with chemical or electrochemical potential further highlights that it is crucial to assess electrochemical activity in addition to other methods to find the best WOC.

In collaboration with groups at Loughborough and Toronto, immobilisation of **Ir1*** onto different photoactive electrode surfaces, $BiVO_4$, $ZnFe_2O_4$ and Fe_2O_3 was performed. All functionalised materials showed a decreased overpotential for the water oxidation activity of the photoanode in the dark CV. Deposition onto an ITO|FTO electrode surface was also performed, although issues with the transparency of the resulting films prevented analysis of surface binding.

Further complications with the nanoITO|FTO films were exposed when attempting to use the electrodes in FTACV experiment as part of work conducted at Monash University. By perturbation of the input potential signal, FTACV allows for investigation of redox events that would otherwise be obscured by catalytic or non-Faradaic current, but the double interface of the nanoITO|FTO electrode prevented the necessary fast electron kinetics. By using a graphite electrode in an activated solution of **Ir1***, redox features were successfully observed with FTACV, crucially with peaks at ~0.7 V and 1.4 V vs NHE. The first redox peak was assigned to an $Ir^{III,III}$ to $Ir^{IV,IV}$ couple, while the second peak, which was under the catalytic water oxidation wave, was assigned to the $Ir^{IV,IV}$ to $Ir^{V,V}$ couple; the first time such a redox feature has been observed under catalytic turnover.

During the experiments in **Ir1*** solution, some [Ir] bound to the graphite surface. Subsequent experiments with varying pH indicated a decrease in the potential of both the [Ir] redox events, but a lack of information about the surface coverage of [Ir] on the graphite electrode prevented accurate modelling of the system to confirm the electron processes.

Collating the FTAC data, assignments can be made to the previously described water oxidation cycle (Figure 5.33).

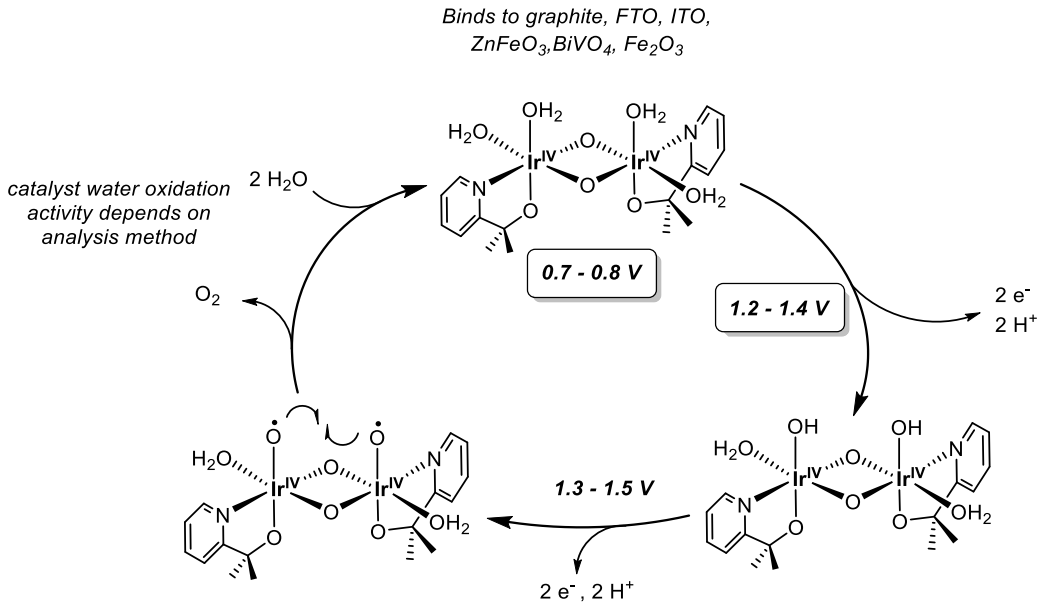

Figure 5.33. *Proposed cycle for water oxidation showing the possible redox potentials of the key [Ir] intermediates as determined by FTAC*

5.6 Experimental

All water oxidation experiments were performed with a Hansatech Oxygraph Plus system with a DW2/2 Clark-type electrode chamber (with temperature control and magnetic stirring) measuring dissolved O_2 in solution. The electrode was prepared with 2 M KCl electrolyte under a PTFE membrane and spacer paper, and the instrument was zeroed with the appropriate background solution depending on the reaction thoroughly degassed with argon. Solution pHs were measured with a 913 Metrohm pH meter.

All standard electrochemical data was collected using a standard three-electrode set-up and measurements carried out on an Ivium Technologies CompactStat. All electrodes were purchased from Bioanalytical Systems, Inc. in all cases the reference electrode used was Ag/AgCl in 3 M KCl, potentials were reported vs NHE or RHE according to the following:

$$E_{RHE} = E_{Ag/AgCl} + 0.205 + 0.059 \times pH$$

$$E_{NHE} = E_{Ag/AgCl} + 0.205$$

All iridium complexes were synthesised as previously described. Activation procedures are listed for each experiment. All other chemicals were purchased from major suppliers and used as received. Milli-Q water was used for all aqueous solutions.

CVs of Activated Ir for FOWA

Stock solutions of **Ir1**-**Ir7** (1 mM in H_2O) were activated with $NaIO_4$ (50 equivalents, 50 mM, 250 µmols, 53.5 mg) and stirred for 24 hours at room temperature. $NaNO_3$ (0.1 M, 0.5 mmols, 42.5 mg) was added as electrolyte. A CV of $NaIO_3$ (50 mM, in H_2O with 0.1 M $NaNO_3$) was also collected in the absence of Ir. CVs were collected at 100 mVs^{-1} scan rate, with a glassy carbon working electrode, (0.3 cm diameter, 0.07 cm^2 surface area), and the counter electrode was a 1 mm diameter platinum wire. Before use, carbon electrodes were thoroughly polished with alumina paste (1.0 µm then 0.3 µm), briefly sonicated (10 seconds), rinsed extensively with Milli-Q water and dried under a stream of Argon.

Electrochemical water oxidation

Concurrent water and electrochemical experiments were run simultaneously by insertion of the working, reference and counter electrodes into the chamber of the Clark electrode

containing the desired catalyst solution. In all cases the reference used was Ag/AgCl in 3 M KCl, and the counter electrode (Pt wire) was encased in a thin glass tube. Together with the working electrode, the three electrodes were taped together to ensure consistent spacing between them, and so that they were at the same depth in the Clark electrode chamber during each experiment. In the first instance, a Pt mesh electrode (size 0.5 cm by 0.5 cm, surface area unspecified) was used as the working electrode. Subsequently, and for all tests with catalyst solutions, a boron doped diamond plate (0.25 cm^2) attached to a copper wire with epoxy resin was used as the working electrode. Crucially, the Clark electrode was powered from the mains whilst the potentiostat was powered by a laptop via USB. During the experiments, the Clark electrode data was collected for 55 seconds, after which time the chronoamperometry was started, with a 5 second equilibration time. Data collected prior to the one-minute point was discarded, and the oxygen evolution data normalised by the baseline oxygen at the start of the reaction. In general experiments were run for 100 mins, with potential steps at 1.4, 1.5, 1.6 and 1.7 V held for 25 minutes. Water oxidation data collected after this time was discarded. Electrodes were washed thoroughly between runs with water. For all experiments, 2 mL of the appropriate solution was used each time.

Pre-activated catalyst solutions were prepared as follows. A solution of **Ir1**-**Ir7** (2.5 mM in 5 mL H_2O) were pre-activated with 100 equivalents $NaIO_4$ (250 mM, 1.25 mmols, 267 mg) and stirred at room temperature for 24 hours. Deposition and background checks were carried out in $NaIO_3$ (250 mM, 1.25 mmols, 247 mg in H_2O). Solution pHs were adjusted with NaOH and HNO_3 to approximately pH 6.

Electrode synthesis

NanoITO|FTO electrodes were prepared as follows. FTO glass was cleaned by sonication for 10 minutes in H_2O, then ethanol and the acetone and dried using a stream of argon. A 22 wt% suspension of nanoITO (0.3 g) in glacial acetic acid (0.3 g) and proof ethanol (1 mL). The resulting mixture was sonicated for 30 mins and then spin-coated (1000 rpm) onto a defined area of the clean FTO slide. The electrodes were then dried at 500 °C in air for 3 hours, before being annealed with 5 % H_2 in N_2 at 300 °C for 1 hour, resulting in a colour change of the ITO from yellow to pale blue. The resulting electrodes were soaked in a 5 mM solution of activated **Ir1** (with 50 equivalents $NaIO_4$) in H_2O and CVs were tested in 0.1 M KNO_3 electrolyte solution in H_2O with a Ag/AgCl reference electrode and a Pt counter electrode at pH 7 at a scan rate of 10 mvs^{-1}.

The photoactive electrodes ($BiVO_4$, Fe_2O_3, $ZnFe_2O_4$) were prepared by collaborators and sent for functionalisation and preliminary testing. The received electrodes were soaked in a solution of **Ir1** in H_2O (10 mM), activated with 30 equivalents of $NaIO_4$. The electrodes were left overnight and tested in 0.1 M KNO_3 electrolyte solution in H_2O with a Ag/AgCl reference electrode and a Pt counter electrode at pH 7 and a scan rate of 10 mvs^{-1}. An unfunctionalised electrode was used for comparison in each case.

FTAC CV

FTAC data was collected with a specially designed potentiostat in collaboration with Dr. Jie Zhang and Prof. Alan Bond at Monash University. Frequency, amplitude and scan rate variables were set for each experiment and are detailed in the appropriate figure caption. For all experiments, the counter electrode was a 1 mm diameter Pt wire and the reference was a Ag/AgCl in 3 M KCl. FTAC analysis was performed using a specially designed programme developed at Monash. For experiments with an ITO|FTO electrode, the electrode was prepared as described above and functionalised with Ir by soaking overnight in a solution of **Ir1*** (5 mM, pH 2.5, 50 equivalents $NaIO_4$ in H_2O). Experiments were conducted in 0.1 M KNO_3 or K_2SO_4 as described. The 'thicker' ITO|FTO electrode was prepared by three successive coatings of the ITO suspension and functionalised in the same solution.

The residual **Ir1*** solution used for electrode functionalisation was diluted to 0.3 mM **Ir1*** with H_2O and 0.1 M KNO_3. This was subsequently tested with a graphite carbon working electrode, (0.3 cm diameter, 0.07 cm^2 surface area). The graphite carbon electrode was thoroughly polished with alumina paste (1.0 µm then 0.3 µm), briefly sonicated (10 seconds), rinsed extensively with Milli-Q water and dried under a stream of Argon.

The graphite electrode was 'functionalised' by repeated cycling (25 times) between 0 and 1.5 V vs Ag/AgCl in 0.3 mM activated **Ir1*** solution at pH 2.5 at 100 mVs^{-1}. Subsequent testing of the electrode was conducted in 0.1 M KNO_3, which was pH adjusted (HNO_3/KOH.A solution of electrochemically activated **Ir5***^{E} was prepared according to the previously published procedure. A solution of **Ir5** (0.3 mM in H_2O with 0.5 M K_2SO_4) was subjected to a voltage of 1.45 V for 24 hours with continuous stirring. The resultant blue solution was used with a fresh graphite electrode for FTAC measurements. Again, pH adjustments were made with HSO_4 and KOH.

5.7 References

1. E. S. Rountree, B. D. McCarthy, T. T. Eisenhart, and J. L. Dempsey, *Inorg. Chem.*, 2014, **53**, 9983–10002.

2. K. J. Lee, N. Elgrishi, B. Kandemir, and J. L. Dempsey, *Nat. Rev. Chem.*, 2017, **1**, 1–14.

3. R. Matheu, S. Neudeck, F. Meyer, X. Sala, and A. Llobet, *ChemSusChem*, 2016, **9**, 3361–3369.

4. C. Costentin, S. Drouet, M. Robert, and J. M. Sav?ant, *J. Am. Chem. Soc.*, 2012, **134**, 11235–11242.

5. J. H. T. Luong, K. B. Male, and J. D. Glennon, *Analyst*, 2009, **134**, 1965–1979.

6. H. B. Martin, *J. Electrochem. Soc.*, 1996, **143**, 133–136.

7. R. Pokhrel, M. K. Goetz, S. E. Shaner, X. Wu, and S. S. Stahl, *J. Am. Chem. Soc.*, 2015, **137**, 8384–8387.

8. S. W. Sheehan, J. M. Thomsen, U. Hintermair, R. H. Crabtree, G. W. Brudvig, and C. A. Schmuttenmaer, *Nat. Commun.*, 2015, **6**, 6469–6478.

9. Z. Chen, J. J. Concepcion, J. F. Hull, P. G. Hoertz, and T. J. Meyer, *Dalt. Trans.*, 2010, **39**, 6950–6952.

10. S. Saremi-Yarahmadi, B. Vaidhyanathan, and K. G. U. Wijayantha, *Int. J. Hydrogen Energy*, 2010, **35**, 10155–10165.

11. P. Brack, J. S. Sagu, T. A. N. Peiris, A. McInnes, M. Senili, K. G. U. Wijayantha, F. Marken, and E. Selli, *Chem. Vap. Depos.*, 2015, **21**, 41–45.

12. J. W. Moir, E. V. Sackville, U. Hintermair, and G. A. Ozin, *J. Phys. Chem. C*, 2016, **120**, 12999–13012.

13. A. J. . L. R. F. Bard, *Electrochemical Methods*, 2000, vol. ISBN 0-471.

14. H. Adamson, A. M. Bond, and A. Parkin, *Chem. Commun.*, 2017, **53**, 9519–9533.

15. S.-X. Guo, A. M. Bond, and J. Zhang, *Rev. Polarogr.*, 2015, **61**, 21–32.

16. A. M. Bond, N. W. Duffy, S.-X. Guo, and J. Zhang, *Anal. Chem.*, 2005, 827–872.

17. A. M. Bond, K. B. Oldham, and G. A. Snook, *Anal. Chem.*, 2000, **72**, 3492–3496.

18. S. B. Sinha, D. Y. Shopov, L. S. Sharninghausen, C. J. Stein, B. Q. Mercado, D. Balcells, T. B. Pedersen, M. Reiher, G. W. Brudvig, and R. H. Crabtree, *J. Am. Chem. Soc.*, 2017, **139**, 9672–9683.

19. J. M. Thomsen, L. Que Jr., S. M. Hashmi, J. Campos, U. Hintermair, R. H. Crabtree, and G. W. Brudvig, *J. Am. Chem. Soc.*, 2014, **136**, 13826–13834.

CHAPTER 6

CONCLUSIONS AND FUTURE WORK

6. Conclusions and Future Work

6.1 Global Conclusion

A library of novel iridium complexes bearing varying pyridine alkoxide ligands was synthesised and tested for their solution behaviour and oxidative capabilities. Lability of the chloro- ligand in aqueous solution resulted in speciation of the iridium complexes. The extent to which this occurred varied with ligand bulk and electronics, such that complexes bearing slightly electron withdrawing aryl groups, **Ir2** and **Ir7**, retained the chloro- ligand, but the bulky bis-^{t}butyl groups on **Ir3** prevented synthesis of the chloro- compound and resulted in a cationic species. Analysis with cyclic voltammetry showed E_{mid} potentials for the Ir^{III} to Ir^{IV} transition, which varied with the electronics of the ligands. A transition for the cationic complexes was not observed in the potential ranges tested, presumably due to the demands of removing a further electron from a cationic species.

Precatalyst activation with sodium periodate and followed by UV-vis spectroscopy and ^{1}H NMR, revealed that the Cp* ligand was lost for all complexes within 5 mins of activation, but substantially different times were taken for the complexes to evolve the blue colour attributed to the fully activated catalyst.

The complexes were all tested for their activity for both water and C-H oxidation reactions, under varying conditions, such as solvent, pH and oxidant, and kinetic isotope effects and catalyst order were determined. Additionally, true electrochemical water oxidation was investigated, as well as brief investigation into immobilisation of **Ir1*** onto an electrode surface. Investigations into the oxidation state of the [Ir] during electrochemical water oxidation with **Ir1***revealed a clear redox event under the catalytic wave. This transition, which is assigned to $Ir^{IV,IV} \rightarrow Ir^{V,V}$ occurs at a potential suitable for water oxidation, and is an *in situ* glimpse into the active species of the complexes during catalysis.

A comparison of the complexes for their activation, C-H and water activity and electrochemical performance can be found in Figure 6.1. A correlation of the physical data and a proposed mechanism from the relevant Chapters can be seen in Scheme 6.1.

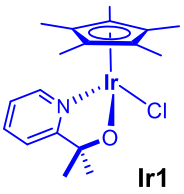

Ir1

Best water oxidation catalyst with chemical oxidant

Reduced C-H selectivity

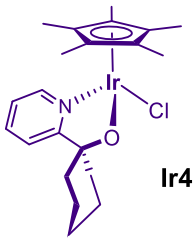

Ir4

Increasing alkyl bulk slightly reduces chemical water oxidation

Lowest C-H oxidation selectivity

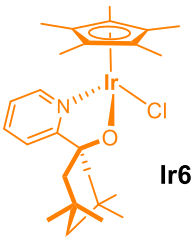

Ir6

Lowest E_{mid} values for $Ir^{III} \rightarrow Ir^{IV}$

Completely inactive for water oxidation with potential

Cyclohexyl groups promote solution speciation

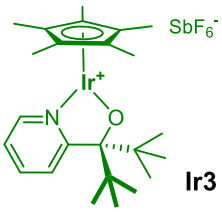

Ir3

Increased bulk with ^{t}butyl prevents Ir-Cl species

Increased bulk improves C-H selectivity by restricting dimer formation

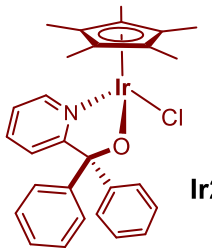

Ir2

Poor water oxidation catalyst with $NaIO_4$

Highest selectivity to C-H oxidation

Best water oxidation catalyst when driven electrochemically

^{t}BuOH completely shifts dimer/monomer

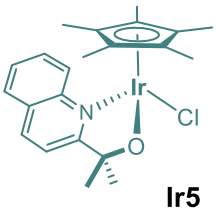

Ir5

Quinoline improves C-H oxidation selectivity

Quinoline reduces chemical and electrochemical water oxidation activity

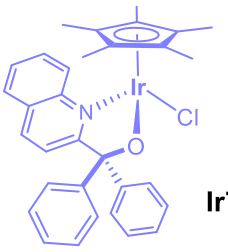

Ir7

Does not form dimeric active species at all

Slow water oxidation catalyst but high C-H selectivity

Figure 6.2 *Summary of ligand effects on water and C-H oxidation catalysis*

Scheme 6.1. *An overall suggested mechanism correlating the key data reported herein*

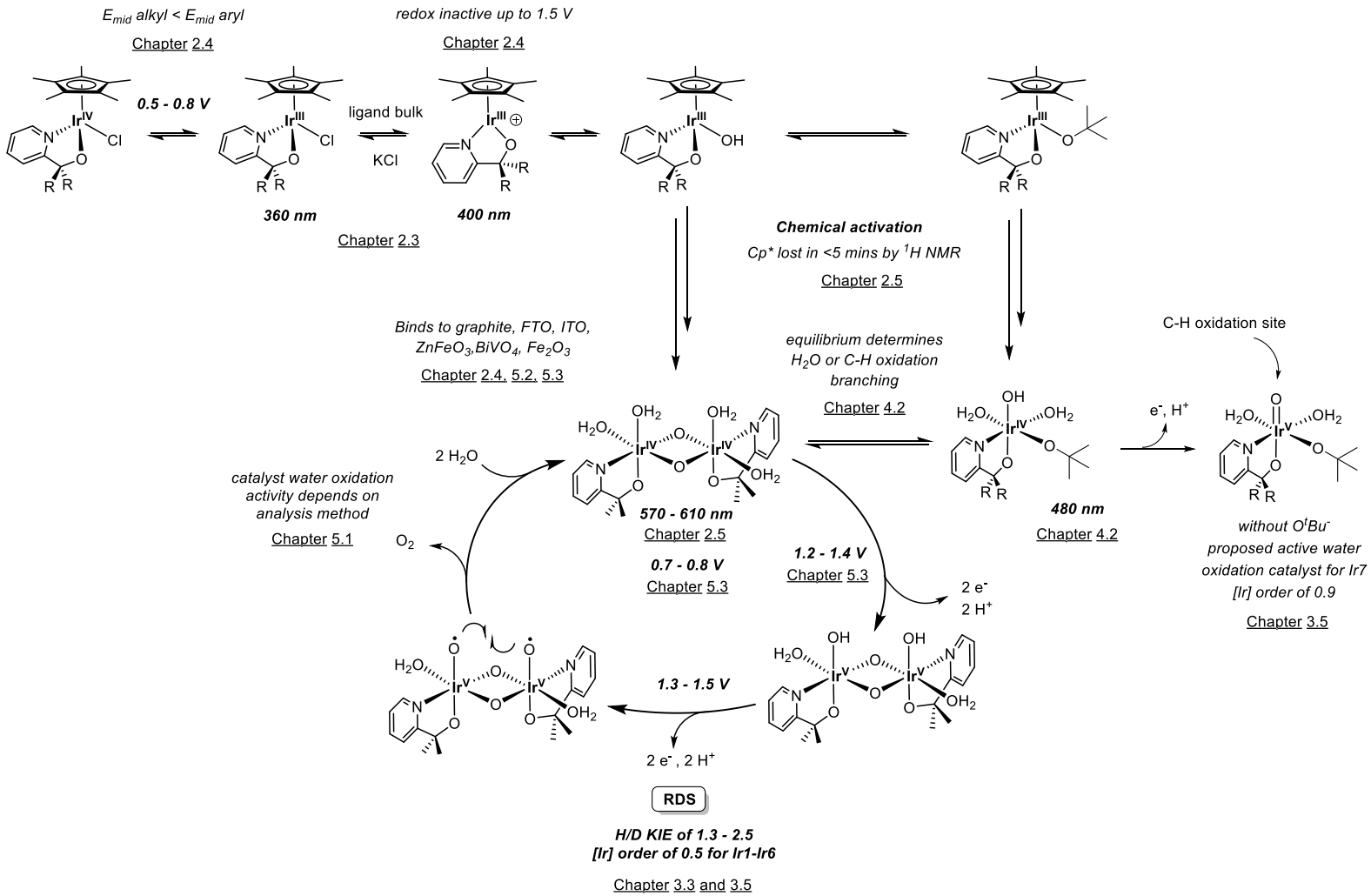

The behaviour of pyridine alkoxide complexes **Ir1**, **Ir3**, **Ir4** and **Ir6** can be explained with Scheme 6.1. The slight electronic effects with **Ir6** > **Ir4** > **Ir3** > **Ir1** influence the E_{mid} values in that order, but in terms of catalytic activity ligand bulk has a more important role. For water oxidation, the smallest dimethyl bearing compound **Ir1** shows the fastest water oxidation kinetics and **Ir3** the slowest. The order is reversed when considering the C-H conversion plateau, with the bulkier **Ir3** complex giving the highest C-H conversion and **Ir4** the lowest. In the presence of C-H substrate, and ^{t}BuOH, the water oxidation activity mirrors the same trends, which are the inverse of the C-H conversion **Ir1** > **Ir4** > **Ir6** > **Ir3**.

Analysis of the UV-vis data of **Ir2** with and without 20% ^{t}BuOH led to the determination that a monomeric species is responsible for the C-H oxidation, whilst the dimeric species is the most active water oxidation catalyst.

Thus, it is suggested that the branching ratio for C-H vs water oxidation, with pyridine alkoxide bearing complexes is dependent on ligand bulk. Bulkier ligands in the **Ir3** complex result in preferential formation of the monomeric species, and thus an enhanced C-H oxidation selectivity.

The diphenyl complex **Ir2**, although also a pyridine bearing compound, has shown markedly different behaviour to the alkyl substituted compounds. It is suggested that the electron withdrawing phenyl groups promote the formation of a monomeric **Ir2**-O^{t}Bu species, if ^{t}BuOH is present in solution, as determined by UV-vis spectroscopy of the activation of **Ir2**. The strongly held OtBu ligand prevents dimerization, and thus entirely suppresses water oxidation activity if C-H oxidation substrate is available. This is evidenced by the almost qualitative conversion of C-H substrate, and a consumption of oxygen as seen during oxygen evolution assays.

Quinoline complex **Ir7** showed loss of its Cp* ligand by ^{1}H NMR during precatalyst activation, but a very small absorbance band for the Ir^{IV}-O-Ir^{IV} species by UV-vis spectroscopy. In combination with VTNA data which showed an order in [Ir] of 0.9, it was proposed that **Ir7** activates to a monomeric species which performs water oxidation by a different mechanism to complexes **Ir1**-**Ir6**.

6.2 Catalyst development and design

Throughout the catalyst comparison data, **Ir2** consistently showed the greatest variation, thus a key focus of any further work would be focussed around this complex. In particular, more directed analysis of species present during water and C-H oxidation by concurrent UV-vis experiments, for example UV-vis analysis during C-H oxidation, kinetics of the C-H oxidation to assess catalyst order. In order to further explore the monomer/dimer equilibrium, titration with increasing ^{t}BuOH could reveal whether the proposed **Ir2**-O^{t}Bu species is formed from the dimer, or during catalyst activation. Similarly, in order to fully investigate the apparent consumption of oxygen during C-H oxidation, experiments under inert conditions, or with no oxidant but with oxygen gas bubbled through the reaction mixture could determine whether **Ir2** truly undergoes aerobic oxidation.

The interesting behaviour of **Ir2** also determines future catalyst development. Further investigation into varying the phenyl groups with electron withdrawing/donating groups is clearly worth undertaking. Synthesis of the bismethoxy version of **Ir2** has already been completed, as has ligand synthesis of a trifluoro ligand analgous to L1. Variation of the pyridine group to the equivalent pyrole system has also been initiated; further electronic variation is expected to yield more interesting catalysis results (Figure 6.2).

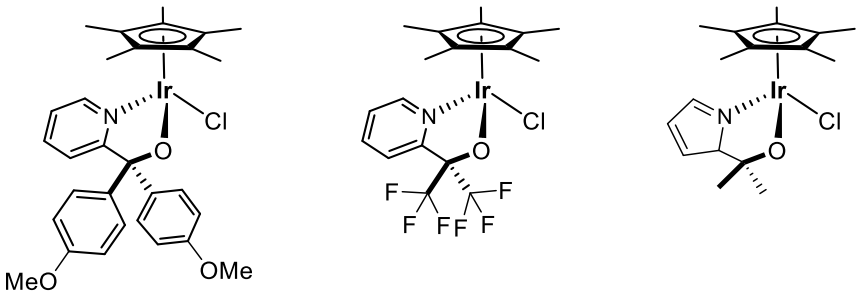

Figure 6.2. *Suggested catalyst systems suitable for further investigation*

Clearly the scope for ligand design is extensive, and variation of the placeholder Cp* ligand and the labile chloro- ligand is also viable; particularly replacement of the Cp* ring with carbonyl ligands, which require less oxidant to remove, and result in a cleaner solution mixture.

6.3 Catalyst immobilisation and application

With regards to catalyst application, extensive work was conducted into the solution behaviour of the catalysts, although the brief investigation into terpene oxidation is worth continuing, particularly with the current desire for renewable feedstock chemicals.

However, issues with the synthesis of the nanoITO|FTO electrodes meant that this area was not explored to its full potential. Variation of the annealing method, for example by reducing the inlet annealing gas from 5% H_2 in N_2 to 2% H_2 in N_2, or by more accurate control of the flow rate, could help produce suitable films. Alternatively, a more precise film synthesis method via Assisted Layer Deposition (ALD) might prove preferable.

There is also scope for changing the metal oxide from the notoriously 'fussy' ITO to a more robust Aluminium Tin Oxide (ATO); ATO is not optically transparent as ITO and has shown a higher capacitance in the background tests,[1] but could prove more robust for the end application of a functionalised anode. Similarly given the result observed by FTAC that **Ir1*** bound to a graphitic carbon electrode means that carbon-based supports are also worth investigating.

If the ITO|FTO electrode can be optimised, analysis of the surface binding kinetics of the varying catalysts could be undertaken with a diffuse reflectance UV-vis instrument. Alternatively, a brief start was made into analysing the catalysts via Surface Plasmon Resonance (SPR), which would allow for investigation into their binding kinetics without the need for ITO.

6.4 Catalyst oxidation state

The preliminary FTACV data was extremely promising, with clear redox events seen under the catalytic wave for water oxidation with **Ir1***. As detailed, concrete assignment of these features as single or double electron transfer events requires knowledge of how much catalyst is bound to the surface. One way to circumvent this is to use graphite plates as the working electrode. With the activated **Ir1*** apparently binding to graphite during electrochemical cycling, and by using a disposable graphite plate of known area, the amount of Ir could be calculated by destruction of the plate allowing for accurate modelling. The preliminary pH data is also interesting enough to warrant further exploration.

6.4 Wider Implications

These systems have further demonstrated the robustness of the pyalk ligand and as such there is potential to move the away from the Cp* iridium complexes to more benign metal such as iron or copper. It is clear that variation of the oxidatively robust N^O ligand has a significant impact on the catalytic activity; the ability to molecularly tune a catalyst's selectivity with intelligent ligand design is of great importance for the development of catalyst systems which can perform such crucial transformations.

APPENDIX

Chapter 2

Original NMR spectra of L6-L7

3,3,5,5-Tetramethyl-1-(2-pyridyl)cyclohexanol, ***L6***

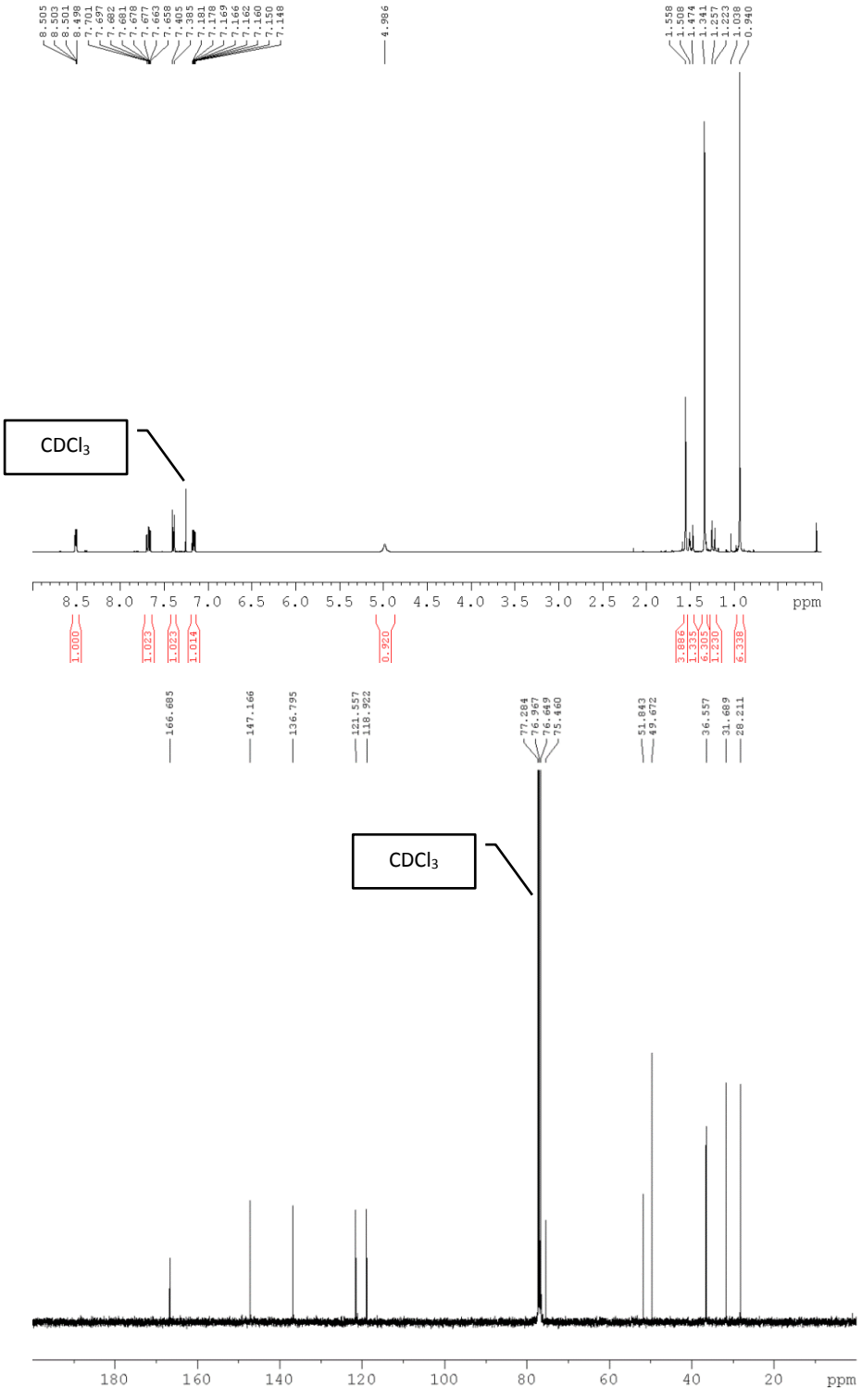

1,1-Diphenyl-1-(2-quinolyl)methanol, ***L7***

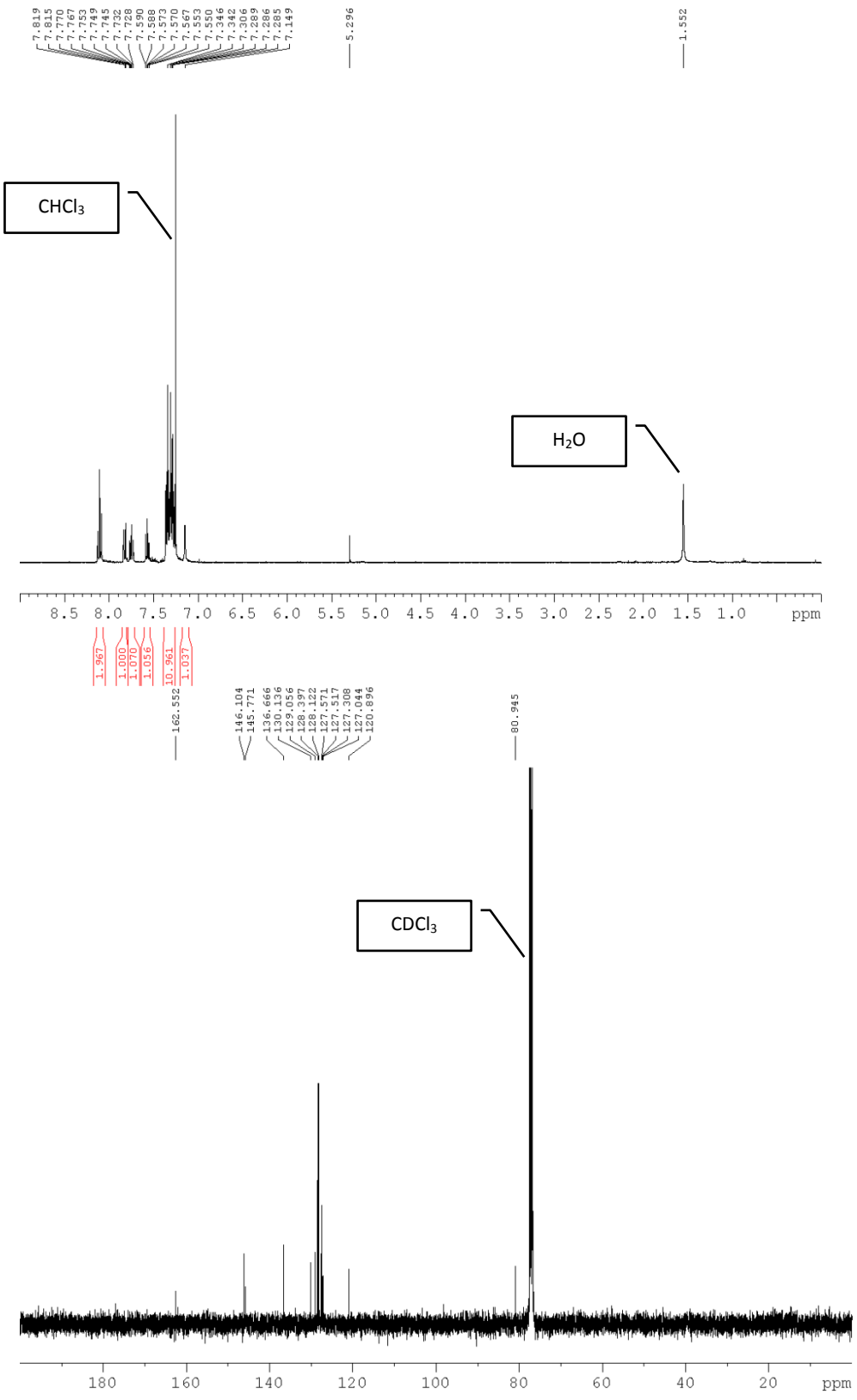

Original NMR spectra of Ir2-Ir7

[η⁵(C₅Me₅)Ir^{III}{Diphenyl(2-pyridyl)methanolate-κO,κN}Cl], ***Ir2***

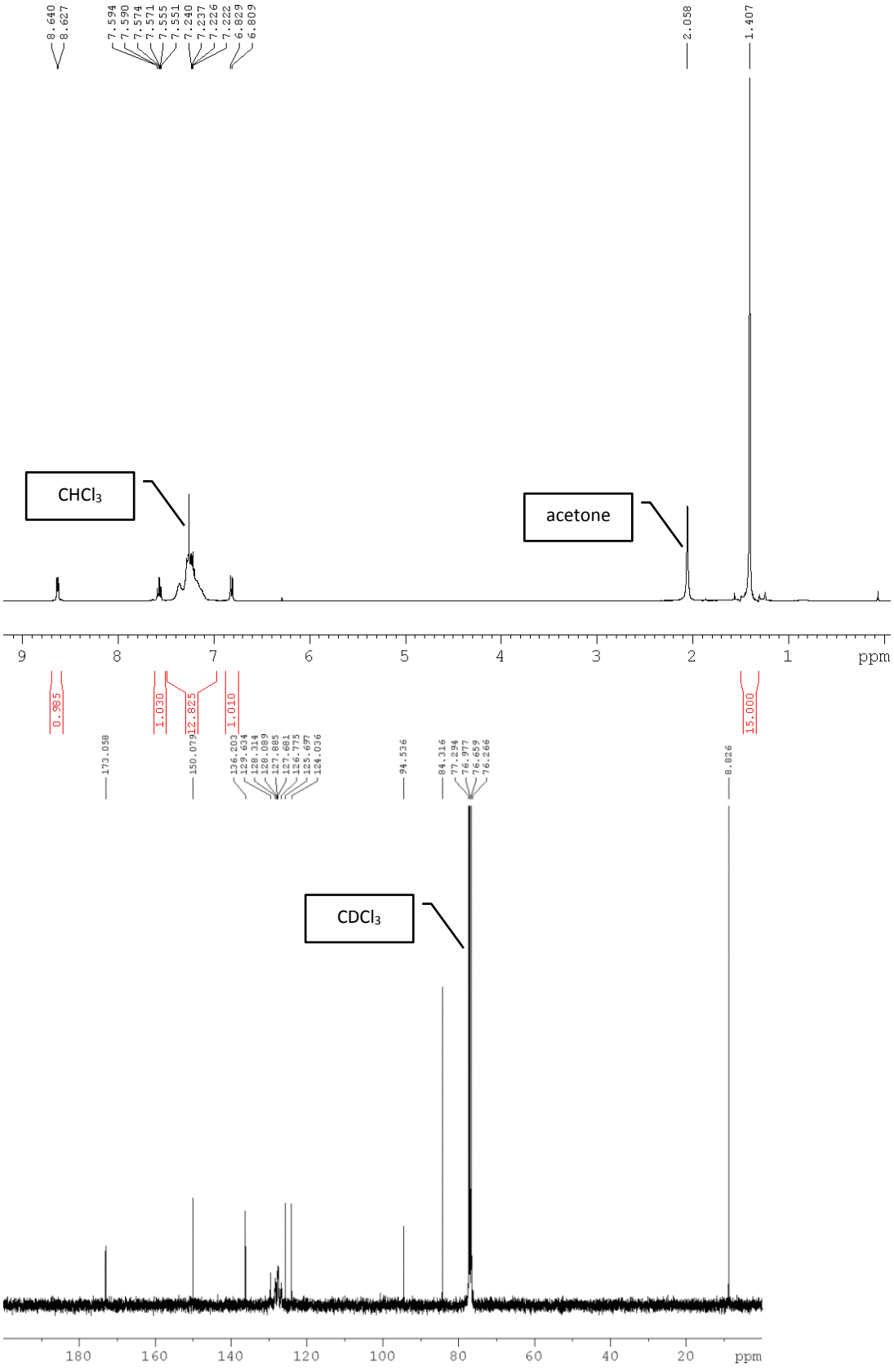

[η^5(C$_5$Me$_5$)Ir^{III}{2,2,4,4-Tetramethyl-3-(2-pyridyl)-3-pentanolate-κO,κN}] [SbF$_6$], ***Ir3$^+$***

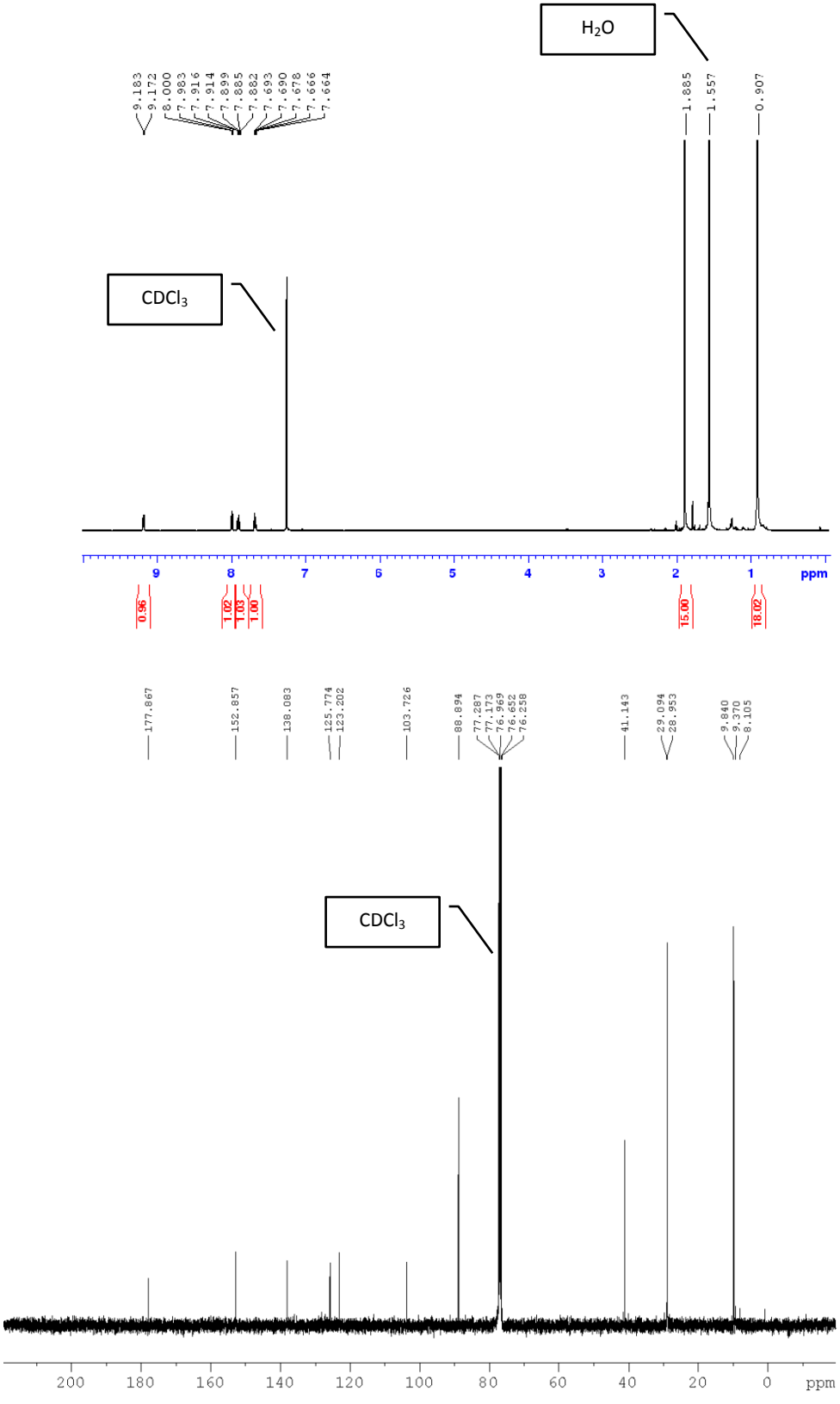

[η^5(C$_5$Me$_5$)Ir^{III}{1-(2-Pyridyl)cyclohexanolate-κO,κN}Cl], ***Ir4***

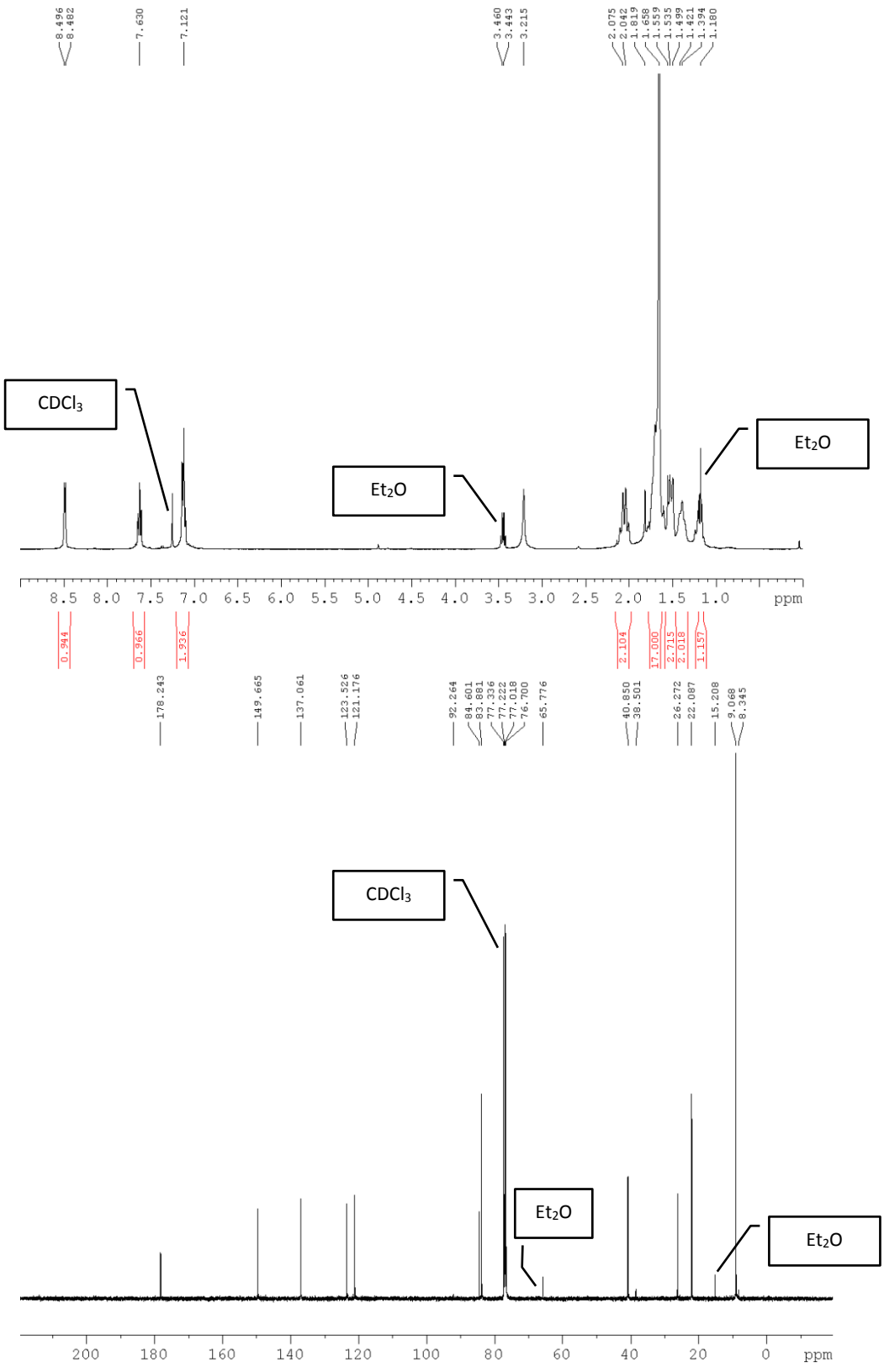

[η^5(C$_5$Me$_5$)Ir^{III}{2-(2-Quinolyl)-2-propanolate-κO,κN}Cl], ***Ir5***

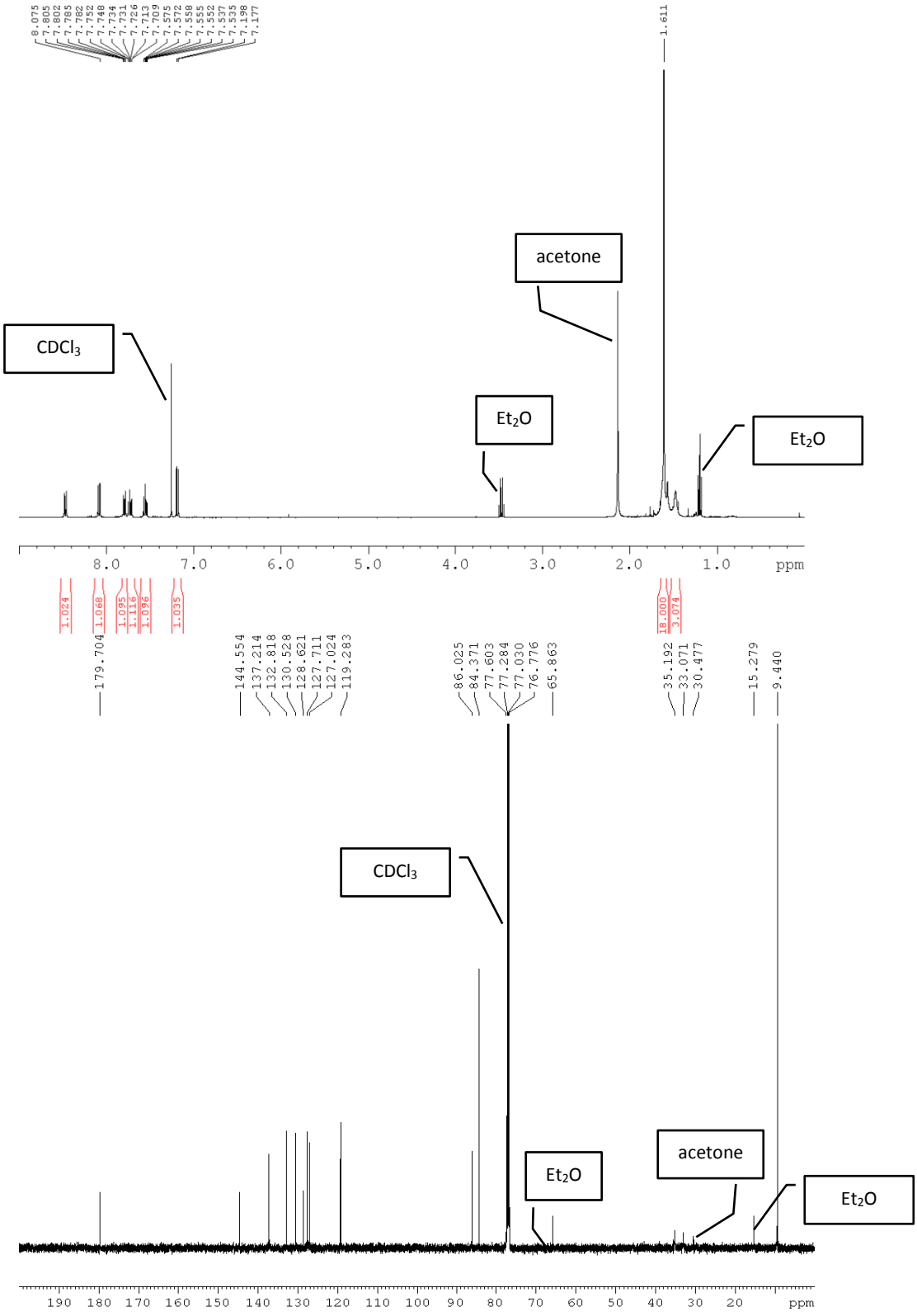

[η^5(C$_5$Me$_5$)Ir^{III}{3,3,5,5-Tetramethyl-1-(2-pyridyl)cyclohexanolate-κO,κN}Cl],
Ir6

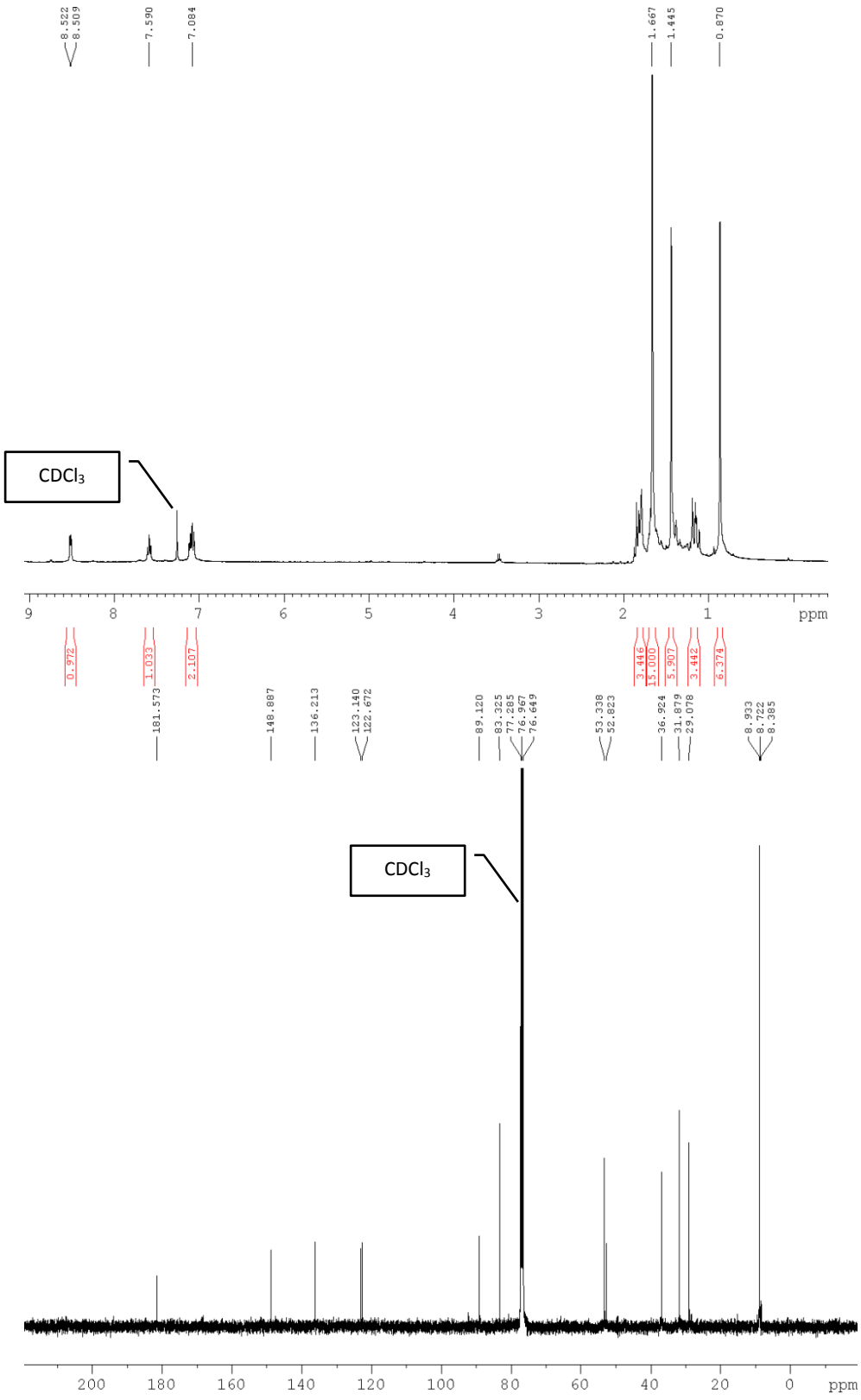

[η⁵(C₅Me₅)Ir^{III}{Diphenyl(2-quinolyl)methanolate-κO,κN}Cl], ***Ir7***

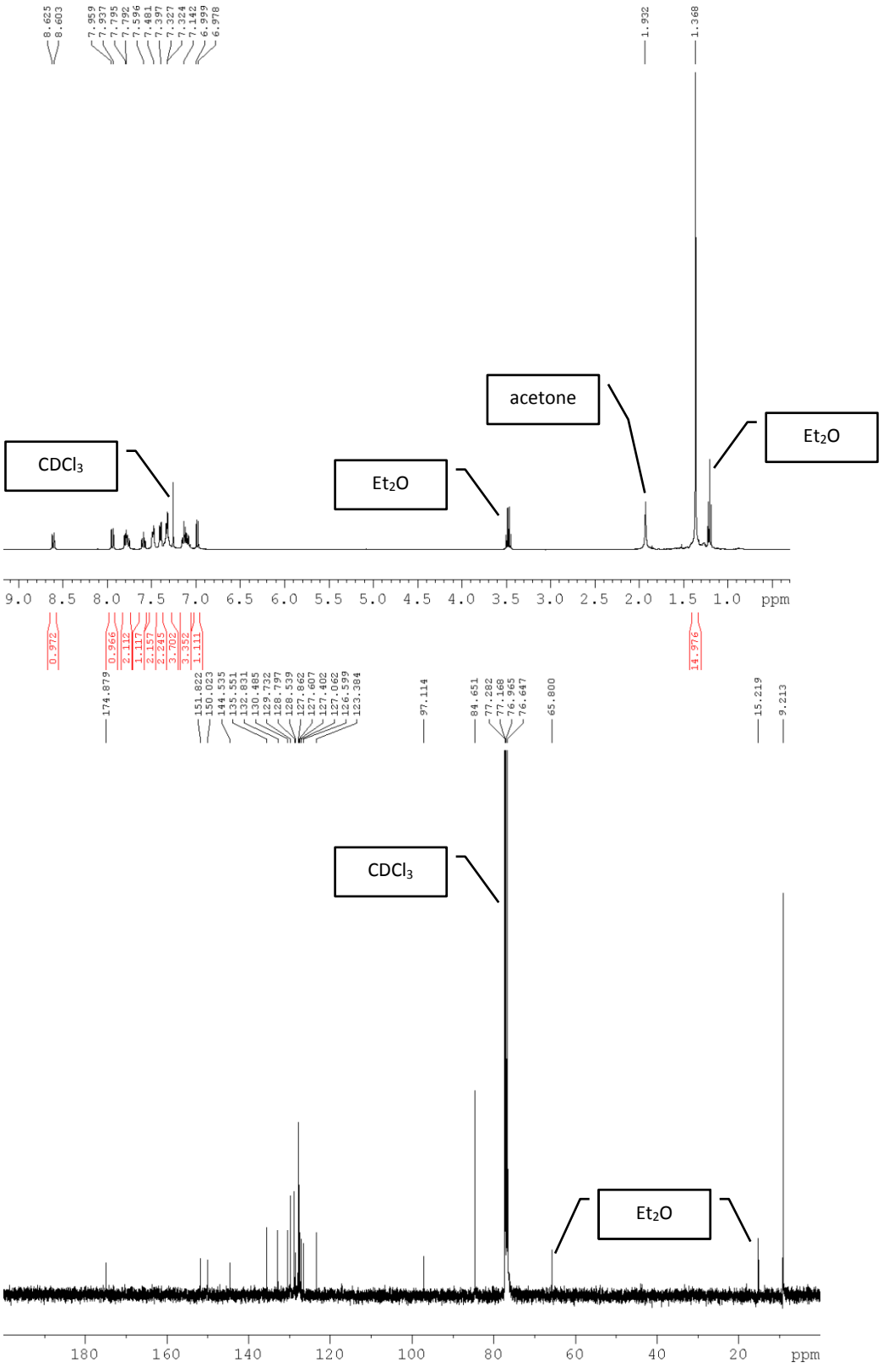

Attempts at anhydrous electrochemistry with µ-electrodes

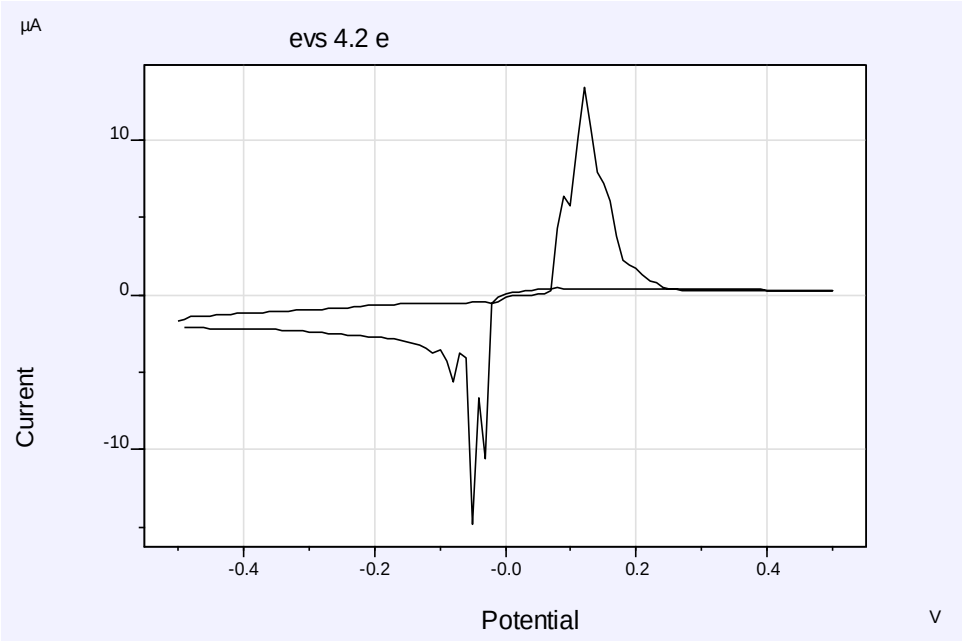

Figure A2.2 *Represenatative attempt using a Pt µ electrode (0.3µM diameter) to investigate Ferrocene, 10 mVs^{-1}, CE: Pt wire, RE: $Ag/AgNO_3$ in MeCN*

Mid-point analysis and Randles-Sevcik analysis for Ir1-Ir7

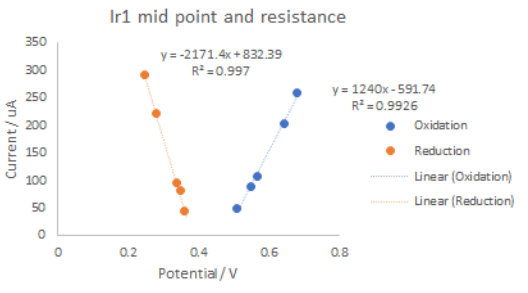

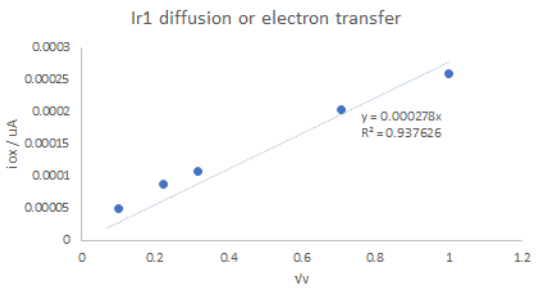

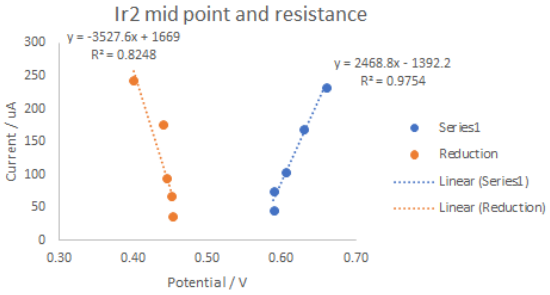

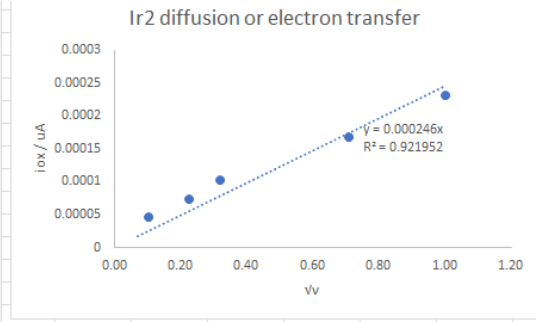

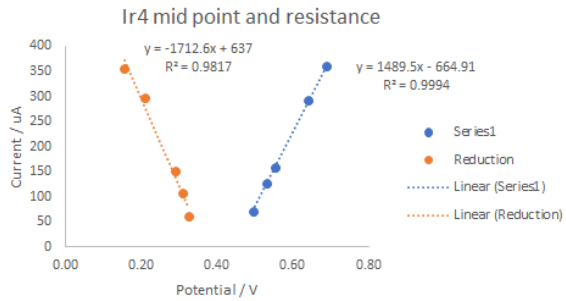

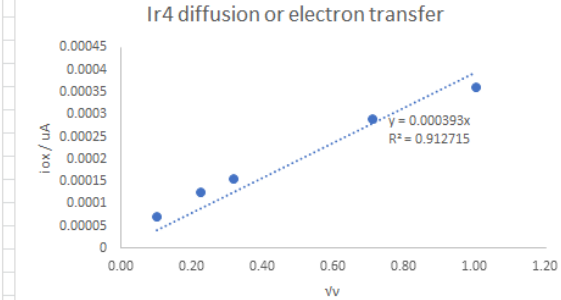

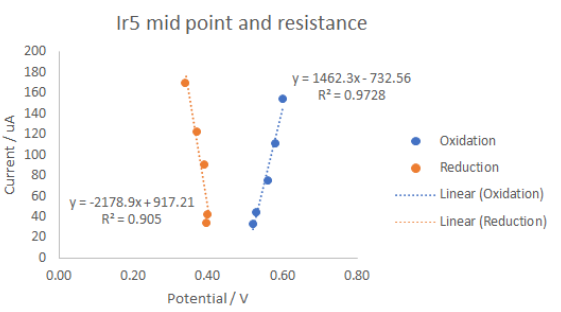

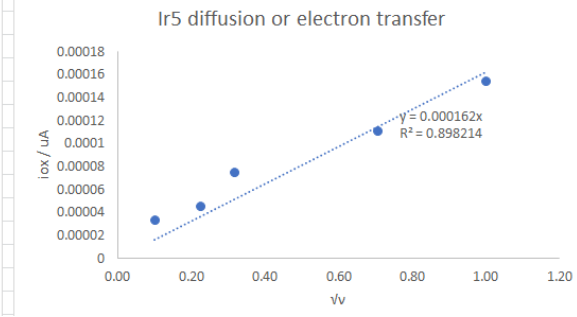

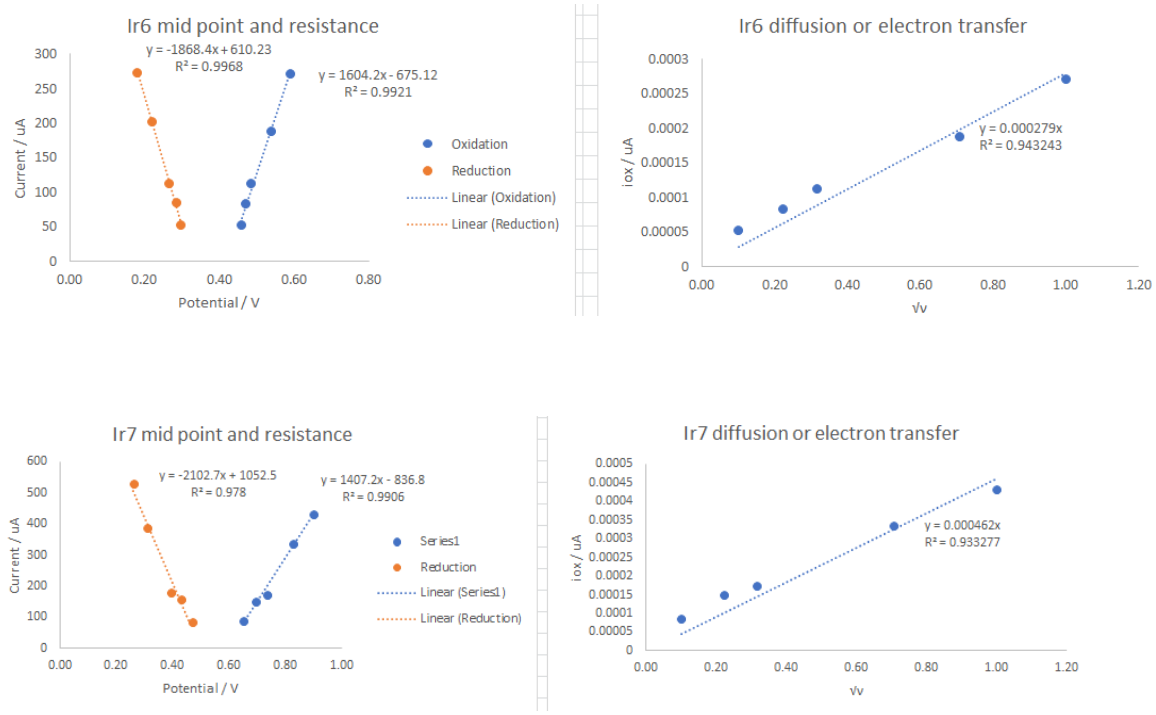

Figure A2.3 *Mid-point analysis and Randles-Sevick analysis for Ir1-Ir7 based on non-aqueous CV data*

Cp* loss for Ir1-Ir7 by ^{1}H NMR

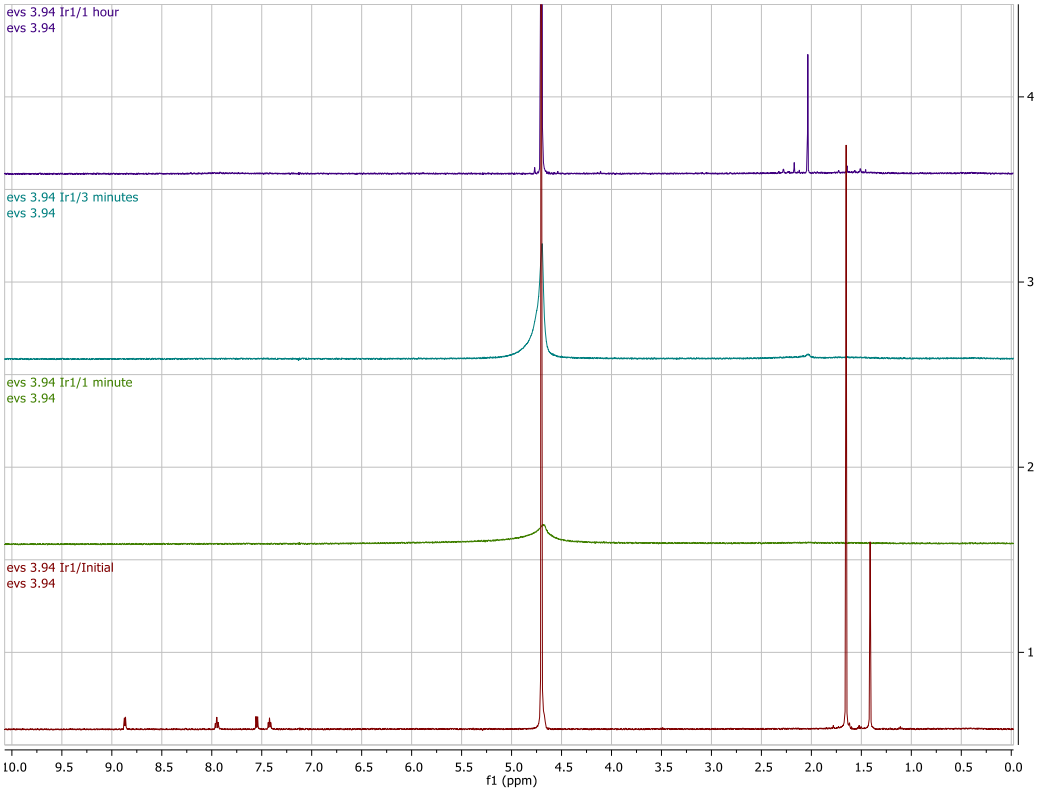

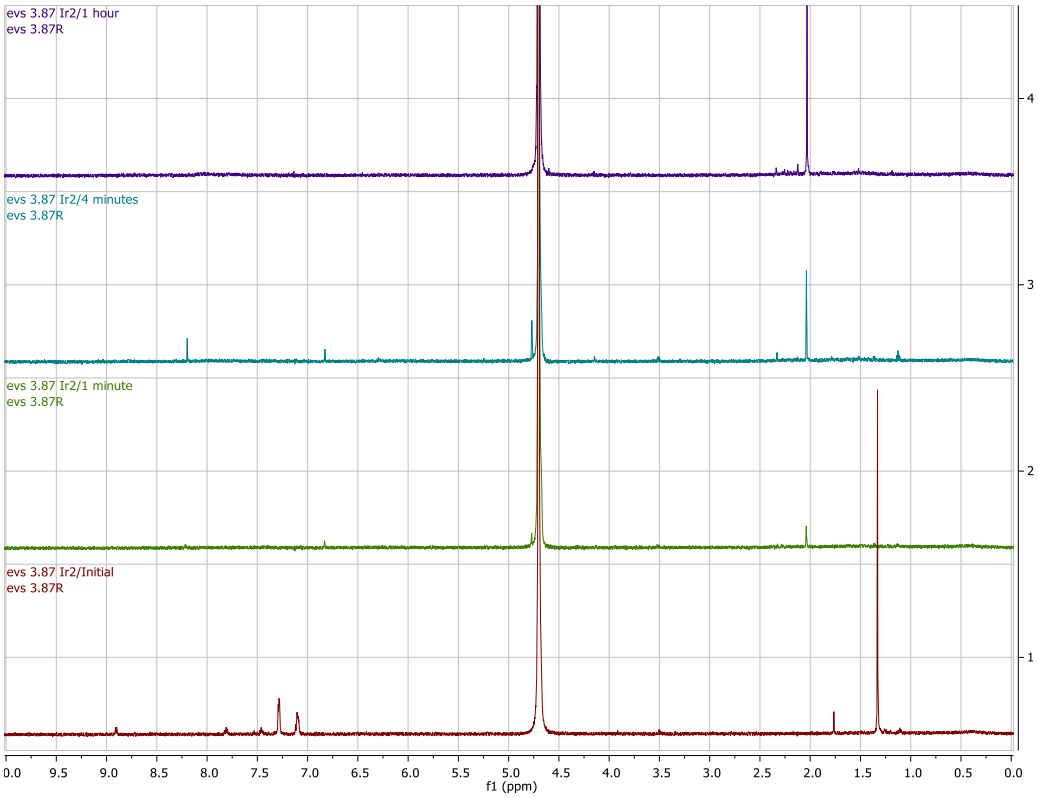

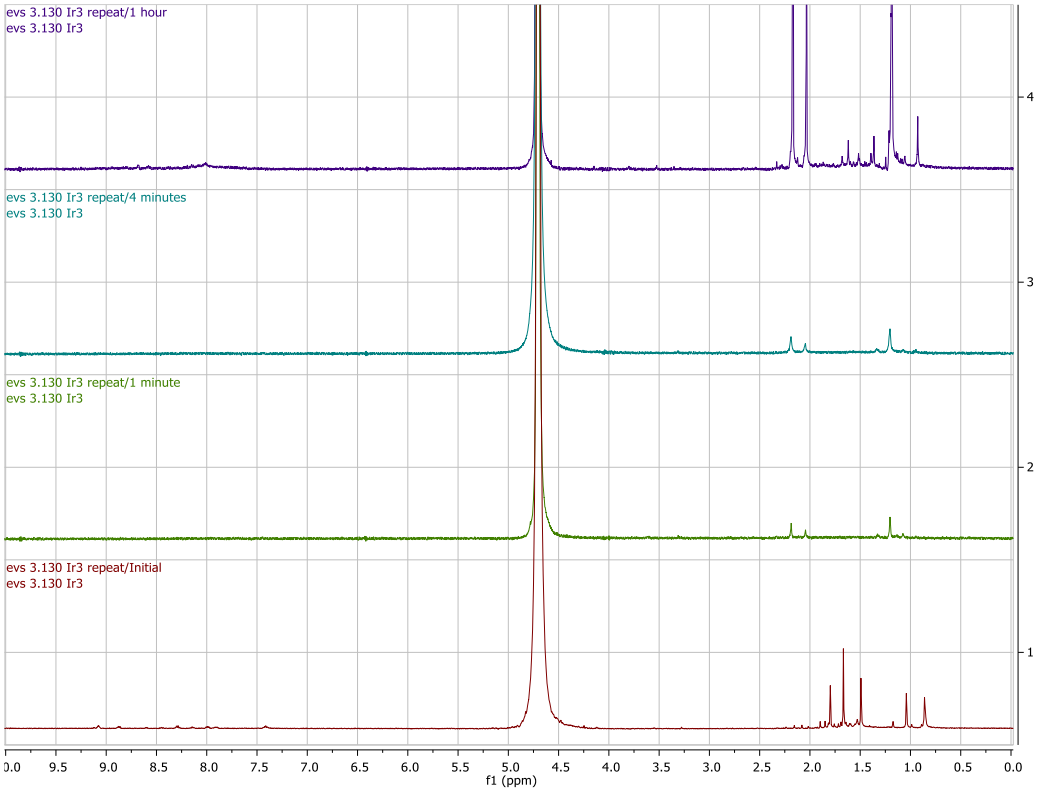
evs 3.130 Ir3 repeat/1 hour
evs 3.130 Ir3
evs 3.130 Ir3 repeat/4 minutes
evs 3.130 Ir3
evs 3.130 Ir3 repeat/1 minute
evs 3.130 Ir3
evs 3.130 Ir3 repeat/Initial
evs 3.130 Ir3
4
3
2
1
0.0 9.5 9.0 8.5 8.0 7.5 7.0 6.5 6.0 5.5 5.0 4.5 4.0 3.5 3.0 2.5 2.0 1.5 1.0 0.5 0.0
f1 (ppm)

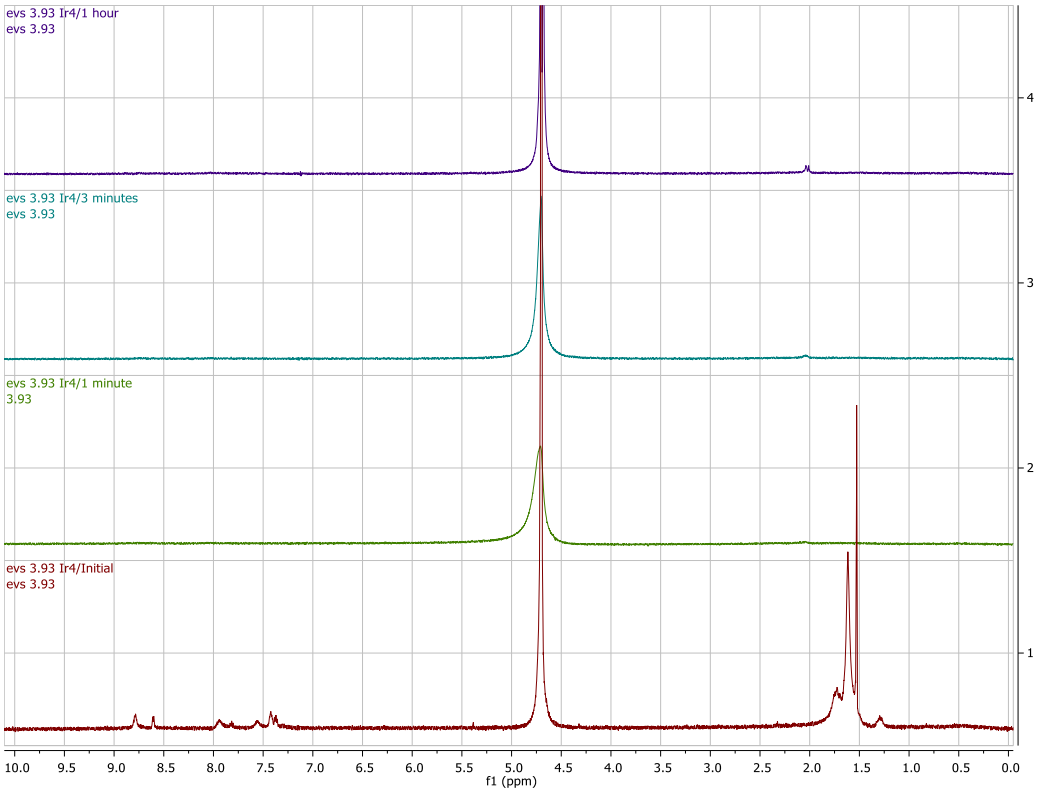
evs 3.93 Ir4/1 hour
evs 3.93
evs 3.93 Ir4/3 minutes
evs 3.93
evs 3.93 Ir4/1 minute
3,93
evs 3.93 Ir4/Initial
evs 3.93
4
3
2
1
10.0 9.5 9.0 8.5 8.0 7.5 7.0 6.5 6.0 5.5 5.0 4.5 4.0 3.5 3.0 2.5 2.0 1.5 1.0 0.5 0.0
f1 (ppm)

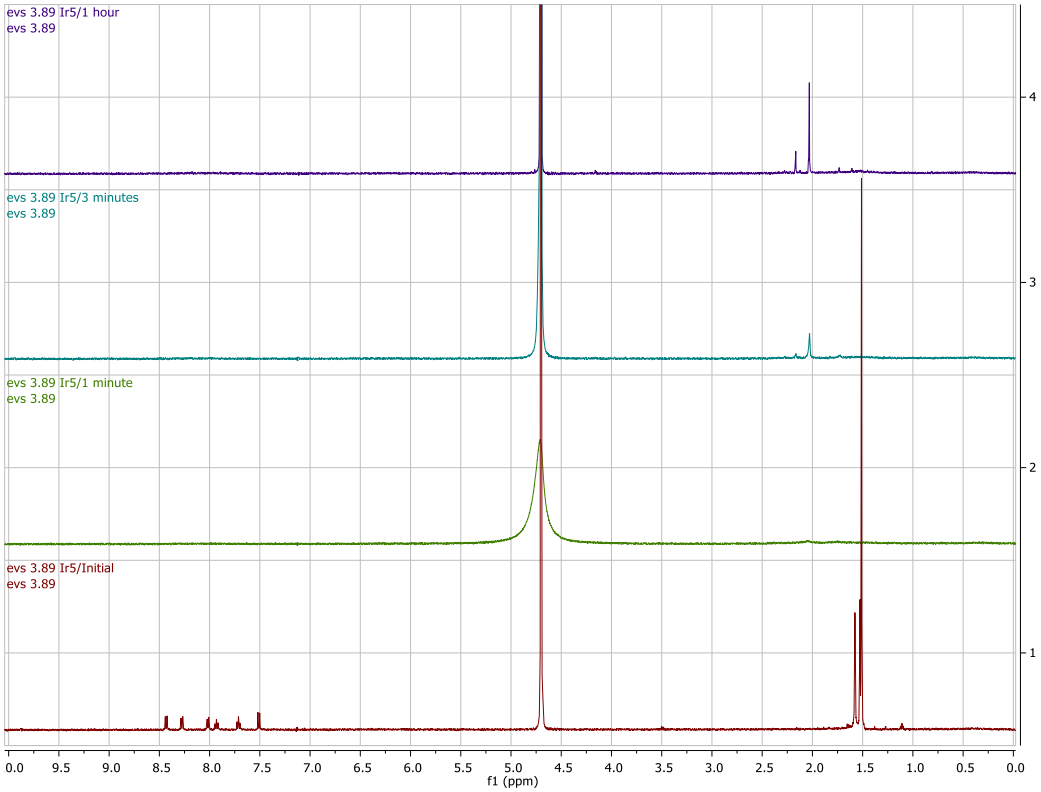
evs 3.89 Ir5/1 hour
evs 3.89
evs 3.89 Ir5/3 minutes
evs 3.89
evs 3.89 Ir5/1 minute
evs 3.89
evs 3.89 Ir5/Initial
evs 3.89
4
3
2
1
0.0 9.5 9.0 8.5 8.0 7.5 7.0 6.5 6.0 5.5 5.0 4.5 4.0 3.5 3.0 2.5 2.0 1.5 1.0 0.5 0.0
f1 (ppm)

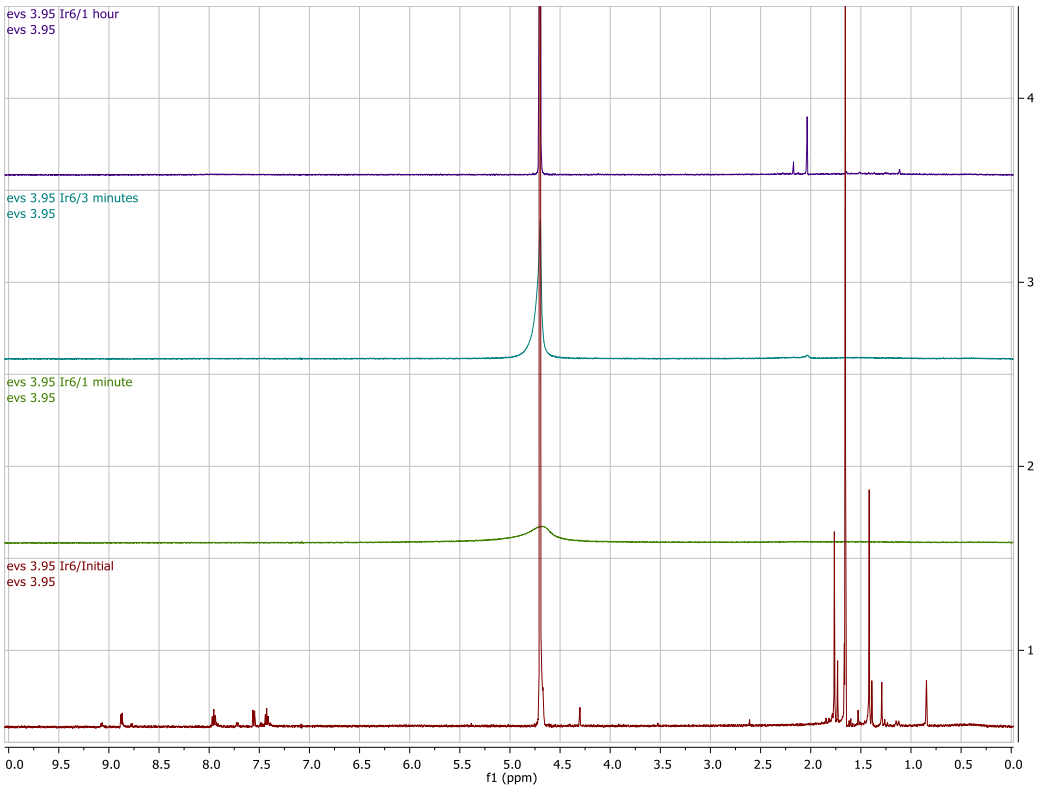
evs 3.95 Ir6/1 hour
evs 3.95
evs 3.95 Ir6/3 minutes
evs 3.95
evs 3.95 Ir6/1 minute
evs 3.95
evs 3.95 Ir6/Initial
evs 3.95
4
3
2
1
0.0 9.5 9.0 8.5 8.0 7.5 7.0 6.5 6.0 5.5 5.0 4.5 4.0 3.5 3.0 2.5 2.0 1.5 1.0 0.5 0.0
f1 (ppm)

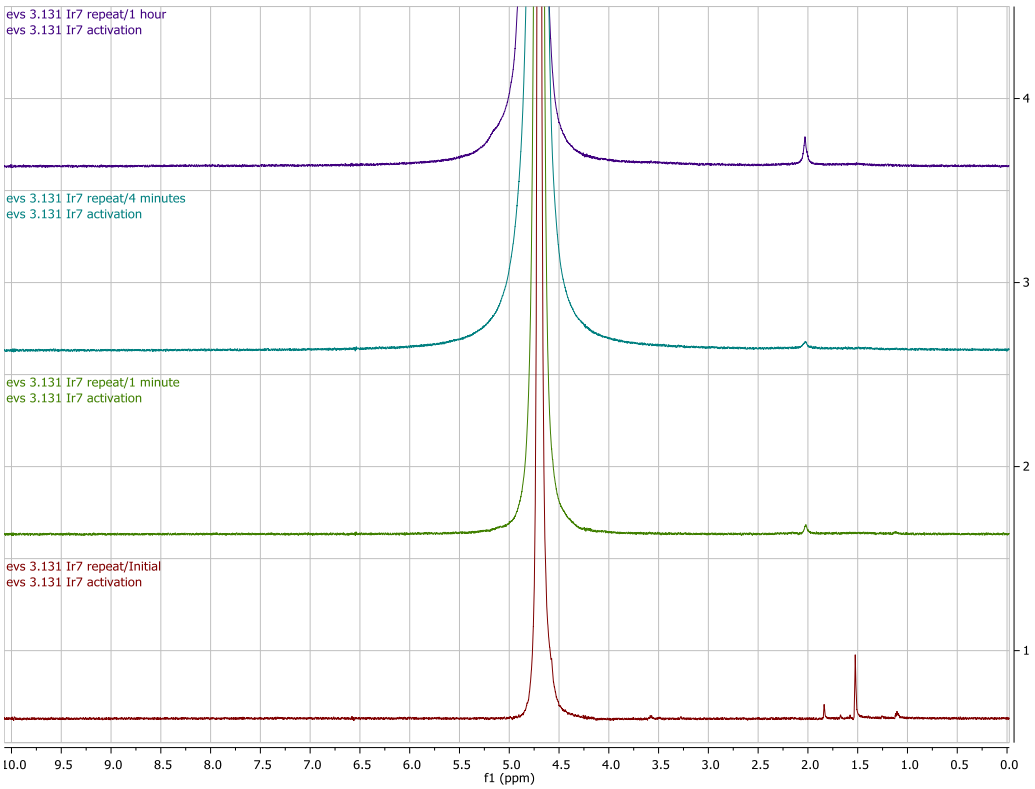

Figure A2.4 *^{1}H NMR spectra of compounds Ir1-Ir7 during precatalyst activation at t = 0 min, t = 1 min, t = 3 or 4 mins, t = 60 mins (from bottom to top). 5 mM [Ir] with 25 mM NaIO4 in D2O at room temperature.*

UV-vis trace of activation of Ir1 in pure H_2O

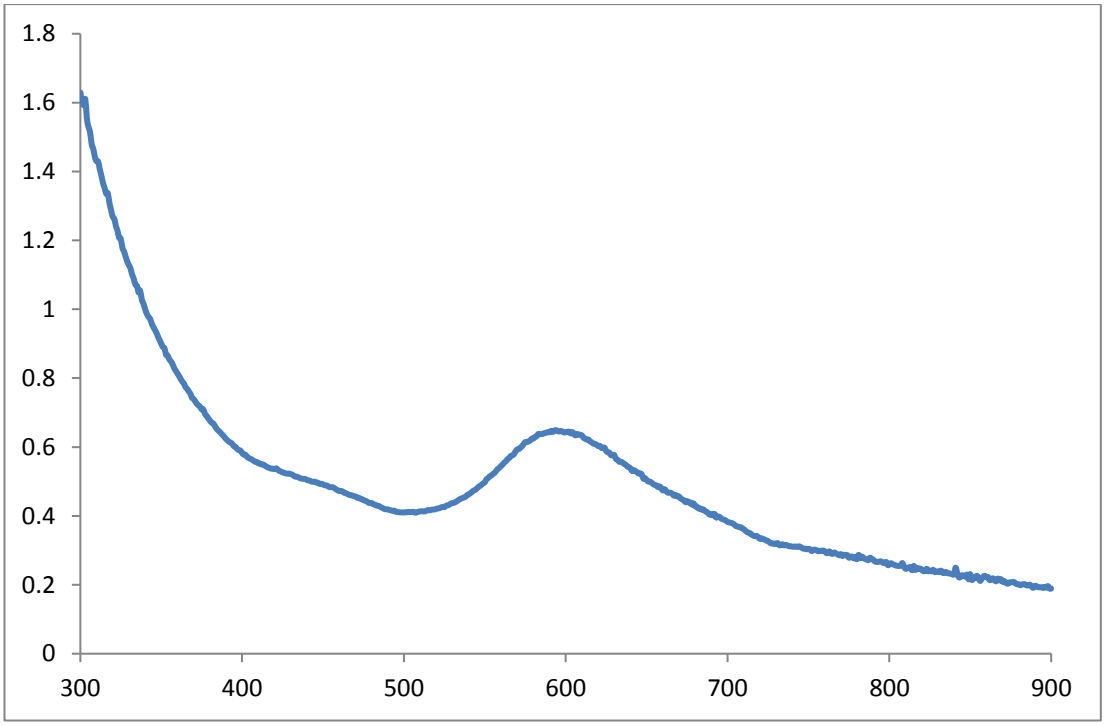

Figure A2.5 *Activation of Ir1 with 50 equivalents $NaIO_4$ in 100% H_2O*

Chapter 3

Water Oxidation Triplicate Data

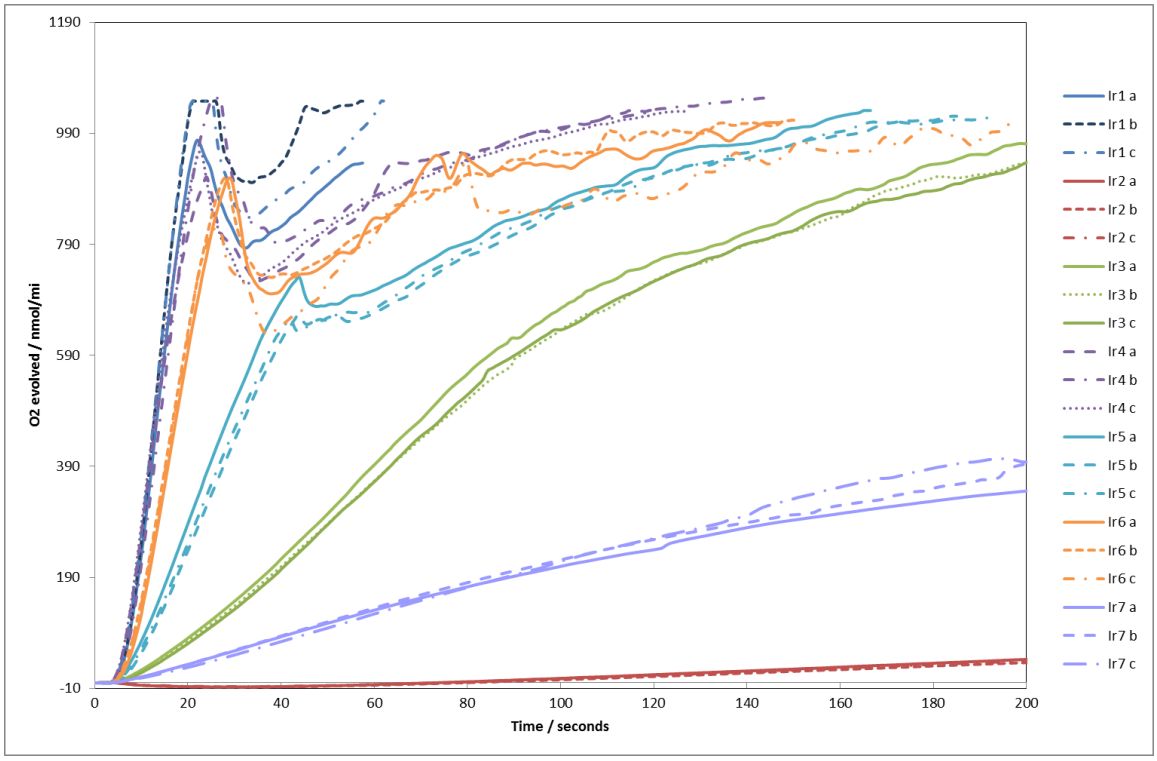

Figure A3.1 *Triplicate data for Ir1-Ir7 with $NaIO_4$ from Figure 3.4*

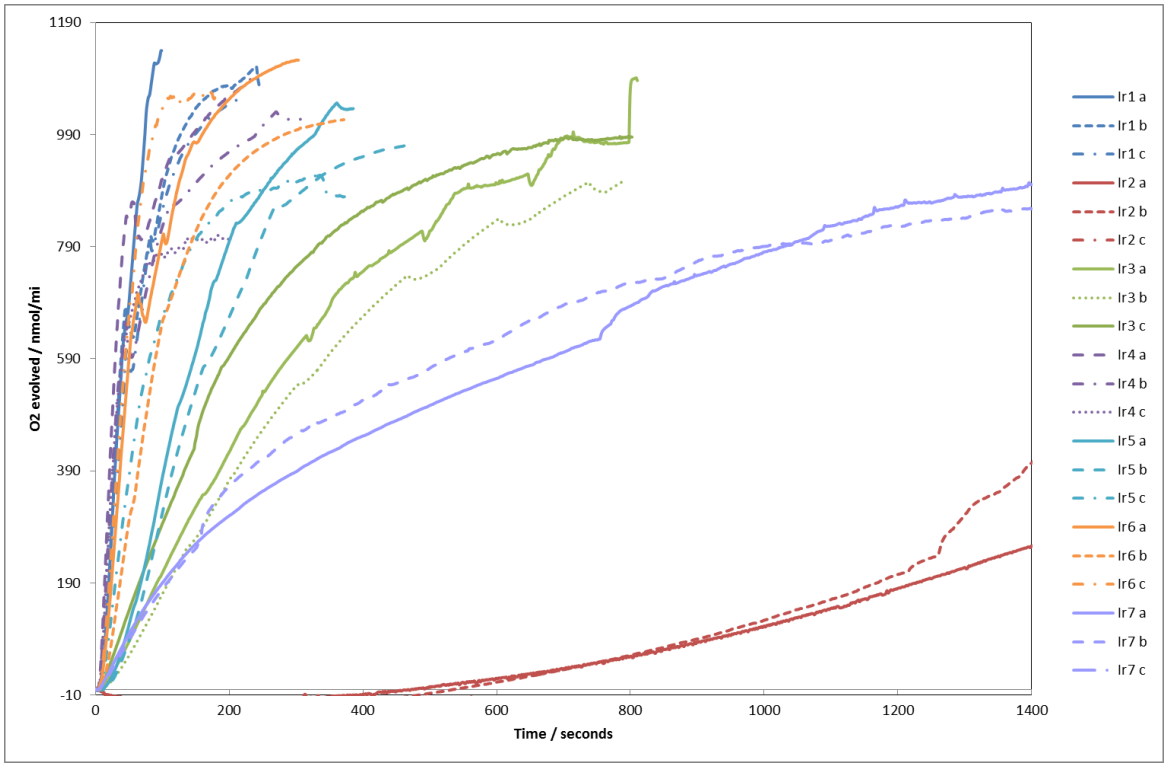

Figure A3.2 *Triplicate data for Ir1-Ir7 with $NaIO_4$ and 20% ^{t}BuOH from Figure 3.6*

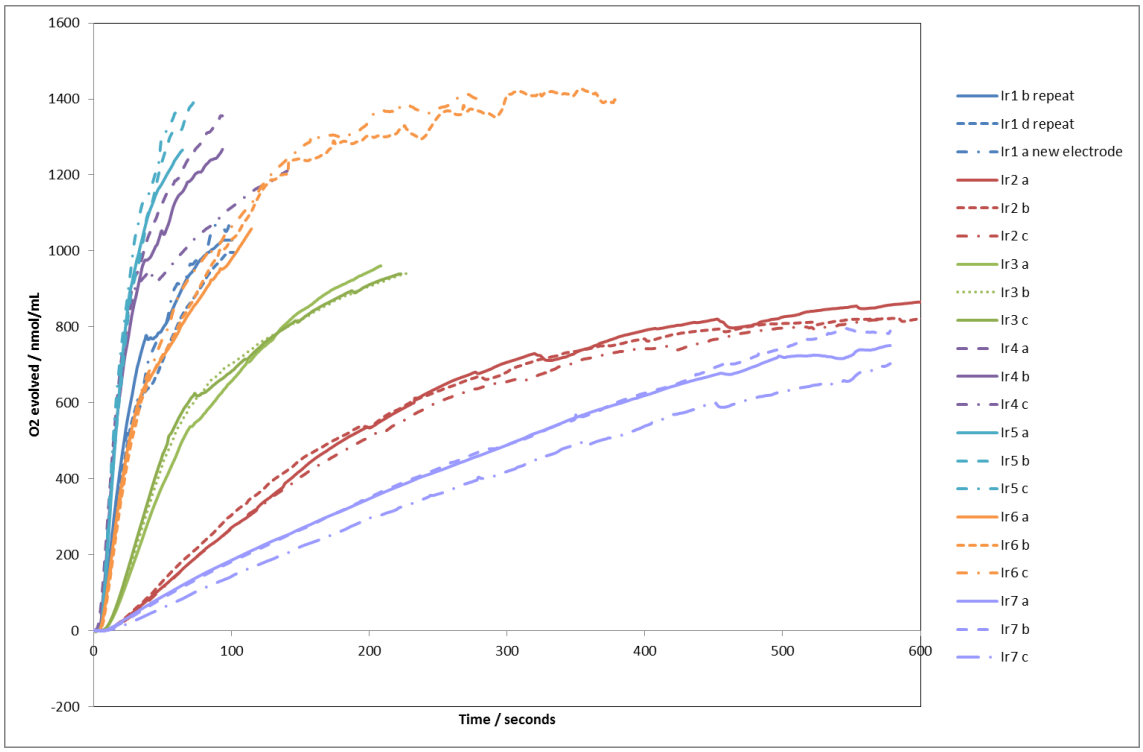

Figure A3.3 *Triplicate data for Ir1-Ir7 with CAN from Figure 3.7*

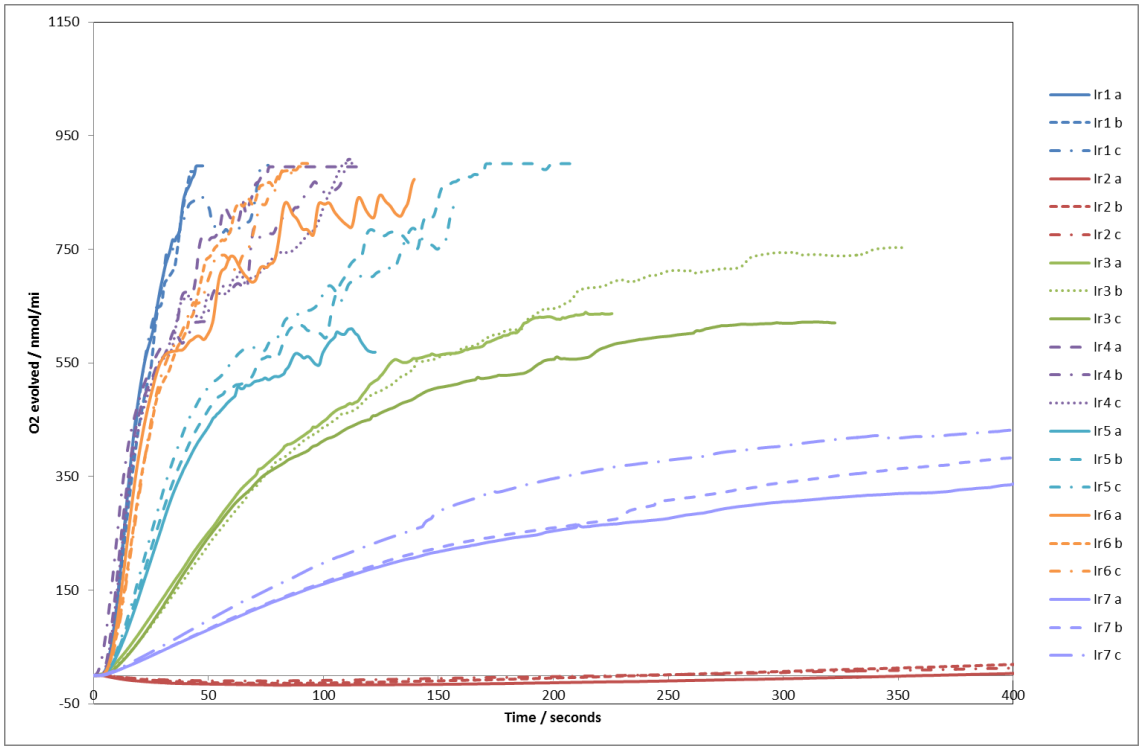

Figure A3.4 *Triplicate data for Ir1-Ir7 with $NaIO_4$ in D_2O from Figure 3.8*

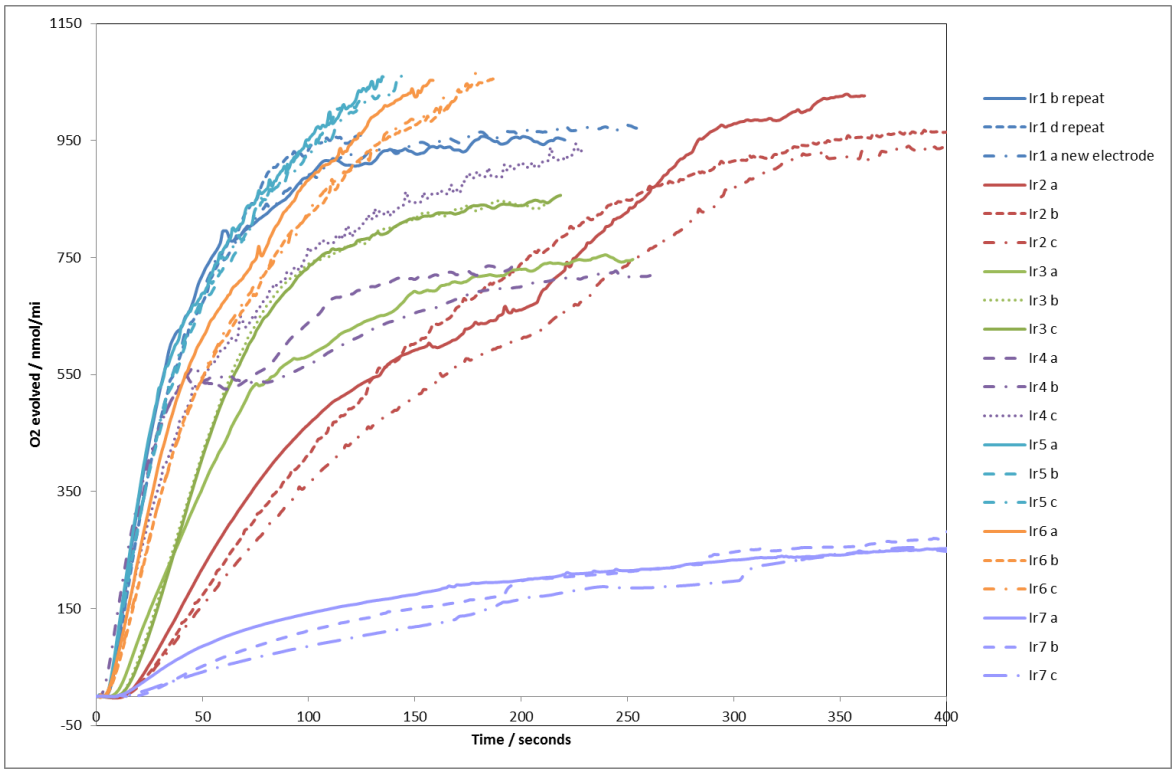

Figure A3.5 *Triplicate data for Ir1-Ir7 with $NaIO_4$ in D_2O from Figure 3.10*

Rate averages for all water oxidation triplicate data

Table S2. Average initial rates for all water oxidation data from triplicate data

		k_{obs} $NaIO_4$ µM min^{-1}			k_{obs} CAN µM min^{-1}			k_{obs} tBuOH µM min^{-1}			k_{obs} D_2O µM min^{-1}		
1	Repeats	4.115	4.619	4.512	1.794	1.718	2.016	1.251	1.267		2.260	1.998	2.147
	Std Dev		0.053			0.126			0.008			0.107	
	Average		4.415			1.842			1.259			2.135	
2	Repeats	0.020	0.018	0.019	0.194	0.292	0.179	0.015	0.018	0.020	0.007	0.008	0.006
	Std Dev		0.001			0.050			0.002			0.001	
	Average		0.019			0.222			0.017			0.007	
3	Repeats	0.437	0.403	0.407	0.515	0.415	0.408	0.145	0.127	0.188	0.336	0.312	0.331
	Std Dev		0.015			0.049			0.025			0.010	
	Average		0.416			0.446			0.153			0.327	
4	Repeats	3.628	3.590	3.914	1.632	1.987	2.055		1.220	1.272	2.126	1.893	1.877
	Std Dev		0.019			0.186			0.026			0.114	
	Average		3.711			1.891			1.246			1.965	
5	Repeats	1.309	1.175	1.207	1.292	1.163	1.197	0.204	0.159		0.680	0.743	0.827
	Std Dev		0.057			0.055			0.022			0.061	
	Average		1.231			1.217			0.181			0.750	
6	Repeats	2.842	2.905	2.901	1.226	1.072	1.075	0.834		0.987	1.769	1.479	1.452
	Std Dev		0.029			0.072			0.076			0.143	
	Average		2.883			1.124			0.910			1.567	
7	Repeats	0.142	0.146	0.128	0.086	0.090	0.094	0.135	0.122		0.101	0.103	0.125
	Std Dev		0.008			0.004			0.007			0.010	
	Average		0.139			0.090			0.126			0.110	

Data for log / log plot of [Ir]

[Ir]	ln([Ir])	Rate	ln(rate)
0	#NUM!	0	#NUM!
5.00E-06	-12.2061	16	2.772589
1.00E-05	-11.5129	27	3.295837
2.00E-05	-10.8198	43	3.7612
5.00E-05	-9.90349	76	4.330733
1.00E-04	-9.21034	85	4.442651
2.00E-04	-8.51719	125	4.828314

Table A3.7 *Log/log plot data for catalyst order determination*

Chapter 4

HSQC Plot for product of eucalyptol oxidation

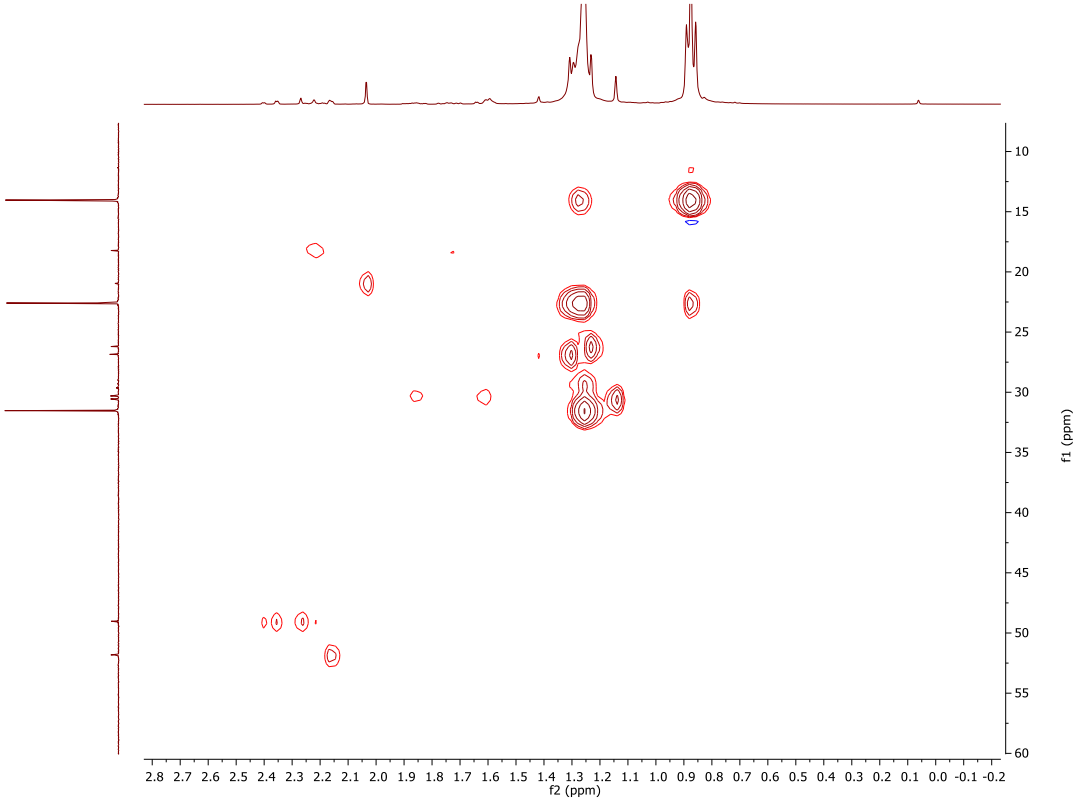

Figure A4.1 *2D NMR data of eucalyptol oxidation product*

^{1}H NMR data for β-elemene oxidation

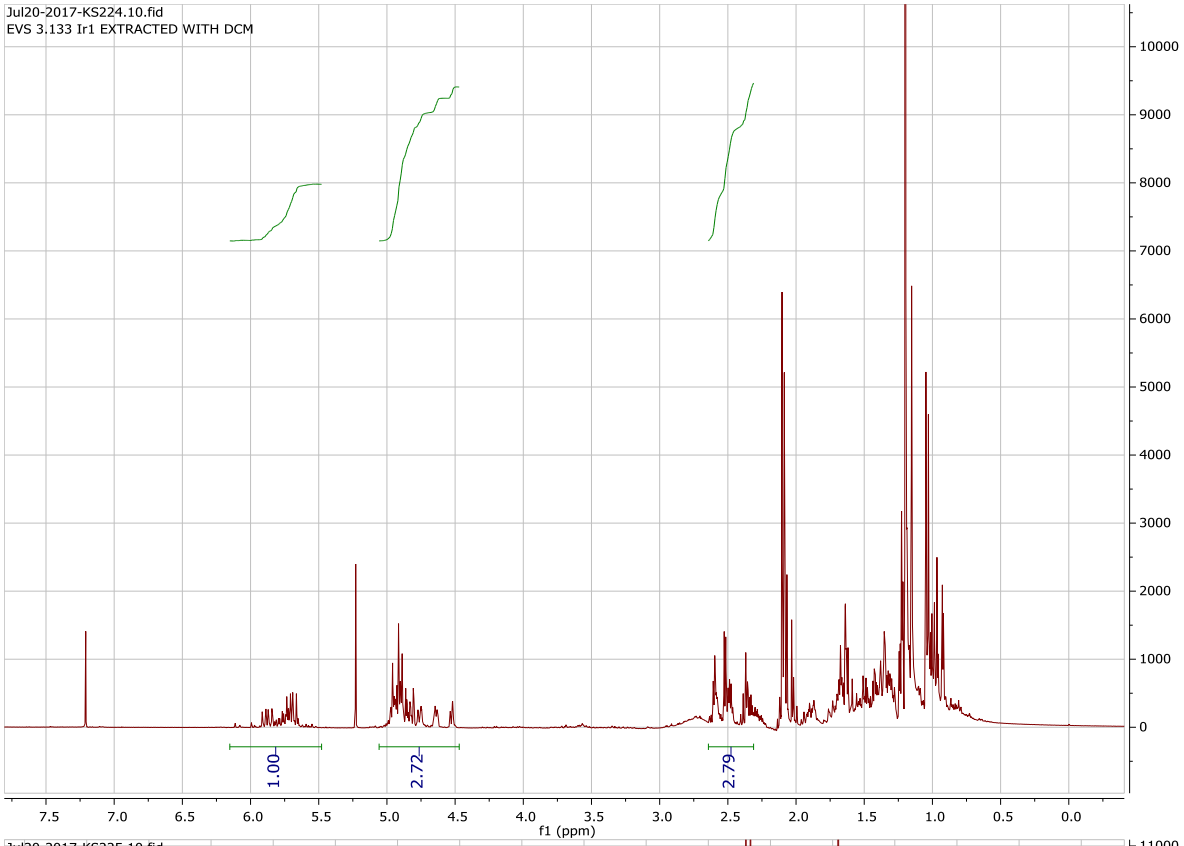

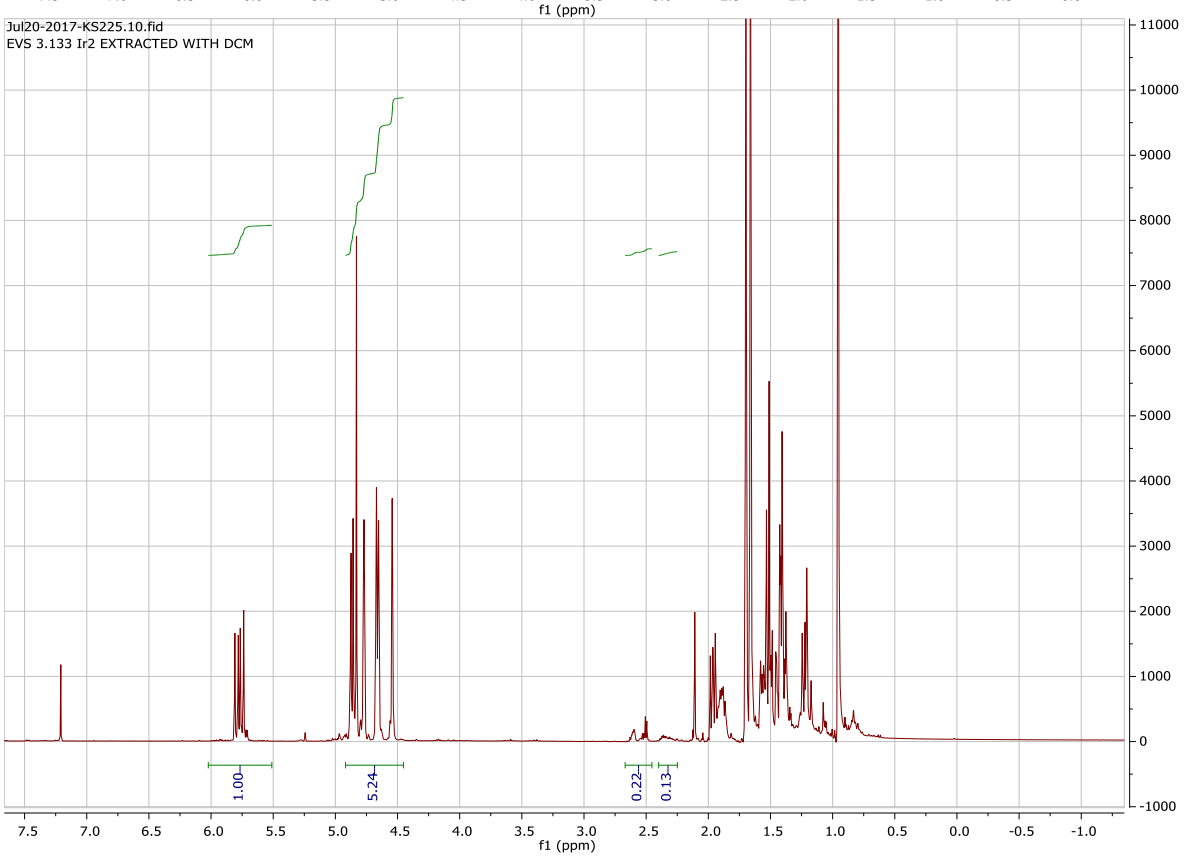

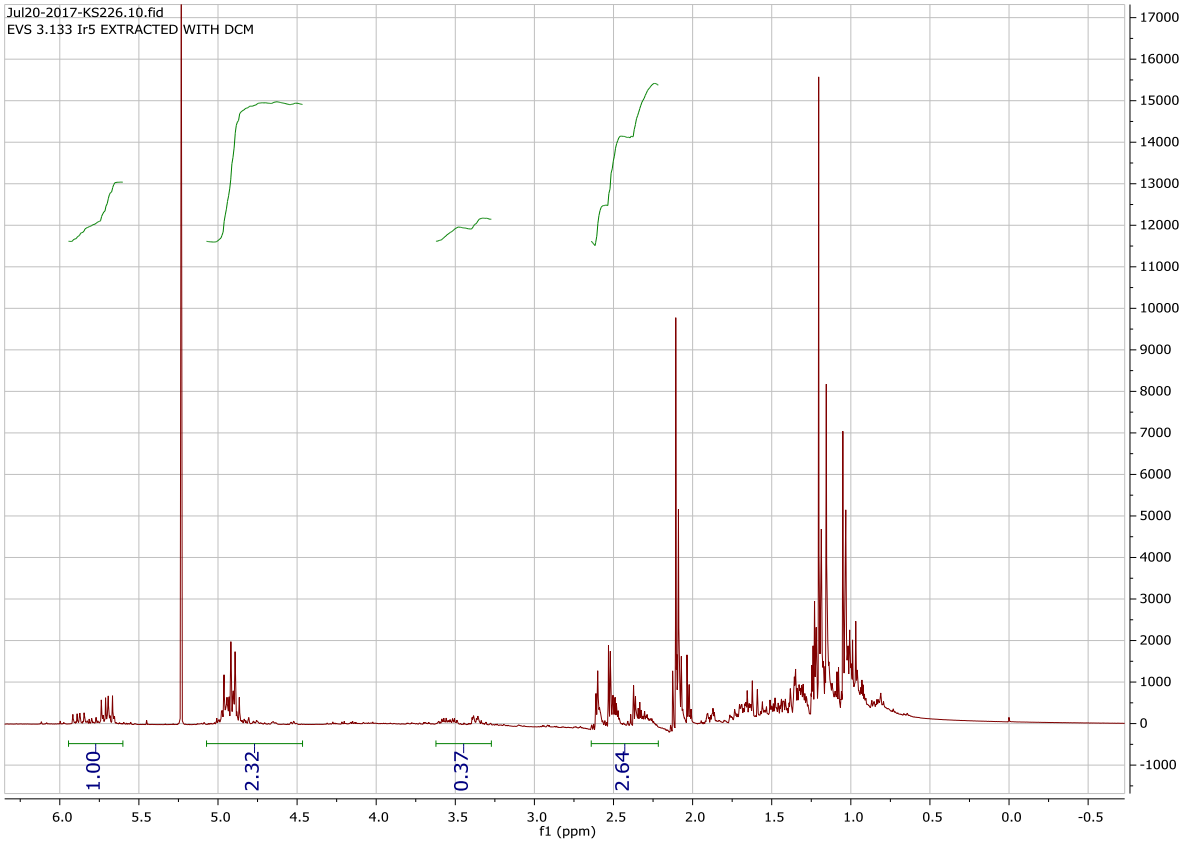

Figure A4.2. *^{1}H spectra of β-elemene oxidation with Ir1, Ir2 and Ir5*

Chapter 5

Data between catalyst run for electrochemical water oxidation showing no deposition

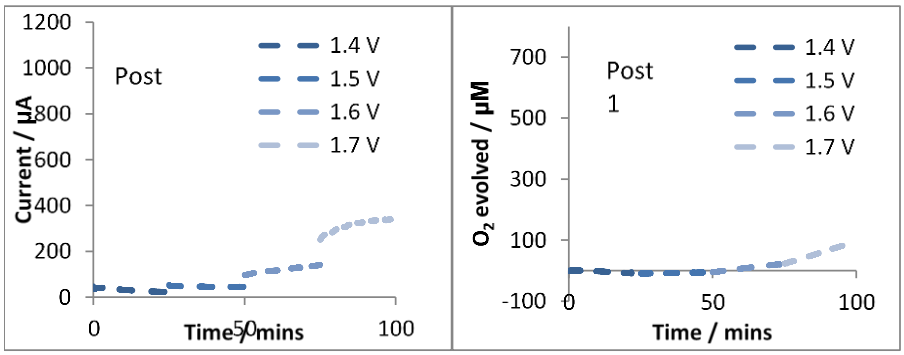

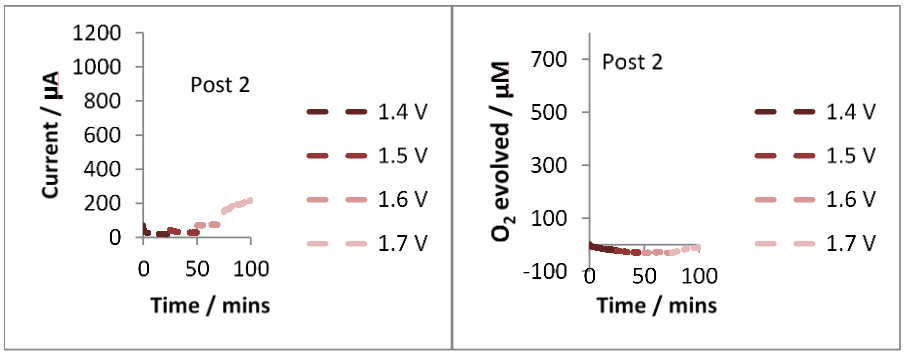

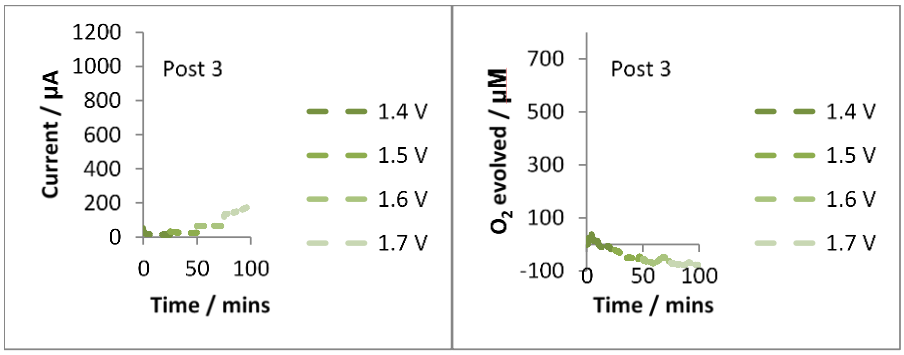

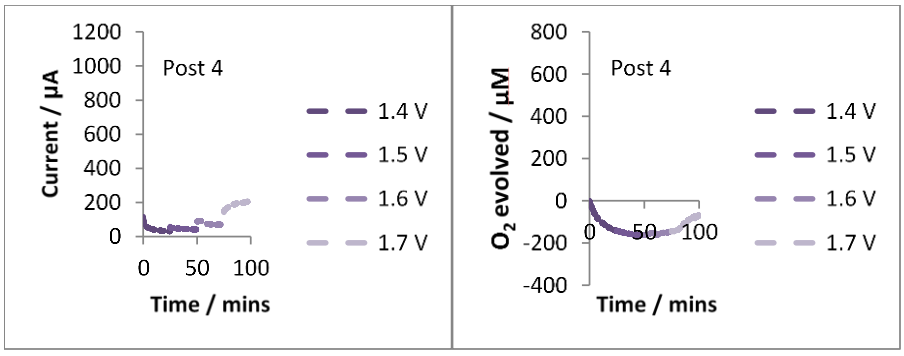

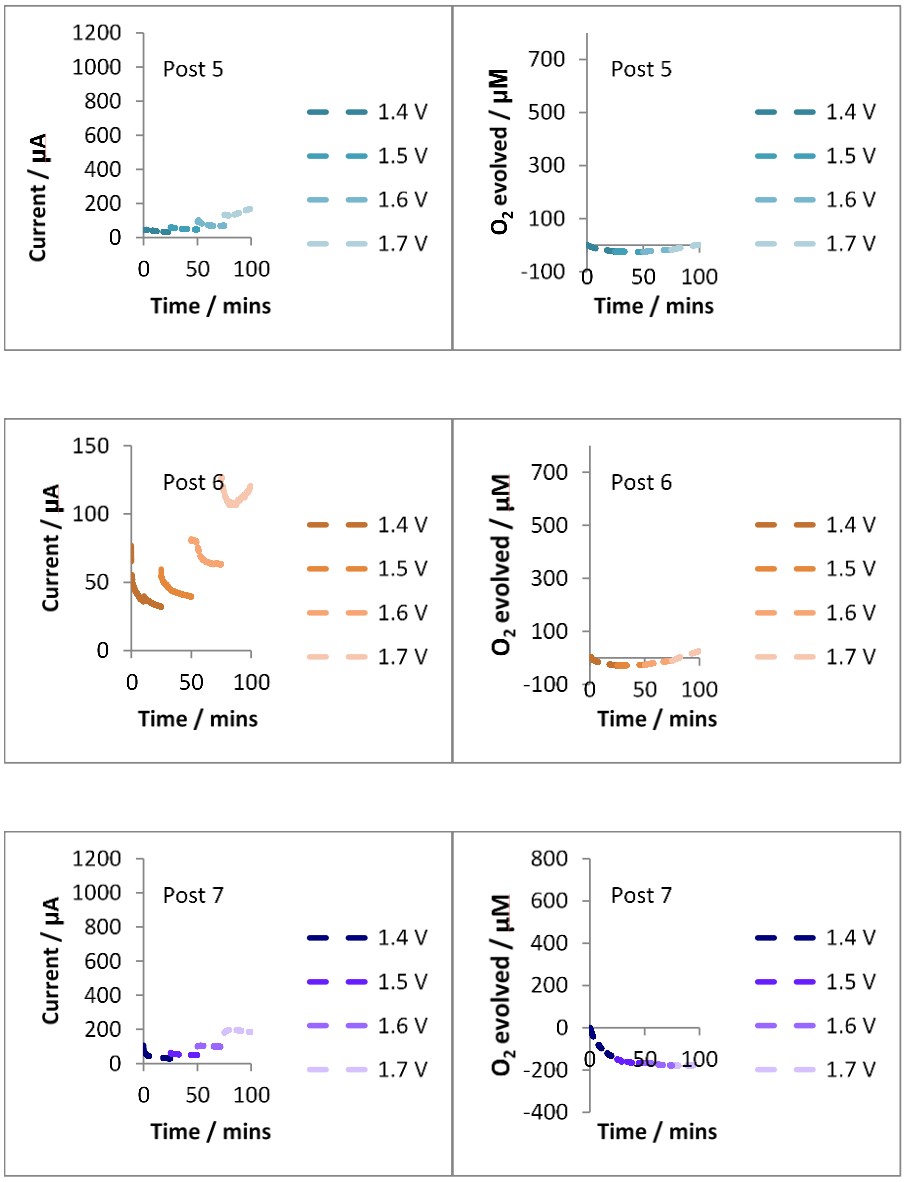

Figure A5.1. *Chronoamperometry (left) and oxygen evolution (right) traces for electrochemically driven water oxidation in a solution of $NaIO_3$ (250 mM). All solutions were adjusted to a pH of ~6 with NaOH and HNO_3 WE: BDD plate 1cm², CE: Pt wire, RE: Ag/AgCl, 2.5 mM [Ir1], 250mM $NaIO_3$. Chronoamperometry experiments were done for 25 mins at 1.4, 1.5, 1.6 and 1.7 V.*